Journal of
Mechanics of
Materials and Structures

FINITE STRAIN MICROMECHANICAL ANALYSIS FOR THERMOELASTOPLASTIC MULTIPHASE MATERIALS

JACOB ABOUDI

A micromechanical model that is based on the homogenization technique for periodic composites is developed for the prediction of the response of multiphase materials undergoing large deformations. Every one of the constituents is supposed to be either a rate-independent thermoelastoplastic material or a thermoelastic one, both of which are formulated in the framework of finite strains. Hyperelastic constituents are obtained as a special case. The resulting macroscopic (global) constitutive equations of the composite involve the instantaneous mechanical and thermal tangent tensors. The reliability of the prediction is examined by comparisons with the composite cylinder assemblage model, which is formulated for a finite strain rate-independent thermoplasticity and is valid under axisymmetric loading. Applications are given for a system of a rubber-like matrix reinforced by metallic fibers. In addition, the behavior of rate-independent elastoplastic laminated materials undergoing large deformations and subjected to in-plane loading is investigated. Finally, the response of an elastoplastic auxetic metallic material, which is capable of generating a negative Poisson's ratio at any stage of a finite strain loading is examined by employing the proposed micromechanical model.

1. Introduction

Finite strain inelastic anisotropic constitutive relations have been proposed for the modeling of the mechanical behavior of biological tissues. To this end, Tanaka and Yamada [1990] and Tanaka et al. [1996] combined the deformation due to an elastic transversely isotropic energy function with a viscoplastic deformation part in order to establish inelastic anisotropic constitutive relations for the finite strain modeling of the behavior of arteries and ventricular walls. More recently, Gasser and Holzapfel [2002] proposed a rate-independent finite strain elastoplastic anisotropic constitutive model for biological fiber-reinforced composites. The elastic part of the deformation is described by an anisotropic energy function, whereas the inelastic part is described by plastic slip on given planes which is the concept of slip systems used in rate-independent crystal plasticity. It should be noted that, in general, the modeling of the large deformations of hyperelastic anisotropic materials requires a formulation of a strain-energy function that consists of a dependence on five invariants for transversely isotropic behavior. For orthotropic materials a dependence on seven invariants is necessary, while for composites with two families of fibers the number of invariants is eight [Spencer 1971; 1984; Holzapfel 2000]. Thus, it is quite obvious that, in general, the establishment of such energy functions is very complicated.

A micromechanical analysis that is based on the properties of the constituents and the detailed representation of their interaction forms an alternative approach for the finite strain inelastic anisotropic

modeling of materials and biological tissues. Such an approach was followed by van der Sluis et al. [2001] where the homogenization method for periodic composites has been employed to analyze a composite that consists of a polycarbonate elastic-viscoplastic matrix reinforced by elastic particles. The elastic-viscoplastic matrix is modeled as a hyperelastic isotropic material in the elastic region, whereas Perzyna's viscoplasticity [1966] is used to characterize the inelastic part. The additive decomposition of the rate of deformation tensor is used in conjunction with the objective Truesdell stress rate. The rubber inclusions are modeled by a hyperelastic compressible isotropic neo-Hookean constitutive law. Finally, the finite element procedure is employed to solve the governing equations. Finite strain viscoplastic composites were also modeled by a micromechanical analysis referred to as *high-fidelity generalized method of cells* (HFGMC) which is based on the homogenization technique for periodic composites [Aboudi 2004a; 2004b]. To this end, the monolithic inelastic matrix was modeled by the elastic-viscoplastic constitutive relations with isotropic and directional hardening of Rubin [1987] (in which, in particular, the stress is not characterized by a hypoelastic equations so that no special rates of stress need to be considered).

In the present investigation, we offer to generalize the HFGMC micromechanical model for predicting the large rate-independent thermoelastoplastic deformation of multiphase composites in which any one of the constituents is considered either as a rate-independent isotropic thermoelastoplastic material or a isotropic thermoelastic one. In order to carry out such an investigation, a suitable rate-independent finite strain thermoelastoplastic constitutive law must be established. Formulations of the theory of plasticity with large deformation have been presented by Lubliner [1990] where related references are given. A particular constitutive model for a rate-independent finite plasticity that avoids the difficulties posed by the rate formulation is given by Simo [1988b; 1988a] and summarized by Simo and Hughes [1998]. It is based on the multiplicative decomposition of the deformation gradient and the stress-deformation relation is derived from a suitable energy function. This is followed by a radial-mapping algorithm for the integration of the flow rule and hardening law and the establishment of a consistent elastoplastic tangent tensor. This rate-independent finite strain plasticity formulation is adopted herein to model the rate-independent elastoplastic constituents of some of the multiphase composites whose behavior is micromechanically analyzed by the HFGMC model. A generalization is also proposed in order to include thermal effects by introducing a suitable free-energy function.

This paper is organized as follows. A very brief summary of the finite strain rate-independent plasticity is given in Section 2. This is followed in Section 3 by presenting the finite strain macroscopic constitutive rate equations that govern the multiphase thermoelastoplastic material which are established by employing the homogenization technique for periodic composites. In Section 4, verifications of the HFGMC micromechanical predictions are made by a comparison with the concentric cylinder assemblage (CCA) model which is valid for an axisymmetric loading. To this end, the average radial stress of a porous thermoelastoplastic material that is subjected to axisymmetric thermomechanical loading (a one-dimensional problem in polar coordinates) is compared with the HFGMC prediction of a porous composite subjected to a biaxial and thermal loading (a two-dimensional problem). It should be noted that in the derivation of the thermoelastoplastic CCA model, the instantaneous tangent tensors are not utilized whereas they are an essential ingredient in the development of the HFGMC model, thus rendering the comparison between the two models significant since they are based on totally different approaches. Section 5 presents several applications of the micromechanical model. To this end a hypothetical system of a rubber-like matrix reinforced by unidirectional metallic fibers is considered. The fibers are modeled

by the finite thermoplasticity theory which was discussed in Section 2, whereas the matrix is modeled as a neo-Hookean hyperelastic material. Furthermore, the present finite strain elastoplastic micromechanics model is employed as a constitutive equation in a lamination theory to investigate the response of several types of symmetric laminates subjected to in-plane loading. Auxetic materials become thicker when stretched and thinner when compressed. This implies that the Poisson's ratio of this type of materials is negative. A recent review of auxetic materials and their utilization in various practical applications has been given by Alderson and Alderson [2007]. This review includes the fabrication, characterization, testing, and possible applications of auxetic cellular solids, polymers, and fiber-reinforced materials. In the present section, a reentrant configuration of a metallic elastoplastic material undergoing finite deformation, which is capable to generate instantaneous negative Poisson's ratios, is considered. The conclusion offers several possible applications and generalizations of the present micromechanical approach.

2. Finite thermoplasticity of monolithic materials

Let $\mathbf{X}$ and $\mathbf{x}$ denote the location of a point in the material with respect to the initial (Lagrangian) and current systems of coordinates, respectively, and let t denote the time. In terms of the local deformation gradient tensor $\mathbf{F}(\mathbf{X}, t)$, $d\mathbf{x} = \mathbf{F}(\mathbf{X}, t)d\mathbf{X}$. The finite plasticity theory that was presented by Simo [1988b; 1988a] and summarized by Simo and Hughes [1998] is based on the introduction of a stress-free intermediate configuration and a multiplicative decomposition of the local deformation gradient $\mathbf{F}(\mathbf{X}, t)$ in the form $\mathbf{F}(\mathbf{X}, t) = \mathbf{F}^e(\mathbf{X}, t)\mathbf{F}^p(\mathbf{X}, t)$, where $\mathbf{F}^p(\mathbf{X}, t)$ and $\mathbf{F}^e(\mathbf{X}, t)$ are the deformation gradient tensors from the initial to the intermediate and from the intermediate to the current configuration, respectively. The corresponding right Cauchy–Green tensors are given by

$$\mathbf{C} = \mathbf{F}^T\mathbf{F}, \quad \mathbf{C}^p = \mathbf{F}^{pT}\mathbf{F}^p, \tag{1}$$

where superscript T denotes the transpose operation. The left Cauchy–Green tensors $\mathbf{B}$ and $\mathbf{B}^e$ are defined by

$$\mathbf{B} = \mathbf{F}\mathbf{F}^T, \quad \mathbf{B}^e = \mathbf{F}^e\mathbf{F}^{eT}$$

For an isotropic elastoplastic material, Simo [1988b; 1988a] and Simo and Hughes [1998] introduced an energy function which is decomposed into volumetric and deviatoric parts. Here a generalization is offered that provides a thermoelastoplastic free-energy function W in the form

$$W = \frac{\kappa}{2}\left[\tfrac{1}{2}(J^2 - 1) - \ln J\right] - 3\kappa\hat{\alpha}(\theta - \theta_0)\ \ln J + \frac{\mu}{2}\left[\mathrm{tr}(\bar{\mathbf{B}}^e) - 3\right],$$

where κ, $\hat{\alpha}$, and $\theta - \theta_0$ are the bulk modulus, the thermal expansion coefficient, and the current temperature deviation from a reference temperature θ_0, respectively, and $\bar{\mathbf{B}}^e = J^{-2/3}\mathbf{B}^e$, with $J = \det \mathbf{F}$.

The Kirchhoff stress tensor $\boldsymbol{\tau}$ can be derived from the energy function W to yield

$$\boldsymbol{\tau} = \left[\tfrac{1}{2}\kappa(J^2 - 1) - 3\kappa\hat{\alpha}(\theta - \theta_0)\right]\mathbf{I} + \mu\,\mathrm{dev}(\bar{\mathbf{B}}^e), \tag{2}$$

where $\mathbf{I}$ is the unit second-order tensor and $\mathrm{dev}(\mathbf{T})$ denotes the deviatoric part of tensor $\mathbf{T}$.

For isotropic hardening, the von Mises yield criterion is given by $f(\boldsymbol{\tau}, \alpha) = \|\mathbf{s}\| - \sqrt{\tfrac{2}{3}}\big(Y + k(\alpha)\big) \le 0$, where $\mathbf{s} = \mathrm{dev}(\boldsymbol{\tau}) = \mu\,\mathrm{dev}(\bar{\mathbf{B}}^e)$, and Y is the initial yield stress and $k(\alpha)$ is the isotropic hardening law with respect to the variable α. For a linear isotropic hardening $k(\alpha) = K\alpha$.

The associative flow rule was determined by Simo [1988a; 1988b] by the principle of maximum plastic dissipation [Lubliner 1990]. It is given by

$$\frac{\partial}{\partial t}\mathbf{C}^{p-1} = -\tfrac{2}{3}\gamma \operatorname{tr}(\mathbf{B}^e) \, \mathbf{F}^{-1} \, \frac{\mathbf{s}}{\|\mathbf{s}\|} \, \mathbf{F}^{-T},$$

and the evolution of the hardening variable α is determined, as in the infinitesimal theory of plasticity, from the consistency parameter γ in the form $\dot{\alpha} = \sqrt{\tfrac{2}{3}}\gamma$.

The radial return algorithm was extended by Simo [1988b; 1988a] and Simo and Hughes [1998] to the present theory of finite plasticity in order to obtain the variables τ_n, α_n and $\bar{\mathbf{B}}_n^e$ at any time step t_n at which the deformation gradient $\mathbf{F}_n$ is given. One can readily determine $\mathbf{C}_n^{p-1}$ from $\bar{\mathbf{B}}_n^e$ by employing the relation $\bar{\mathbf{B}}^e = J^{-2/3}\mathbf{F}\mathbf{C}^{p-1}\mathbf{F}^T$.

The formulation of the finite strain micromechanical analysis that is presented in the next section is based upon the rate of the actual stresses, referred to the undeformed configuration, which is expressed in terms of the rates of deformation gradient and temperature. Consequently, the constitutive equation of the monolithic thermoelastoplastic materials involves the first (unsymmetric) Piola–Kirchhoff stress tensor $\mathbf{T}$ which is related to the Kirchhoff stress τ as follows

$$\mathbf{T} = \mathbf{F}^{-1}\tau. \tag{3}$$

The rate of the first Piola–Kirchhoff stress tensor $\dot{\mathbf{T}}$ is related to the rates of deformation tensor $\dot{\mathbf{F}}$ and temperature $\dot{\theta}$ in terms of the first tangent $\mathbf{R}$ and thermal stress $\mathbf{H}$ tensors, respectively, as follows

$$\dot{\mathbf{T}} = \mathbf{R} : \dot{\mathbf{F}} - \mathbf{H}\dot{\theta}, \tag{4}$$

where the expression $\mathbf{R} : \dot{\mathbf{F}}$ provides the double contraction of the fourth-order tensor $\mathbf{R}$ with the second-order tensor $\dot{\mathbf{F}}$. The fourth-order tensor $\mathbf{R}$ is given in terms of the consistent elastoplastic spatial tangent tensor $\mathbf{c}^{ep}$ by

$$R_{ijkl} = F_{ip}^{-1}\big[c_{jpkq}^{ep} + \tau_{jk}\delta_{pq}\big]F_{lq}^{-1},$$

where δ_{pq} is the Kronecker delta. The consistent elastoplastic spatial tangent tensor $\mathbf{c}^{ep}$ is given by Simo and Hughes [1998]. The second-order thermal stress tensor $\mathbf{H}$ is given by $\mathbf{H} = 3\kappa\hat{\alpha}\mathbf{F}^{-1}$.

In order to illustrate an application of these constitutive equations, we consider a metallic thermoelastoplastic linear hardening material whose properties are given in Table 1 (in the range of small deformation, these parameters correspond to the characterization of the aluminum alloy 2024–T4 at room temperature). Figure 1(a) shows the uniaxial Kirchhoff stress variation against the deformation gradient of this material under one cycle of a mechanical loading and unloading. This figure shows also the material response when the plasticity effects are neglected, thus yielding a nonlinearly elastic behavior. Here, there is a slight nonlinearity which can be well observed. As a result, the linear hardening is slightly affected by this nonlinearly elastic behavior. Figure 1(b) shows the corresponding behavior of this material when

κ (GPa)	μ (GPa)	$\hat{\alpha}$ (K^{-1})	Y (MPa)	K (GPa)
71	27.2	22.5×10^{-6}	286.67	11.7

Table 1. Material parameters of the metallic material.
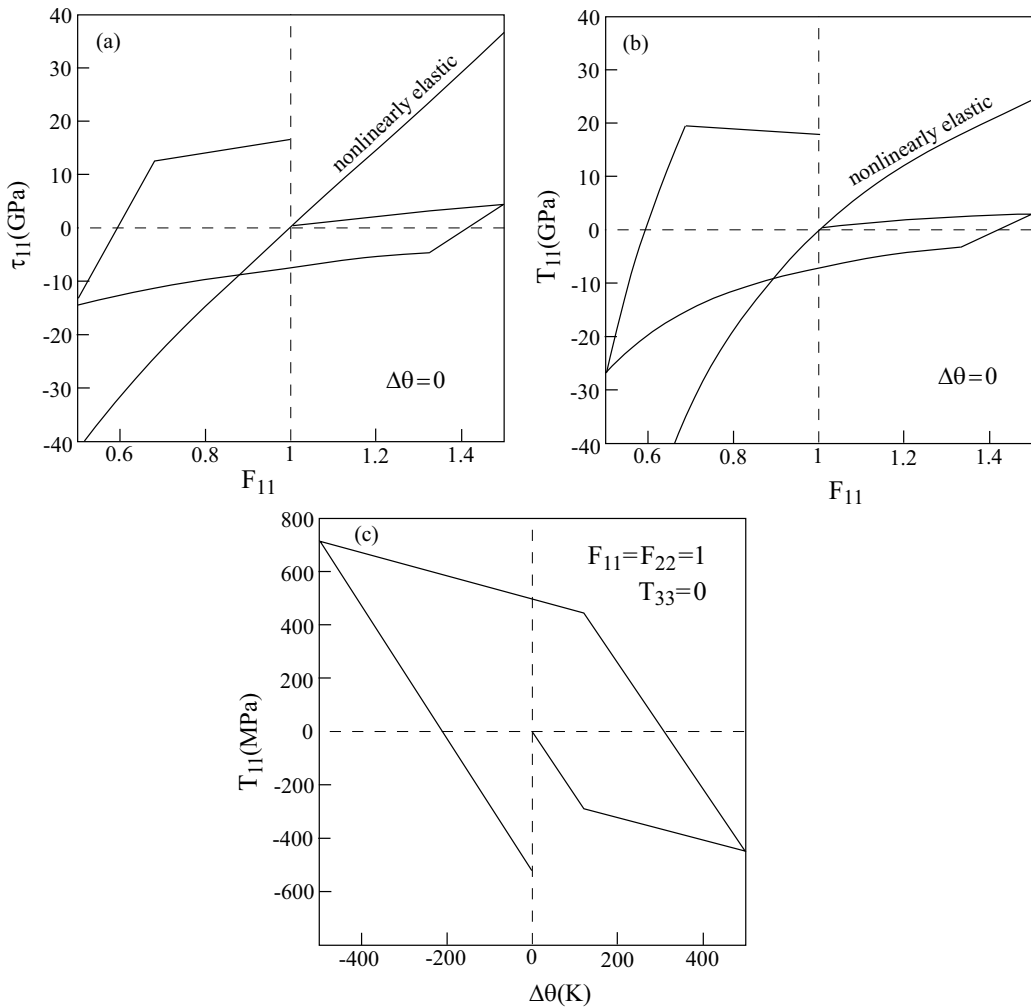
Figure 1. The behavior of the thermoelastoplastic monolithic metallic material, whose properties are given in Table 1. Shown are (a) the uniaxial Kirchhoff stress-deformation response, (b) the uniaxial first Piola–Kirchhoff stress-deformation response, and (c) the stress-temperature response.

it is represented in terms of the first Piola–Kirchhoff stress against the deformation gradient. It should be emphasized that the elastoplastic response shown in Figure 1(b) is based on a direct computation of T_{11} without utilizing the tangent tensor $\mathbf{R}$. This response however coincides with the corresponding one computed by utilizing $\mathbf{R}$. Also shown in Figure 1(b) is the behavior of the material when the plasticity effects are ignored. Here, the nonlinearity of the elastic material is well observed (the stress at a compression of $F_{11} = 0.5$ attains the value of -84 GPa). Figures 1(a) and 1(b) exhibit the material response under isothermal conditions $\Delta\theta = \theta - \theta_0 = 0$. Figure 1(c) shows the response of the material under one cycle of heating-cooling of a 500 K temperature deviation. Here, the material is subjected to the following conditions $F_{11} = F_{22} = 1$ and $T_{33} = 0$. It should be noted that the resulting maximum amount

of deformation gradient in this case is $F_{33} = 1.03$, that is, 3%, which can be still considered as a small deformation. Consequently the values of the first Piola–Kirchhoff and Kirchhoff stresses are practically identical.

## 3. Finite strain micromechanical modeling of fiber-reinforced materials

Finite strain micromechanical analyses of fiber-reinforced materials with periodic microstructure have been previously proposed [Aboudi 2002; 2003; 2004a; 2004b] for the determination of the behavior of thermoelastic, viscoplastic, and thermoviscoelastic multiphase composites, respectively. An extensive verification of the micromechanical analysis in the elastic case of continuous fiber composites was presented by Aboudi and Pindera [2004]. These micromechanical analyses are based on the homogenization technique in which a repeating unit cell of the periodic composite is identified.

In Figure 2, a multiphase composite with a doubly periodic microstructure defined with respect to the initial macroscopic (global) material coordinates of the X_2-X_3 plane is shown together with its repeating unit cell, defined with respect to the initial microscopic (local) material coordinates Y_2-Y_3. In the framework of the homogenization method [Parton and Kudryavtsev 1993], the rate of the displacement vector is asymptotically expanded in terms of a small parameter δ. The size of the unit cell is further assumed to be much smaller than the size of the body so that the relation between the global and local systems is $\mathbf{Y} = \mathbf{X}/\delta$. This implies that a movement of order unity on the local scale corresponds to a very small movement on the global scale.

The homogeneization procedure ultimately provides the following strong form of the Lagrangian equilibrium equations

$$\nabla_{\mathbf{Y}} \cdot \dot{\mathbf{T}}^1 + \nabla_{\mathbf{Y}} \cdot \dot{\mathbf{T}}^0 = 0 \tag{5}$$

where $\dot{\mathbf{T}}^0 = \mathbf{R}(\mathbf{Y}, t) : \dot{\bar{\mathbf{F}}}(\mathbf{X}, t) - \mathbf{H}(\mathbf{Y}, t)\,\dot{\theta}(t)$, which is the rate of the stress tensor due to the externally applied rate of the deformation gradient $\dot{\bar{\mathbf{F}}}(\mathbf{X}, t)$ and temperature $\dot{\theta}(t)$, and $\dot{\mathbf{T}}^1 = \mathbf{R}(\mathbf{Y}, t) : \dot{\tilde{\mathbf{F}}}(\mathbf{X}, \mathbf{Y}, t)$ is the resulting fluctuating stress tensor rate which is given in terms of the rate of the fluctuating displacement gradient $\dot{\tilde{\mathbf{F}}}(\mathbf{X}, \mathbf{Y}, t)$. It is readily seen that the first terms in Equations (5) involve the unknown fluctuating
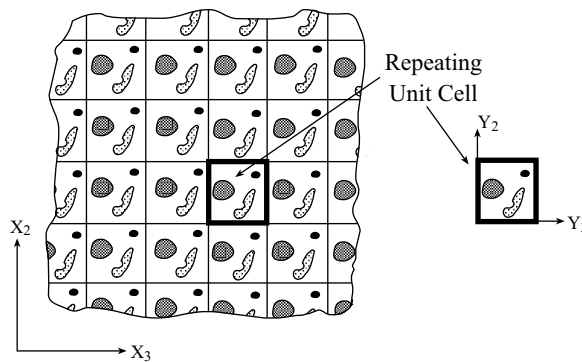
Figure 2. A multiphase composite with doubly-periodic microstructures defined with respect to global initial coordinates of the plane X_2-X_3. The repeating unit cell is defined with respect to local initial coordinates of the plane Y_2-Y_3.

periodic displacement rate $\dot{\tilde{\mathbf{u}}}$ while the second term in these equations produce pseudo-body forces whose derivatives are actually zero everywhere except at the interfaces between the phases.

For imposed values of the average deformation gradient rate $\dot{\bar{\mathbf{F}}}$ and temperature rate $\dot{\theta}$, the unknown fluctuating displacement rate is governed by Equations (5) subject to periodic boundary conditions that are prescribed at the boundaries of the repeating unit cell. Referring to Figure 2, the periodic boundary conditions are expressed by the requirement that the displacements and tractions should be equal on opposite sides of the repeating unit cell. Thus at the top and bottom surfaces, right and left surfaces of the repeating unit cell, the displacement and traction rates should be identical. In addition to these periodic boundary conditions one needs to impose continuity of displacements and tractions at the internal interfaces between the phases that fill the repeating unit cell.

Once the solution of Equations (5), subject to the internal interfacial conditions and periodic boundary conditions, has been established, one can proceed and determine the instantaneous mechanical fourth-order and thermal second-order concentration tensors $\mathbf{A}^M(\mathbf{Y}, t)$ and $\mathbf{A}^{TH}(\mathbf{Y}, t)$ that relate the local rate of deformation gradient $\dot{\mathbf{F}}(\mathbf{Y}, t)$ at a material point $\mathbf{Y}$ within the repeating unit cell at time t to the rate of the externally applied deformation gradient $\dot{\bar{\mathbf{F}}}(t)$ and temperature $\dot{\theta}(t)$. Thus

$$\dot{\mathbf{F}}(\mathbf{Y}, t) = \mathbf{A}^M(\mathbf{Y}, t) : \dot{\bar{\mathbf{F}}}(t) + \mathbf{A}^{TH}(\mathbf{Y}, t)\,\dot{\theta}(t).$$

It follows from Equation (4) that the local stress rate at this point is given by

$$\dot{\mathbf{T}}(\mathbf{Y}, t) = \mathbf{R}(\mathbf{Y}, t) : \left[\mathbf{A}^M(\mathbf{Y}, t) : \dot{\bar{\mathbf{F}}}(t) + \mathbf{A}^{TH}(\mathbf{Y}, t)\,\dot{\theta}\right] - \mathbf{H}(\mathbf{Y}, t)\,\dot{\theta}(t).$$

Hence the resulting macroscopic constitutive rate equation for the multiphase thermoelastoplastic composite undergoing large deformation is given by

$$\dot{\bar{\mathbf{T}}}(t) = \mathbf{R}^*(t) : \dot{\bar{\mathbf{F}}}(t) - \mathbf{H}^*(t)\,\dot{\theta}(t), \tag{6}$$

where $\mathbf{R}^*(t)$ and $\mathbf{H}^*(t)$ are the instantaneous effective stiffness and thermal stress tensors of the multiphase composite which are given in terms of properties of the constituents in the form

$$\mathbf{R}^*(t) = \frac{1}{V_Y} \iint_{V_Y} \mathbf{R}(\mathbf{Y}, t) \cdot \mathbf{A}^M(\mathbf{Y}, t)\,dV_Y \tag{7}$$

and

$$\mathbf{H}^*(t) = -\frac{1}{V_Y} \iint_{V_Y} \left[\mathbf{R}(\mathbf{Y}, t) : \mathbf{A}^{TH}(\mathbf{Y}, t) - \mathbf{H}(\mathbf{Y}, t)\right]dV_Y, \tag{8}$$

where V_Y is the volume of the repeating unit cell.

In the framework of the HFGMC model, the repeating unit cell of Figure 2 is divided into several subcells, and the integrals in Equations (7) and (8) are discretized by summing over these subcells. More details can be found in the aforementioned references.

4. Verification of the micromechanical prediction

In the present section, verifications of the offered micromechanical analysis are given under isothermal and combined thermoelastic loadings.

4.1. *Axisymmetric mechanical loading.* The reliability of the micromechanically established finite strain macroscopic elastoplastic constitutive equations can be verified by considering a hollow cylinder under externally applied radial stretch and zero axial deformation.

The employed cylindrical geometry and loading correspond to the response of the concentric cylinder assemblage (CCA) model proposed by Hashin and Rosen [1964] which in the present context represents a porous composite with an axial pore content subjected to large axisymmetric deformations. In the framework of this model, the radial stress-radial stretch ($T_{RR} - \lambda_{RR}$) response of the outer surface of a single hollow cylinder subjected to axisymmetric loading coincides with that of the effective response ($\bar{T}_{RR} - \bar{\lambda}_{RR}$) of the entire porous composite subjected to the same type of loading. For a hollow core that accounts for a volume fraction v_f of the total cross-sectional area transverse to the reinforcement direction, one can perform a direct comparison with the present HFGMC micromechanical model predictions based on the repeating unit cell with a void volume fraction of v_f subjected to biaxial tension $\bar{F}_{22} = \bar{F}_{33}$ that provides $\bar{T}_{22} = \bar{T}_{33}$. A direct comparison between $\bar{T}_{RR}$ and $\bar{T}_{22}$ provides information about the accuracy of the micromechanical prediction.

It should be emphasized that the offered reliability verification is significant because although the concentric cylinder assemblage problem is one-dimensional, the present micromechanical doubly periodic model is two-dimensional. In addition, the micromechanical model constitutive equations are based on the effective instantaneous tangent tensors $\mathbf{R}^*$ and $\mathbf{H}^*$; see Equation (6). The derived CCA model given in the following, however, is not dependent on the use of instantaneous tangent tensors $\mathbf{R}$ and $\mathbf{H}$ of Equation (4), since it is based on the direct use of the stress tensor $\mathbf{T}$, see Equation (3), rather than its rate.

The specific discretization of the repeating unit cell that mimic the circular character of the central void surrounded by the nonlinear material is performed herein by employing 8×8 subcells. This discretization is shown herein to yield reliable results.

Consider the plane strain deformation of a hollow cylinder under a uniform radial stretch at the outer radius and zero traction at the inner radius. Let R, Θ, and Z denote the cylindrical coordinates of a material particle in the initial configuration, where $A \leq R \leq B$ and $0 \leq \Theta \leq 2\pi$ with A and B denoting the inner and outer radii, respectively. The current location of this particle is given by r, θ and z such that the deformation is described by $r(R, t)$, $\theta = \Theta$, and $z = Z$, where $a \leq r(R, t) \leq b$ and a and b denote the current inner and outer radii.

For this type of deformation, the deformation gradient is given in terms of the principal stretches $\lambda_{RR} = dr(R, t)/dR$, $r(R, t)/R$, and 1 by

$$\mathbf{F} = \operatorname{diag}\left(\frac{dr(R, t)}{dR}, \frac{r(R, t)}{R}, 1\right). \tag{9}$$

In addition, $\mathbf{C}^{p-1}$ in Equation (1) can be represented by

$$\mathbf{C}^{p-1} = \operatorname{diag}\left(1 + G_{RR}(R, t), 1 + G_{\Theta\Theta}(R, t), 1 + G_{ZZ}(R, t)\right),$$

such that in the absence of plasticity effects $G_{RR} = G_{\Theta\Theta} = G_{ZZ} = 0$. These functions can be determined at any loading increment by employing the definition of $\bar{\mathbf{B}}^e$. In conjunction with Equation (9), the tensor

$\bar{\mathbf{B}}^e$ can be readily determined in the form

$$\bar{\mathbf{B}}^e = \text{diag}\left(\frac{r'(1+G_{RR})}{J^{2/3}}, \frac{r^2(1+G_{\Theta\Theta})}{R^2 J^{2/3}}, \frac{(1+G_{ZZ})}{J^{2/3}}\right), \tag{10}$$

where $J(R, t) = r'r/R$ and $r' = dr(R, t)/dR$.

The deviatoric stress $\mathbf{s}$ can be readily determined from Equation (10) and, consequently, the Kirchhoff stress $\boldsymbol{\tau}$ follows from Equation (2)

$$\tau_{RR} = \frac{\kappa}{2}[J^2 - 1] + \frac{\mu}{J^{2/3}}\left[a(r')^2(1+G_{RR}) + b\frac{r^2(1+G_{\Theta\Theta})}{R^2} + c(1+G_{ZZ})\right], \tag{11}$$

where $a = 2/3$, $b = c = -1/3$. The component $\tau_{\Theta\Theta}$ is given by same expression but with $a = c = -1/3$, $b = 2/3$. Similarly, τ_{ZZ} is of the same form shown by Equation (11) with $a = b = -1/3$, $c = 2/3$. The Kirchhoff stress tensor $\boldsymbol{\tau}$ provides the first Piola–Kirchhoff stress tensor $\mathbf{T}$ by employing Equation (3).

The equilibrium equations reduce to the single equation

$$\frac{dT_{RR}}{dR} + \frac{T_{RR} - T_{\Theta\Theta}}{R} = 0, \tag{12}$$

where T_{RR} and $T_{\Theta\Theta}$ are the components of the first Piola–Kirchhoff stress tensor. The explicit form of the resulting second-order nonlinear ordinary differential equation that is obtained from Equation (12) is very lengthy and thus it is not given here. It can be formally represented as follows

$$\Phi(r'', r', r, G'_{RR}, G'_{\Theta\Theta}, G'_{ZZ}, G_{RR}, G_{\Theta\Theta}, G_{ZZ}) = 0, \tag{13}$$

where the primes denote differentiation with respect to R.

The solution of this equation for $r(R)$ is obtained subject to a traction-free condition at the inner radius, and a specified deformation at the outer radius in the current configuration, that is,

$$T_{RR} = 0, \quad R = A \tag{14}$$

and

$$r(B, t) = b = \bar{\lambda}_{RR}B, \quad R = B, \tag{15}$$

where $\bar{\lambda}_{RR}$ is the current prescribed radial stretch. Consequently, the second-order nonlinear ordinary differential Equation (13) and the boundary conditions, Equations (14) and (15), form a two-point boundary value problem. Its solution determines at any stage of loading the current location $r(R)$ of any point $A \leq R \leq B$, which leads to the determination of the stress field, including the radial stress T_{RR} at the outer surface $R = B$. The use of the average stress theorem produces the average radial stress $\bar{T}_{RR}$ for the entire hollow cylinder, namely, $\bar{T}_{RR} = T_{RR}(R = B)$. Consequently, the effective stress-deformation relationship of the porous material, with the initial volume concentration of pores given by $A^2/B^2 < 1$, subjected to the specified plane strain axisymmetric loading by $\bar{\lambda}_{RR} = b/B$, is established. The solution of the present second-order nonlinear ordinary differential equation can be obtained by a finite-difference procedure for two-point boundary value problems [Roberts and Shipman 1972]. According to this method, the interval $A \leq R \leq B$ is divided into several subintervals and the derivatives with respect to R are replaced by their corresponding finite differences in these intervals. As a result, a system of nonlinear algebraic equations is obtained, which is solved at any loading increment by an iterative procedure until convergence is achieved up to a preassigned degree of accuracy.
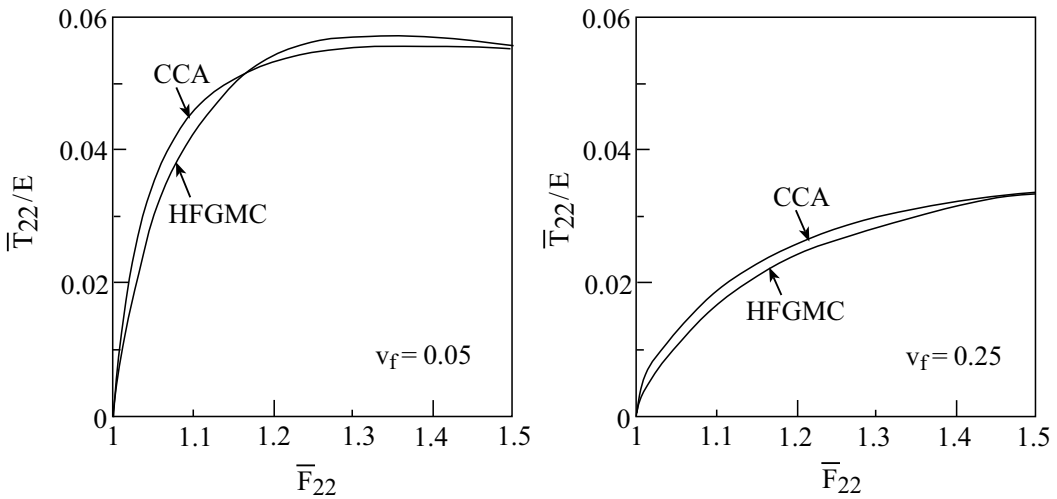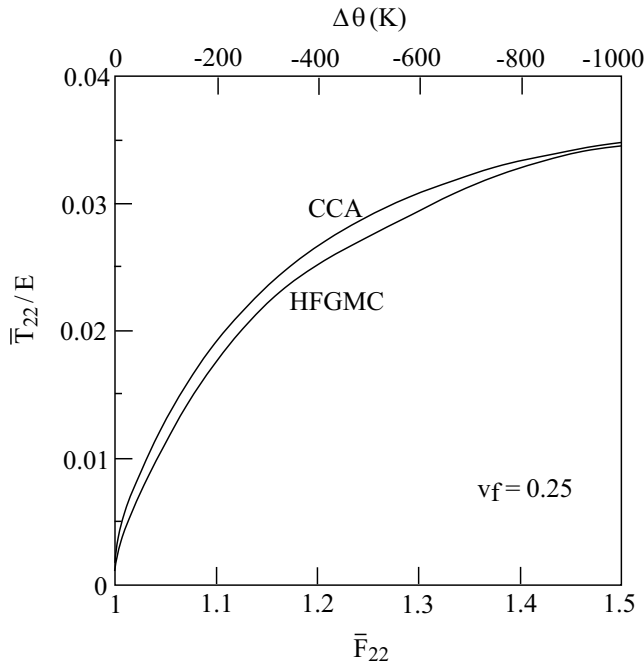
Figure 3. Macroscopic response of a porous material with (a) 5% and (b) 25% porosities subjected to a biaxial loading. The figure compares the HFGMC and the CCA model predictions. The stresses are normalized with respect to the Young's modulus E of the metallic material, whose properties are given in Table 1.

Figure 3 presents a comparison between the isothermal response predictions of the HFGMC and CCA models for void volume fraction of $v_f = 0.05$ and 0.25. The metallic elastoplastic material is characterized by Table 1. It can be observed that quite good correspondence between the two models exists in both cases. In the case of a void volume fraction of $v_f = 0.25$ the slight difference between the yield stresses predicted by the two methods may be attributed to the fact that in the CCA and HFGMC models, the governing equations and boundary conditions are imposed in a pointwise manner and in average sense, respectively.

It is worth mentioning that by taking $\mu = 0$ in Equation (11), a hyperelastic material whose strain-energy function depends on J, so that it is of the Varga type [Horgan 1995; Horgan 2001], is obtained. This class of materials admits, under the present axisymmetry conditions, an exact solution of the equilibrium Equation (12) of the form $r(R) = \sqrt{\xi R^2 + \eta}$, where ξ and η are arbitrary constants. It follows from Equation (9) that $J = \xi$. This implies, according to Equation (11) and boundary condition (14) that in this case the CCA model yields zero stresses everywhere in the region. This situation is also obtained from the HFGMC model in this type of porous material.

4.2. *Axisymmetric thermomechanical loading.* As a check of the reliability of the micromechanical prediction of a composite under thermoelastic loading, we consider again the CCA model in which a thermal loading θ is applied this time at the region $A \leq R \leq B$ in addition to the mechanical loading applied at the outer surface $R = B$ (given by the boundary conditions (15)). The resulting nonlinear ordinary differential equation that governs the two-point boundary value problem is solved as before by a finite difference method. The resulting radial stress T_{RR} at the outer surface $R = B$ is the average stress $\bar{T}_{RR}$ of the composite cylinder and it can be compared with the macroscopic stress $\bar{T}_{22} = \bar{T}_{33}$ of the HFGMC model in which the same thermal loading is applied.

Figure 4. Macroscopic response of a porous metallic material with a 25% porosity subjected to a combined biaxial and thermal loading. The figure compares the HFGMC and the CCA model predictions. The stress is normalized with respect to the Young's modulus E of the metallic material whose properties are given in Table 1.

In Figure 4, a comparison between the CCA and HFGMC prediction is shown for the thermoelastic metallic material that is specified in Table 1. It shows the normalized transverse stress (with respect to the Young's modulus E of the material) caused by a combined thermomechanical loading in which the porous material is biaxially stretched up to $\bar{F}_{22} = \bar{F}_{33} = 1.5$ with $\bar{F}_{11} = 1$ together with a simultaneous temperature deviation of $\theta - \theta_0$. In the absence of a mechanical loading, the normalized stress at the final temperature loading is $\bar{T}_{22}/E = \bar{T}_{33}/E = 0.0083$, which can be readily obtained from the metallic material clamped in the 1-direction. The combined thermomechanical loading generates the value of $\bar{T}_{22}/E = \bar{T}_{33}/E = 0.035$ at the final stretch and temperature. Thus the thermal loading generates a response of about 23% of the combined thermomechanical loading which is an appreciable value. The graphs in Figure 4 clearly show the yield points and the saturation caused by the plasticity effects. The correspondence between the two models, which are based on two different systems of constitutive equations, is reasonable.

5. Applications: isothermal behavior of a metal/rubber-like composite

The established finite strain macroscopic constitutive equations for thermoelastoplastic multiphase materials are implemented to investigate the behavior of a rubber-like matrix reinforced by metallic material whose properties are given in Table 1 (page 812). The behavior of the composite is presented under isothermal conditions.

In the present isothermal case, the hyperelastic matrix is modeled by the compressible neo-Hookean material the constitutive equations of which have been presented by Peric [1992] and van der Sluis et al. [2001]. With $\mathbf{F}$, $\mathbf{C}$, and J representing, as before, the deformation gradient, the right Cauchy–Green deformation tensor, and the determinant of $\mathbf{F}$, respectively, let I_1 denote the first invariant, that is, the trace of $\mathbf{C}$. Accordingly, the strain-energy W of this material is given by

$$W = \frac{\mu}{2}(I_1 - 3 - 2\ln J) + \frac{\lambda}{2}(\ln J)^2, \tag{16}$$

where λ and μ are the Lame' constants.

The second Piola–Kirchhoff stress tensor $\mathbf{S}$ is determined from $\mathbf{S} = 2\frac{\partial W}{\partial \mathbf{C}}$. By utilizing the relation between the first and second Piola–Kirchhoff stress tensor, $\mathbf{T} = \mathbf{S}\mathbf{F}^T$, the following constitutive equation that relates the rate of the first Piola–Kirchhoff stress tensor $\dot{\mathbf{T}}$ to the rate of the deformation gradient $\dot{\mathbf{F}}$ is obtained

$$\dot{\mathbf{T}} = \mathbf{R} : \dot{\mathbf{F}}, \tag{17}$$

where $\mathbf{R}$ is the current fourth-order tangent tensor given by $R_{ijkl} = D_{irls} \, F_{jr} \, F_{ks} + S_{il} \, \delta_{jk}$ with the material fourth-order tangent tensor $\mathbf{D}$ defined by

$$\mathbf{D} = 2\frac{\partial \mathbf{S}}{\partial \mathbf{C}} = 4\frac{\partial^2 W}{\partial \mathbf{C} \partial \mathbf{C}}.$$

As in van der Sluis et al. [2001], the Lame' constants in Equation (16) are chosen as $\lambda = 980\,\text{MPa}$ and $\mu = 30\,\text{MPa}$. Figure 5 shows the behavior of this material under a uniaxial stress loading in the 1-direction. The effect of nonlinearity and compressibility can be well observed.
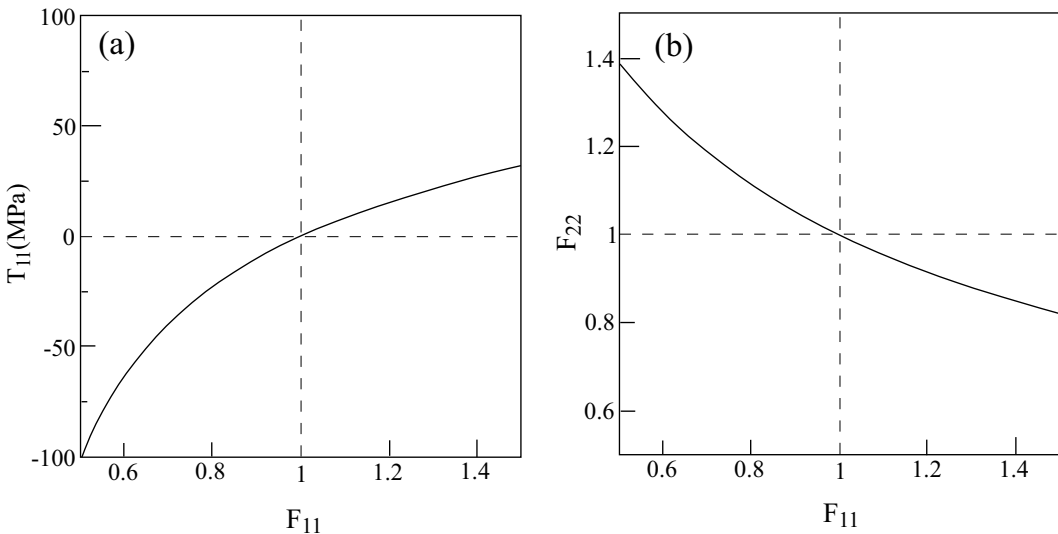
Figure 5. The uniaxial stress response of the rubber-like material modeled by the neo-Hookean constitutive law Equation (16). Shown are (a) the uniaxial stress against axial deformation gradient and (b) the transverse against axial deformation gradient.

5.1. *Unidirectional metal/rubber-like composite.* Consider a hypothetical composite system that consists of a rubber-like matrix reinforced by unidirectional continuous metallic fibers that are oriented in the 1-direction. The constitutive equations of the hyperelastic rubber-like material and the elastoplastic metallic fibers are given by Equations (17) and (4), respectively. In all cases, the volume fraction of the fibers is $v_f = 0.1$. As discussed previously, the specific discretization of the repeating unit cell that mimic a circular fiber surrounded by matrix material is performed by employing 8×8 subcells. This discretization was verified to provide a accurate results.

Let the composite be subjected to an off-axis uniaxial stress loading. Here, the unidirectional composite, in which the fibers are oriented in the 1-direction, is rotated around the 3-direction by an angle ϕ. As a result, a new system of coordinates (X, Y, Z) is obtained such that $Z = X_3$. The uniaxial stress loading is applied in the X-direction which is at angle ϕ with respect to the fibers direction. Referring to this new system of coordinates, the composite is loaded by the application of the deformation gradient F_{XX}, and all other components of the stress tensor $\mathbf{T^X}$, referred to the new coordinate system, are equal to zero except T_{XX}. In particular, $\phi = 0°$ and $90°$ correspond to longitudinal and transverse uniaxial stress loading.

Figure 6 shows the response of the composite including the associated Poisson's effect to off-axis uniaxial stress loading for $\phi = 0°, 10°, 30°$ and $45°$. The effect of plastic flow of the metallic fibers can be well detected by observing the yield stresses in the cases of $\phi = 0°$ and $10°$. For the off-axis loading at $\phi = 30°$, the location of the yield stress is shown by the arrow. For the off-axis angle $\phi = 45°$, however, plasticity does not occur and the response of the composite in this case is merely nonlinearly elastic. It is interesting that while the stress T_{XX} decreases monotonically with the increase of the off-axis angle ϕ, the transverse deformation F_{YY} exhibits a peculiar behavior in the sense that there is a sudden jump in the
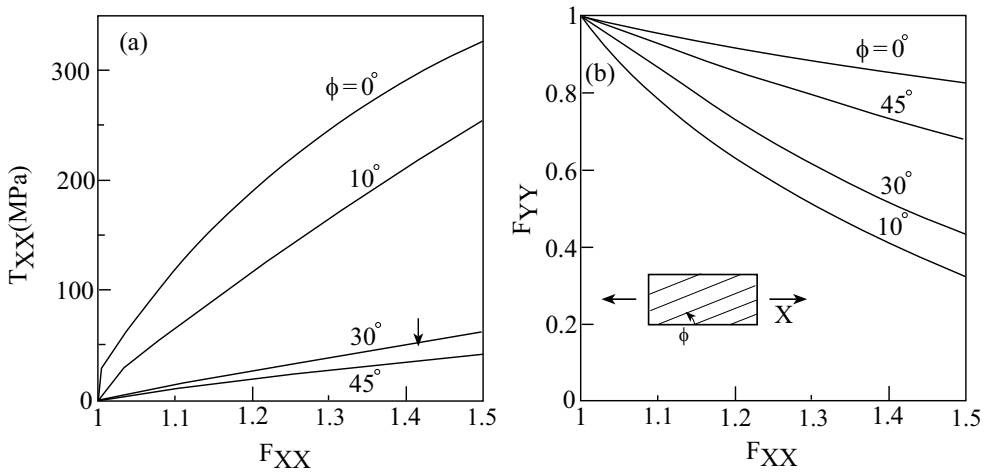
Figure 6. Off-axis uniaxial stress response of a unidirectional metal/rubber-like composite. The rotation ϕ around the 3-direction denotes the angle between the fibers (oriented in the 1-direction) and the loading (applied in the X-direction). The arrow indicates the yield stress in the case of $\phi = 30°$. Shown are (a) the stress against the applied deformation gradient and (b) the transverse deformation gradient against the applied one.

magnitude of this deformation from $\phi = 0°$ to $\phi = 10°$; see Figure 6(b). This feature was checked by generating the response at off-axis angle increments of $0.1°$. It turned out that a transition from the off-axis angle $\phi = 4.1°$ to $\phi = 4.2°$ gives rise to a jump of F_{YY} from 0.82 to 0.7. A comparison with the corresponding finite strain elastic case in which the plasticity effects of the aluminum are ignored revealed that this jump occurs at the transition from $\phi = 4.1°$ to $\phi = 4.2°$, where the transverse deformation F_{YY} abruptly changes from 0.82 to 0.3. This jump may be attributed to the variation of the combined stresses (which induce the plastic flow) to which the elastoplastic phase is exposed as the off-axis angle changes. Thus the plastic flow of the aluminum has a significant effect on the instantaneous Poisson's ratio of the composite.

It is interesting to compare the resulting responses of the composite in the two extreme cases in which the uniaxial stress loading is applied in the fiber direction: $\phi = 0°$, where the response is dominated by the fibers, and the perpendicular direction $\phi = 90°$, where the response is dominated by the matrix, while ignoring any plasticity effects by simply assuming that the yield stress of the metallic fiber is very high. The composite behavior in these two extreme cases is shown in Figure 7 together with the corresponding axial and transverse Poisson's effects. By comparing the curves shown in Figure 6 with those shown in Figure 7, the effect of the plastic flow in the fibers can be realized. Thus for a longitudinal loading in the fiber direction, the plasticity effects decrease the stress at a stretch of $\bar{F}_{11} = 1.5$ from $\bar{T}_{11} = 2465$ MPa to 325 MPa, but for a loading in the transverse direction, no yielding occurs.

5.2. *Laminated metal/rubber-like composite subjected to in-plane loading.* We now embed the finite strain elastoplastic micromechanical model just developed in a standard lamination theory for a symmetrically layered medium that is subjected to in-plane loading. In this case, each layer undergoes
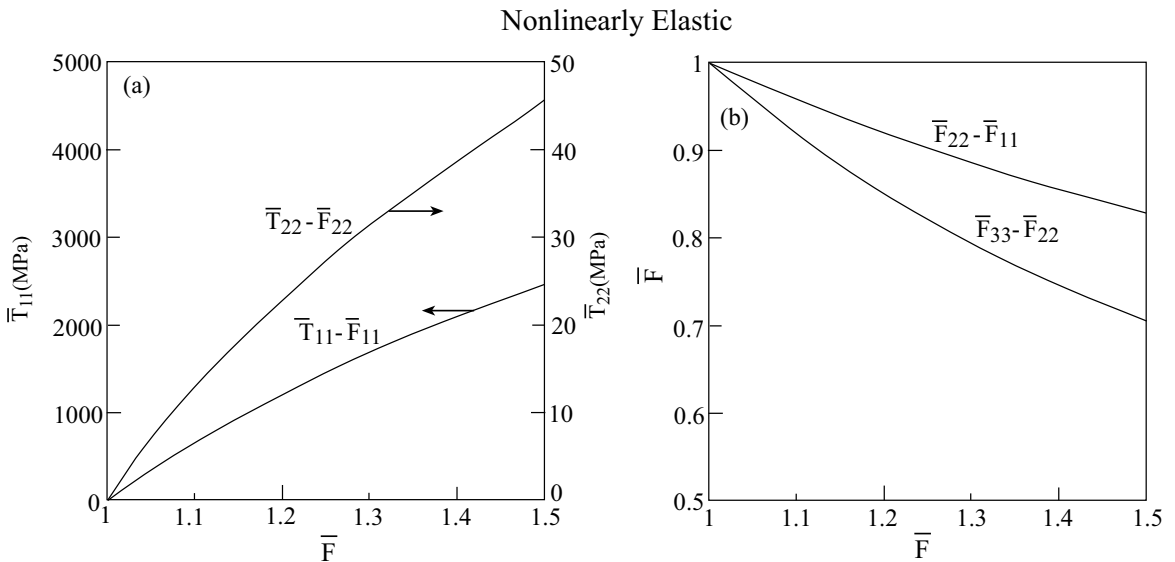
Figure 7. Axial and transverse response of the unidirectional metal/rubber-like composite in which the plasticity effects in the metallic fibers are neglected. Shown are (a) the axial stress against the applied axial deformation gradient, and transverse stress against the applied transverse deformation gradient and (b) the transverse deformation gradient against the corresponding applied ones.

the same deformation, rendering the finite strain elastoplastic lamination theory solution exact (since all equilibrium equations in the layers and continuity conditions between the layers are satisfied). The laminated material is referred to the global coordinates $\mathbf{X} = (X, Y, Z)$ such that the fiber direction in a layer is oriented at angle ϕ with respect to the lamination axis X in the direction of which the axial deformation gradient F_{XX} is applied, and Y is the other in-plane axis perpendicular to X. The laminated medium consists of L layers, each of which has an initial thickness t_k, $k = 1, 2, \ldots, L$, forming a total initial thickness H. The initial positions of the layers with respect to the global system (X, Y, Z) are denoted by h_k.

Let $\mathbf{F^X}$ denote the deformation gradient of the laminate described with respect to the global coordinates (X, Y, Z) and $\bar{\mathbf{F}}^{(k)}$ denote the deformation gradient of the layer k, referred to the material coordinates (X_1, X_2, X_3) of this layer with X_1 oriented in the fiber direction. At any instant of loading, the components of $\mathbf{F^X}$ are known from the prescribed loading F_{XX} and from the conditions that the laminate is traction-free. Hence the deformation gradient tensor $\bar{\mathbf{F}}^{(k)}$ of any layer can be determined from $\mathbf{F^X}$ by using the standard transformation law of second order tensors

$$\bar{\mathbf{F}}^{(k)} = \mathbf{A}_k^T \, \mathbf{F^X} \, \mathbf{A}_k, \tag{18}$$

where $\mathbf{A}_k$ is the transformation matrix from the global system to the material coordinates of the k-th layer.

Let $\bar{\mathbf{T}}^{(k)}$ denote the first Piola–Kirchhoff stress tensor in the k-th layer defined with respect to the material coordinates. With the known deformation gradient $\bar{\mathbf{F}}^{(k)}$ of the k-th layer given by Equation (18), the micromechanical analysis of the unidirectional lamina is employed subject to the condition that each layer is under plane stress. The finite strain elastoplastic micromechanical analysis readily provides $\bar{\mathbf{T}}^{(k)}$, which can be transformed back to the global coordinates by employing the transformation law of second-order tensors as follows $\mathbf{T}^{\mathbf{X}(k)} = \mathbf{A}_k \, \bar{\mathbf{T}}^{(k)} \, \mathbf{A}_k^T$, where $\mathbf{T}^{\mathbf{X}(k)}$ is the first Piola–Kirchhoff stress tensor in the k-th layer referred to the laminate coordinates. This procedure is repeated for all layers $k = 1, 2, \ldots, L$. The resultant force (per unit length) vector $\mathbf{N}$ for the current applied deformation gradient is obtained from $\mathbf{N} = \sum_{k=1}^{L} (h_k - h_{k-1}) \, \mathbf{T}^{\mathbf{X}(k)}$.

The average axial stress N_{XX}/H against the applied deformation gradient F_{XX} is shown in Figure 8 for a symmetric angle-ply laminate $[\pm\phi]_s$ whose layers consist of the unidirectional metal/rubber-like composite. Also shown is the transverse deformation against the axial one that provides the Poisson's effect of the laminate at any stage of loading. For $\phi = 0°$ and $30°$, the yield stresses can be well observed. For $\phi = 45°$, the yield stress occurs at $N_{XX}/H = 24.1$ MPa. For $\phi = 60°$, on the other hand, plasticity does not take place and the behavior of the angle-ply laminate is nonlinearly elastic. The nonlinearity of the response is clearly exhibited in all cases. It should be noted that for $\phi = 30°$, a slope change occurs at about $F_{XX} = 1.17$ due to plasticity effects (It is of course absent in the corresponding finite strain elastic case. Here, $N_{XX}/H = 1136$ MPa at $F_{XX} = 1.5$, while, as shown in Figure 8(a), N_{XX}/H reaches 275 MPa at this point). Figure 8(b) exhibits the Poisson's effects of the considered elastoplastic laminates. Here too there is a discontinuous behavior in the response between $\phi = 0°$ and $\phi = 10°$. Similar behavior exists also when the plasticity flow of the aluminum is neglected while retaining the large deformation effects.

In order to enhance the plasticity effects of the laminate material, a ply in which the fibers are oriented in the X-direction is added to previous type of angle-ply laminate. As a result a symmetric laminated
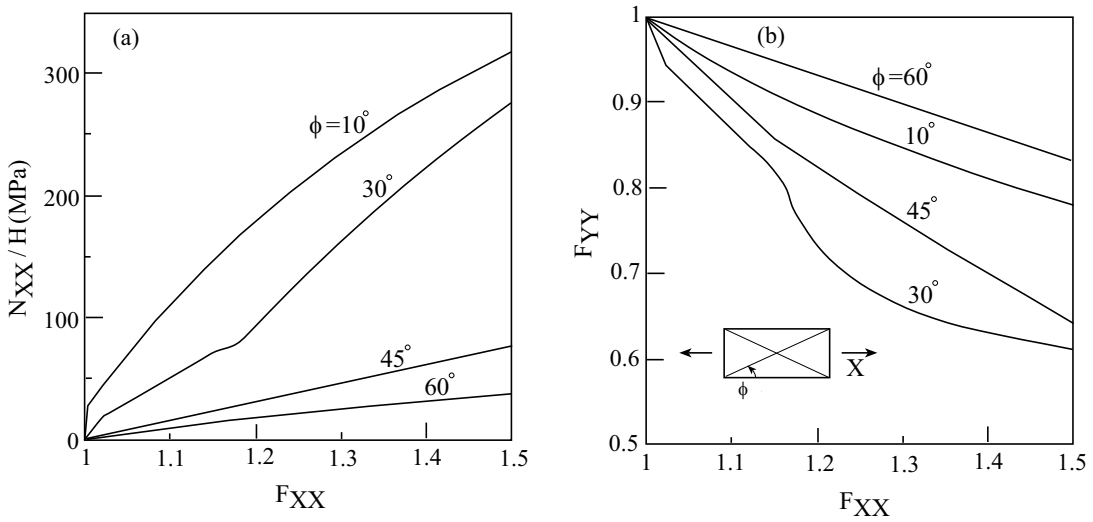
Figure 8. Shown are (a) the average axial stress and (b) the transverse deformation gradient against the applied deformation gradient of several symmetric angle-ply $[\pm\phi]_s$ laminates.

material of the type $[\pm\phi, 0]_s$ is obtained whose response is depicted in Figure 9 for various values of the angle ϕ. Here, plasticity effects occur in all angles ϕ with the corresponding yield stresses close to each other. In the special case of $\phi = 90°$, a cross-ply laminate is obtained in which plastic flow starts at a stress level of about $N_{XX}/H = 10.4\,\text{MPa}$ which is very close to to the other yield stresses.
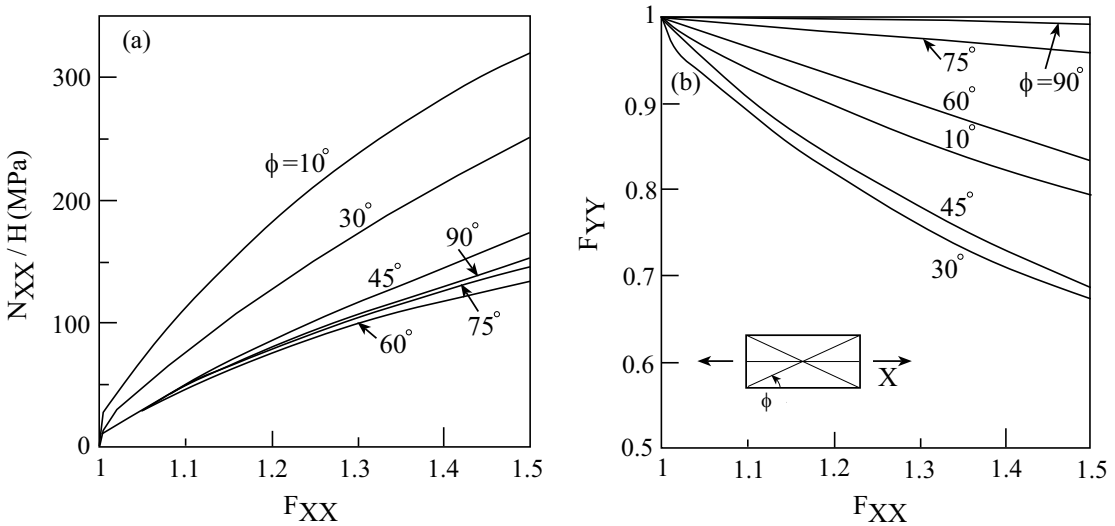
Figure 9. Shown are (a) the average axial stress and, (b) transverse deformation gradient against the applied deformation gradient of several symmetric $[\pm\phi, 0]_s$ laminates. For $\phi = 90°$, a symmetric cross-ply $[90, 0]_s$ laminate is obtained.

5.3. *Auxetic metallic material.* Auxetic materials are a new class of materials which have a negative Poisson's ratio. This implies that they expand in the lateral direction when stretched longitudinally. A reentrant configuration provides a means to construct such materials. To this end, the metallic elastoplastic material whose properties are given in Table 1 is employed in a reentrant configuration to study its finite strain elastoplastic response.

A specific configuration is employed in which the volume fraction of the metallic material is $1 - v_f = 0.28$. The inset in Figure 10(a) shows this configuration in which the angle between X_2 (along which the loading is applied) and the inclined arm is $15°$ and the ratio between the thickness to length of the solid strip is $1/6$. It should be noted that in the framework of the present micromechanical analysis, the entire X_2-X_3 plane is assumed to be filled by this configuration in the periodic manner shown by
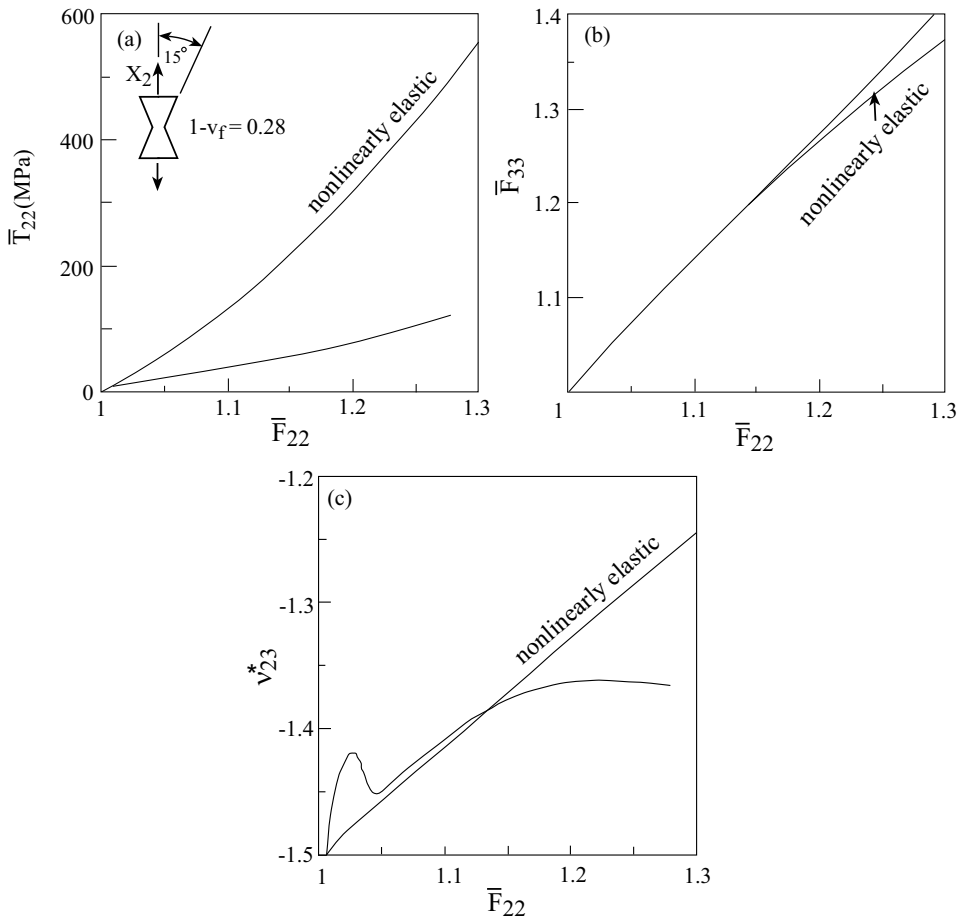
Figure 10. The behavior of a reentrant configuration that forms a type of auxetic material. The volume fraction of the metallic material is $1 - v_f = 0.28$. Shown are (a) the average stress in the 2-direction against the applied stretch in this direction, (b) the transverse in-plane stretch against the applied one, and (c) the effective transverse Poisson's ratio against the applied stretch.

Figure 2. Figure 10(a) shows the macroscopic stress-deformation gradient response $\bar{T}_{22} - \bar{F}_{22}$ of this configuration. The special case in which the plasticity effects in the metallic material are ignored is shown for comparison. It is clearly seen that these effects are significant. Figure 10(b) shows the macroscopic transverse stretch in the 3-direction against the applied stretch in the 2-direction. The in-plane effective transverse Poisson's ratio ν_{23}^* can be determined at any instant of loading from

$$\nu_{23}^* = -\frac{\bar{F}_{33} - 1}{\bar{F}_{22} - 1}.$$

This ratio is shown in Figure 10(c). It starts at $\nu_{23}^* = -1.5$ which correspond to the Poisson's ratio of the considered configuration at the region of infinitesimal elastic deformations. Plastic flow starts at a stretch of $\bar{F}_{22} = 1.008$ and a corresponding stress $\bar{T}_{22} = 8.4$ MPa (yield stress). When plasticity effects are ignored, the resulting effective Poisson's ratio rises linearly up to about -1.25. In the actual situation when plasticity effects are present, the Poisson's ratio exhibits a peculiar behavior in the form of an increase followed by a decrease. For stretches $\bar{F}_{22}$ larger than 1.15, ν_{23}^* is seen to be more negative than the corresponding one where the plasticity effects are ignored. Thus in the present circumstances, the elastoplastic material provides a more effective auxetic metallic material at large strains than the corresponding nonlinearly elastic one. In conclusion, the present finite strain elastoplastic micromechanics forms a quantitative tool for the prediction of the instantaneous negative Poisson's ratios of auxetic metallic material.

6. Conclusions

A finite strain micromechanical model is offered for the prediction of the macroscopic response of multiphase composites in which any constituent is considered as a rate-independent thermoelastoplastic material, a thermoelastic material, or a hyperelastic material. The response is governed by the established global constitutive equations of the composite in conjunction with the derived instantaneous mechanical and thermal tangent tensors. The macroscopic constitutive equations are subsequently employed in a finite strain lamination theory to investigate the behavior of symmetric elastoplastic laminates subjected to in-plane loading. The variation of the negative Poisson's ratio of an auxetic configuration undergoing large elastoplastic deformation is shown. The reliability of the micromechanical model prediction is examined by employing the CCA model which is valid under an axisymmetrical thermomechanical loading. The results for unidirectional and laminated elastoplastic composite as well as for auxetic materials show that the effect of the plastic flow is significant. In some situations, peculiar behavior caused by the finite strain plasticity effects is exhibited when the applied strains attain appreciable values. This behavior is absent when the plastic flow of the metallic constituent is neglected.

The present article continues a series of investigations [Aboudi 2002; 2003; 2004a] concerning the development of the finite strain micromechanical analysis (HFGMC) that is capable of predicting the behavior of multiphase materials undergoing large deformations. Any constituent in the composite can be selected to behave as a thermoelastic, thermoviscoelastic, and thermoinelastic material. In the latter case either rate-dependence (viscoplasticity) or rate-independence (plasticity which is the subject of the present paper) can be assumed. It is worth mentioning that the strategy of the finite strain modeling of composites with rate-dependent (viscoplastic and viscoelastic) constituents that was previously followed

[Aboudi 2003; 2004a], differs from the the one adopted in the present investigation of the behavior of composites that consist of rate-independent elastoplastic phases. In the former strategy, the inelastic effects were totally separated from the tangent tensor of the viscoplastic and viscoelastic constituents. In the present investigation, on the other hand, the rate-independent plasticity effects are incorporated with the tangent tensor (see Equation (4)), which is given in terms of the consistent elastoplastic spatial tangent tensor of Simo and Hughes [1998]. It is possible, however, to adopt just a single strategy and develop a unified finite strain HFGMC model for all these types of composites.

It is worth mentioning that in both the finite strain HFGMC model for viscoplastic phases [Aboudi 2003] and the present one for time-independent elastoplastic constituents, no special invariant rate of stresses (like the Jaumann rate) need to be introduced. This follows from the fact that the flow rules in both cases are formulated in the strain space.

The advantage of HFGMC model stems in its capability of modeling a periodic composite material by discretizing the repeating unit cell into quite few subcells. For example, in the present investigation 8×8 subcells were found to be sufficient to in providing good accuracy. This also implies that the running time of the program is quite short (several minutes). In addition, due to the rectangular shape of the subcells, the repeating unit cell discretization is quite simple. Due to the simplicity of HFGMC model, it should not be difficult to link it to a finite element procedure in order to analyze a composite structure (for example, composite beams, plates, and shells). Indeed, the capability for such structural investigations has been already performed in the infinitesimal strain domain by the Life Prediction Branch of NASA Glenn Research Center, who integrated HFGMC and its predecessor GMC model into a commercial finite element package. This software is referred to as *Finite Element Analysis Micromechanics Analysis Code* (FEAMAC) (see: www.lerc.nasa.gov/WWW/LPB/mac). Extensions of such a capability to the the finite strain domain should be also possible.

The present theory can be further extended for the investigation of the behavior of rubber matrix elastoplastic unidirectional and laminated composites with emphasis on the thermal effects. In such an investigation, a proper entropic elasticity modeling of the rubber-like matrix must be employed in order to simulate the Gough–Joule effect in such materials. Such an energy function, which was employed in [Aboudi 2002; 2004a] to analyze the behavior of thermoelastic and thermoviscoelastic of rubber-like matrix composites, can be utilized to model the finite strain thermoelastoplastic behavior of rubber-like matrix with embedded elastoplastic constituents.

A related issue is the potential application of the present methodology in the study of the behavior of certain biological tissues. Indeed, the finite strain HFGMC model with quasilinear viscoelastic (QLV) constituents has been recently employed by Surucu et al. [2005] for the investigation of the behavior of mitral valve chordae. Thus, it should be possible to implement the present micromechanical model to investigate the behavior of elastoplastic biological tissues. Concerning the study of the behavior of auxetic materials, other types of auxetic cellular solids (for example, metallic honeycombs and foams) can by analyzed by the present approach. Furthermore, auxetic composite laminates and composite containing metallic auxetic phases can be considered by employing the present micromechanical model. In addition, it is known that laminated elastic materials with certain stacking sequences can produce negative Poisson's ratios [Herakovich 1998]. It should be interesting to examine the effect of large plastic deformations on such laminated materials when plasticity effects are present. By employing the finite strain HFGMC model with nonlinearly elastic constituents, Bruck et al. [2007] presented an optimal design approach of

porous microstructures for porous materials. The material that was considered in this investigation was hyperelastic (compressible Mooney–Rivlin). It should be interesting to extend this optimization approach to elastoplastic materials undergoing large deformations. Finally, the present investigation was confined to the analysis of two-dimensional composites. It should be possible to generalize this micromechanical analysis to a three-dimensional one, thus enabling the study of the behavior of particle filled composites such as rubbery polymers filled with metallic inclusions. In addition, the behavior of metallic foams with open or closed cells can be predicted by employing such a three-dimensional generalization.

References

[Aboudi 2002] J. Aboudi, "Micromechanical analysis of the fully coupled finite thermoelastic response of rubber-like matrix composites", *Int. J. Solids Struct.* **39** (2002), 2587–2612.

[Aboudi 2003] J. Aboudi, "Micromechanical analysis of the finite elastic-viscoplastic response of multiphase composites", *Int. J. Solids Struct.* **40** (2003), 2793–2817.

[Aboudi 2004a] J. Aboudi, "Micromechanics-based thermoviscoelastic constitutive equations for rubber-like matrix composites at finite strains", *Int. J. Solids Struct.* **41** (2004), 5611–5629.

[Aboudi 2004b] J. Aboudi, "The generalized method of cells and High-fidelity generalized method of cells micromechanical models - a review", *Mech. Adv. Materl. Struct.* **11** (2004), 329–366.

[Aboudi and Pindera 2004] J. Aboudi and M.-J. Pindera, "High-fidelity micromechanical modeling of continuously reinforced elastic multiphase materials undergoing finite deformations", *Math. Mech. Solids* **9**:6 (2004), 599–628.

[Alderson and Alderson 2007] A. Alderson and K. L. Alderson, "Auxetic materials", pp. 565–575 in *Proc. I. Mech E, Part G: J. Aerospace Eng.*, vol. 221, 2007.

[Bruck et al. 2007] H. A. Bruck, R. Gilat, J. Aboudi, and A. L. Gershon, "A new approach for optimizing the mechanical behavior of porous microstructures for porous materials by design", *Modelling Simul. Mater. Sci. Eng.* **15** (2007), 653–674.

[Gasser and Holzapfel 2002] T. C. Gasser and G. A. Holzapfel, "A rate-independent elastoplastic constitutive model for biological fiber-reinforced composites at finite strains: continuum basis, algorithmic formulation and finite element implementation", *Comp. Mech.* **29** (2002), 340–360.

[Hashin and Rosen 1964] Z. Hashin and B. W. Rosen, "The elastic moduli of fiber-reinforced materials", *J. Appl. Mech.* **31** (1964), 223–232.

[Herakovich 1998] C. T. Herakovich, *Mechanics of fibrous composites*, Wiley, New York, 1998.

[Holzapfel 2000] G. A. Holzapfel, *Nonlinear solid mechanics*, John Wiley & Sons Ltd., Chichester, 2000. A continuum approach for engineering.

[Horgan 1995] C. O. Horgan, "On axisymmetric solutions for compressible nonlinearly elastic solids", *Z. Angew. Math. Phys.* **46**:Special Issue (1995), S107–S125. Theoretical, experimental, and numerical contributions to the mechanics of fluids and solids.

[Horgan 2001] C. O. Horgan, "Equilibrium solutions for compressible nonlinearly elastic materials", pp. 135–159 in *Nonlinear elasticity: theory and applications*, London Math. Soc. Lecture Note Ser. **283**, Cambridge Univ. Press, Cambridge, 2001.

[Lubliner 1990] J. Lubliner, *Plasticity theory*, Macmillan, New York, 1990.

[Parton and Kudryavtsev 1993] V. Z. Parton and B. A. Kudryavtsev, *Engineering mechanics of composite structures*, CRC Press, Boca Raton, FL, 1993.

[Peric 1992] D. Peric, "On consistent stress rates in solid mechanics: computational implications", *Int. J. Num. Meth. Eng.* **33** (1992), 799–817.

[Perzyna 1966] P. Perzyna, "Fundamental problems in viscoplasticity", pp. 243–377 in *Advances in Applied Mechanics*, vol. 9, Academic Press, New York, 1966.

[Roberts and Shipman 1972] S. M. Roberts and J. S. Shipman, *Two-point boundary value problems: shooting methods*, Modern Analytic and Computational Methods in Science and Mathematics **31**, Elsevier, New York, 1972.

[Rubin 1987] M. B. Rubin, "An elastic-viscoplastic model exhibiting continuity of solid and liquid states", *Int. J. Eng. Sci.* **25** (1987), 1175–1191.

[Simo 1988a] J. C. Simo, "A framework for finite strain elastoplasticity based on maximum plastic dissipation and the multiplicative decomposition. I. Continuum formulation", *Comput. Methods Appl. Mech. Engrg.* **66**:2 (1988), 199–219.

[Simo 1988b] J. C. Simo, "A framework for finite strain elastoplasticity based on maximum plastic dissipation and the multiplicative decomposition: Part II, computational aspects", *Comput. Meth. Appl. Mech. Eng.* **68** (1988), 1–31.

[Simo and Hughes 1998] J. C. Simo and T. J. R. Hughes, *Computational inelasticity*, Interdisciplinary Applied Mathematics **7**, Springer, New York, 1998.

[van der Sluis et al. 2001] O. van der Sluis, P. J. G. Schreurs, and H. E. H. Meijer, "Homogenisation of structured elasticviscoplastic solids at finite strains", *Mech. Mater.* **33** (2001), 499–522.

[Spencer 1971] A. J. M. Spencer, "Theory of invariants", pp. 239–353 in *Continuum physics*, vol. 1, edited by A. C. Eringen, Academic Press, New York, 1971.

[Spencer 1984] A. J. Spencer, "Constitutive theory for strongly anisotropic solids", pp. 1–32 in *Continuum Theory of the Mechanics of Fibre-Reinforced Composites*, vol. 282, edited by A. J. Spencer, Springer-Verlag, Wien, 1984. CISM Courses and Lectures.

[Surucu et al. 2005] M. Surucu, D. Einstein, and I. Vesely, "Micromechanical modeling of nonlinear viscoelastic behavior of mitral valve chordae", pp. 924 in *ISB XXth Congress - ASB 29th Annual Meeting*, Cleveland, Ohio, 2005.

[Tanaka and Yamada 1990] E. Tanaka and H. Yamada, "An inelastic constitutive model of blood vessels", *Acta Mech.* **82** (1990), 21–30.

[Tanaka et al. 1996] E. Tanaka, H. Yamada, and S. Murakami, "Inelastic constitutive modeling of arterial and ventricular walls", pp. 137–163 in *Computational Biomechanics*, edited by K. Hayashi and H. Ishikawa, 1996.

JACOB ABOUDI: aboudi@eng.tau.ac.il
Faculty of Engineering, Tel Aviv University, Ramat Aviv 69978, Israel
http://www.eng.tau.ac.il/~aboudi/

THE INFLUENCE OF AN INITIAL SIMPLE SHEAR DEFORMATION ON LONG-WAVE MOTION IN AN ELASTIC LAYER

SVETLANA R. AMIROVA AND GRAHAM A. ROGERSON

Long wave dispersion in an incompressible elastic layer subject to an initial static simple shear deformation is investigated. Long wave approximations of the dispersion relation associated with zero incremental traction on the faces are derived for both low and high-frequency motion. Comparison of approximate and numerical solutions is shown to provide excellent agreement over a surprisingly large wave number range. Within both the low and high-frequency regimes, the approximations are employed to establish the relative asymptotic orders of the displacement components and hydrostatic pressure. In the high-frequency case, the in-plane component of displacement is shown to be asymptotically larger than the normal component; motion is, therefore, essentially that of thickness shear resonance. The influence of this specific form of initial deformation is, therefore, seemingly minor in respect of long-wave high-frequency motion. However, in the long-wave low-frequency case, considerable differences are noted in comparison with both the classical and previously published prestressed cases. Specifically, both the normal and in-plane displacement components are of the same asymptotic order, indicating the absence of any natural analogue of either classical bending or extension.

1. Introduction

The theory of infinitesimal time-dependent motion, superimposed upon a large static primary deformation, has been used by a number of authors to study infinitesimal wave propagation in elastic bodies subject to an initial pure homogeneous strain. Within this present study, our concern is long-wave motion in a layer of finite thickness and infinite lateral extent. The layer is composed of incompressible elastic material and subject to a simple shear primary deformation. Wave propagation in homogeneously pre-stressed rectangular plates has been discussed in detail by a number of authors — see for example [Ogden and Roxburg 1993; Rogerson 1997; Rogersion and Fu 1995] — in regard to incompressible elastic plates, [Roxburgh and Ogden 1994] and [Nolde et al. 2004] for compressible elastic plates, and [Rogerson 1998] for anisotropic plates. All these studies concern scenarios for which one of the principal axes of primary deformation is normal to the surface of a plate or half-space. In the context of SH waves, Bar and Pal [1985] investigated the possibility of Love waves under initial shear stress. Connor and Ogden [1995] investigated the influence of simple shear on the existence of surface waves and later [1996] discussed its influence on dispersion in a plate. In the latter of these two references, they derived the dispersion relations associated with incrementally traction-free and traction-fixed faces, investigated questions of stability, and provided numerical solutions for the dispersion and bifurcation relations in the traction-free case for plates composed of neo-Hookean material. In the case of a simple shear primary deformation,

---

no principal axis of deformation is normal to the plane of the plate or half-space. We remark that a similar phenomenon is also possible with anisotropy and with the specific orientation of the principal axes relative to a free surface; see for example [Fu 2005; Triantafyllidis and Abeyarante 1983].

Shear-type deformations may occur in a number of scenarios and are commonly encountered in geomechanics. As examples, we cite the Earth's crust, for which the influence of hydrostatic pressure is significant; see for example [Gessner et al. 2007]. Natural mechanisms also exist within layered systems whereby movements over long timescales may cause shear-type deformations; see [Ide et al. 2007].

In our present study, an asymptotic long-wave analysis of the dispersion relation associated with infinitesimal wave propagation in a layer with an initial simple shear deformation and incrementally traction-free faces is carried out. An asymptotic methodology has previously been exploited in a number of papers, see for example [Kaplunov et al. 2002] and [Kaplunov et al. 2000]. Our specific aim is to carry out a long-wave asymptotic investigation of the dispersion relation and use it to establish the relative asymptotic orders of the field variables, thereby providing the theoretical framework for long-wave asymptotic models to be derived.

We begin this paper with a review of basic dynamic equations in Section 2. In Section 3, the dispersion relation, derived using traction-free boundary conditions, is established and numerical results concerning a Varga material are presented. In Section 4, long-wave low-frequency approximations for dispersion relations are derived up to, and including, second order. These expansions are derived for the most general appropriate strain energy function. For neo-Hookean materials, a constitutive simplification is exploited, and higher-order approximations are established. The approximations are shown to agree well with a number of numerical solutions.

In Section 5, long-wave high-frequency motion is investigated. In the most general constitutive case, the general form of the cut-off frequencies is established, with second- and third-order corrections established for materials of neo-Hookean type. Again, good agreement between asymptotic and numerical solutions is demonstrated. Finally, in Section 6 the relative asymptotic orders of the displacement components and hydrostatic pressure are established for both long-wave high- and low-frequency motion. Regarding high-frequency motion, the results were very similar to those previously established for pre-stresses for which one principal axis is normal to the free surface; see [Kaplunov et al. 2002]. However, in respect of low-frequency motion, the results were quite different, with both the in-plane and normal displacement components having the same asymptotic orders. It is then the case that the prestressed analogs of classical bending and extension, as discussed in [Kaplunov et al. 2000], are not possible. This notwithstanding, we show that as the amount of shear tends to zero the relative asymptotic orders of displacement components and incremental pressure do all in fact concur with those of [Kaplunov et al. 2000].

2. Governing equations

In this section, we summarize the basic equations which govern infinitesimal motion superimposed upon a finite static deformation in an incompressible elastic solid. For further details of the basic equations, the reader is referred to [Ogden 1984]. Our ultimate aim is to investigate infinitesimal wave propagation in a layer of finite thickness and infinite lateral extent, composed of incompressible elastic material. The layer is subject to an initial finite simple shear deformation parallel to its incrementally traction free faces. Initially, the layer occupies the unstressed natural isotropic state B_u, upon which the primary simple shear

deformation is imposed, resulting in the finitely deformed equilibrium configuration B_e. Finally, a small time-dependent motion is superimposed on B_e, with the ultimate current configuration denoted by B_t. The position vectors of a representative particle, relative to a common Cartesian coordinate system, are denoted by X_A, $x_i(X_A)$, and $\tilde{x}_i(X_A, t)$ in B_u, B_e, and B_t, respectively. These position vectors may be related through

$$\tilde{x}_i(X_A, t) = x_i(X_A) + u_i(x_j, t), \tag{2-1}$$

where $u_i(x_j, t)$ denotes the infinitesimal time-dependent superimposed motion.

In this paper, we specifically consider two-dimensional, two-component infinitesimal motions, with $u_3 = 0$ and u_1 and u_2 independent of x_3. In view of incompressibility, $\lambda_1\lambda_2\lambda_3 = 1$, where $\lambda_i > 0$, $i = 1, 2, 3$, are the principal stretches of the primary deformation. The particular simple shear primary deformation concerned may be defined by

$$x_1 = X_1 + \epsilon X_2, \qquad x_2 = X_2, \qquad x_3 = X_3, \tag{2-2}$$

where ϵ is the finite amount of shear. The equations of motion may be represented in the component form

$$B_{jilk}u_{k,jl} - p_{t,i} = \rho\ddot{u}_i, \tag{2-3}$$

with B_{ijkl} components of the fourth-order elasticity tensor, p_t a time dependent pressure increment, ρ the material density, a comma indicating differentiation with respect to the indicated spatial coordinate component and a dot differentiation with respect to time. As was shown in [Destrade and Ogden 2005], within the so-called Eulerian coordinate system, coincident with the principal axes of the primary deformation there are 6 nonzero components of the elasticity tensor entering our equations of motion. In contrast, within what might be regarded as the plate's natural coordinate system, with one axis normal to the free surfaces, there are 10. An important feature of this simple shear deformation is that no principal axis is normal to the incrementally traction-free faces of the plate, with the Eulerian and natural axes noncoincident. The *natural* (x_1, x_2) and Eulerian (x_1', x_2') coordinate systems are connected via the relations

$$\mathbf{x} = \mathbf{R}\mathbf{x}', \qquad \mathbf{x}' = \mathbf{R}^T\mathbf{x}, \qquad \mathbf{x} = \begin{pmatrix} x_1 \\ x_2 \end{pmatrix}, \qquad \mathbf{x}' = \begin{pmatrix} x_1' \\ x_2' \end{pmatrix}, \qquad \mathbf{R} = \begin{pmatrix} c_\theta & -s_\theta \\ s_\theta & c_\theta \end{pmatrix},$$
$$s_\theta = \sin\theta, \qquad c_\theta = \cos\theta, \tag{2-4}$$

where the origin is located on the plate's upper face and occupies $-\infty \le x_1 \le \infty$, $-h \le x_2 \le 0$. With respect to Eulerian axes, with displacement components u_1' and u_2', the governing equations are provided by

$$(B_{1111} - B_{1122} + p_0)u_{1,11}' - p_{t,1}' + B_{2121}u_{1,22}' + (B_{2121} - \sigma_2)u_{2,12}' = \rho\ddot{u}_1',$$
$$(B_{2222} - B_{1122} + p_0)u_{2,22}' - p_{t,2}' + B_{1212}u_{2,11}' + (B_{2121} - \sigma_2)u_{1,21}' = \rho\ddot{u}_2'. \tag{2-5}$$

Within these equations, a comma indicates differentiation with respect to a spatial component of Eulerian coordinates, and p_0 is a static pressure brought into play by incompressibility. Before proceeding, we

note the following definitions, symmetries, and a connection between σ_2 and p_0:

$$p_0 = B_{2121} - B_{2112} - \sigma_2, \qquad B_{iijj} = B_{jjii}, \qquad B_{ijji} = B_{jiij},$$

$$\alpha = B_{1212}, \qquad \gamma = B_{2121}, \qquad 2\beta = B_{1111} + B_{2222} - 2B_{1122} - 2B_{1221}. \tag{2-6}$$

We adopt a comma convention whereby the indicated spatial derivatives of $\mathbf{u}'$ are always with respect to $\mathbf{x}'$, and $\mathbf{u}$ always with respect to $\mathbf{x}$. Within this spirit, although the pressure is a scalar, we utilize the notation p_t' and p_t to distinguish between which coordinate system the implied differentiation refers to. In view of the plane strain nature of the problem, we assume also that $\lambda_3 \equiv 1$, and note for future use that

$$\alpha\lambda_2^2 = \gamma\lambda_1^2, \qquad \lambda_1 = \lambda, \qquad \lambda_2 = 1/\lambda, \qquad \alpha = \gamma\lambda^4. \tag{2-7}$$

Recalling that the spatial derivatives in Equation (2-5) are with respect to Eulerian coordinates, we will perform appropriate changes to express these equations within the plate's natural coordinate system and introduce

$$\mathcal{H}_1 = B_{2112} + B_{1122} - B_{1111}, \qquad \mathcal{H}_2 = B_{2112} + B_{1122} - B_{2222}, \qquad \mathcal{H}_1 + \mathcal{H}_2 = -2\beta, \tag{2-8}$$

noting also that the properties of the simple shear deformation dictate that

$$\cot\theta = \lambda, \qquad s_\theta = \frac{1}{\sqrt{\lambda^2 + 1}}, \qquad c_\theta = \frac{\lambda}{\sqrt{\lambda^2 + 1}}, \qquad 2\lambda = \epsilon + \sqrt{\epsilon^2 + 4}. \tag{2-9}$$

The equations of motion, within the natural system, are therefore representable in the form

$$\begin{aligned}
&-\lambda(1+\lambda^2)p_{t,1} - (1+\lambda^2)p_{t,2} - \rho\lambda(1+\lambda^2)\ddot{u}_1 - \rho(1+\lambda^2)\ddot{u}_2 \\
&\quad + \lambda\big((\gamma - \mathcal{H}_1 - \sigma_2)\lambda^2 + 2\gamma - \sigma_2\big)u_{1,11} - \lambda\big(\mathcal{H}_1 - \gamma\lambda^2\big)u_{1,22} \\
&\quad - \big((2\mathcal{H}_1 + \sigma_2 + \gamma)\lambda^2 + \sigma_2 - \gamma\big)u_{1,12} - \big(\mathcal{H}_1\lambda^2 - \gamma\big)u_{2,11} \\
&\quad - \big((\sigma_2 - 2\gamma)\lambda^2 - \gamma + \mathcal{H}_1 + \sigma_2)\big)u_{2,22} - \lambda\big((\sigma_2 - \gamma)\lambda^2 + 2\mathcal{H}_1 + \sigma_2 + \gamma)\big)u_{2,12} = 0, \tag{2-10}
\end{aligned}$$

$$\begin{aligned}
&(1+\lambda^2)p_{t,1} - \lambda(1+\lambda^2)p_{t,2} + \rho(1+\lambda^2)\ddot{u}_1 - \rho\lambda(1+\lambda^2)\ddot{u}_2 \\
&\quad - \big((\alpha - \sigma_2 + \gamma)\lambda^2 - \sigma_2 - \mathcal{H}_2 + \gamma\big)u_{1,11} - \big(\alpha - \mathcal{H}_2\lambda^2\big)u_{1,22} \\
&\quad - \lambda\big((\sigma_2 - \gamma)\lambda^2 + 2\mathcal{H}_2 + 2\alpha + \sigma_2 - \gamma\big)u_{1,12} + \lambda\big(\alpha\lambda^2 - \mathcal{H}_2\big)u_{2,11} \\
&\quad - \lambda\big((\sigma_2 + \mathcal{H}_2 - \gamma)\lambda^2 - \alpha + \sigma_2 - \gamma\big)u_{2,22} + \big((2\mathcal{H}_2 + 2\alpha + \sigma_2 - \gamma)\lambda^2 - \gamma + \sigma_2\big)u_{2,12} = 0. \tag{2-11}
\end{aligned}$$

These equations of motion are supplemented by the incremental incompressibility condition

$$u_{1,1} + u_{2,2} = 0. \tag{2-12}$$

Solutions of the three governing equations are sought in the form

$$(u_1, u_2, p_t) = (U_1, U_2, kP)e^{ikqx_2}e^{ik(vt-x_1)}, \tag{2-13}$$

where k is the wave number, v the phase speed and q is a parameter which will be determined from the governing equations. From the incompressibility condition, we first establish that $U_1 = qU_2$, which

when used within the two equations of motion provides a system of two homogeneous equations in two unknowns, representable in the form

$$c_{11}U_2 + c_{12}P = 0, \qquad c_{21}U_2 + c_{22}P = 0 \tag{2-14}$$

with

$$c_{11} = k^2(C_1^{(3)}q^3 + C_1^{(2)}q^2 + C_1^{(1)}q + C_1^{(0)}), \quad c_{12} = k^3 v\,(-c_\theta + q s_\theta),$$
$$c_{21} = k^2(C_2^{(3)}q^3 + C_2^{(2)}q^2 + C_2^{(1)}q + C_2^{(0)}), \quad c_{22} = k^3 v\,(q c_\theta + s_\theta),$$

where

$$C_1^{(3)} = -c_\theta(\gamma\, c_\theta{}^2 - \mathcal{K}_1 s_\theta{}^2), \qquad\qquad C_2^{(3)} = s_\theta(-K_2 c_\theta{}^2 + \alpha\, s_\theta{}^2),$$
$$C_1^{(2)} = -s_\theta(-\mathcal{K}_1 s_\theta{}^2 + (3\,\gamma + 2\mathcal{K}_1)\,c_\theta{}^2 + 2\,c_\theta{}^2\mathcal{K}_1), C_2^{(2)} = -c_\theta(-\mathcal{K}_2 c_\theta{}^2 + (3\,\alpha + 2\mathcal{K}_2)\,s_\theta{}^2),$$
$$C_1^{(1)} = c_\theta(c_\theta{}^2\mathcal{K}_1 - (3\,\gamma + 2\mathcal{K}_1)\,s_\theta{}^2 + \rho v^2), \qquad C_2^{(1)} = s_\theta(-s_\theta{}^2\mathcal{K}_2 + (3\,\alpha + 2\,\mathcal{K}_2)\,c_\theta{}^2 - \rho v^2),$$
$$C_1^{(0)} = s_\theta(-\gamma\, s_\theta{}^2 + c_\theta{}^2\mathcal{K}_1 + \rho v^2), \qquad\qquad C_2^{(0)} = -c_\theta(\alpha\, c_\theta{}^2 - s_\theta{}^2\mathcal{K}_2 - \rho v^2).$$

This system possesses a nontrivial solution provided the determinant of its coefficients is equal to zero; this leads, after use of (2-7), to the quartic equation

$$q^4 - 2\,\epsilon\, q^3 + \big(4\,\delta + 2 + \epsilon^2 - (1+\delta)\,\hat{v}\big)\,q^2 - 2\,(1+2\,\delta)\,\epsilon\, q + 1 + (1+\delta)\,\epsilon^2 - (1+\delta)\,\hat{v} = 0, \tag{2-15}$$

in q, where

$$\hat{v} = \frac{\rho v^2}{\sqrt{\alpha\gamma}}, \qquad \delta = \frac{\alpha + \gamma - 2\beta}{2(\beta + \sqrt{\alpha\gamma})} \tag{2-16}$$

are the dimensionless squared wave speed and a material parameter.

We note in passing that strong ellipticity dictates that $\alpha > 0$, $\gamma > 0$, $\beta > -\sqrt{\alpha\gamma}$, thus $\delta + 1 > 0$. The characteristic equation, (2-15), is the same as that previously derived by Connor and Ogden [Connor and Ogden 1996], using a different approach involving employment of a stream function. The motivation for our differing approach is to retain the hydrostatic pressure explicitly within the governing equations. This will later allow comparison of its relative order with the two displacement components, within the long-wave regimes. If we now multiply (2-14)$_1$ by c_θ and (2-14)$_2$ by s_θ, then subtract them and make use of (2-9), we obtain

$$P = \mathcal{P}(q)U_2, \qquad \mathcal{P}(q) = \frac{\mathcal{P}^{(3)}q^3 + \mathcal{P}^{(2)}q^2 + \mathcal{P}^{(1)}q + \mathcal{P}^{(0)}}{(\lambda^2 + 1)^2 k v},$$

with

$$\mathcal{P}^{(3)} = -\lambda^4\gamma - 2\,\beta\,\lambda^2 - \alpha,$$
$$\mathcal{P}^{(2)} = -(2\mathcal{K}_1 + \mathcal{K}_2 + 3\gamma)\lambda^3 + (\mathcal{K}_1 + 3\,\alpha + 2\mathcal{K}_2)\lambda,$$
$$\mathcal{P}^{(1)} = (\rho v^2 + \mathcal{K}_1)\lambda^4 - (3\gamma - 4\beta - 2\rho v^2 + 3\alpha)\lambda^2 + \mathcal{K}_2 + \rho v^2, \tag{2-17}$$
$$\mathcal{P}^{(0)} = (\alpha + \mathcal{K}_1)\lambda^3 - (\mathcal{K}_2 + \gamma)\lambda.$$

The solutions for u_1, u_2, and p_t may now be expressed as the linear combinations

$$u_1 = (q_1 A_1 e^{ikq_1 x_2} + q_2 A_2 e^{ikq_2 x_2} + q_3 B_1 e^{ikq_3 x_2} + q_4 B_2 e^{ikq_4 x_2}) e^{ik(vt - x_1)},$$

$$u_2 = (A_1 e^{ikq_1 x_2} + A_2 e^{ikq_2 x_2} + B_1 e^{ikq_3 x_2} + B_2 e^{ikq_4 x_2}) e^{ik(vt - x_1)}, \tag{2-18}$$

$$p_t = k(\mathscr{P}(q_1) A_1 e^{ikq_1 x_2} + \mathscr{P}(q_2) A_2 e^{ikq_2 x_2}) e^{ik(vt - x_1)} + k(\mathscr{P}(q_3) B_1 e^{ikq_3 x_2} + \mathscr{P}(q_4) B_2 e^{ikq_4 x_2}) e^{ik(vt - x_1)},$$

where A_1, A_2, B_1, B_2 are constants. The incremental traction components across any plane with outward unit normal along $\mathbf{n}$ in B_e are given by

$$\tau_i = B_{milk} u_{k,l} n_m + p_0 u_{m,i} n_m - p_t n_i. \tag{2-19}$$

Relative to the Eulerian system, the two nonzero traction components associated with the upper and lower faces of the plate are given by

$$\tau_1' = (B_{1111} u_{1,1}' + B_{1122} u_{2,2}') s_\theta + (B_{2112} u_{2,1}' + B_{2121} u_{1,2}') c_\theta + p_0 (u_{1,1}' s_\theta + u_{2,1}' c_\theta) - p_t s_\theta,$$

$$\tau_2' = (B_{1212} u_{2,1}' + B_{1221} u_{1,2}') s_\theta + (B_{2211} u_{1,1}' + B_{2222} u_{2,2}') c_\theta + p_0 (u_{1,2}' s_\theta + u_{2,2}' c_\theta) - p_t c_\theta. \tag{2-20}$$

The spatial derivatives in (2-20) are all referred to the Eulerian system. We now change and recalculate all the derivatives of displacement components and pressure relative to the natural system, obtaining

$$\begin{aligned} \tau_1 (\lambda^2 + 1)^{5/2} = & -(\lambda^2 + 1)^2 p_t \\ & + ((-B_{1221} - \gamma + B_{1111}) \lambda^4 + (-\mathscr{K}_1 - \gamma + 2 B_{1122}) \lambda^2 + B_{1122}) u_{1,1} \\ & + ((2\gamma - \sigma_2 + B_{1122}) \lambda^4 + (-\mathscr{K}_1 - 2\sigma_2 + 3\gamma + 2 B_{1122}) \lambda^2) u_{2,2} \\ & + (-\sigma_2 - \mathscr{K}_1 + \gamma + B_{1122}) u_{2,2} + (\lambda^5 \gamma - \mathscr{K}_1 \lambda + (-K_1 + \gamma) \lambda^3) u_{1,2} \\ & + ((\gamma - \sigma_2) \lambda^5 + (-\mathscr{K}_1 - \sigma_2) \lambda + (\gamma - 2\sigma_2 - \mathscr{K}_1) \lambda^3) u_{2,1}, \end{aligned} \tag{2-21}$$

$$\begin{aligned} \tau_2 (\lambda^2 + 1)^{5/2} = & -\lambda (\lambda^2 + 1)^2 p_t \\ & + (B_{1122} \lambda^5 + (-\mathscr{K}_2 - \alpha + 2 B_{1122}) \lambda^3 + (-\alpha + B_{1122} - \mathscr{K}_2) \lambda) u_{1,1} \\ & + ((\gamma + B_{1122} - \sigma_2 - \mathscr{K}_2) \lambda^5 + (-\sigma_2 + \alpha + \gamma + B_{1122}) \lambda) u_{2,2} \\ & + (\alpha + 2\gamma - \mathscr{K}_2 - 2\sigma_2 + 2 B_{1122}) \lambda^3 u_{2,2} + (\mathscr{K}_2 \lambda^4 - \alpha (\mathscr{K}_2 - \alpha) \lambda^2) u_{1,2} \\ & + ((\mathscr{K}_2 - 2\gamma + \alpha + 2\sigma_2) \lambda^2 - \gamma + (-\gamma + \alpha + \mathscr{K}_2 + \sigma_2) \lambda^4 + \sigma_2) u_{2,1}. \end{aligned} \tag{2-22}$$

After using the form of solutions (2-13) for displacements and pressure components, these two traction components may be expressed as

$$\tau_1 = \frac{1}{(\lambda^2 + 1)^{5/2}} \mathscr{T}_1(q), \qquad \mathscr{T}_1(q) = \mathscr{T}_1^{(3)} q^3 + \mathscr{T}_1^{(2)} q^2 + \mathscr{T}_1^{(1)} q + \mathscr{T}_1^{(0)},$$

$$\tau_2 = \frac{1}{(\lambda^2 + 1)^{5/2}} \mathscr{T}_2(q), \qquad \mathscr{T}_2(q) = \mathscr{T}_2^{(3)} q^3 + \mathscr{T}_2^{(2)} q^2 + \mathscr{T}_2^{(1)} q + \mathscr{T}_2^{(0)}, \tag{2-23}$$

where

$$
\begin{aligned}
\mathcal{T}_1^{(3)} &= \gamma\lambda^4 + 2\beta\lambda^2 + \alpha, \\
\mathcal{T}_1^{(2)} &= \lambda^5\gamma - (2\beta - 4\gamma)\lambda^3 + (4\beta - 3\alpha)\lambda, \\
\mathcal{T}_1^{(1)} &= (3\gamma - \sigma_2 - \rho v^2)\lambda^4 + (3\alpha - 2\rho v^2 - 2\sigma_2 + 7\gamma - 4\beta)\lambda^2 + 2\beta - \rho v^2 + \gamma - \sigma_2, \\
\mathcal{T}_1^{(0)} &= (\sigma_2 - \gamma)\lambda^5 + (2\sigma_2 - \alpha - \gamma)\lambda^3 - (2\beta - \gamma - \sigma_2)\lambda
\end{aligned}
\tag{2-24}
$$

and

$$
\begin{aligned}
\mathcal{T}_2^{(3)} &= \gamma\lambda^5 + 2\beta\lambda^3 + \lambda\alpha, \\
\mathcal{T}_2^{(2)} &= (3\gamma - 4\beta)\lambda^4 + (2\beta - 4\alpha)\lambda^2 - \alpha, \\
\mathcal{T}_2^{(1)} &= (2\beta - \sigma_2 + \gamma - \rho v^2)\lambda^5 - (4\beta + 2\sigma_2 - 5\alpha + 2\rho v^2 - 5\gamma)\lambda^3 + (2\alpha - \rho v^2 + \gamma - \sigma_2)\lambda, \\
\mathcal{T}_2^{(0)} &= (2\beta - 2\alpha + \gamma - \sigma_2)\lambda^4 + (3\gamma - \alpha - 2\sigma_2)\lambda^2 - \sigma_2 + \gamma.
\end{aligned}
\tag{2-25}
$$

The complete general solutions for τ_1 and τ_2, as a sum of partial wave solutions, are provided by

$$
\begin{aligned}
\tau_1 &= \mathcal{C}(\mathcal{T}_1(q_1)A_1 e^{ikq_1 x_2} + \mathcal{T}_1(q_2)A_2 e^{ikq_2 x_2})e^{ik(vt-x_1)} + \mathcal{C}(\mathcal{T}_1(q_3)B_1 e^{ikq_3 x_2} + \mathcal{T}_1(q_4)B_2 e^{ikq_4 x_2})e^{ik(vt-x_1)}, \\
\tau_2 &= \mathcal{C}(\mathcal{T}_2(q_1)A_1 e^{ikq_1 x_2} + \mathcal{T}_2(q_2)A_2 e^{ikq_2 x_2})e^{ik(vt-x_1)} + \mathcal{C}(\mathcal{T}_2(q_3)B_1 e^{ikq_3 x_2} + \mathcal{T}_2(q_4)B_2 e^{ikq_4 x_2})e^{ik(vt-x_1)}.
\end{aligned}
\tag{2-26}
$$

As a numerical illustration, we will employ in turn the neo-Hookean and Varga strain-energy functions

$$
W = \tfrac{1}{2}\mu(\lambda_1^2 + \lambda_2^2 + \lambda_3^2 - 3), \qquad W = \mu(\lambda_1 + \lambda_2 + \lambda_3 - 3),
\tag{2-27}
$$

where μ is the infinitesimal shear modulus. For the future reference, we note that the parameter δ from (2-16) is expressible in terms of ϵ:

$$
\text{(neo-Hookean)} \qquad \beta = \alpha + \gamma, \qquad \delta = 0;
$$

$$
\text{(Varga)} \qquad \beta = \sqrt{\alpha\gamma}, \qquad \delta = \frac{\left[\left(\frac{\alpha}{\gamma}\right)^{1/4} - \left(\frac{\gamma}{\alpha}\right)^{-1/4}\right]^2}{4} = \frac{\left(\lambda - \frac{1}{\lambda}\right)^2}{4} = \frac{\epsilon^2}{4}.
\tag{2-28}
$$

In passing, we remark that within the plane strain assumption neo-Hookean and Mooney–Rivlin materials coincide.

3. Analysis of the dispersion relation

The quartic characteristic equation (2-15) has four roots which affect the character of the dispersion relation. In particular, we note that solutions of (2-15) may in general form two complex conjugate pairs, be all real, or there may be two real together with a complex conjugates pair. In order to derive a dispersion relation we specify the boundary conditions:

$$
\tau_1 = \tau_2 = 0 \qquad \text{on} \qquad x_2 = 0, -h.
\tag{3-1}
$$

Before proceeding to the derivation of the dispersion relation, we note that the two traction components (2-26) may be represented as

$$
\begin{aligned}
\tau_1 = s_\theta \sqrt{\alpha\gamma}(f(q_1)A_1 e^{ikq_1x_2} + f(q_2)A_2 e^{ikq_2x_2})e^{ik(vt-x_1)} \\
+ s_\theta \sqrt{\alpha\gamma}(f(q_3)B_1 e^{ikq_3x_2} + f(q_4)B_2 e^{ikq_4x_2})e^{ik(vt-x_1)}, \\
\tau_2 = c_\theta \sqrt{\alpha\gamma}(g(q_1)A_1 e^{ikq_1x_2} + g(q_2)A_2 e^{ikq_2x_2})e^{ik(vt-x_1)} \\
+ c_\theta \sqrt{\alpha\gamma}(g(q_3)B_1 e^{ikq_3x_2} + g(q_4)B_2 e^{ikq_4x_2})e^{ik(vt-x_1)};
\end{aligned}
\tag{3-2}
$$

this representation concurs with that of [Connor and Ogden 1996], with $f(q)$ and $g(q)$ given by

$$
\begin{aligned}
f = \frac{(q-\lambda)\left(q+\lambda^{-1}\right)^2}{1+\delta} + 3q - \lambda + 2\lambda^{-1} + p(q-\lambda) - \hat{v}q, \quad \text{with } p = \frac{\gamma-\sigma_2}{\sqrt{\alpha\gamma}}; \\
g = \frac{(q-\lambda)^2\left(q+\lambda^{-1}\right)}{1+\delta} + 3q - 2\lambda + \lambda^{-1} + p\left(q+\lambda^{-1}\right) - \hat{v}q.
\end{aligned}
\tag{3-3}
$$

We now use the solutions for incremental tractions, together with the boundary conditions, to derive a system of four linear homogeneous equations in A_1, A_2, B_1, and B_2. The dispersion relation results from the condition that this system has a nontrivial solution, yielding a 4×4 determinant. After a little algebraic manipulation, this condition is expressible in the form

$$
\det \begin{vmatrix} f(q_1)C_1 & f(q_2)C_2 & f(q_3)C_3 & f(q_4)C_4 \\ g(q_1)C_1 & g(q_2)C_2 & g(q_3)C_3 & g(q_4)C_4 \\ f(q_1)S_1 & f(q_2)S_2 & f(q_3)S_3 & f(q_4)S_4 \\ g(q_1)S_1 & g(q_2)S_2 & g(q_3)S_3 & g(q_4)S_4 \end{vmatrix} = 0, \qquad S_j = \sin\frac{q_j kh}{2}, \quad C_j = \cos\frac{q_j kh}{2}.
\tag{3-4}
$$

We note that the dispersion relation may be shown to always provide a real equation. In the case of a neo-Hookean material [Connor and Ogden 1996] the characteristic equation (2-15) has the roots

$$
q_1 = i, \qquad q_2 = -i, \qquad q_3 = \epsilon + i\kappa, \qquad q_4 = \epsilon - i\kappa, \qquad \kappa^2 = 1 - \hat{v}.
\tag{3-5}
$$

When κ is real ($\hat{v} < 1$) there are four complex roots exist, and when κ is imaginary ($\hat{v} > 1$) two are complex and two real; the case of four real roots is not possible. If we introduce the small dimensionless parameter η, defined as the ratio of a layer thickness h to typical wave length l, so $\eta \equiv h/l \equiv kh$, the dispersion relation for a neo-Hookean material reduces to

$$
\begin{aligned}
\left(q_0(p^2 - \kappa^2)^2 + q_0\kappa^2(q_0 + 2p)^2 + 4\kappa^2(p^2 - \kappa^2)(q_0 + 2p)\right)\sinh(\eta)\sinh(\eta\kappa) \\
+ 2\kappa(pq_0 + p^2 + \kappa^2)^2\left(\cos(\eta\epsilon) - \cosh(\eta)\cosh(\eta\kappa)\right) = 0,
\end{aligned}
\tag{3-6}
$$

where $q_0 = 1 + \epsilon^2 + \kappa^2$.

To illustrate the behavior of the solution for the dispersion relation (3-4), some numerical results are presented for a plate composed of Varga material. Figure 1 shows dispersion curves of dimensionless frequency (vertical axis) against scaled wave number (horizontal axis) for several parameter sets, and Figure 2 has the corresponding plots of dimensionless squared wave speed (vertical scale) against scaled wave number (horizontal scale). From both figures it is possible to note that as ϵ increases a wave-front is observed, most strikingly in the lower right pane. Also, Figure 2 illustrates the fact that depending
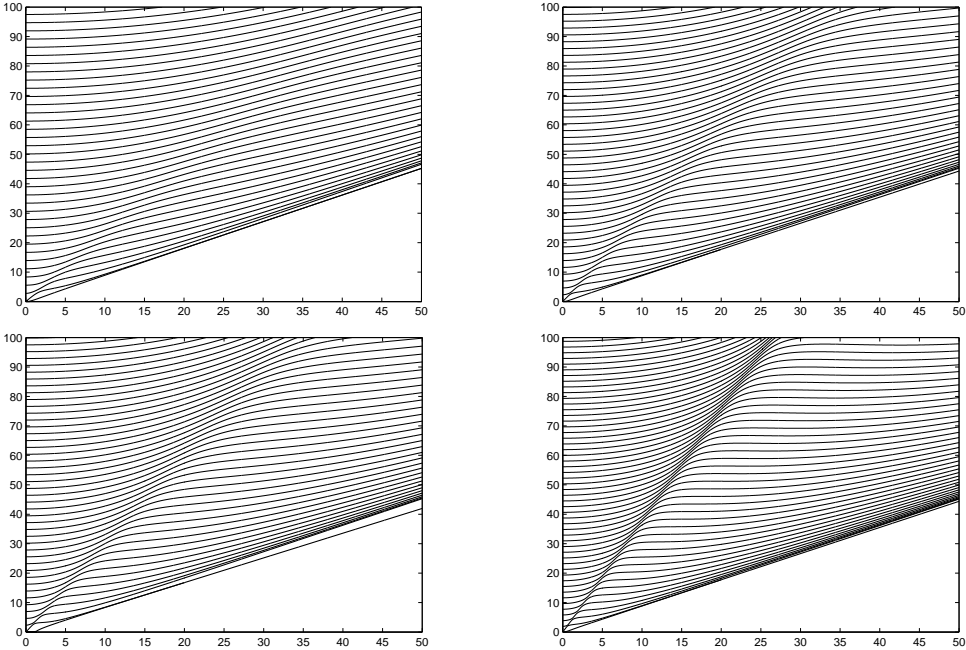
Figure 1. Numerical solution of dispersion relation, showing dimensionless frequency ω (vertical axis) against scaled wave number η (horizontal axis) for a Varga material. Clockwise from top left: $\epsilon = 1, 2, 3$, all with $p = 1$; lower left, $\epsilon = 2$, $p = 1.5$.

Figure 2. Numerical solution of dispersion relation, showing dimensionless squared wave speed $\hat{v}$ (vertical axis) against scaled wave number η (horizontal axis) for a Varga material. Clockwise from top left: $\epsilon = 1, 2, 3$, all with $p = 1$; lower left, $\epsilon = 2$, $p = 1.5$.

on the numerical values of ϵ and p there may be one (lower left pane) or two fundamental mode long-wave limits (remaining panes). Such phenomena will be investigated analytically through long-wave asymptotic expansion.

4. Long-wave low-frequency motion

4A. *Leading order.* Approximations for the phase speed will now be derived in the long-wave region. The term long-wave is introduced to indicate that the wavelength considerably exceeds the plate thickness and therefore $\eta \ll 1$, with $\eta \to 0$ indicating the long-wave limit. Our first consideration is so-called low-frequency motion, for which $\hat{v}$ generally remains finite as $\eta \to 0$. We therefore assume that the roots of the characteristic equation are not large and within the long-wave region

$$C_j = 1 + O(\eta^2), \qquad S_j = \frac{q_j \eta}{2} + O(\eta^3), \qquad j = 1, 2, 3, 4. \tag{4-1}$$

The appropriate leading-order term of the dispersion relation is then provided by

$$D = \det \begin{vmatrix} f(q_1) & f(q_2) & f(q_3) & f(q_4) \\ g(q_1) & g(q_2) & g(q_3) & g(q_4) \\ q_1 f(q_1) & q_2 f(q_2) & q_3 f(q_3) & q_4 f(q_4) \\ q_1 g(q_1) & q_2 g(q_2) & q_3 g(q_3) & q_4 g(q_4) \end{vmatrix} = 0. \tag{4-2}$$

Calculating the 4×4 determinant results in the following quadratic in $\hat{v}$:

$$\mathscr{D}^{(0)} \equiv \hat{v}^2 + (p^2(\delta+1) - 2p(\delta+1) + \delta - 3 - \epsilon^2)\hat{v} - (p^2 - 1)(2p(1+\delta) - 2(\delta-1) + 2 + \epsilon^2) = 0, \tag{4-3}$$

with the two roots taking the explicit forms

$$\hat{v}_1^{(0)} = \frac{-(p-1)^2(\delta+1) + \epsilon^2 + 4 + \sqrt{R}}{2},$$

$$\hat{v}_2^{(0)} = \frac{-(p-1)^2(\delta+1) + \epsilon^2 + 4 - \sqrt{R}}{2},$$

$$R = \left((p-1)^2 \delta + (p+1)^2 - \epsilon^2\right)^2 + 4\epsilon^2 (p+1)^2. \tag{4-4}$$

In passing, we note that the discriminant of the quadratic in $\hat{v}$ is a perfect square in each of the cases in which δ or ϵ vanish or $p = -1$.

4B. *Second order.* To obtain second-order correction terms of dispersion relation, the trigonometrical functions in (3-4) are expanded to the next order, resulting in

$$C_j = 1 - \frac{q_j^2 \eta^2}{8} + O(\eta^4), \qquad S_j = \frac{q_j \eta}{2} - \frac{q_j^3 \eta^3}{48} + O(\eta^4), \qquad j = 1, 2, 3, 4. \tag{4-5}$$

The dispersion relation is then expanded and may be represented in the form

$$\mathscr{D} = \mathscr{D}^{(0)} + \eta^2 \mathscr{D}^{(2)} + O(\eta^4). \tag{4-6}$$
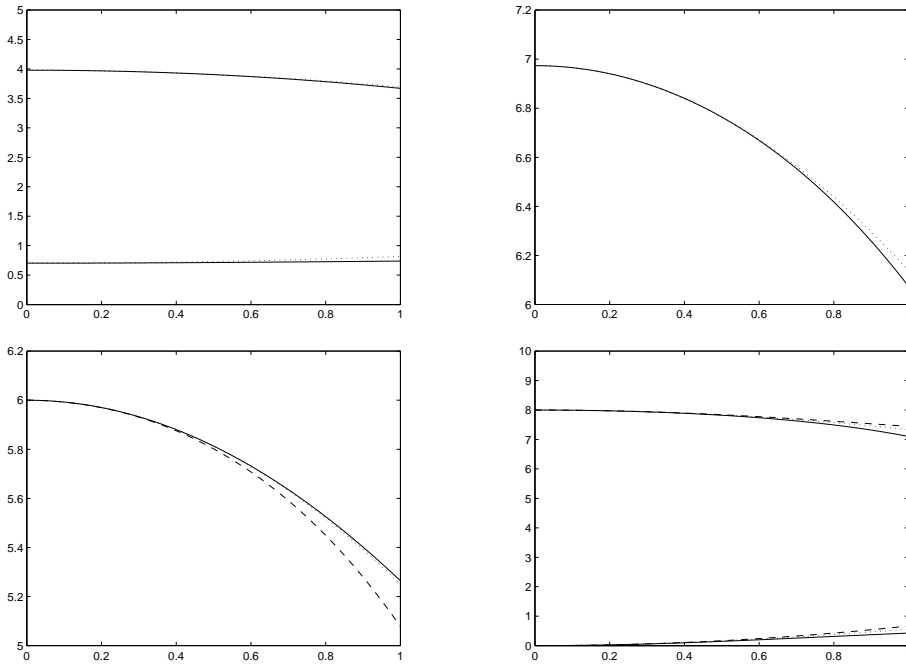
Figure 3. Comparison of numerical (solid lines) and asymptotic results for the fundamental modes, showing $\hat{v}$ (vertical axis) against η (horizontal axis). Top row: Varga material with $\epsilon = 1$, $p = 0.5$ (left, two fundamental modes), and with $\epsilon = 1$, $p = 2$ (right, one fundamental mode); the dotted curve represents the second-order approximation. Bottom row: neo-Hookean material with $\epsilon = 0$, $p = 2$ (left, one fundamental mode), and with $\epsilon = 2$, $p = 1$ (right, two fundamental modes); the dotted curve is the third-order approximation and the dashed curve is the second-order approximation.

We note that both $\mathcal{D}^{(0)}$ and $\mathcal{D}^{(2)}$ are quadratic in $\hat{v}$. The form of $\mathcal{D}^{(2)}$ is sufficiently complicated that it is not of value to write it explicitly here. Notwithstanding this, a corrected expansion may be readily established and written down in the form

$$\hat{v}_i = \hat{v}_i^{(0)} - \eta^2 \frac{\mathcal{D}^{(2)}(\hat{v}_i^{(0)})}{\mathcal{D}'^{(0)}(\hat{v}_i^{(0)})} + O(\eta^4). \tag{4-7}$$

Although the explicit representation of $\mathcal{D}^{(2)}$ is complex, nevertheless approximations afforded by (4-7) can be readily generated and compared with the purely numerical solution. Figure 3 confronts numerical results with second- and third-order approximations for the fundamental modes. The second-order approximation curves in the case of a Varga material (top panes) already show very good agreement over a wide wave number regime; third-order approximation curves are omitted in this case.

4C. *Long-wave low-frequency approximations in the case $\delta = 0$.* In this section we consider a class of materials for which $\delta = 0$, implying that $2\beta = \alpha + \gamma$. As first noted in [Connor and Ogden 1996], in such cases the characteristic equation (2-15) factorizes and the dispersion relation takes the particularly simple form given in (3-6). Using (3-6), we are able to derive long-wave low-frequency approximations

up to and including $O(\eta^4)$. We begin by noting the following expansions:

$$\sinh(\eta) = \eta + \tfrac{1}{6}\eta^3 + O(\eta^5), \qquad \cosh(\eta) = 1 + \tfrac{1}{2}\eta^2 + \tfrac{1}{24}\eta^4 + O(\eta^5),$$

$$\kappa = \sqrt{1 - \hat{v}_0} - \frac{1}{2}\frac{\hat{v}_1\,\eta^2}{\sqrt{1 - \hat{v}_0}} - \frac{4\hat{v}_2(1 - \hat{v}_0) + \hat{v}_1^2}{8(1 - \hat{v}_0)^{3/2}}\eta^4 + O(\eta^5),$$

$$\cos(\eta\epsilon) = 1 - \tfrac{1}{2}\eta^2\epsilon^2 + \tfrac{1}{24}\eta^4\epsilon^4 + O(\eta^5), \tag{4-8}$$

$$\sinh(\eta\kappa) = \sqrt{1 - \hat{v}_0}\eta + \frac{(\hat{v}_0 - 1)^2 - 3\hat{v}_1}{6\sqrt{1 - \hat{v}_0}}\eta^3 + \frac{(\hat{v}_0 - 1)^2}{8}\eta^4 + O(\eta^5),$$

$$\cosh(\eta\kappa) = 1 + \tfrac{1}{2}\left(1 - \hat{v}_0\right)\eta^2 - \tfrac{1}{12}\left(6\hat{v}_1 + (\hat{v}_0 - 1)^2\right)\eta^4 + O(\eta^5).$$

Employing expansions (4-8) in (3-6), we obtain a representation of the dispersion relation in a form

$$\mathscr{D} = \mathscr{D}^{(0)} + \eta^2\mathscr{D}^{(2)} + \eta^4\mathscr{D}^{(4)} + O(\eta^6), \tag{4-9}$$

providing, at leading order,

$$\mathscr{D}^{(0)} = \sqrt{1 - \hat{v}_0}(1 - p^2 - \hat{v}_0)(\hat{v}_0^2 - 2\epsilon^2\hat{v}_0 + \epsilon^4 + 4\epsilon^2)(2 + \epsilon^2 - \hat{v}_0 + 2p) = 0. \tag{4-10}$$

In (4-10) the root $\hat{v}_0 = 1$ is a spurious root associated with a double root of the characteristic equation. Additionally, the third factor cannot provide any real solutions and we therefore conclude that the two long-wave limits are provided by

$$\hat{v}_1^{(0)} = 1 - p^2, \qquad \hat{v}_2^{(0)} = \epsilon^2 + 2p + 2. \tag{4-11}$$

It is now possible to show that the second-order term $\mathscr{D}^{(2)}$ provides a linear function in $\hat{v}$, from which we deduce the two second-order corrections:

$$\hat{v}_1^{(2)} = \tfrac{1}{12}(\epsilon^2 + (p+1)^2)p^2, \qquad \hat{v}_2^{(2)} = -\tfrac{1}{12}(\epsilon^2 + (p+1)^2). \tag{4-12}$$

Finally, the third dispersion term $\mathscr{D}^{(4)}$ is again a linear term in $\hat{v}^{(2)}$ and provides the following third-order corrections:

$$\hat{v}_1^{(4)} = \frac{p^2\mathscr{L}_1}{576(\epsilon^2 + 1 + 3\,p^2 - 4\,p)}, \qquad \hat{v}_2^{(4)} = \frac{\mathscr{L}_2}{576(2p + \epsilon^2 + 1)(7p + 3\epsilon^2 + 3)}, \tag{4-13}$$

where

$$\mathscr{L}_1 = \epsilon^6 + (3p^2 - 12p - 13)\epsilon^4 - (13p^4 - 24p^3 - 10p^2 + 24p + 29)\epsilon^2$$
$$- 15p^6 + 4p^5 + 55p^4 + 88p^3 + 23p^2 - 12p - 15,$$

$$\mathscr{L}_2 = -24(p^2 + p + 1)\epsilon^6 - (136p^3 + 168p^2 - 73p - 72)\epsilon^4$$
$$- (256p^4 + 366p^3 - 28p^2 - 218p - 72)\epsilon^2 - 159p^5 - 252p^4 - 34p^3 + 172p^2 + 121p + 24.$$

For the class of materials considered, expansions for the two long-wave low-frequency dimensionless squared wave speeds may be expressed as

$$\hat{v}_m = \hat{v}_m^{(0)} + \eta^2\hat{v}_m^{(2)} + \eta^4\hat{v}_m^{(4)} + O(\eta^6), \tag{4-14}$$

within which $\hat{v}_m^{(n)}$, $m = 1, 2$, $n = 0, 2, 4$, are as given in equations (4-11), (4-12) and (4-13). For certain sets of parameters, these approximations might not be valid because third-order corrections may become large within the vicinity of certain combinations of ϵ and p. These combinations of parameters may be identified as

$$\epsilon^2 + 1 + 3\,p^2 - 4\,p = 0,$$
$$2\,p + \epsilon^2 + 1 = 0,$$
$$7\,p + 3\epsilon^2 + 3 = 0, \tag{4-15}$$

noting that both leading-order approximations should stay positive. Using these conditions, we obtain some regions close to which the approximations are not valid, given by

$$\text{(a)} \qquad 0 \le \epsilon \le \frac{1}{\sqrt{3}} \qquad \text{with} \qquad p = \frac{2 \pm \sqrt{1 - 3\epsilon^2}}{3},$$

$$\text{(b)} \qquad 0 \le \epsilon \le 1 \qquad \text{with} \qquad p = \frac{(\epsilon^2 + 1)}{2}, \tag{4-16}$$

$$\text{(c)} \qquad 0 \le \epsilon \le \frac{2}{\sqrt{3}} \qquad \text{with} \qquad p = \frac{3(\epsilon^2 + 1)}{7}.$$

The bottom panes in Figure 3 show good agreement between these expansions and numerical solutions for the fundamental modes in the case of a neo-Hookean strain-energy function.

5. Long-wave high-frequency motion

The long-wave high-frequency case can be characterized by the fact that the scaled phase speed $\hat{v} \to \infty$ as $\eta \to 0$. We will also assume that the associated cut-off frequencies are finite. We begin by examining the four roots of the characteristic equation (2-15) when $\hat{v} \gg 1$ and consider expansions of its roots in the form

$$q = s_1 \hat{v} + s_0 + \frac{s_2}{\hat{v}} + \frac{s_3}{\hat{v}^2} + \frac{s_4}{\hat{v}^3}, \qquad \hat{v} = \frac{\Omega}{\eta}. \tag{5-1}$$

After some algebraic manipulation, the following approximations for the roots of (2-15) are obtained:

$$q_1 = i - \frac{i\delta\,(\epsilon - 2\,i)^2\,\eta^2}{2\,(1 + \delta)\,\Omega^2} + O(\eta^4), \qquad q_2 = -i + \frac{i\delta\,(\epsilon + 2\,i)^2\,\eta^2}{2\,(1 + \delta)\,\Omega^2} + O(\eta^4),$$

$$q_3 = \frac{\sqrt{1 + \delta\Omega}}{\eta} + \epsilon - \frac{1}{2}\frac{(4\,\delta + 1)\,\eta}{\sqrt{1 + \delta\Omega}} + \frac{2\epsilon\,\delta\,\eta^2}{(1 + \delta)\,\Omega^2} - \frac{1}{8}\frac{(16\,\delta^2 + 20\,\epsilon^2\delta - 8\,\delta + 1)\,\eta^3}{(1 + \delta)^{3/2}\,\Omega^3} + O(\eta^4), \tag{5-2}$$

$$q_4 = -\frac{\sqrt{1 + \delta\Omega}}{\eta} + \epsilon + \frac{1}{2}\frac{(4\,\delta + 1)\,\eta}{\sqrt{1 + \delta\Omega}} + \frac{2\epsilon\,\delta\,\eta^2}{(1 + \delta)\,\Omega^2} + \frac{1}{8}\frac{(16\,\delta^2 + 20\,\epsilon^2\delta - 8\,\delta + 1)\,\eta^3}{(1 + \delta)^{3/2}\,\Omega^3} + O(\eta^4),$$

where Ω is the associated scaled frequency and η the dimensionless wave number.

5A. *Leading order.* To derive the leading-order approximations, we represent the dispersion relation in terms of the finite scaled frequency Ω_0 and small scaled wave number η. Before doing this, we establish

the roots of the characteristic equation up to and including $O(\eta^2)$, which yields

$$q_1 = i\left(1 + O(\eta^2)\right), \qquad q_2 = i\left(1 + O(\eta^2)\right),$$

$$q_3 = \frac{\Omega_0\sqrt{1+\delta}}{\eta} + \epsilon - \frac{(4\delta+1)\eta}{2\Omega_0\sqrt{1+\delta}} + O(\eta^2), \tag{5-3}$$

$$q_4 = -\frac{\Omega_0\sqrt{1+\delta}}{\eta} + \epsilon + \frac{(4\delta+1)\eta}{2\Omega_0\sqrt{1+\delta}} + O(\eta^2),$$

allowing the following expansions for the $f(q_i)$ to be obtained:

$$f(q_1) \approx -\frac{((1+\delta)\,p+\delta)\,\lambda^2+1-2\,\delta}{(1+\delta)\,\lambda} - i\left(\frac{\Omega_0^2}{\eta^2} - \frac{1+((1+\delta)\,p+3\,\delta)\,\lambda^2}{(1+\delta)\,\lambda^2}\right),$$

$$f(q_3) \approx \left(\frac{2\,\epsilon\,\lambda-\lambda^2+2}{\lambda}\right)\frac{\Omega_0^2}{\eta^2} + \frac{\left(2\,\epsilon^2+2\,\delta+1\right)\lambda+\epsilon}{(1+\delta)\,\lambda^2}$$

$$+ \left(\frac{1-2\,\epsilon\,\lambda^3+\left(3\,\epsilon^2+1+(1+\delta)\,p+3\,\delta\right)\lambda^2+4\,\epsilon\,\lambda}{\sqrt{1+\delta}\lambda^2}\right)\frac{\Omega_0}{\eta}$$

$$+ \frac{-(\epsilon^2+(1+\delta)\,(p+1))\lambda^3+\left(\epsilon^3+((1+\delta)\,p+3\,\delta+1)\,\epsilon\right)\lambda^2}{(1+\delta)\,\lambda^2}, \tag{5-4}$$

and likewise for the $g(q_i)$:

$$g(q_1) \approx \frac{(1-2\,\delta)\,\lambda^2+(1+\delta)\,p+\delta}{(1+\delta)\,\lambda} - i\left(\frac{\Omega_0^2}{\eta^2} - \frac{3\,\delta+\lambda^2+(1+\delta)\,p}{1+\delta}\right),$$

$$g(q_3) \approx \left(\frac{2\,\epsilon\,\lambda-2\,\lambda^2+1}{\lambda}\right)\frac{\Omega_0^2}{\eta^2} + \frac{\epsilon^2+\delta+(1+\delta)\,p+1}{(1+\delta)\,\lambda}$$

$$+ \left(\frac{\lambda^3-4\,\epsilon\,\lambda^2+\left(3\,\epsilon^2+1+(1+\delta)\,p+3\,\delta\right)\lambda+2\,\epsilon}{\sqrt{1+\delta}\lambda}\right)\frac{\Omega_0}{\eta}$$

$$+ \frac{\epsilon\,\lambda^3-\left(2\,\epsilon^2+2\,\delta+1\right)\lambda^2+\left(\epsilon^3+((1+\delta)\,p+3\,\delta+1)\,\epsilon\right)\lambda}{(1+\delta)\,\lambda}. \tag{5-5}$$

To derive a leading-order form of the dispersion relation Equation (3-4), expansions for sin and cos are required, these being obtainable as

$$S_1 = \tfrac{1}{2}i\eta + O(\eta^2), \qquad S_2 = -\tfrac{1}{2}i\eta + O(\eta^2),$$

$$S_3 = \sin\left(\tfrac{1}{2}\sqrt{1+\delta}\Omega_0\right) + \tfrac{1}{2}\cos\left(\tfrac{1}{2}\sqrt{1+\delta}\Omega_0\right)\epsilon\,\eta + O(\eta^2),$$

$$S_4 = -\sin\left(\tfrac{1}{2}\sqrt{1+\delta}\Omega_0\right) + \tfrac{1}{2}\cos\left(\tfrac{1}{2}\sqrt{1+\delta}\Omega_0\right)\epsilon\,\eta + O(\eta^2),$$

$$C_1 = 1 + O(\eta^2), \qquad C_2 = 1 + O(\eta^2), \tag{5-6}$$

$$C_3 = \cos\left(\tfrac{1}{2}\sqrt{1+\delta}\Omega_0\right) - \tfrac{1}{2}\sin\left(\tfrac{1}{2}\sqrt{1+\delta}\Omega_0\right)\epsilon\,\eta + O(\eta^2),$$

$$C_4 = \cos\left(\tfrac{1}{2}\sqrt{1+\delta}\Omega_0\right) + \tfrac{1}{2}\sin\left(\tfrac{1}{2}\sqrt{1+\delta}\Omega_0\right)\epsilon\,\eta + O(\eta^2).$$

Substituting these expansions, together with (5-4), (5-5) and (5-3), into (3-4) results in a dispersion relation of the form $\mathscr{D}^{(0)} + O(\eta^2)$. At leading order, we obtain $\mathscr{D}^{(0)} = 0$, implying that

$$\sin\left(\sqrt{1+\delta}\,\Omega_0\right) = 0 \implies \Omega^{(0)} = \frac{n\pi}{\sqrt{1+\delta}}. \tag{5-7}$$

5B. *Long-wave high-frequency approximations in the case $\delta = 0$.* In the case $\delta = 0$, we establish long-wave high-frequency approximations to higher order than in the general case.

5B.1. *Leading-order approximations.* Motivated by the general case, we assume that $\Omega = \Omega_0 + O(\eta^2)$. The following expansions are obtainable for the neo-Hookean material dispersion relation (3-6)

$$\kappa = \sqrt{1 - \frac{\Omega^2}{\eta^2}} = \frac{i\Omega_0}{\eta} - \left(\frac{i}{2\Omega_0}\right)\eta + O(\eta^2),$$

$$\cos(\eta\epsilon) = 1 + O(\eta^2), \qquad \sinh(\eta) = \eta + O(\eta^2), \qquad \cosh(\eta) = 1 + O(\eta^2), \tag{5-8}$$

$$\sinh(\eta\kappa) = i\sin(\Omega_0) + O(\eta^2), \qquad \cosh(\eta\kappa) = \cos(\Omega_0) + O(\eta^2),$$

from which the dispersion relation takes the approximate form

$$\mathscr{D} = \mathscr{D}^{(0)} + O(\eta^2), \qquad \mathscr{D}^{(0)} = i\Omega_0{}^8 \sin(\Omega_0). \tag{5-9}$$

From (5-9) we deduce that the cut-off frequencies are given by $\Omega_0 = n\pi$, a result which could have been obtained directly from (5-7).

5B.2. *Higher-order approximations.* Corrections to the cut-off frequencies are now sought in the form

$$\Omega = n\pi + \Omega_2\eta^2 + \Omega_4\eta^4 + O(\eta^5). \tag{5-10}$$

Keeping in mind that $\cos\Omega_0 = (-1)^n$ and $\sin\Omega_0 = 0$, we obtain the following expansions up to and including $O(\eta^4)$:

$$\kappa = \frac{i\pi n}{\eta} + \frac{i\,(-1 + 2\pi n\Omega_2)}{2\pi n}\eta + \frac{i\left(8\pi^3 n^3\Omega_4 - 1 + 4\pi n\Omega_2\right)}{8\pi^3 n^3}\eta^3 + O(\eta^5),$$

$$\sinh(\eta) = \eta + \tfrac{1}{6}\eta^3 + O(\eta^5), \qquad \cosh(\eta) = 1 + \tfrac{1}{2}\eta^2 + \tfrac{1}{24}\eta^4 + O(\eta^5),$$

$$\cos(\eta\epsilon) = 1 - \tfrac{1}{2}\eta^2\epsilon^2 + \tfrac{1}{24}\eta^4\epsilon^4 + O(\eta^5), \tag{5-11}$$

$$\sinh(\eta\kappa) = \frac{i\,(-1)^n\,(-1 + 2\pi n\Omega_2)}{2\pi n}\eta^2 + \frac{i\,(-1)^n\left(8\pi^3 n^3\Omega_4 - 1 + 4\pi n\Omega_2\right)}{8\pi^3 n^3}\eta^4 + O(\eta^5),$$

$$\cosh(\eta\kappa) = (-1)^n - - \frac{(-1)^n + 4\,(-1)^{1+n}\pi n\Omega_2 + 4\,(-1)^n\pi^2 n^2\Omega_2{}^2}{8\pi^2 n^2}\eta^4 + O(\eta^5).$$

The dispersion relation correction is now expressible as

$$\mathscr{D} = \mathscr{D}^{(2)}\eta^2 + \mathscr{D}^{(4)}\eta^4 + O(\eta^6), \tag{5-12}$$

leading to the corrections

$$\Omega_2 = \frac{4\,(p+1)^2\left((-1)^n - 1\right) + (-1)^n\pi^2 n^2}{2\pi^3 n^3\,(-1)^n}, \qquad \Omega_4 = \frac{\mathscr{H}}{24n^5\pi^5(-1)^n},$$

where

$$\mathcal{H} = -192\,\pi^4 n^4 (-1)^n \Omega_2{}^2$$
$$+ \Big(240\,\pi\,n((-1)^n - 1)(p^2 + 1) + 36\,\pi^3 n^3 (-1)^n (5 + 2\,\epsilon^2)$$
$$+ \big(96\,\pi^3 n^3 (-1)^n + 480\,\pi\,n((-1)^n - 1)\big)p - 4\,\pi^5 n^5 (-1)^n\Big)\Omega_2$$
$$+ ((96(1 - (-1)^n) + 24\,\pi^2 n^2)p^2 + (96(1 - (-1)^n) + 48\,\pi^2 n^2)p)\epsilon^2$$
$$+ 96\,(1 - (-1)^n)p^3 + (24\,(-1)^n\pi^2 n^2 + 312(1 - (-1)^n))p^2$$
$$- 336\,((-1)^n - 1)p + 12\,\pi^2 n^2 (2 - 3\,(-1)^n)\epsilon^2 + 120(1 - (-1)^n) - 21\,(-1)^n\pi^2 n^2 + 2\,(-1)^n\pi^4 n^4.$$

Although the corrections, especially Ω_4, are quite complex, they are readily plotted, and provide excellent agreement with numerical solutions (Figure 4).

6. Relative asymptotic orders of displacements and hydrostatic pressure

We now wish to establish the relative orders of displacement and pressure within both the long-wave low and high-frequency regimes. Before moving on to this, we first introduce the notation $\zeta = x_2/h$; after which the solutions for displacement components and hydrostatic pressure may, from (2-18), be represented in the form

$$u_1 = (q_1 A_1 e^{i\eta q_1 \zeta} + q_2 A_2 e^{i\eta q_2 \zeta} + q_3 B_1 e^{i\eta q_3 \zeta} + q_4 B_2 e^{i\eta q_4 \zeta})e^{ik(vt - x_1)},$$
$$u_2 = (A_1 e^{i\eta q_1 \zeta} + A_2 e^{i\eta q_2 \zeta} + B_1 e^{i\eta q_3 \zeta} + B_2 e^{i\eta q_4 \zeta})e^{ik(vt - x_1)}, \tag{6-1}$$
$$p_t = k\big(P(q_1)A_1 e^{i\eta q_1 \zeta} + P(q_2)A_2 e^{i\eta q_2 \zeta}\big)e^{ik(vt - x_1)} + k\big(P(q_3)B_1 e^{i\eta q_3 \zeta} + P(q_4)B_2 e^{i\eta q_4 \zeta}\big)e^{ik(vt - x_1)},$$

where A_1, A_2, B_1 and B_2 may, through the use of (3-1) and (3-2), be related through

$$f(q_1)A_1 + f(q_2)A_2 + f(q_3)B_1 + f(q_4)B_2 = 0,$$
$$g(q_1)A_1 + g(q_2)A_2 + g(q_3)B_1 + g(q_4)B_2 = 0,$$
$$f(q_1)e^{-iq_1\eta}A_1 + f(q_2)e^{-iq_2\eta}A_2 + f(q_3)e^{-iq_3\eta}B_1 + f(q_4)e^{-iq_4\eta}B_2 = 0, \tag{6-2}$$
$$g(q_1)e^{-iq_1\eta}A_1 + g(q_2)e^{-iq_2\eta}A_2 + g(q_3)e^{-iq_3\eta}B_1 + g(q_4)e^{-iq_4\eta}B_2 = 0.$$

6A. *Long-wave low-frequency leading-order displacements and hydrostatic pressure.* In the long-wave low-frequency regime the squared wave speed is generally $O(1)$. Accordingly, there are generally no large or small parameters in the characteristic equation (2-15), and we may assume that to leading order $\exp(-i\eta q_j \zeta) = 1 + O(\eta)$. Thus, in the long-wave low-frequency region

$$u_1 \approx (q_1 A_1 + q_2 A_2 + q_3 B_1 + q_4 B_2), \qquad u_2 \approx A_1 + A_2 + B_1 + B_2,$$
$$p_t \approx k(P(q_1)A_1 + P(q_2)A_2 + P(q_3)B_1 + P(q_4)B_2). \tag{6-3}$$

To obtain the dependence of the coefficients A_1, A_2, B_1, and B_2, and thereby the displacement components and pressure increment, on η, we first use the fact that $\exp(-i\eta q_j) = 1 - i\eta q_j + O(\eta^2)$, for $j \in [1, 4]$, and note the two associated long-wave low-frequency phase speed limits given by (4-4). In complete generality it is possible to establish the relative asymptotic orders of A_1, A_2, B_1, and B_2 and

$\epsilon = 1,\ p = 0.5$ $\qquad\qquad\qquad\qquad$ $\epsilon = 2,\ p = 1$
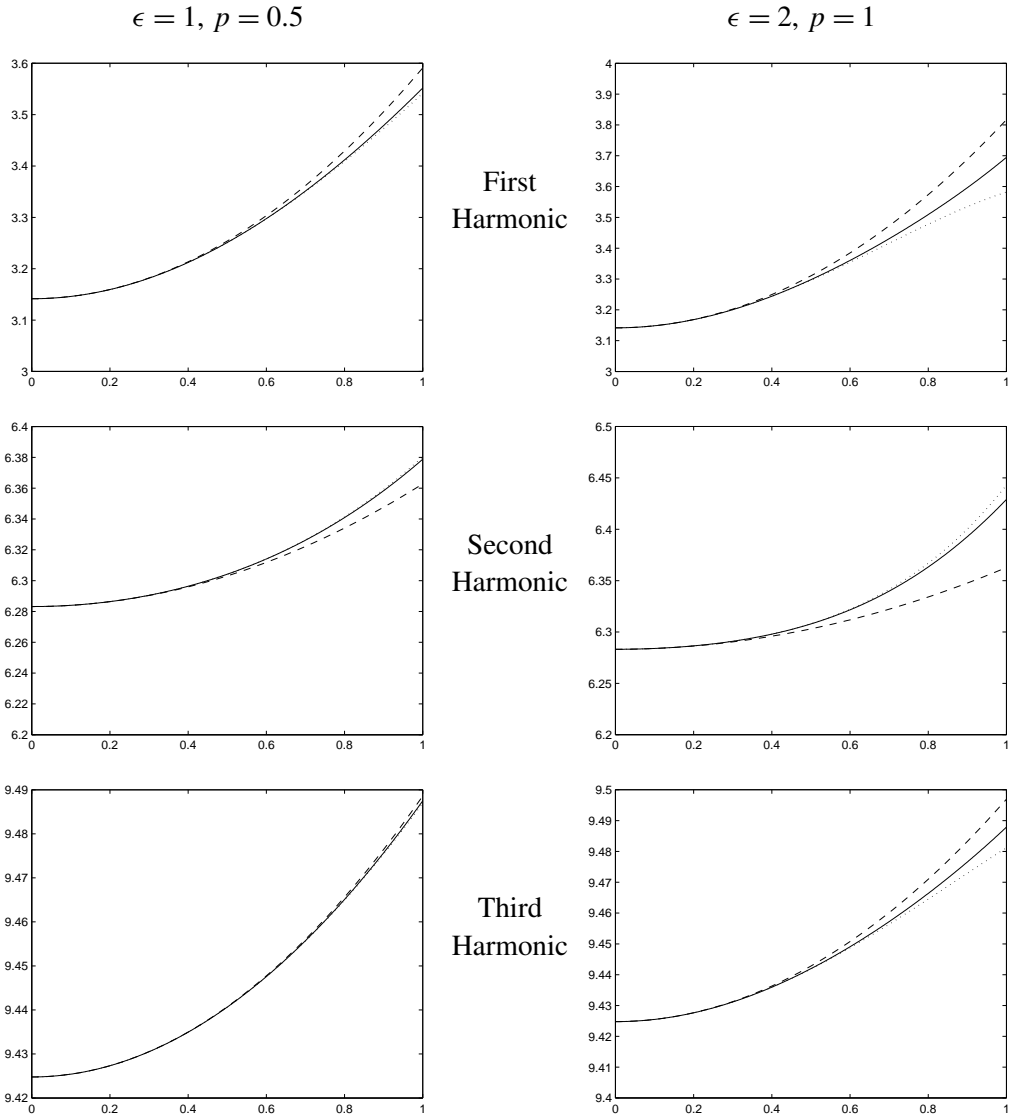
Figure 4. Second- and third-order approximations for first three harmonics compared with numerical results: dimensionless frequency Ω (vertical axis) against scaled wave number η (horizontal axis) for neo-Hookean material. Dotted curves correspond to third order, dashed curves to second order and unbroken curves to numerical results.

hence establish the relative orders of u_1, u_2, and p_t. However, the complexity of the algebra is immense. Accordingly, only explicit results relating to a neo-Hookean material are presented. In this case, A_1, A_2, B_1, and B_2 may be expressed in terms of one parameter, $\tilde{U}$ say, from which the leading order displacements are established as shown in Table 1 at the top of the next page, where we remark that the exponential function $e^{ik(x_1-vt)}$ has been incorporated into the definition of $\tilde{U}$. It is of interest to note that in Case 1 the in-plane displacement component u_1 has a factor ϵ at leading order, whereas in Case 2, the

Case 1: $\hat{v}^{(0)} = \hat{v}_1^{(0)} = 1 - p^2,$

$$u_1 = \left(\frac{16 \mathcal{M}_1^1 \left((p-1)^2 + \epsilon^2\right) \left((p+1)^2 + \epsilon^2\right) p\epsilon}{\left(\epsilon + \sqrt{\epsilon^2 + 4}\right)^3} \right) \tilde{U}\eta + O(\eta^2),$$

$$u_2 = \left(\frac{32 \mathcal{M}_2^1 \left((p-1)^2 + \epsilon^2\right) \left((p+1)^2 + \epsilon^2\right) (p+1) p}{\left(\epsilon + \sqrt{\epsilon^2 + 4}\right)^4} \right) \tilde{U}\eta + O(\eta^2),$$

$$\mathcal{M}_1^1 = \sqrt{\epsilon^2 + 4} \left(2(p+1) + \epsilon^2(p+4) + \epsilon^4\right) + \epsilon^5 + \epsilon^3(p+6) + 4\epsilon(p+2)$$

$$\mathcal{M}_2^1 = \left(\epsilon^5 + \epsilon^3(p+5) + \epsilon(3p+5)\right)\sqrt{\epsilon^2 + 4} + \epsilon^6 + \epsilon^4(p+7) + \epsilon^2(5p+13) + 4(p+1).$$

Case 2: $\hat{v}^{(0)} = \hat{v}_2^{(0)} = \epsilon^2 + 2p + 2,$

$$u_1 = \left(\frac{64 \mathcal{M}_1^2 \left((p+1)^2 + \epsilon^2\right) (p+1) \sqrt{1 + \epsilon^2 + 2p}}{\left(\epsilon + \sqrt{\epsilon^2 + 4}\right)^3} \right) \tilde{U}\eta + O(\eta^2),$$

$$u_2 = -\left(\frac{128 \mathcal{M}_2^2 \left((p+1)^2 + \epsilon^2\right) \epsilon \sqrt{1 + \epsilon^2 + 2p}}{\left(\epsilon + \sqrt{\epsilon^2 + 4}\right)^4} \right) \tilde{U}\eta + O(\eta^2),$$

$$\mathcal{M}_1^2 = \left(\epsilon^2 p + 3p + 1\right) \epsilon\sqrt{\epsilon^2 + 4} + \epsilon^4 p + \epsilon^2(5p+1) + 4$$

$$\mathcal{M}_2^2 = \left(\epsilon^4 p + \epsilon^2(4p+1) + 2(p+1)\right)\sqrt{\epsilon^2 + 4} + \epsilon^5 p + \epsilon^3(6p+1) + 4\epsilon(2p+1),$$

Table 1. Leading-order displacements (see previous page).

normal displacement component u_2 has a similar factor. We may therefore conclude that if $\epsilon \sim O(1)$, u_1 and u_2 have the same asymptotic orders. This contrasts with the classical case, discussed for example [Kaplunov et al. 1998], in which $u_2 \gg u_1$ in Case 1 (bending) and $u_1 \gg u_2$ Case 2 (extension). It also contrasts with their prestress counterparts for which one principal axis is normal to the plate — see [Kaplunov et al. 2000] — within which the classical structure is preserved. In the case $\epsilon = 0$, the results above reduce to

Case 1: Bending

$$\hat{v}_1^{(0)} = 1 - p^2, \quad u_1 = O(\eta^2), \quad u_2 = 8(p+1)^4(p-1)^2 p\tilde{U}\eta + O(\eta^2), \quad \mathcal{M}_1^2 = \mathcal{M}_2^2 = 4(p+1),$$

Case 2: Extension

$$\hat{v}_2^{(0)} = 2p + 2, \quad u_1 = 32(p+1)^4 \tilde{U}\sqrt{1 + 2p}\,\eta + O(\eta^2), \quad u_2 = O(\eta^2), \quad \mathcal{M}_1^1 = \mathcal{M}_2^1 = 4(p+1).$$

From this we see that if $\epsilon = 0$, the relative orders agree with previously mentioned classical results. In passing we note that the relative asymptotic orders may need modification within the vicinity of certain critical states of prestress. The order of hydrostatic pressure in case of a neo-hookean material may similarly be established and shown to be of the form

$$p_t = k\mathcal{Q}\tilde{U}\eta + O(\eta^2), \tag{6-4}$$

with $\mathcal{Q}$ generally $O(1)$. For both associated fundamental modes, the coefficient $\mathcal{Q}$ is algebraically complex and is therefore not written explicitly here. However, in the case of $\epsilon = 0$, more explicit results are

obtainable, yielding

$$\textbf{Case 1: } \hat{v}_1^{(0)} = 1 - p^2: \qquad \mathscr{Q}^{(1)} = 0,$$

$$\textbf{Case 2: } \hat{v}_2^{(0)} = 2p + 2: \qquad \mathscr{Q}^{(2)} = 32\gamma\,\sqrt{1 + 2p}(1 + p)^5\tilde{U},$$

indicating that in Case 1 (Bending) $p_t \sim \eta^2$ and in Case 2 (extension) $p_t \sim \eta$. These results, together with those for u_1 and u_2, are a particular case of those obtained in [Kaplunov et al. 2000].

6B. *Long-wave high-frequency leading-order displacements and hydrostatic pressure.* As $\eta \to 0$, appropriate approximations of the characteristic equation, (2-15), are readily obtainable and the exponential functions in (6-1) are therefore representable in the approximate forms

$$e^{i\eta q_1 \zeta} = 1 + O(\eta), \qquad e^{i\eta q_2 \zeta} = 1 + O(\eta),$$

$$e^{i\eta q_3 \zeta} = e^{i\zeta n\pi} + O(\eta), \qquad e^{i\eta q_4 \zeta} = e^{-i\zeta n\pi} + O(\eta).$$

Hence, in the long-wave high-frequency regime, the displacement components and hydrostatic pressure are given approximately by

$$u_1 \approx q_1 A_1 + q_2 A_2 + q_3 B_1 e^{i\zeta n\pi} + q_4 B_2 e^{-i\zeta n\pi},$$

$$u_2 \approx A_1 + A_2 + B_1 e^{i\zeta n\pi} + B_2 e^{-i\zeta n\pi},$$

$$p_t \approx k\big(P(q_1)A_1 + P(q_2)A_2 + P(q_3)B_1 e^{i\zeta n\pi} + P(q_4)B_2 e^{-i\zeta n\pi}\big).$$

In order to estimate the dependence of the coefficients A_1, A_2, B_1, and B_2 on η, we expand the exponential functions in powers of η, up to $O(\eta^2)$, which yields

$$e^{-i\eta q_1} = 1 + \eta + O(\eta^2), \qquad e^{-i\eta q_2} = 1 - \eta + O(\eta^2),$$

$$e^{-i\eta q_3} = (-1)^n(1 - i\eta\epsilon) + O(\eta^2), \qquad e^{-i\eta q_4} = (-1)^n(1 - i\eta\epsilon) + O(\eta^2).$$

The displacement components are now expressible in terms of a single parameter $\tilde{U}$ in the form

$$u_1 = C_6^{(1)}\eta^{-6} + C_5^{(1)}(\eta^{-5}) + O(\eta^{-4}),$$

$$u_2 = C_5^{(2)}(\eta^{-5}) + O(\eta^{-4}),$$

$$C_6^{(1)} = \frac{4n^7\pi^7\,(-1)^n\,(\lambda^2 + 1)\,\cosh(\zeta n\pi)\tilde{U}}{\lambda\,(1 + \delta)^3},$$

$$C_5^{(1)} \neq 0,$$

$$C_5^{(2)} = \frac{2i\,(\lambda^2 + 1)\,\pi^5 n^5\tilde{U}}{\lambda^3\,(1 + \delta)^3}\mathscr{C}_u,$$

for

$$\mathscr{C}_u = -2i\pi\,\lambda^2 n(-1)^n\sinh(\zeta n\pi) + 2\,(1 - (-1)^n)\big(\lambda^4 - 2\lambda^3\epsilon - \lambda^2(p(1 + \delta) + \epsilon^2 + 6 + 2\delta) + 2\epsilon + 1\big),$$

and the pressure takes the form

$$p_t = kc^{(7)}\eta^{-7} + kc^{(6)}\eta^{-6} + O(\eta^{-5}),$$

where

$$c_7 = c_1^{(7)}\epsilon + c_0^{(7)}, \qquad c_6 = c_2^{(6)}\epsilon^2 + c_1^{(6)}\epsilon + c_0^{(6)}.$$

All the coefficients are quite lengthy both in general and for the neo-Hookean strain energy function. However, in general all coefficients are $O(1)$. We note from the above long-wave representations that the incremental pressure is asymptotically leading, with the in-plane displacement component very much larger than its normal counterpart. We note that in the case $\epsilon = 0$,

$$c_0^{(7)}(\epsilon = 0, \Omega = \Omega^{(0)}) = 0,$$
$$c_0^{(6)}(\epsilon = 0, \Omega = \Omega^{(0)}) = 8\gamma\pi^7 n^7(-1)^n(p+1)\tilde{U},$$

indicating that now the incremental pressure and in-plane displacement are the same order. This is in agreement with the result in [Kaplunov et al. 2000]. We conclude by remarking that in general the incremental pressure is asymptotically leading and this will have consequences in the derivation of appropriate asymptotic long-wave models.

7. Some concluding remarks

In this paper we have investigated the influence of a simple shear primary deformation on long wave motion in an incompressible elastic layer. For high-frequency motion, the results are broadly similar to those previously published in regard to pure homogeneous strain. However, the results for low-frequency motion show a significant departure from previous investigations. In this case it is not possible to decompose the problem into symmetric and antisymmetric components. It is therefore not possible to establish analogs of classical extension and bending. The reason for this is that whenever the amount of shear is finite, within the long-wave low-frequency regime both the in-plane and normal displacement components have the same asymptotic order. This contrasts with the classical cases of extension and bending, together with their homogeneously strained counterparts, for which the in-plane and normal component are asymptotically leading, respectively. Knowledge of the asymptotic orders of displacement components will provide the necessary basis for deriving an appropriate asymptotic model. Although such a model would be a great simplification, with the displacements having the same order, it would seem unlikely that it will be one-dimensional. Work to clarify this is currently being carried out and the results will be published in due course.

References

[Bar and Pal 1985] B. K. Bar and A. K. Pal, "On the possibility of Love propagation under initial shear stress", *Procedings of the Indian National Academy* **51** (1985), 686–688.

[Connor and Ogden 1995] P. Connor and R. W. Ogden, "The effect of shear on the propagation of elastic surface waves", *Int. J. Engng Sci.* **33** (1995), 973–982.

[Connor and Ogden 1996] P. Connor and R. W. Ogden, "The influence of shear strain and hydrostatic stress on stability and elastic waves in a layer", *Int. J. Engng Sci.* **34** (1996), 375–397.

[Destrade and Ogden 2005] M. Destrade and R. W. Ogden, "Surface waves in a stretched and sheared incompressible material", *Int. J. Non-Linear Mech.* **40** (2005), 241–253.

[Fu 2005] Y. B. Fu, "An explicit expression for the surface-impedance matrix of a generally anisotropic incompressible elastic material in a state of plain strain", *International Journal of Non-linear Mechanics* **40** (2005), 229–239.

[Gessner et al. 2007] K. Gessner, C. Wijns, and L. Moresi, "Significance of strain localization in the lower crust for structural evolution and thermal history of metamorphic core complexes", *Tectonics* **26**:2 (2007), TC2012.

[Ide et al. 2007] S. Ide, G. C. Beroza, D. R. Shelly, and T. Uchide, "A scaling law for slow earthquakes", *Nature* **447**:7140 (2007), 76–79.

[Kaplunov et al. 1998] J. D. Kaplunov, L. Y. Kossovich, and E. V. Nolde, *Dynamics of thin walled elastic bodies*, Academic Press, 1998.

[Kaplunov et al. 2000] J. D. Kaplunov, E. V. Nolde, and G. A. Rogerson, "A low-frequency model for dynamic motion in pre-stressed incompressible elastic structures", *Proc. R. Soc. Lond, A* **456** (2000), 2589–2610.

[Kaplunov et al. 2002] J. D. Kaplunov, E. V. Nolde, and G. A. Rogerson, "An asymptotically consistent model for long-wave high-frequency in a pre-stressed elastic plate", *Mathematics and Mechanics of Solids* **7** (2002), 581–606.

[Nolde et al. 2004] E. V. Nolde, L. Prikazchikova, and G. A. Rogerson, "Dispersion of small amplitude waves in a pre-stressed, compressible elastic plate", *Journal of Elasticity* **75** (2004), 1–29.

[Ogden 1984] R. W. Ogden, *Non-linear elastic deformations*, Ellis Horwood, Chichester, 1984.

[Ogden and Roxburg 1993] R. W. Ogden and D. G. Roxburg, "The effect of pre-stress on the vibration and stability of elastic plates", *Int. J. Engng Sci.* **31** (1993), 1611–1639.

[Rogersion and Fu 1995] G. A. Rogersion and Y. B. Fu, "An asymptotic analysis of the dispersion relation of a pre-stressed incompressible elastic plate", *Acta Mech* **111** (1995), 59–77.

[Rogerson 1997] G. A. Rogerson, "Some asymptotic expansions of the dispersion relation for an incompressible elastic plate", *Int. J. Solid Structures* **34** (1997), 2785–2802.

[Rogerson 1998] G. A. Rogerson, "On the existence of surface waves and the propagation of plate waves in pre-stressed fibre-reinforced composites", *J. Mech. Phys. Solids* **46** (1998), 1581–1612.

[Roxburgh and Ogden 1994] D. G. Roxburgh and R. W. Ogden, "Stability and vibration of pre-stressed compressible elastic plates", *Int. J. Engng. Sci.* **32** (1994), 427–454.

[Triantafyllidis and Abeyarante 1983] N. Triantafyllidis and R. Abeyarante, "Instabilities of a finitely-deformed elastic material", *ASME Journal of Applied Mechanics* **50** (1983), 149–156.

SVETLANA R. AMIROVA: s.amirova@epsam.keele.ac.uk
Department of Mathematics, University of Keele, Keele, Staffordshire, ST5 5BG, United Kingdom

GRAHAM A. ROGERSON: g.a.rogerson@keele.ac.uk
Department of Mathematics, University of Keele, Keele, Staffordshire, ST5 5BG, United Kingdom

RENORMALIZATIONS IN SOLID AND FRACTURE MECHANICS

H. D. BUI

We show how some inconsistencies and infinities arising in solid and fracture mechanics can be avoided by renormalization techniques widely used in theoretical physics. Some examples, already known in solid mechanics or recently discovered in fracture mechanics, are given as illustrations.

1. Introduction

There are at least two kinds of renormalization that can be considered in the mechanics of continuous media. The first (type I) corresponds to models described by a given level of observation or scale for which an improper mathematical analysis leads to the divergence of a physical quantity. Very often, a suitable choice of a small parameter and then a correct limit procedure avoids the inconsistencies. Renormalization of type I appears to be a purely *mathematical* procedure. The second type of renormalization (type II) is more often considered in physics, for example when one changes the description of the physical system by using an appropriate scale of observation. Examples are known in quantum field theory [Gell-Mann and Low 1964; Bogolioubov and Chirkov 1960], phase transitions [Wilson 1971a; 1971b; Goldenfeld 1993], scaling [Kadanov 1966], and turbulence [Adzhemyan et al. 1999]. Here renormalization procedures consist in introducing physical arguments for treating the new scale and removing the singularities. Renormalization of type II is viewed as a *physical* justification of the singularity removal. Both types of renormalization will be considered in this paper and adapted to solid and fracture mechanics.

We recall briefly the purpose of renormalization in physics. Suppose that, for some level of description, a physical quantity, for example the (unit) mass of a naked electron in the absence of electromagnetic field, is described by a wave function, the norm of which is related to the mass m_0. Such a fictional naked electron does not exist. At a finer observation, there is an interaction between the naked electron and electromagnetic fields. One finds that the true mass m is given by the self-energy equation $mc^2 = (m_0 + am_1)c^2$, where $a = 1/127$ is the fine structure constant and am_1 is the first-order radiative correction. To recalculate or renorm the mass (the word renormalization comes from this purpose) one has to evaluate m_1, which is provided by a divergent integral. Therefore, to give a sense to the first-order solution, one needs a regularization procedure that consists in taking the finite part of a divergent integral. In this procedure, one may consider that the infinite part of am_1 will be further compensated by singularities of higher-order radiative corrections am_2 etc, in a hierarchical manner, like Russian dolls.

In such a procedure, the words renormalization and regularization become synonymous. In this paper, we still make use of the terminology 'renormalization' since it relates, for type II, to a physical change of the primary model. We shall adapt the renormalization procedure to solid and fracture mechanics. For

example, in linear fracture mechanics, the best known singularity, associated with the stress intensity factor at the crack tip, indicates that some modified form of physics (and hence mathematics) must take over at a sufficiently *fine* scale.

To the author's best knowledge, the concept of renormalization is seldom fully recognized in solid and fracture mechanics, even if many examples of regularization procedures can be found in the literature. This paper focuses on some examples; some classical, others recently discovered in fracture mechanics. Type I renormalization will be illustrated by many examples: as the first one, considered in Section 2, we shall look at the divergence arising in boundary integral formulations employed in elastoplasticity, which has been removed by techniques based on the convected differentiation of integrals proposed in [Bui 1978]. The second example of renormalization of type I, given in Section 3, is related to the fundamental solution of the Helmholtz equation in acoustics, which must verify the 'perturbed' equation, in the sense that it corresponds to the continuous solution of the Helmholtz equation when the frequency or wave number k tends towards zero [Bonnet 1995]. One knows that such a fundamental solution is not unique and the fundamental Green's function usually selected in textbooks does not converge towards the static solution as k tends toward zero. To obtain a continuous solution, subtraction of a constant from the classic Green's function will be made.

Renormalization of type II is discussed in Section 4 for some models of fracture mechanics, such as Barenblatt's cohesive model [1959a; 1959b], or hierarchical models of fracture [Bui and Ehrlacher 1980]. In Section 5 we discuss a new example of type II renormalization that takes place in the differentiation of the energy release rate for point load. We propose to adequately handle some inconsistencies encountered in this process by a new renormalization procedure.

2. Renormalization of type I

How to deal with divergent integrals? We consider a simple example of a divergent integral, namely, the function $F(x)$ defined by the line integral

$$F(x) = \int_{-1}^{+1} \frac{dt}{t-x} = \ln\left|\frac{1-x}{1+x}\right|. \tag{1}$$

Its derivative is obviously given by $F'(x) = 1/(x-1) - 1/(x+1)$, but the formal integral expression is divergent for $-1 < x < +1$, since

$$F'(x) = \int_{-1}^{+1} \frac{dt}{(t-x)^2} = \infty. \tag{2}$$

To deal with such a divergent integral, many regularization procedures exist, one of them being Hadamard's definition [1932] of the finite part of a divergent integral. One first has to single out the singularity of the integral $F'_h(x)$ depending on a small parameter h, which is the infinite part $S_h = 2/h$, as $h \to 0$:

$$F'(x) := \left(\int_{-1}^{x-h} + \int_{x+h}^{+1}\right) \frac{dt}{(t-x)^2} = \frac{2}{h} + \text{regular terms} \tag{3}$$

The finite part of $F'(x)$ is precisely given by the regular terms, $(\text{fp})F'(x) := F'(x) - S_h(x)$ [Schwartz 1978; Sellier 1996]:

$$(\text{fp})F'(x) := F'(x) - \frac{2}{h} \quad (h \to 0). \tag{4}$$

What is the mathematical justification for this subtraction procedure? Looking at the origin of the divergence, we observe that Equation (2) is an improper definition of the derivative $F'(x)$ because the integral $F(x)$ itself must be understood as a principal value (pv) integral, defined here with the symmetric excluded zone $x - h < t < x + h$:

$$F(x) \equiv (\text{pv})F(x) := \lim_{h \to 0} \left(\int_{-1}^{x-h} + \int_{x+h}^{+1} \right) \frac{dt}{(t-x)} = \ln \left| \frac{1-x}{1+x} \right|. \tag{5}$$

Therefore, the derivative of the pv integral $F(x)$ consists of two terms—the first, $1/(t-x)^2$, given by the pv integral of the derivative, and the second given by the *convected* differentiation at the endpoints $t = x \pm h$:

$$F'(x) = \lim_{h \to 0} \left(\int_{-1}^{x-h} + \int_{x+h}^{+1} \right) \frac{dt}{(t-x)^2} + \left[\frac{1}{t-x} \right]_{t=x-h} - \left[\frac{1}{t-x} \right]_{t=x+h}. \tag{6}$$

It follows that convected terms cancel the singularity of the hypersingular integral. We obtain the correct result

$$F'(x) = \lim_{h \to 0} \left(\frac{2}{h} + \frac{1}{x-1} - \frac{1}{x+1} - \frac{2}{h} \right) = \frac{1}{x-1} - \frac{1}{x+1}. \tag{7}$$

Thus Hadamard's finite part of a divergent integral and convected differentiation are just two different ways to renormalize the same divergent integral.

So far in the discussion, the excluded region $x - h < t < x + h$ has been symmetric—an assumption justified by the use of Cauchy's pv integrals. If we take an asymmetric segment $x - h < t < x + \lambda h$, where λ is a positive number not equal to 1, a different infinite part of the divergent integral (2) is obtained, $S_h = (\lambda + 1)/(\lambda h)$. Let the divergent integral (2) be written, for h tending towards zero, as

$$F_\lambda'(x) = \lim_{h \to 0} \left(\int_{-1}^{x-h} + \int_{x+\lambda h}^{+1} \right) \frac{dt}{(t-x)^2} = \frac{1}{x-1} - \frac{1}{x+1} + S_h.$$

We obtain the same result (7) given by the finite part integral (fp) $F_\lambda'(x) := F_\lambda'(x) - S_h = 1/(x-1) - 1/(x+1)$. In the asymmetric excluded zone case, for consistency, function $F_\lambda(x)$ must be written as

$$F_\lambda(x) = \lim_{h \to 0} \left(\int_{-1}^{x-h} + \int_{x+\lambda h}^{+1} \right) \frac{dt}{(t-x)} = \ln \left| \frac{1-x}{1+x} \right| - \ln \lambda.$$

After differentiation with respect to x, the constant $\ln \lambda$ does not contribute to $F_\lambda'(x)$.

Boundary integral equation formulations of three-dimensional elastoplasticity.

An important application of the convected differentiation procedure has been given for the formulation of boundary integral equations in elastoplasticity, which does not involve hyper-singular integrals [Bui 1978]. Let us recall the boundary integral equations in elastoplasticity, for domain Ω with a smooth boundary $\partial \Omega$. The

displacement rate $\dot{\boldsymbol{u}}$ and the traction rate $\dot{\boldsymbol{T}}$ on the boundary are related to the plastic strain rate $\dot{\epsilon}^p$, with unit outward normal $\boldsymbol{n}$ as follows (see [Mendelson 1973]):

$$\alpha(\boldsymbol{x})\,\dot{u}_k(\boldsymbol{x}) + \int_{\partial\Omega} \Sigma_{kij}(\boldsymbol{x},\boldsymbol{y})\,\dot{u}_k(\boldsymbol{y})n_j(\boldsymbol{y})\,dS_y - \int_{\partial\Omega} G_{ki}(\boldsymbol{x},\boldsymbol{y})\dot{T}_i(\boldsymbol{y})\,dS_y = \int_P \Sigma_{kij}(\boldsymbol{x},\boldsymbol{y})\,\dot{\epsilon}_{ij}^p(\boldsymbol{y})\,dV_y, \quad (8)$$

where P is the active plastic zone, $G(\boldsymbol{x},\boldsymbol{y})$ is the fundamental Green's tensor in linear and isotropic elasticity and $\Sigma(\boldsymbol{x},\boldsymbol{y}) = \sigma[G(\boldsymbol{x},\boldsymbol{y})]$ is the associated fundamental stress tensor. The notation $\sigma[\boldsymbol{u}]$ means $\sigma = L : \nabla\boldsymbol{u}$, where L is the isotropic symmetric moduli tensor. The Green's tensor and the fundamental stress tensor have the singularities $O(\|\boldsymbol{x}-\boldsymbol{y}\|^{-1})$ and $O(\|\boldsymbol{x}-\boldsymbol{y}\|^{-2})$ respectively. Finally, in Equation (8) the coefficient $\alpha(\boldsymbol{x})$ satisfies, for a domain with smooth boundary,

$$\alpha(\boldsymbol{x}) = \begin{cases} 1 & \text{for } \boldsymbol{x} \in \Omega, \\ 0 & \text{for } \boldsymbol{x} \notin \overline{\Omega}, \\ \frac{1}{2} & \text{for } \boldsymbol{x} \in \partial\Omega. \end{cases}$$

To complete the system of equations (8), one needs another relation between the displacement rate $\dot{\boldsymbol{u}}$ and the stress rate $\dot{\boldsymbol{T}}$, which requires the calculation of the gradient $\nabla\dot{\boldsymbol{u}}$ in the entire domain, by differentiating (8) term by term. For interior points $\boldsymbol{x}$, we have $\alpha = 1$ and the term $\Sigma_{kij,h}(\boldsymbol{x},\boldsymbol{y})$ (where the subscript $_{,h}$ indicates partial differentiation with respect to x_h) is integrable over $\partial\Omega$ (because $\|\boldsymbol{x}-\boldsymbol{y}\| \neq 0$ for $\boldsymbol{y}$ on the boundary). By contrast, as soon as $\boldsymbol{x}$ lies inside the domain, there is a nonintegrable kernel with

$$\Sigma_{kij,h}(\boldsymbol{x},\boldsymbol{y}) = O(\|\boldsymbol{x}-\boldsymbol{y}\|^{-3}). \quad (9)$$

For interior points $\alpha = 1$, the gradient of the displacement rate is strictly given by

$$\dot{u}_{k,h}(\boldsymbol{x}) + \int_{\partial\Omega} \frac{\partial}{\partial x_h}\Sigma_{kij}(\boldsymbol{x},\boldsymbol{y})\,\dot{u}_i(\boldsymbol{y})n_j(\boldsymbol{y})\,dS_y - \int_{\partial\Omega} \frac{\partial}{\partial x_h}G_{ki}(\boldsymbol{x},\boldsymbol{y})\dot{T}_i(\boldsymbol{y})\,dS_y$$
$$= \frac{\partial}{\partial x_h} \int_P \Sigma_{kij}(\boldsymbol{x},\boldsymbol{y})\,\dot{\epsilon}_{ij}^p(\boldsymbol{y})\,dV_y. \quad (10)$$

On the right-hand side of this equation, it would be incorrect to interchange the differentiation and integration operators. In the 1970s, most workers were not aware of this difficulty [Bui 1978]. Today one recognizes that the hypersingular integral (with kernel $\Sigma_{kij,h}(\boldsymbol{x},\boldsymbol{y})$) must be understood in the *finite part* sense and properly evaluate either by Hadamard's expansion at infinity or by a convected differentiation of a pv integral.

To calculate the hypersingular integral, it is simplest to use the notion of convected differentiation of integrals, similar to (6). First, the integral of $\Sigma_{kij}(\boldsymbol{x},\boldsymbol{y})\,\dot{\epsilon}_{ij}^p(\boldsymbol{y})$, which is of order $O(\|\boldsymbol{x}-\boldsymbol{y}\|^{-2})$ over the three-dimensional domain P, can be written as a pv integral, since the contribution of the spherical ball $B_e(\boldsymbol{x})$ of radius e and centered at $\boldsymbol{x}$, being of order $O(e)$, can be neglected:

$$\int_P \Sigma_{kij}(\boldsymbol{x},\boldsymbol{y})\,\dot{\epsilon}_{ij}^p(\boldsymbol{y})\,dV_y \equiv (\text{pv}) \int_P \Sigma_{kij}(\boldsymbol{x},\boldsymbol{y})\,\dot{\epsilon}_{ij}^p(\boldsymbol{y})\,dV_y := \lim_{e\to 0} \int_{P-B_e(x)} \Sigma_{kij}(\boldsymbol{x},\boldsymbol{y})\,\dot{\epsilon}_{ij}^p(\boldsymbol{y})\,dV_y.$$

This relation holds due to the symmetry of the excluded subdomain. In differentiating the pv integral we have two terms: the principal value integral, with kernel $(\partial/\partial x_h)\Sigma_{kij}(\boldsymbol{x},\boldsymbol{y})$, and the second term,

coming from convected differentiation along the sphere $\partial B_e(\boldsymbol{x})$ with unit outward normal $\nu(\boldsymbol{y})$ to the sphere

$$\frac{\partial}{\partial x_h}\int_P \Sigma_{kij}(\boldsymbol{x},\boldsymbol{y})\,\dot{\epsilon}^p_{ij}(\boldsymbol{y})\,dV_y = (\text{pv})\int_P \frac{\partial}{\partial x_h}\Sigma_{kij}(\boldsymbol{x},\boldsymbol{y})\,\dot{\epsilon}^p_{ij}(\boldsymbol{y})\,dV_y - \lim_{e\to 0}\int_{\partial B_e(x)}\Sigma_{kij}(\boldsymbol{x},\boldsymbol{y})\,\dot{\epsilon}^p_{ij}(\boldsymbol{y})\nu_h(\boldsymbol{y})\,dV_y.$$

For linear and isotropic elasticity, and for deviatoric plastic strain rate, it can be shown that the convected differentiation of the above integral is [Bui 1978]

$$\frac{\partial}{\partial x_h}\int_P \Sigma_{kij}(\boldsymbol{x},\boldsymbol{y})\,\dot{\epsilon}^p_{ij}(\boldsymbol{y})\,dV_y = (\text{pv})\int_P \frac{\partial}{\partial x_h}\Sigma_{kij}(\boldsymbol{x},\boldsymbol{y})\,\dot{\epsilon}^p_{ij}(\boldsymbol{y})\,dV_y + \frac{8-10\nu}{15(1-\nu)}\dot{\epsilon}^p_{ij}(\boldsymbol{x}). \tag{11}$$

There is an extra term[1] appearing in the regularization process of the hyper-singular integral. Thus the concept of renormalization is necessary to properly derive boundary-integral equations in elastoplasticity. Examples of renormalization in (7) and (11) show that, when dealing with singular integrals, differentiation and integration are noncommutative operators. Other examples of finite-part integrals in fracture mechanics can be found in [Bui 1978; Lazarus 1998],

3. The fundamental solution of the Helmholtz equation in acoustics and its regularization

Another example of type I renormalization is provided by the classical fundamental solution of the Helmholtz equation

$$\Delta_{\boldsymbol{y}}G(\boldsymbol{y},\boldsymbol{x};k)+k^2 G(\boldsymbol{y},\boldsymbol{x};k)+\delta(\boldsymbol{y}-\boldsymbol{x})=0, \tag{12}$$

where δ is the Dirac delta pseudofunction. In this equation, $k=\omega/c$ is the wave number and $\Delta_{\boldsymbol{y}}$ is the Laplacian operator with respect to the observation point $\boldsymbol{y}$, while $\boldsymbol{x}$ is the so-called source point. Let us consider the solution of the equation for small k and examine the continuity of the solution as k tends to zero. If $G(\boldsymbol{y},\boldsymbol{x};k)$ tends towards the static fundamental solution $G(\boldsymbol{y},\boldsymbol{x})$, one says that $G(\boldsymbol{y},\boldsymbol{x};k)$ satisfies the regularly perturbed equation. Such a solution is also called a regularized one. Otherwise, the Green's function is not necessarily continuous at $k=0$. In three dimensions, the fundamental solution satisfies the continuity condition, because (with $r=\|\boldsymbol{y}-\boldsymbol{x}\|$)

$$G(\boldsymbol{y},\boldsymbol{x};k)=\frac{\exp(ikr)}{4\pi r}, \qquad G(\boldsymbol{y},\boldsymbol{x})=\frac{1}{4\pi r}, \qquad G(\boldsymbol{y},\boldsymbol{x};k)-G(\boldsymbol{y},\boldsymbol{x})=O(k). \tag{13}$$

But this is not true anymore in two dimensions. Indeed, the two-dimensional Green's function given in standard textbooks reads

$$G(\boldsymbol{y},\boldsymbol{x};k)=\frac{i}{4}H_0^1(kr), \tag{14}$$

where $H_0^1(kr)$ is the Hankel function of the first kind and order zero. The Hankel function $H_0^1(z)$ can be expanded as [Abramovitz and Stegun 1972; Gradshteyn and Ryzhik 1965]

$$H_0^1(z)=J_0(z)+iN_0(z), \tag{15}$$

---

[1]The extra term $E(B)$ given by the second term in the right-hand side of (11) depends on the geometry of the symmetric ball B. With another symmetric excluded domain B' (ellipsoid, cube) the extra term $E(B')$ is different. The difference $E(B)-E(B')$ is hidden in the pv integral corresponding to B' [Sellier 1996]. Therefore the numerical calculation of the pv integral must be carefully undertaken with a correct excluded domain, which is a spherical ball in (11).

where

$$J_0(z) = 1 - \tfrac{1}{4}z^2 + O(z^4), \qquad N_0(z) = \frac{2}{\pi}\left(\ln\frac{z}{2} + \gamma\right) - \frac{1}{2\pi}\left(\ln\frac{z}{2} + \gamma - 1\right) + O(z^4) \tag{16}$$

with $\gamma = 0.577215\ldots$ Euler's constant.

This yields

$$G(\boldsymbol{y}, \boldsymbol{x}; k) = -\frac{1}{2\pi}\ln r + \frac{i}{4} - \frac{1}{2\pi}(\ln\frac{k}{2} + \gamma) + O(k^2\ln k). \tag{17}$$

The first term on the right is the static two-dimensional solution $G = -(1/2\pi)\ln r$. Thus

$$G(\boldsymbol{y}, \boldsymbol{x}; k) - G(\boldsymbol{y}, \boldsymbol{x}) = \frac{i}{4} - \frac{1}{2\pi}(\ln\frac{k}{2} + \gamma) + O(k^2\ln k)$$

The classical Green's function is not continuous at $k = 0$, where it diverges as $O(\ln k)$ as $k \to 0$. Therefore, to obtain the fundamental solution G^{reg} of the perturbed Helmholtz equation, which is continuous at $k = 0$, one subtracts the constant revealed by the expansion (which does not change the integral equation). Thus the regularized fundamental solution is [Bonnet 1995]

$$G^{\text{reg}}(\boldsymbol{y}, \boldsymbol{x}; k) = G(\boldsymbol{y}, \boldsymbol{x}; k) - \frac{i}{4} + \frac{1}{2\pi}\left(\ln\frac{k}{2} + \gamma\right). \tag{18}$$

## 4. Renormalization of type II in fracture mechanics

Barenblatt's cohesive force model. In linear fracture mechanics, it is well known that the stress has a square root singularity at the crack tip in two dimensions, $\sigma \approx O(r^{-1/2})$ while the normal crack displacement discontinuity is of $O(r^{1/2})$. In order to remove the stress singularity, Barenblatt [1959a; 1959b] proposed a model of cohesive force in the vicinity of the process zone. We may interpret Barenblatt's model as a physical renormalization (type II) of the Griffith crack. In a narrow zone AB, cohesive forces are introduced so that the corresponding stress intensity factor is opposite to the one calculated at point B from external loads, thus $K_{\text{I}}(\text{external}) + K_{\text{I}}(\text{cohesive}) = 0$. As the consequence of cohesive force, the crack opening displacement varies in a smooth manner and differs from Griffith's solution in a narrow zone (Figure 1). Despite the change on the crack geometry and the stress near the crack tip zone, the crack opening displacement of both models are practically the same *outside* the cohesive zone AB.

More precisely, we consider two scales: the macroscopic scale of the structure (including singularities), which determines the SIF from boundary conditions, and the microscopic scale of the process zone. The macroscopic solution influences Barenblatt's fine-scale solution through the condition

$$K_{\text{I}}(\text{external}) + K_{\text{I}}(\text{cohesive}) = 0.$$

But the reverse is not true because, for the same external K_{I}, there are different fine-scale solutions depending on the cohesive model considered, and also as long as there is a large ratio between the two scales, the finite-stress distribution in the narrow zone AB does not influence the macroscopic solution. In the process zone, the displacement is $O(r^{3/2})$; while immediately outside the process zone, where we are still in the dominant singular zone, the displacement is $O(r^{1/2})$. There is a smooth transition between the two asymptotics which depends on the model of the process zone considered.

The inner solution of the process zone is generally obtained by an asymptotic expansion matching. This means that (i) the fine-scale problem can be treated as a semi-infinite domain subjected to the stress
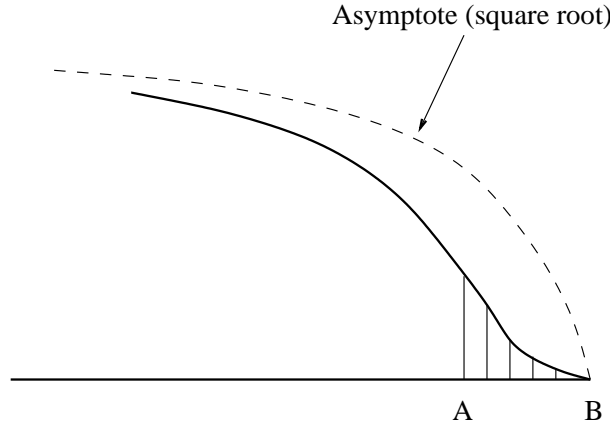
Figure 1. Barenblatt's model of an autonomous cohesive zone.

field at infinity specified by the remote singularities (parameterized by the SIF); (ii) the fine-scale field has only as many degrees of freedom as the singular terms in the macroscale solution. Solutions of the fine-scale problem have thus a great generality. An example of the fine-scale solution for a damage theory [Bui and Ehrlacher 1980], will be discussed further in the context of renormalization.

The asymptotic behaviour outside the cohesive zone governed by the SIF is important for applications since Barenblatt's model does not change the linear theory for global quantities: the macroscopic SIF is the same since it is the parameter which governs the *outer* field, the energy release rate remains unchanged. This renormalization of type II provides a better physical description of the process zone which avoids singularity of the stress in the fine-scale zone. To establish the link with classical linear fracture mechanics, for example the existence of a toughness K_{Ic}, Barenblatt assumed that the near tip region is *autonomous* in crack propagation. In other words, the asymptote of the crack opening profile $O(r^{1/2})$ is unchanged during crack propagation, or K_{I} is constant and identified to the toughness. A simpler model of the process zone, with constant normal stress equation, equal to the yield stress σ^o was proposed in [Leonov and Panasyuk 1959; Dugdale 1960].

Hierarchical models of fracture. The Griffith crack in an elastic medium has been extended to perfect plasticity in [Rice 1968]. Rice's model is an attempt to remove the deviatoric stress singularity of a crack, by considering perfect plasticity. In mode III, the solution in small scale yielding [2] is a circular disc. The plastic zone is governed by the stress singular field, and the fine-scale problem has been treated as a semi-infinite domain with the remote stress field $\sigma_{ij} = K_{\text{III}} \, g_{ij}(\theta)/\sqrt{2\pi r}$. Because of the yield stress assumption, the deviatoric stress field is finite while the strain is singular as $\epsilon \approx O(1/r)$. Does a model exist in which both stress and strain are regular in the continuum? Suppose that the behavior law of the body involves a yield stress σ_0 and a limit strain ϵ_R beyond which local stresses vanish. This model of sudden damage has been studied for mode III loading in [Bui and Ehrlacher 1980]. In the stationary case (Figure 2), a solution satisfying the equilibrium equation, the compatibility equation, under the assumption of negligible elastic strain in the plastic zone, has the following features:

---

[2]The plastic zone size a_p is assumed to be very small in comparison with the crack size a; that is, $a_p \approx (K_{\text{III}}/\sigma_0)^2/\pi \ll a$, where σ_0 is the shear yield stress.

1. An elastic zone with the remote stress field $\sigma_{ij} = K_{\text{III}}\, g_{ij}(\theta)/\sqrt{2\pi r}$,

2. An active plastic zone with straight characteristics along α − lines, with strain varying between points N and M, $\epsilon_{3\beta} = \epsilon_R$, $\sigma_0 = 2\mu\epsilon_0$.

3. A damage zone with width $2h$, containing particles that undergo a strain greater than ϵ_R and where the stress tensor vanishes.

We recall the solution for perfect plasticity $\sigma_0 = \sigma_R$, without going into the details of the derivation [Bui and Ehrlacher 1980; Bui 2006]. The solution is characterized by the following equations, using complex variables $z = x_1 + i x_2$, $\tau = \sigma_{32} + i\sigma_{31}$. The field solution $\tau(z)$ in the physical plane is searched for in its inverted form $z(\tau)$.

Point B ($z = -ih$) is mapped to point $\tau = i\sigma_R$:

$$z(\tau) = \frac{K_{\text{III}}^2}{2\pi\tau^2} - \frac{2h}{\pi}\ln\frac{\tau}{\sigma_R} + \text{constant}, \tag{19}$$

$$u_3 = \text{Im}\left(K_{\text{III}}^2 \frac{(\sigma_R - \tau)}{\pi\mu\tau\sigma_R} - \frac{2h(\tau - \sigma_R)}{\pi\mu} \right). \tag{20}$$

The real constant is chosen so that $x_1(B) = 0$, thus const $= -K_{\text{III}}^2/(2\pi\sigma_R^2)$. Solution (20) exists for $\sigma_R/2\mu \leq \epsilon_{3t} < \epsilon_R$. The latter conditions imply conditions on the SIF, $K_R^2 \leq K_{\text{III}}^2 < 2h\sigma_R(4\mu\epsilon_R - \sigma_R)$, where

$$K_R^2 = 2h\sigma_R^2. \tag{21}$$

The damage front BNB' (the locus of N) is the cusped cycloid ($-\pi < \theta < +\pi$)

$$N_1(\theta) = \frac{h}{\pi}(1 + \cos 2\theta), \quad N_2(\theta) = -\frac{h}{\pi}(2\theta + \sin 2\theta) \tag{22}$$

The elastic-plastic boundary is defined by the circle $|\tau| = \sigma_R$ of the stress plane. Thus, the locus of point M is the curled cycloid

$$M_1(\theta) = K_{\text{III}}^2 \frac{1}{2\pi\sigma_R^2}(1 + \cos 2\theta), \quad M_2(\theta) = -K_{\text{III}}^2 \frac{1}{2\pi\sigma_R^2}\sin 2\theta + \frac{2h\theta}{\pi}. \tag{23}$$

For unlimited ϵ_R, the cusped cycloid BNB' (damage front) reduces to the crack tip point, while the curled cycloid BMB' (elastic-plastic boundary) becomes Rice's circle, tangent to the x_2 axis. For finite ϵ_R, the thickness of the damage zone is $2h = K_{\text{III}}^2/\sigma_R^2$. The elastic strain energy on the damage front is $W = \sigma_R^2/2\mu$. The J-integral with contour along the damage zone takes the value

$$J_{tip} = \frac{h}{\mu}\sigma_R^2 = \frac{1}{2\mu}K_{\text{III}}^2. \tag{24}$$

Thus damage model does not change global quantities like the energy release rate, which can be calculated from the asymptotic outer field. But it gives more details on the inner process zone. Renormalization of type II as considered here serves successively to remove the stress singularity only [Rice 1968] and then to ensure that both stress and strain in the continuum are finite. These models, like
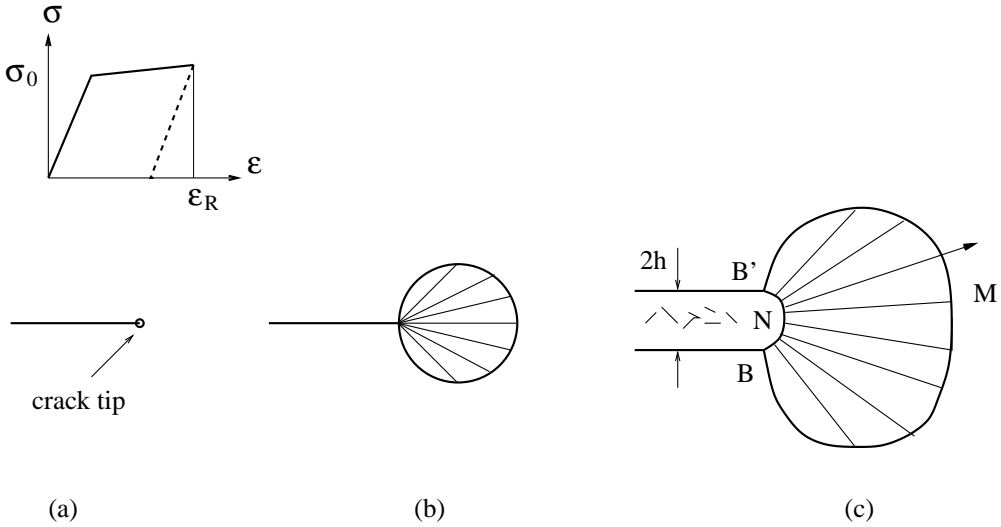
Figure 2. Hierarchical models in mode III: (a) crack tip in elastic medium; (b) Rice's plastic correction; (c) sudden damage model.

Russian dolls, are hierarchical in the sense that finer and finer scales of description have been used for renormalization (Figure 2):

$$\text{Griffith crack} \ll \text{Plastic correction} \ll \text{Damage model}$$

5. Renormalization of the energy release rate for point loads

In linear fracture mechanics, it is well known that the formula for the energy release rate $G = -dP/da$, defined as the rate of the potential energy P with respect to the crack length, holds under the assumption of square integrable stress and strain fields. Irwin's formula then relates G to the SIF, in plane strain mode I, by

$$G = \frac{1 - \nu^2}{E} K_{\mathrm{I}}^2. \tag{25}$$

What happens when the potential energy is infinite? This is the case where one deals with a pair of point loads acting on the crack faces, at a distance a from the crack tip. For a pair of point forces $\pm F\delta(\boldsymbol{x})$ acting on the crack at the distance $a > 0$ from the crack tip, the plane strain solution for an infinite plane is known in textbooks as $K_{\mathrm{I}} = 2F(\pi/a)^{1/2}$; see [Sih 1973; Tada 1973]. Now let us try to make use of Irwin's formula (25) for calculating the stress intensity factor. We realize that we are unable to calculate the potential energy P before differentiating it with respect to a, $G = -dP/da$. The reason is that, for point loads, stress and strain fields in two dimensions are not in $L^2(\Omega)$. The displacement under the point load is logarithmically singular in two dimensions, the strain energy density is singular as $O(r^{-2})$, so the potential energy is divergent $P = \infty$. How can we take a derivative with respect to a of an infinite quantity?

To avoid these inconsistencies, we shall introduce a renormalization of type II.

Before doing that, let us address some general remarks on point loads giving rise to unbounded energy. There is a strong connection of this section with the whole issue of existence and uniqueness theorems in linear quasistatic elasticity, which involve bounded energy solutions, as discussed in [Sternberg and Eubanks 1955]. It is known that Green's solution exists for point loads in an unbounded domain, as given explicitly by the Kelvin–Somigliana fundamental solution $G(x, y)$ (see classical textbooks). The fundamental solution for a *bounded* solid Ω does not exist for a point load alone, because the point load alone is not in equilibrium. For the existence of a Green's function for bounded solid, one needs to impose either a distribution of appropriate surface loads on its boundary which equilibrates the point load [Bergman and Schiffer 1953] or a homogeneous Dirichlet boundary condition $u_i(x) = 0$ on some part of the boundary (not reduced to a single point). The fundamental solution is not unique since there are many types of boundary conditions.[3]

In what follows, we shall consider bounded energy solutions in elasticity, so we modify the physics of the problem. Instead of a point force, we consider a finite distribution of normal stress on a small zone of width h, with σ_{22} constant over a finite zone $0 < x_1 < h$, $x_2 = 0$. The mollified applied stress is

$$\sigma_{22}(x_1, x_2 = 0; h) = \begin{cases} -\dfrac{F}{h} & \text{for } 0 < x_1 < h, \\ 0 & \text{otherwise.} \end{cases} \tag{26}$$

Function (26) is *independent* of the crack tip location. Its limit as h tends to zero is the Dirac delta. For $h \neq 0$, stress, strain and displacement are finite and square integrable. The energy release rate of the original problem is therefore given by the limit

$$G = -\lim_{h \to 0+} \frac{d P_h}{d a}, \tag{27}$$

where P_h is the potential energy. We will indicate below another expression for G.

To prove that the limit (27) exists we can, by virtue of the symmetry of the geometry, restrict ourselves to the lower half-plane and double the result for the potential energy. On the boundary of the lower half-plane, the normal applied stress consists of the mollified stress (26), denoted hereafter by $\sigma^{(1)}(x; h)$, and the normal tensile stress on the ligament, denoted by $\sigma^{(2)}(x; a, h)$. The stress solution decomposes as

$$\sigma(x; a, h) = \sigma^{(1)}(x; h) + \sigma^{(2)}(x; a, h). \tag{28}$$

The normal loads for small h together with the corresponding normal displacements $u_2^{(1)}, u_2^{(2)}$ on the line $x_2 = 0$ are displayed in Figure 3. The potential energy of the cracked body is written in line integral form as

$$P_h = 2 \times \frac{1}{2} \int_0^h \sigma_{22}^{(1)} u_2 dx_1. \tag{29}$$

---

[3]The proofs of existence and uniqueness, for a specific boundary condition, are not based on bounded energy considerations, but rather on singular boundary integral equations with unknown $C(\partial\Omega)$ density. The two fundamental solutions for a bounded solid, of both the Neumann and the Dirichlet types, are provided in [Pham 1967].
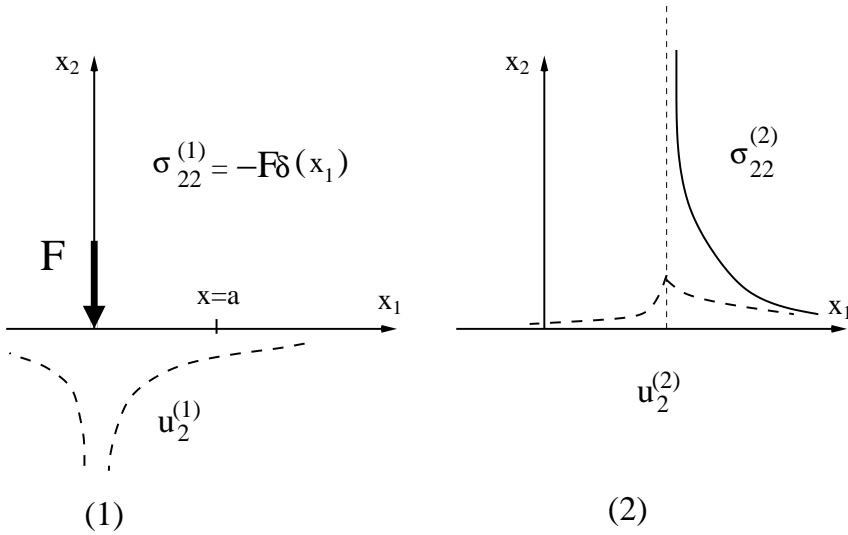
Figure 3. (1) Point load F on the boundary of a half-plane, defining the stress field $\sigma_{22}^{(1)}$ on $x_2 = 0$ and the logarithmically singular displacement $u_2^{(1)}$. (2) Distributed normal load $\sigma_{22}^{(2)}$ equal to the stress in the ligament, with continuous surface displacement $u_2^{(2)}$.

The displacement u_2 is equal to the sum $u_2^{(1)} + u_2^{(2)}$. The field $u_2^{(2)}$ satisfies the condition $u_2^{(2)} = -u_2^{(1)}$ on the ligament $x_1 > a$. The potential energy is

$$P_h = \int_0^h \sigma_{22}^{(1)}(x_1; h) u_2^{(1)}(x_1; h) \, dx_1 + \int_0^h \sigma_{22}^{(1)}(x_1; h) u_2^{(2)}(x_1; a, h) \, dx_1. \tag{30}$$

The first integral diverges logarithmically as h tends to zero. It is the singular part of the potential energy, denoted by S_h. We observe that the singular part S_h of P_h is *independent* of a, $(d/da)S_h = 0$ for any h. Therefore G is given by either of the formulas

$$G = - \lim_{h \to 0+} \frac{d}{da} \int_0^h \sigma_{22}^{(1)}(x_1; h) u_2^{(2)}(x_1; a, h) \, dx_1, \tag{31}$$

$$G = - \lim_{h \to 0+} \frac{d}{da}(P_h - S_h). \tag{32}$$

Equation (32) is nothing but Hadamard's finite part procedure, which has been considered in type I renormalization. It remains to prove that (27) or (32) provides the classical formula in mode I, $G = (1 - v^2)K_I^2/E$.

Proof. The solution for the mollified load (26) is continuous in h. Therefore, stress $\sigma^{(h)}$ converges to the stress solution σ for point loads and $K_I^{(h)}$ converges to K_I. Since we have $G^{(h)} = -dP_h/da = (1 - v^2)K_I^{(h)2}/E$ for any h, upon taking the limit for vanishing h we obtain the expected result. $\qquad\square$

6. Conclusions

By discussing some examples in previous sections, we forgot the primary purpose of renormalization in physics, more precisely in quantum electrodynamics, which deals with perturbation methods applied to solutions for some scale of observation. The calculation of the norm of higher-order solutions involves divergent integrals. Mathematical techniques to overcome some divergences appearing in the renormalization procedure seem to be useful in other contexts of solid mechanics. Some of these techniques have been considered here, but not all. For example, scaling laws in fatigue and fracture [Barenblatt 2006] and the cutoff method (by ignoring energies greater than mc^2 [Feymann 1948] have not been considered in this paper. The cutoff method was recently considered in [Dini et al. 2007] for contact problems with a sharp corner defined by a distribution of curvature that goes to infinity at the corner. A cutoff of the curvature distribution will round up the corner. The cutoff of curvature of a sharp punch profile will remove the singularity arising in frictional sliding contact and resolve a paradox pointed out in [Adams et al. 2005] in violation of the kinematic Coulomb friction condition, as done in [Hills et al. 2005].

Singularity removal is very often encountered in solid and fracture mechanics. It is shown that operators like differentiation and singular integration are not commutative, nor can we interchange differentiation and the limiting process. Examples of noncommutative limiting processes also exist in the literature of homogeneization; for example in models with a small parameter a of the microscopic cell and a small thickness h of the macrostructure, the successive limits $a \to 0$ and $h \to 0$ are not commutative [Geymonat et al. 1987]. But these noncommutative limits are not considered here since they are not related to renormalization procedures.

The use of different levels of observation is considered in hierarchical models of the process zone. However, it seems that no simple scaling laws are found for the latter models which can be compared to size dependent scaling laws in damage theory [Bazant 2002].

References

[Abramovitz and Stegun 1972] Abramowitz, M. and Stegun, I., (1972). *Handbook of Mathematical Functions*. Dover Publications, New York.

[Adams et al. 2005] Adams, G. G., Barber, J. R., Ciavarella, M. and Rice, J. R., (2005). A Paradox in Sliding Contact Problems With Friction. *J. Appl. Mech*. **72**, N°3, p. 450-452.

[Adzhemyan et al. 1999] Adzhemyan, L. T., Antonov, N. V. and Vasiliev, A. N., (1999). *The field theoretic renormalization group in fully developed turbulence*. Gordon and Breach.

[Barenblatt 1959a] Barenblatt, G.I., (1959). The formation of equilibrium cracks during brittle fracture: General ideas and hypotheses, axially symmetric cracks. *Appl. Math. and Mech*. (PMM) **23**, 622-636.

[Barenblatt 1959b] Barenblatt, G.I., (1959). Concerning equilibrium cracks forming during brittle fracture : The stability of isolated cracks, relationship with energetic theories. *Appl. Math. and Mech*. (PMM) **23**, 1273-1282.

[Barenblatt 2006] Barenblatt, G. I., (2006). Scaling phenomena in fatigue and fracture. In *Advances in Fracture Research*, A. Carpinteri, Yiu-Wing Mai and R. O. Ritchie (Eds.), Springer, pp. 19-35.

[Bazant 2002] Bazant, Z.P., (2002). *Scaling of Structural Strength*. HPS London.

[Bergman and Schiffer 1953] Bergman, S. and Schiffer, M., (1953). *Kernel functions and elliptic differential equations in Math. Physics*. Academic Press.

[Bogolioubov and Chirkov 1960] Bogolioubov, N.N. and Chirkov, D.V., (1960). *Introduction to Quantum Field theory*. Dunod, Paris.

[Bonnet 1995] Bonnet, M., (1995). *Equations integrales et elements de frontiere*. CNRS Editions/Eyrolles, Paris.

[Bui 1978] Bui, H.D., (1978). Some remarks about the formulation of three-dimensional thermo-elasto-plasticity by integral equations. *Int. J. Solids and Structures*, **14**, p. 935.

[Bui 2006] Bui, H.D., (2006). *Fracture Mechanics. Inverse problems and solutions*. Springer.

[Bui and Ehrlacher 1980] Bui, H.D. and Ehrlacher, A., (1980). Propagation of damage in elastic and plastic solids. *Advances in Fracture Mechanics* (Eds. Francois, D. et al.) Pergamon Press, Oxford, New York, **3**, p.533.

[Dini et al. 2007] Dini, D., Barber, J.R., Churchman, C.M., Sackfield, A. and Hills, D.A., (2007). The application of asymptotic solutions to contact problems characterized by logarithmic singularities. *European J. of Mechanics, A/ Solids*.

[Dugdale 1960] Dugdale, D.S., (1960). Yielding of steel sheets containing slits. *J. Mech. Phys. Solids*, **80** N.2, p.100-104.

[Feymann 1948] Feynmann, R., (1948). Relativistic cut-off for quantum electrodynamics. *Phys. Rev.* 1430-1438.

[Gell-Mann and Low 1964] Gell-Mann, M. and Low, F.E., (1964). The origin of renormalization group. *Phys. Rev.*, **95**, 5,1300.

[Geymonat et al. 1987] Geymonat, G., Krasucki, F. and Marigo, J.J., (1987). Sur la commutativite des passages a la limite en theorie asymptotique des poutres composites. *C. R. Acad. Sci. Paris*, Serie II, **305**, 225-228.

[Goldenfeld 1993] Goldenfeld, N., (1993). *Lectures on phase transitions and the renormalization group*. Addison-Wesley.

[Gradshteyn and Ryzhik 1965] Gradshteyn, I. S. and Ryzhik, I. M., (1965). *Table of integrals, Series and Products*. Acad. Press.

[Hadamard 1932] Hadamard, J. (1932). *Le probleme de Cauchy et les equations aux derivees partielles hyperboliques*. Hermann, Paris.

[Hills et al. 2005] Hills, D.A., Sackfield, A., Churchman, C.M., (2005). Discussion 'A paradox in sliding contact problems with friction', by Adams, G.G., Barber, J.R., Ciavarelle, M. and Rice, J.R. (2005). ASME, J. Appl. Mech., **72**, p. 450-452. *ASME, J. Appl. Mech.*, **73**, p. 884-886.

[Kadanov 1966] Kadanov, L.P., (1966). Scaling laws for Ising models near Tc. *Physics* (Long Island City, N.Y.) **2**, p.263.

[Lazarus 1998] Lazarus, V. and Leblond, J.B., (1998). Three-dimensional crack-face weight functions for the semi-infinite interface crack-I: Variation of the stress intensity factors due to some small perturbation of the crack front. *J. Mech. Phys. Solids*, **46**, p.489-511.

[Leonov and Panasyuk 1959] Leonov, M. Y. and Panasyuk, V. V., (1959). Development of very small cracks in a solid body. *Prykl. Mekh.*, **5**, N.4, p.391-400.

[Mendelson 1973] Mendelson, A., (1973). Boundary integral equations method in elasticity and plasticity. *NASA TND-7416*.

[Pham 1967] Pham, T. L., (1967). Potentiels elastiques, tenseurs de Green et de Neumann. *Journal Meca*, **6**, N.2, p.211.

[Rice 1968] Rice, J. R., (1968). Mathematical analysis in the mechanics of fracture. *Fracture*, H. Liebowitz (Ed.), **2**, Academic Press.

[Schwartz 1978] Schwartz, L., (1978). *Théorie des distributions*. Hermann, Paris.

[Sellier 1996] Sellier, A. (1996). Application of the Hadamard's Finite Part Concept to the Asymptotic Expansion of a Class of Multidimensional Integrals, *Phil. Trans.: Math., Phys. and Engng. Sciences*, **354**, N.1710, pp. 1195-1246.

[Sih 1973] Sih, G.C., (1973). *Handbook of stress intensity factors*. Institute of Fracture and Solids Mechanics. Lehigh University.

[Sternberg and Eubanks 1955] Sternberg, A. and Eubanks, R.A. (1955). On the concept of concentrated loads and an extension of the uniqueness theorem in the linear theory of elasticity, *J. Rat. Mech. and Anal.*, **4**, pp. 135-168.

[Tada 1973] Tada, H., Paris, F. and Irwin, G.R., (1973). *The stress Analysis of cracks. Handbook*, Del Research Corp.

[Wilson 1971a] Wilson, K., (1971). Renormalization group and critical phenomena : a) Renormalization group and the Kadanoff scaling picture. *Phys. Rev.* **B4**, p.3174.

[Wilson 1971b] Wilson, K., (1971). b) Phase space cell analysis of critical behaviour. *Phys. Rev.* **B4**, p.3184.

H. D. BUI: `hdbui37@yahoo.fr`
Laboratoire de Mécanique des Solides (CNRS UMR 7649), École Polytechnique, Palaiseau Cedex 91128, France
and
LaMSID/CNRS UMR 2932, EDF Clamart, France

A THERMOMECHANICAL FRAMEWORK OF PLASTICITY BASED ON PROBABILISTIC MICROMECHANICS

ITAI EINAV AND IAN F. COLLINS

A conventional thermomechanical elasto-plastic constitutive modelling framework is proposed but which allows an effective physical interpretation of the micromechanical internal variables and inherent parameters in a representative volume element (RVE). The statistical distribution of the elastic-plastic parameters within the RVE is described using a simple statistical method of probabilistic rearrangement (MPR). This method facilitates deriving analytical approximating formulas to the stress-strain response of the RVE under unidirectional monotonic loading conditions. The applicability of the MPR is validated numerically by comparing the analytical formulas against numerical experiments of a probabilistic boundary value problem initially under monotonic conditions. The assumptions associated with the MPR are embedded within the simple micro thermomechanical constitutive framework and further evaluated numerically by applying the methodology for the case of cyclic loads. For the limited experimental program the constitutive modelling framework seems to give a rather effective estimation of the full boundary value problem. The results for the cyclic case demonstrate how hysteresis behaviour of materials could be modelled without incorporating kinematic hardening parameters.

1. Introduction

The physical properties of most solid materials in nature are spatially randomly distributed. While in some materials the randomness is given by a weak noise from the mean average, the coefficient of variance of many other materials is high. This paper will focus on modelling the class of randomly distributed heterogeneous materials, such as soils and bones, in which their micro subelements could be well described using the concepts of elasto-plasticity. Various other methods have been used to describe these materials, but the theories that are established based on physical arguments are arguably more attractive. During the years three of such continuum mechanics frameworks have been developed based on thermomechanics and micromechanics.

A first approach is to formulate the constitutive behaviour of elasto-plastic solid materials based on thermomechanics. For that purpose the class of the theories with internal variables have been described in the past including the theories of Maugin [1992] and Ulm and Coussy [2003]. Further examples follow the thermomechanical approach of Ziegler [1977], Collins and Houlsby [1997], Houlsby and Puzrin [2000], and Einav [2002]. The models of this approach are entirely derived from an explicit definition of only two potentials: energy and rate of dissipation. It is worth mentioning that there are other theories which do not use a dissipation potential [Rice 1971]. The thermomechanical frameworks provide a systematic way to describe the physical processes behind the behaviour of constitutive elements. This advantage was utilized before, based on the hyperplasticity framework, to explain the

different microphysical aspects in the behaviour of granular materials [Collins and Kelly 2002; Collins and Hilder 2002; Collins and Muhunthan 2003]. In particular, the bimodal model of Collins [2005a; 2005b] provides realization based on some micromechanical interpretation. In this thermomechanical approach one actually adopts a single stress tensor and a single strain tensor to qualitatively describe the deformation within a RVE. More realistically, however, within the RVE there are variations between the local values of the microstrain and microstress tensors.

A second approach is to base the mesodomain continuum mechanics constitutive relations on the micromechanics interrelations between the microelements (or subelements). Then some form of homogenisation technique is often employed to link between the micromechanical quantities and the mesodomain RVE averaged properties [Suquet 1987; Maugin 1992; Doghri 2000]. In highly heterogeneous materials homogenisation may often lead to oversmoothening effects that are triggered by high gradients or even irregularities within the RVE. For that purpose higher order homogenisation estimates have been introduced, but they are usually developed for elastic materials [Ponte Castañeda 1996]. Such an approach was also employed to study granular materials via the use of the stored free energy [Pasternak and Mühlhaus 2005 and references cited herein]. The possibility of having frictional sliding between the grains in granular materials requires us to consider an additional potential in the form of the rate of dissipation. It is thus necessary to extend the study beyond elasticity as developed for granular materials by Vardoulakis [1983] and Chang and Ma [1991]. The main problems of this approach are that for plastic materials the existing solutions do not normally provide engineering constitutive models that can account for any loading conditions and the existing form of homogenisation either smear or fully lose the inherent memory properties of the plastic materials.

A third approach, which has recently motivated several researchers, is to combine the previous approaches in a kind of micro thermomechanics framework. Chaboche [2003] has recently proposed such a theory for elasto-plastic heterogeneous materials but was not concerned with the random aspects of the property distributions. Further examples include the works of Gurtin [2000] who has studied the constitutive behaviour of crystals, and Walsh and Tordesillas [2004] and Tordesillas et al. [2004], who have dealt with the problem of granular materials.

This paper follows the third approach dealing with a (rather large) set of problems that includes ergodic materials in which their mesodomain contains a spatially random distribution of elasto-plastic subelements [Ostoja-Starzewski 2002]. The stochastic nature of these problems is often treated numerically by assigning a particular spatial distribution of the properties in a boundary value simulation and solving this as a representative problem (see a recent review of the methods by Ostoja-Starzewski [2005]). In this way the deterministic problem carries over to the stochastic one. A second approach is to formulate the effective continuum media directly based on the governing statistics of the stochastic material [Frantziskonis 1998]. The main challenge in these works was to find analytical solutions for particular loading conditions either in the form of theoretical bounds or closed form solutions. The general statistical description of elastic-plastic media could be entirely described via an infinite set of probability functions and spatial correlation functions [Adams et al. 1989]. Approximate analytical solutions were obtained for the limiting case of a two-phase medium using the two-point probability distribution function via the correlation length [Garmestani et al. 1988]. A wider set of problems includes the infinite-phase mediums. If those phases are correlated, one has to adopt a conceptual infinite-point probability distribution function. However, when the material tends to be ergodic (and the correlation
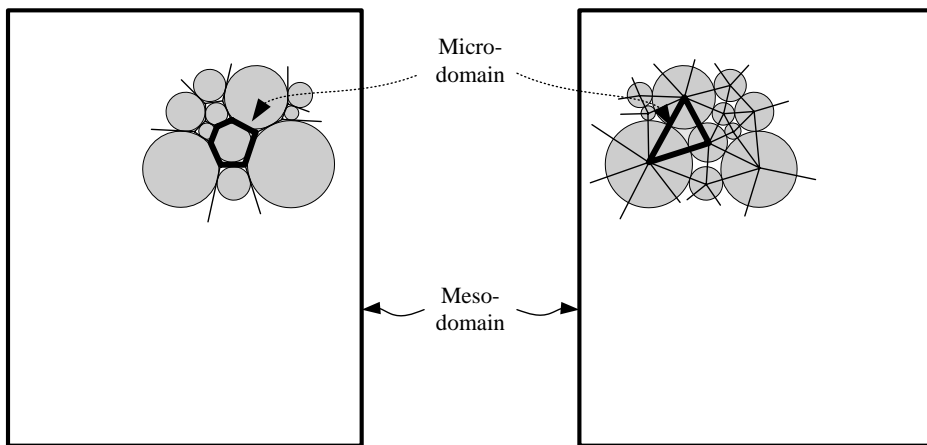
Figure 1. Definition of mesodomain and microdomain using optional tessellations (modified Voronoi or Delaunay) for the granular materials.

length becomes essentially zero), it is possible to adopt an alternative approach which we explore in this paper.

The above works, however, were mainly demonstrated for cases in which monotonic unidirectional external loads are applied to the boundaries of the RVE. The question of how to take into account cyclic events was not treated in effective manner. This paper demonstrates one possible methodology in which this could be accounted for by enabling to capture memory features that are inherent in plastic material. In particular, we find that hysteresis behaviour of random elastic-plastic materials could be attributed directly to heterogeneities without adding any *kinematic hardening parameters*. The constitutive modeling framework is also wide enough to allow estimations when the applied loads change directions.

2. Micro meso probabilistic approach

Consider a RVE that contains a collection of separate elasto-plastic subelements. Also consider materials where their microscale subelements geometries could be tessellated. For example, Figure 1 shows two optional tessellations for granular medium, discussed with other options by Satake [1978]. Due to the random physical properties of the subelements and their random geometrical configuration within the tessellation yielding occurs gradually within the RVE and this is often ignored.

Because the geometry within the RVE of a random material may be quite complicated, no attempt is made at computing the exact evolution of the micromechanics variate. Instead the goal should be to obtain estimates in terms of point statistics of the microstructure. Behind the concept of the RVE there are at least three length scales denoting the average sizes of the microscale subelements l, the mesoscale RVE size L to which the constitutive model refers to, which should be less than the macroscale size L_{macro} that corresponds to the macroscopic body size. While in the conventional homogenisation methods the averaging equation is normally additional to the constitutive equations, in the current method (which will allow creation of general constitutive models) this equation is not employed though it will be used to help in expressing the physical meaning of variables. The general average formula for general heterogeneous

problems of a variate $\hat{\bullet} = \bullet(x)$ (being the function of position x) is given by

$$\langle \hat{\bullet} \rangle = \frac{1}{V} \sum_{i=1}^{N} \bullet_i(x) \Delta v_i(x), \tag{1}$$

where V denotes the total volume of the RVE; i is an index counted over N homogeneous micro-subelement phases with a subvolume $\Delta v_i(x)$. The smaller length scale could be approximated by using $l \cong \sqrt[3]{\langle \Delta \hat{v} \rangle}$ and the mesolength scale by $L \cong \sqrt[3]{V}$.

Assume that $\delta = L/l \to \infty$, $L \ll L_{\text{macro}}$, and $\Delta v_i(x) = dv = l^3$ for any i, then

$$\langle \hat{\bullet} \rangle = \frac{1}{V} \int_{\text{RVE}} \bullet(x) \, dv. \tag{2}$$

If we further denote the use of the normalised coordinate h such that $dh = \frac{1}{v} dv = (l/L)^3$, then the length scales become nondimensional and we can integrate over a statistical volume element (SVE) [Ostoja-Starzewski 2002] from 0 to 1 rather than over the RVE

$$\langle \hat{\bullet} \rangle = \int_0^1 \bullet(h) \, dh. \tag{3}$$

In the above lines the hat sign over the variate $\hat{\bullet}$ was used to denote if the specific coordinate system is irrelevant, that is, $\hat{\bullet}$ could stand for both $\hat{\bullet} = \bullet(x)$ or $\hat{\bullet} = \bullet(h)$), such that $\langle \hat{\bullet} \rangle$ designates the average of the variate regardless of the coordinate system and regardless of the use of RVE (or SVE).

Methodology. Our first motivation is to set up a thermomechanical elasto-plastic framework that enables the definition of constitutive models that are complete in the classical engineering sense of providing estimates to the material response under most general loading conditions (cyclic and multidirectional). Our second motivation is to be able to deduce some micromechanical physical interpretation to the field variables and parameters. Current theories are barely achieving both tasks simultaneously. The models are either limited to monotonic unidirectional loads or they are incapable of providing a clear micromechanical interpretation. Due to the complexity of the problem this work will be based on some relaxing assumptions but in a way that allows addressing both aims.

Method of probabilistic rearrangement (MPR). In randomly distributed materials it is simply impossible to measure the physical location of all the subelements or/and their physical quantities. Thus for ergodic materials where internal geometric patterning is not present, the probability of any subelement variate in the RVE is similar to that of any other subelement. This means that the modelling of such materials may not prefer any arrangement of subelements throughout the RVE over the other and should take into account the location independency. Therefore, for example in granular materials, a change in position of two particles in infinite assembly (as represented schematically in Figure 2) should not affect the structure of the constitutive models, since we have no means to distinguish one arrangement as being practically better than the other. This is a rather different approach to take deterministically a particular spatial configuration and carry out computations based on it.

Assume that the micromechanical variates (such as the strength and stiffness coefficients) are constant in each of the subelements but randomly distributed throughout the RVE. The volume that each subelement captures could be denoted as Δv_i. The values of a particular variate could be arranged in a
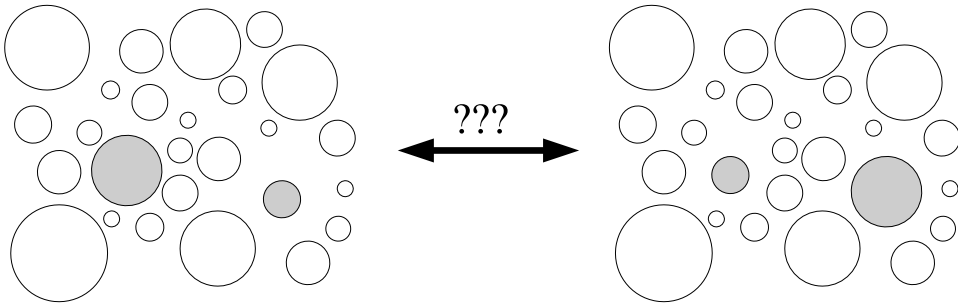
Figure 2. The enigma of what is the right deterministic representation: any discrete particle configuration is possible from a mesoscopic point of view thus none of them could be viewed as better when formulating *engineering* continuum models.

line according to its spatial physical volume coordinate order x, and since the micromechanics quantity is assumed constant within each subelement, its variation throughout the entire RVE with the index i may be schematically described by Figure 3a. Since any optional deterministic spatial arrangement of subelements may not be viewed as better than the others, the chaotic distribution of Figure 3a could be rearranged in a monotonic order as in Figure 3b.

When the number of elements in the RVE is essentially infinite, the discrete plot can be effectively replaced by a continuous distribution function denoting the changes of the micromechanics quantity over the rearranged normalised volume coordinate h in a SVE. We identify a statistical physical meaning to the coordinate $h \equiv p$ as the significance cumulative probability of the system. The distribution function of the micromechanics quantity is identified as the percent point function or the inverse cumulative distribution function (inverse cdf), as it returns the critical values of the micromechanics variate for hypothesis testing
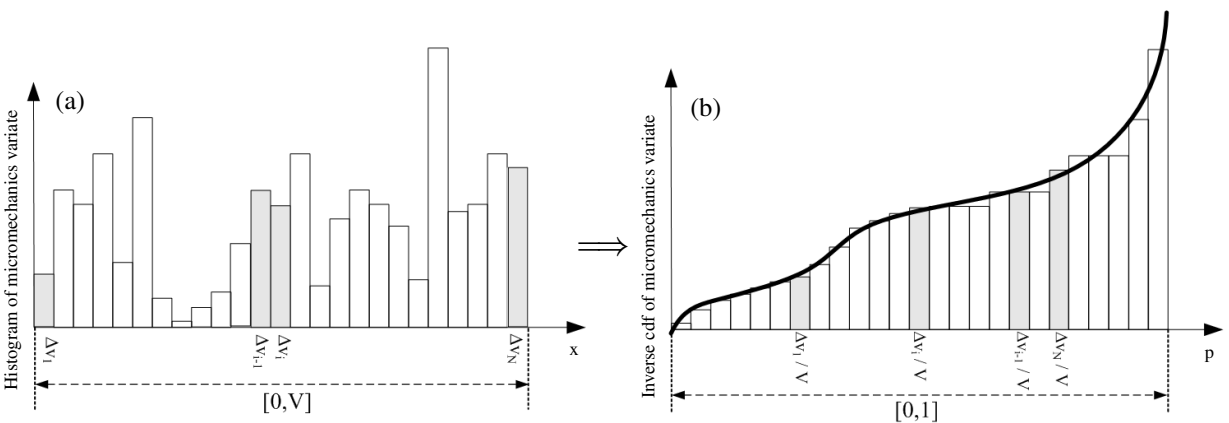
Figure 3. Method of probabilistic rearrangement (a) Histogram of a micromechanics along physical volume coordinate x in the RVE, and (b) Inverse cumulative distribution along the rearranged relative volume p (being the cumulative probability).
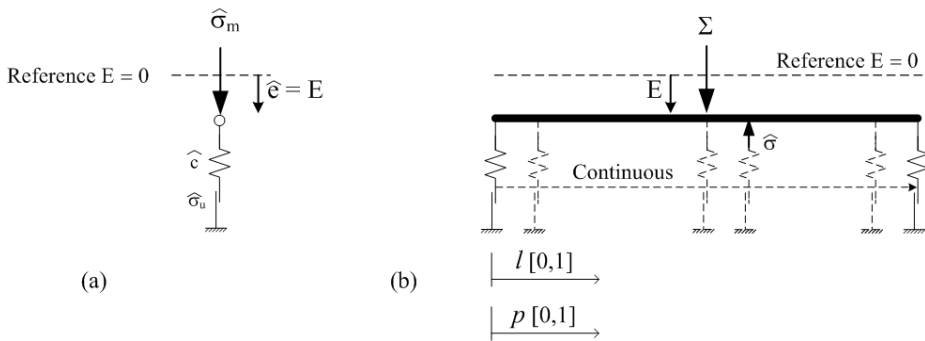
Figure 4. The construction of conceptual micro thermomechanical one-dimensional plasticity model: (a) St-Venant model. (b) continuous Masing-Iwan model (after [Einav 2005]).

given significance cumulative probabilities. Therefore Equation (3) could be rewritten

$$\langle \hat{\bullet} \rangle = \int_0^1 \bullet(p)\,dp$$

while the integration from zero to one is activated over the entire cumulative probability space.

3. Conceptual one-dimensional micro thermomechanical plasticity model

Let us start with the one-directional model proposed by Einav [2005] as an extension to the discrete Masing-Iwan model. The model is built on a continuous parallel system of pointwise St-Venant spring-slider elements (see Figure 4 for the description of an individual St-Venant element and the complete continuous Masing-Iwan system). The mechanical/structural properties of this model are reinterpreted based on the probabilistic approach. The model provides motivation and serves as a simple introduction towards the formalism which is being derived in the next section.

3.1. *Interlinks between mechanical and probabilistic concepts.* All of the "legs" in the continuous Masing-Iwan system undergo the same total scalar strain E. The model is initially dependent on two stochastic distributions $\sigma_u(x)$ and $c(x)$ denoting the slider threshold and elastic stiffness coefficients along the physical spatial volume coordinate $x \in [0, V]$. Using MPR the previous distribution function may also be expressed based on the probability coordinate $p \in [0, 1] : \sigma_u(p)$ and $c(p)$. Further suppose that $\sigma_u(p)$ is a monotonically increasing function and that $c(p)$ is smooth. The distribution $\sigma_u(p)$ is interpreted as the inverse cdf returning the value of significant plastic threshold $\sigma_u(p_a)$ for a given cumulative probability $p = p_a$. $c(p)$ is identified as the distribution of the microscale elastic moduli along the plastic threshold cumulative probability p.

To designate the interchangeable nature of the original system ($\sigma_u(x)$ and $c(x)$) and the rearranged system ($\sigma_u(p)$ and $c(p)$), we shall use the hat sign over the variates and remove the coordinate, that is, $\hat{\sigma}_u$ and $\hat{c}$ will denote the microscale slider threshold and elastic stiffness coefficients regardless of the coordinate. This designation method is used throughout the text.

If $\hat{\sigma}$ denotes the microstress within a corresponding St-Venant element (Figure 4a) then from equilibrium the total stress Σ (not to be mistaken with the summation sign) is given by

$$\Sigma = \frac{1}{V} \int_0^V \sigma(x)\,dx = \int_0^1 \sigma(p)\,dp = \langle \hat{\sigma} \rangle$$

such that it is observed that Σ also equals the average over the microscale stresses $\hat{\sigma}$ within the RVE using Equation (2) or within the SVE using Equation (3). Furthermore it is noted that equilibrium in the mechanical system has nothing to do with the order of the St-Venant constituents thus demonstrating that the MPR is valid whenever strains are uniform throughout the RVE.

The microstress is linearly related to the microelastic strain within the micro Saint-Venant element. In the original system this is expressed by

$$\sigma(x) = c(x)\big(E - e_p(x)\big) = c(x)\,e_e(x),$$

where E is the mesostrain and is uniform in this model, that is, $E = e(x)$ for any x; $e(x)$, $e_e(x)$, and $e_p(x)$ denote the total, elastic, and plastic microstrains at the spatial coordinate x.

In the rearranged system this may be expressed by

$$\sigma(p) = c(p)\big(E - e_p(p)\big) = c(p)\,e_e(p), \tag{4}$$

where $e_e(p)$ and $e_p(p)$ are now functions of the cumulative probability p.

3.2. *Thermomechanical potentials.* The Helmholtz free energy density at the x spatial coordinate or the p probability coordinate of the microscale spring are given by

$$\hat{\psi} = \psi(E, e_p(x), x) = \frac{c(x)}{2}\,e_e(x)^2 = \frac{c(x)}{2}\big(E - e_p(x)\big)^2,$$

$$\hat{\psi} = \psi(E, e_p(p), p) = \frac{c(p)}{2}\,e_e(p)^2 = \frac{c(p)}{2}\big(E - e_p(p)\big)^2.$$

Both could be integrated to give the total Helmholtz free energy functional of the system

$$\Psi(E, \hat{e}_p) = \frac{1}{V} \int_{\text{RVE}} \frac{c(x)}{2}\big(E - e_p(x)\big)^2\,dx = \int_0^1 \frac{c(p)}{2}\big(E - e_p(p)\big)^2\,dp = \langle \hat{\psi} \rangle. \tag{5}$$

It is shown how the total Helmholtz free energy functional agrees with the average of the local potential densities within the RVE.

The rate of local rate of dissipation density associated with the microscale slider in the x spatial coordinate or the p probability coordinate is given by[1]

$$\hat{\tilde{\phi}} = \tilde{\phi}(\dot{e}_p(x), x) = \sigma_u(x)|\dot{e}_p(x)| \geq 0, \quad \hat{\tilde{\phi}} = \tilde{\phi}(\dot{e}_p(p), p) = \sigma_u(p)|\dot{e}_p(p)| \geq 0. \tag{6}$$

---

[1]We are using a "tilde" instead of the more usual "dot" notation for the time derivative, to emphasize that there is no state dissipation function $\hat{\phi}$.

The rate of dissipation is not a point function and it is path dependent. Integration of the rate of local dissipation density over the full domains suggests the total rate of dissipation

$$\tilde{\Phi}(\dot{\hat{e}}_p) = \frac{1}{V} \int_{RVE} \tilde{\phi}(\dot{e}_p(x), x)\,dx = \int_0^1 \tilde{\phi}(\dot{e}_p(p), p)\,dp = \langle \dot{\hat{\phi}} \rangle \geq 0. \tag{7}$$

It is shown that the total rate of dissipation agrees with the average of the local potential densities within the RVE (or SVE).

Inversely, we will later demonstrate (see the first example in the example section) how the entire constitutive behaviour of the one-dimensional model is encapsulated in Equations (5) and (7).

4. Thermomechanical micro meso plasticity

In this paper we consider a mesocontinuum system which is composed from an infinite field of infinitesimal microcontinua. Each of the microcontinua is described by an elasto-plastic model with a single plastic internal variable, such that the description of the mesocontinuum is given by a set of infinite field of plastic internal variables (or a plastic internal function of the corresponding coordinate). The first and second laws of thermodynamics of the constitutive behaviour of rate independent isothermal materials should hold in both microform (local) and mesoform (global).

In *microform* the laws are given by the expression

$$\tilde{w} = \dot{\hat{\psi}} + \dot{\hat{\phi}}, \qquad \dot{\hat{\phi}} \geq 0, \tag{8}$$

where $\hat{\psi}$ is the (micro) Helmholtz free energy density, $\dot{\hat{\phi}}$ is the (micro) rate of energy dissipation density (which has to be nonnegative), and $\tilde{w} = \hat{\sigma} : \dot{\hat{e}}$ denotes the rate of the mechanical work done on the microcontinuum element, all defined per unit volume; finally the symbol ':' denotes the inner product of two tensors. The notations of the scalar microstress $\hat{\sigma}$ and microstrain $\hat{e}$ from the previous sections are changed by the bold face, denoting the more general case of second order tensors $\hat{\boldsymbol{\sigma}}$ and $\hat{\boldsymbol{e}}$. As stated before the Helmholtz free energy density is assumed to be a function of state unlike the rate of dissipation density and mechanical work density.

In *mesoform* the laws are given by the expression

$$\tilde{W} = \dot{\Psi} + \tilde{\Phi}, \qquad \tilde{\Phi} \geq 0, \tag{9}$$

where Ψ is the (meso) Helmholtz free energy, $\tilde{\Phi}$ is the nonnegative (meso) rate of energy dissipation and

$$\tilde{W} = \Sigma : \dot{\boldsymbol{E}}$$

denotes the rate of the mechanical work done on the boundaries of the mesocontinuum element, all defined per unit volume.

As the laws of thermodynamics should hold anywhere within the RVE, an alternative mesoform of the laws of thermodynamics could be given simply by up-scaling or integrating Equation (8) over the RVE (or the SVE)

$$\langle \tilde{w} \rangle = \langle \dot{\hat{\psi}} \rangle + \langle \dot{\hat{\phi}} \rangle, \qquad \langle \dot{\hat{\phi}} \rangle \geq 0. \tag{10}$$

By identifying the additivity of internal energy and rate of dissipation $\Psi = \langle \hat{\psi} \rangle$ and $\tilde{\Phi} = \langle \dot{\hat{\phi}} \rangle \geq 0$, while for a statically admissible stress field and a kinematically admissible displacement field [Hill 1963; Suquet

1987; Maugin 1992], the classical Hill-Mandel equality could be found

$$\Sigma : \dot{E} = \langle \hat{\sigma} : \dot{\hat{e}} \rangle. \tag{11}$$

The procedure, which relates Σ and E (and possibly their derivatives with respect to the time and other parameters) by means of Equations (8) and (9) and the micro constitutive laws, is termed *homogenisation*. The inverse, termed *localization*, amounts to a micromechanics problem which permits determining microscopic quantities as $\hat{\sigma}$ and $\hat{e}$. For ergodic material, the RVE (or SVE) has a large size with respect of the heterogeneity's size, so that the "stress vector" $\sigma(x) \cdot n(x)$ or the displacement vector $u(x)$ on the boundaries fluctuate about a mean with a small wavelength compared with the dimensions of the RVE. In this case, the boundary stress and strain tensors are equal to the average of the stress and strain field tensors within the RVE.

A localisation analysis is suggested to identify the constitutive relations at the microlevel followed by homogenisation analysis to determine the quantities at the mesolevel.

4.1. *Localisation analysis (microrelations).* For the micro constitutive problem the micro Helmholtz free energy density is given directly as the free energy of elasto-plastic models

$$\hat{\psi} = \hat{\psi}_1(\hat{e} - \hat{e}_p) + \hat{\psi}_2(\hat{e}_p) = \hat{\psi}_1(\hat{e}_e) + \hat{\psi}_2(\hat{e}_p), \tag{12}$$

where $\hat{e}_e$ and $\hat{e}_p$ are the microelastic and plastic strains, satisfying $\hat{e} = \hat{e}_e + \hat{e}_p$. The first component in Equation (12), $\hat{\psi}_1(\hat{e}_e)$, is related to the "stored energy" in the system and is linked with the elasticity law, while the second term $\hat{\psi}_2(\hat{e}_p)$ is referred to as the "frozen energy" [Ulm and Coussy 2003; Collins 2005b]. In the following we ignore the possibility of frozen energy in the microscopic level and specialize the micro free energy density by

$$\hat{\psi} = \hat{\psi}_1(\hat{e} - \hat{e}_p) = \hat{\psi}_1(\hat{e}_e). \tag{13}$$

In the case of rate-independent processes of elasto-plastic models the rate of the dissipation function is a homogeneous first order function of the plastic strain rate. This homogeneity can be expressed by Euler's equation

$$\hat{\dot{\phi}}(\hat{e}, \hat{e}_p, \dot{\hat{e}}_p) = \frac{\partial \hat{\dot{\phi}}}{\partial \dot{\hat{e}}_p} : \dot{\hat{e}}_p \geq 0. \tag{14}$$

Combining the last two equations with Equation (8) gives the micro generalized (dissipative) stress and Cauchy stress tensors

$$\hat{\sigma} = \frac{\partial \hat{\psi}(\hat{e}, \hat{e}_p)}{\partial \hat{e}} = \frac{\partial \hat{\psi}_1(\hat{e} - \hat{e}_p)}{\partial \hat{e}} = \hat{\psi}_1'(\hat{e}_e)$$

$$\hat{\chi} = -\frac{\partial \hat{\psi}_1(\hat{e} - \hat{e}_p)}{\partial \hat{e}_p} = \hat{\psi}_1'(\hat{e}_e) \quad \left(= \frac{\partial \hat{\dot{\phi}}}{\partial \dot{\hat{e}}_p}, \text{ whenever } \dot{\hat{e}}_p \neq 0 \right). \tag{15}$$

The equality in the brackets of Equation (15) agrees with Ziegler's orthogonality condition. In the particular form of Equation (13) we find that the micro generalized stress $\hat{\chi}$ is actually the micro Cauchy stress

$$\hat{\chi} = \hat{\sigma}. \tag{16}$$

Each rate of micro dissipation density could be linked to a single micro yield surface using degenerate Legendre transformation

$$\hat{\tilde{\lambda}}\hat{y}(\hat{\boldsymbol{e}}, \hat{\boldsymbol{e}}_p, \hat{\chi}) = \hat{\tilde{\phi}}(\hat{\boldsymbol{e}}, \hat{\boldsymbol{e}}_p, \dot{\hat{\boldsymbol{e}}}_p) - \hat{\chi} : \dot{\hat{\boldsymbol{e}}}_p \equiv 0. \tag{17}$$

The conventional shift stress term $\hat{\psi}_2'(\hat{\boldsymbol{e}}_p)$ is not added to the micro generalized stress $\hat{\chi}$ expression (16) because of the assumption $\hat{\psi}_2 = 0$. This means that in microscopic terms yield surfaces do not translate in the stress space [Houlsby and Puzrin 2000]. In other words, in this case kinematic hardening in the microlevel is taken out of consideration (although models could still harden in the isotropic hardening sense). In kinematic hardening plasticity or other plasticity variants kinematic hardening parameters are often added within the terms $\hat{\psi}_2(\hat{\boldsymbol{e}}_p)$, which are omitted in the current formulation, to explain the Masing hysteretic behaviour of elasto-plastic materials. It will be shown that at the mesoscopic scale, however, the Masing hysteresis could still be deduced without introducing the $\hat{\psi}_2(\hat{\boldsymbol{e}}_p)$ terms (in other words without including kinematic hardening parameters at the microscopic level).

4.2. *Homogenisation analysis (mesorelations).* The previous subsection detailed the derivation of the microelasto-plastic constitutive relations between the micro stresses $\hat{\sigma}$ and strains $\hat{\boldsymbol{e}}$ from the definition of micro rate of dissipation and free energy density functions. This section describes the derivation of the mesoscopic relation from the meso Helmholtz free energy and rate of dissipation potentials. For the random elasto-plastic problem these are given by integrating the micropotentials over the RVE (or SVE) with Equations (9), (10), (13) and (14)

$$\Psi = \langle \hat{\psi}_1(\hat{\boldsymbol{e}}_e) \rangle = \langle \hat{\psi}_1(\hat{\boldsymbol{e}} - \hat{\boldsymbol{e}}_p) \rangle, \qquad \tilde{\Phi} = \langle \hat{\tilde{\phi}}(\hat{\boldsymbol{e}}, \hat{\boldsymbol{e}}_p, \dot{\hat{\boldsymbol{e}}}_p) \rangle. \tag{18}$$

The mesoscopic relations represent a boundary value problem that links between the internal microscale field variables and the mesoscopic boundary variables Σ and $\boldsymbol{E}$ ideally taking into account microstress equilibrium and compatibility relations while satisfying the Hill-Mandel work equilibrium in Equation (11). For simple problems, such as linear elastic heterogeneous problems, it is then possible to derive closed form solutions [Suquet 1987]. As our problem is much more involved than the linear elastic problem, and the focus is equally given to derive a conventional framework of elasto-plasticity, we take the assumption of uniform strain assuming that the microscale strain is uniform throughout the RVE. The fact that the total strain is the same for all subelements is equivalent to the Voigt homogenisation scheme. A more general analysis would have a different total strain for each subelement. The result is that equilibrium is satisfied only in the weak (Hill-Mandel) work form. In elastic materials the uniform strain assumption is known to provide an upper bound to the overall stiffness of the system, while the alternative assumption of uniform stress would provide a lower bound [Doghri 2000]. The more advanced theories for such materials may in fact narrow the distance between the bounds and may thus offer more predictive models. However, we are concerned with elasto-plastic models. Defining elasto-plasticity models using the more advanced hypotheses would lead to rather more complicated equations that we tend to avoid at this early stage. Between the two simple equivalence hypotheses, the uniform strain and uniform stress, the first is more often used [Walton 1987; Vardoulakis and Sulem 1995; Houlsby and Sharma 1999] as stresses are much more heterogenous as is evidenced from experiments [Drescher and de Josselin de Jong 1972] or from looking at DEM simulations [Cundall and Strack 1979]. The uniform strain assumption suggests that $\hat{\boldsymbol{e}} = \boldsymbol{E}$ for any coordinate x or p. Therefore since the strains

(and strain rates) are essentially deterministic, the statement $\dot{\boldsymbol{E}} = \langle\dot{\hat{\boldsymbol{e}}}\rangle = \dot{\hat{\boldsymbol{e}}}$ is trivial and not a result of statistical averaging. On the other hand, the macrolevel stress is a result of ensemble averaging satisfying the Hill-Mandel relation (11) with

$$\Sigma = \langle\hat{\sigma}\rangle = \langle\hat{\psi}_1'(\hat{\boldsymbol{e}}_e)\rangle. \tag{19}$$

The strain decomposition is thus given by

$$\boldsymbol{E} = \hat{\boldsymbol{e}}_e + \hat{\boldsymbol{e}}_p, \tag{20}$$

where we note that while the strain is uniform, the elastic and plastic strains are not. In this case the potentials could be specialized by

$$\Psi = \langle\hat{\psi}_1(\boldsymbol{E} - \hat{\boldsymbol{e}}_p)\rangle, \qquad \tilde{\Phi} = \langle\dot{\tilde{\hat{\phi}}}(\boldsymbol{E}, \hat{\boldsymbol{e}}_p, \dot{\hat{\boldsymbol{e}}}_p)\rangle. \tag{21}$$

The relations between the above and the simple motivating springs-sliders model example in Equations (5), (7) are apparent. The transformation to the field of yield surfaces (17) is then

$$\dot{\tilde{\hat{\lambda}}}\hat{y}(\boldsymbol{E}, \hat{\boldsymbol{e}}_p, \hat{\chi}) = \dot{\tilde{\hat{\phi}}}(\boldsymbol{E}, \hat{\boldsymbol{e}}_p, \dot{\hat{\boldsymbol{e}}}_p) - \hat{\chi} : \dot{\hat{\boldsymbol{e}}}_p \equiv 0.$$

Thus

$$\dot{\hat{\boldsymbol{e}}}_p = \dot{\tilde{\hat{\lambda}}}\partial\hat{y}/\partial\hat{\chi}.$$

The rate form of Equation (19) is given by

$$\dot{\Sigma} = \langle\hat{\psi}_1''(\hat{\boldsymbol{e}}_e)\rangle : \dot{\boldsymbol{E}} - \langle\hat{\psi}_1''(\hat{\boldsymbol{e}}_e) : \dot{\hat{\boldsymbol{e}}}_p\rangle.$$

The global instantaneous elastic stiffness moduli tensor could be defined when all the microscale plastic strain rates are zero

$$\boldsymbol{M} = \langle\hat{\psi}_1''(\hat{\boldsymbol{e}}_e)\rangle, \tag{22}$$

such that it is found that the elastic stiffness is a function of the microscale elastic strains. This means that the instantaneous modulus is not constant upon unloading-reloading, and is dependent upon the stored elastic energy.

The mesopotentials (21) are functionals of internal plastic strain tensor variable $\hat{\boldsymbol{e}}_p$ of either the x or p internal coordinates, while any yield surface in the field is associated with a given coordinate. The concept of incorporating an internal variable tensor function $\alpha(\eta)$ of some internal coordinate η and defining a continuous field of yield surfaces in a thermomechanically admissible framework was recently introduced by Puzrin and Houlsby [2001]. But the defined class of potentials $\alpha(\eta)$ and η did not receive any significant physical meaning. Masing hystereses were modelled via a separate kinematic hardening distribution function of η, and models were based on curve fitting this distribution function to experimental laboratory data [Puzrin et al. 2001; Einav and Puzrin 2004]. Here Masing hystereses are obtained without including an additional kinematic hardening distribution function.

The above form of the Helmholtz free energy potential functional was proposed independently by Chaboche [2003] and Einav [2005] though in the first case in a more limited form allowing only for linear elasticity (assuming quadratic free energy functions). A more significant change is that the treatment of the derivation is completely different. Chaboche [2003] explored the outcomes of employing these functionals using traditional homogenization techniques seeking to replace the set of plastic internal

variables using a single plastic variable, but here we will adopt the MPR that enables us to keep track of the entire field of plastic internal variables. This, in turn, allows deriving a more detailed set of evolution equations without loosing memory aspects of plastic materials. Also, the result is that a field of yield surfaces in the micro stress space is defined rather than a single yield surface as Chaboche [2003] suggested.

4.3. *Micro thermomechanics with linear microelasticity.* Equation (18) (left) could be specialized by limiting its form to linear microelasticity, by suggesting a general homogeneous function of degree 2 of the microscale elastic strains

$$\Psi = \tfrac{1}{2}\langle \hat{e}_e : \hat{m} : \hat{e}_e \rangle, \quad \text{that is} \quad \hat{\psi}_1(\hat{e}_e) = \tfrac{1}{2}\hat{e}_e : \hat{m} : \hat{e}_e, \tag{23}$$

where $\hat{m}$ is a fourth order tensor function denoting the variation in microscale elastic stiffness coefficients within the RVE; this function is chaotic with the spatial coordinate x but assumed to be smooth with the cumulative probability p. Based on Equations (19) and (20) the stress is given by

$$\Sigma = \langle \hat{m} \rangle : E - \langle \hat{m} : \hat{e}_p \rangle,$$

which upon further derivation gives the fourth-order mesoscale stiffness tensor

$$M = \partial \Sigma / \partial E = \langle \hat{m} \rangle. \tag{24}$$

This equation should be compared with the elastic stiffness tensor of the general nonlinear case (22). This time this tensor is not a function of the microscale elastic strains.

4.4. *A discrete approximation of models (probabilistic system).* In Section 4.2 the general structure of continuous potentials were listed. Under monotonic unidirectional loading conditions, using the smooth probabilistic system, it is possible to derive closed form expressions (as will be demonstrated in the next section) describing the stress-strain curve response of the material. For general loading conditions, when the material is cyclically loaded or the direction of loading alters, it is convenient to use an alternative effective *numerical* scheme. An efficient way to do it is to approximate the general continuous potentials (given by Equation (21)) discretely

$$\Psi = \int_0^1 \psi_1\big(e_e(p), p\big) dp \approx \sum_{n=1}^N \psi_1\big(e_e(p_n), p_n\big)\Delta p_n = \sum_{n=1}^N \psi_1^n\big(e_e^n\big),$$

$$\tilde{\Phi} = \int_0^1 \tilde{\phi}\big(E, e_p(p), \dot{e}_p(p), p\big) dp \approx \sum_{n=1}^N \tilde{\phi}\big(E, e_p(p_n), p_n\big)\Delta p_n = \sum_{n=1}^N \tilde{\phi}_n\big(E, e_p^n, \dot{e}_p^n\big),$$

where p_n denotes a particular cumulative probability point, N is the number of those points, Δp_n is a vector of length N denoting the zone of influence of each of these approximating points. The discrete approximation of the rate of dissipation leads to definition of a field of N yield surfaces rather than a continuous field

$$\tilde{\lambda}_n y_n(E, e_p^n, \chi_n) = \tilde{\phi}_n(E, e_p^n, \dot{e}_p^n) - \chi_n : \dot{e}_p^n \equiv 0,$$

where we note that

$$y_n(E, e_p^n, \chi_n) = y\bigg(E, e_p(p_n), \frac{\chi(p_n)}{\Delta p_n}, p_n\bigg).$$

The above allows one, following a standard computational method, to derive rather effectively the response of the continuous problem in a discrete numerical manner. As $\chi_n = \sigma_n$, the consistency condition of the n-th yield surface is given by

$$\dot{y}_n(E, e_p^n, \sigma_n) = \frac{\partial y_n}{\partial E} : \dot{E} + \frac{\partial y_n}{\partial e_p^n} : \dot{e}_p^n + \frac{\partial y_n}{\partial \sigma_n} : \dot{\sigma}_n = 0,$$

which together with the n-th flow rule $\dot{e}_p^n = \tilde{\lambda}_n \partial y_n / \partial \sigma_n$, the n-th decomposition of strains $\dot{E} = \dot{e}_e^n + \dot{e}_p^n$, and the rate form of the microelasticity rule $\dot{\sigma}_n = \psi_1^{n\prime\prime}(e_e^n) : \dot{e}_e^n$ gives the solution for the n-th nonnegative microplasticity multiplier

$$\tilde{\lambda}_n = \left(\frac{\dfrac{\partial y_n}{\partial E} + \dfrac{\partial y_n}{\partial \sigma_n} : \psi_1^{n\prime\prime}(e_e^n)}{\dfrac{\partial y_n}{\partial \sigma_n} : \psi_1^{n\prime\prime}(e_e^n) : \dfrac{\partial y_n}{\partial \sigma_n} - \dfrac{\partial y_n}{\partial e_p^n}} \right) : \dot{E},$$

which upon elimination and the rate form of $\Sigma = \sum_{n=1}^{N} \sigma_n$ evolution law (note that "Σ" and "$\sum$" denote the meso stress tensor and the sum operator, respectively)

$$\dot{\Sigma} = \sum_{n=1}^{N} \psi_1^{n\prime\prime}(e_e^n) : \left(\dot{E} - \tilde{\lambda}_n \frac{\partial y_n}{\partial \sigma_n} \right).$$

5. Examples

5.1. *One-directional monotonic loading of the one-dimensional basic model.* The potentials of the conceptual model in Section 3 (Equations (5) and (7)) were defined based on the mechanical role of the constituents. Then the structure of those potentials was generalised in Section 4 and we showed how the rate of global dissipation leads to a definition of a field of yield surfaces (each yield surface is associated with a corresponding rate of dissipation density). In this section we will demonstrate how stress-strain relations could be derived directly from the potentials. It is possible to examine the model performance for one-directional monotonic loading conditions. For such derivation, since the original system is chaotic, the rearranged system helps in finding analytical solutions. To this end we adopt the MPR. The local rate of dissipation density is given by Equation (6) and $\tilde{\phi}(\dot{e}_p(p), p) = \sigma_u(p)|\dot{e}_p(p)| \geq 0$. According to the Equation (15), in the rearranged system we can define the dissipative generalised stress as

$$\chi(p) = -\partial\tilde{\phi}/\partial\dot{e}_p(p) = \sigma_u(p)\,\mathrm{sgn}(\dot{e}_p(p)) \geq 0,$$

where sgn( ) denotes the signum function. The presence of the rate of the microplastic strain $\dot{e}_p(p)$ could be eliminated by taking the absolute of both sides, and this defines the yield surface in the local dissipative generalized stress space

$$y(\chi(p), p) = |\chi(p)| - \sigma_u(p) \leq 0.$$

Invoking Ziegler's orthogonality hypothesis, the dissipative stress $\chi(p)$ could also be derived from the Helmholtz free energy potential density

$$\chi(p) = -\partial\psi\big(E, e_p(p)\big)/\partial e_p(p) = \sigma(p) = c(p)\big(E - e_p(p)\big)$$

and thus the sliding condition in the different St-Venant elements could be represented alternatively by yield functions in the microstress or in the mesostrain spaces

$$F(\sigma(p), p) = |\sigma(p)| - \sigma_u(p) \le 0, \quad F(E, e_p(p), p) = \left|c(p)\big(E - e_p(p)\big)\right| - \sigma_u(p) \le 0. \quad (25)$$

The performance of the basic model is dependent on the distribution functions $\sigma_u(p)$ and $c(p)$. The strength distribution curve for ductile solids is very narrow, while that for brittle solids is very broad with a large tail on the larger-strength side that can be explained by a statistical distribution called the Weibull distribution [Weibull 1951]. Weibull statistics was used extensively to describe brittle solids such as ceramics [Espinosa and Zavattieri 2003] and is based on the principle that the survival of a block under tension requires that all its constituents parts remain intact (a chain is as strong as its weakest link). A similar understanding was recently adopted to explain the statistical crushing events in the compression of soils [McDowell and Bolton 1998; Nakata et al. 1999].

The probability density function (pdf) of the two-parameter Weibull distribution is given by $f(x) = (\beta/\alpha)(x/\alpha)^{\beta-1} \exp(-(x/\alpha)^\beta)$, for all $\{x, \alpha, \beta\} \ge 0$, where α is known as the scale parameter and β as the shape parameter. Thus the two-parameters Weibull cumulative distribution function (cdf) is given by $F(x) = P_r[X \le x] = \int_{-\infty}^x f(\mu)d\mu = 1 - \exp(-(x/\alpha)^\beta)$. For the inverse cdf we start with the probability and compute the corresponding x for the cumulative distribution. Mathematically this can be expressed by defining the function $G(p)$ of the cumulative probability p as $P_r[X \le G(p)] = p$, for all $p \in [0, 1]$, such that $x = G(p) = G(F(x))$. Thus for the two-parameters Weibull function the inverse cdf is $G(p) = \alpha[-\ln(1-p)]^{1/\beta}$. Figure 5 shows the normalised Weibull inverse cdf $G(p)/\alpha$ for varying β values. It could be seen that α is the inverse cdf value that corresponds to cumulative distribution of about 67%. Normalising of the last expression by the mean value of the Weibull pdf, given by $\bar{T} = \alpha\Gamma(1 + 1/\beta)$, where $\Gamma(x) = \int_0^\infty \mu^{x-1} \exp(-\mu)d\mu$ is the Gamma function, and multiplying by Σ_u gives

$$\sigma_u(p) = \frac{\Sigma_u}{\bar{T}} G(p) = \frac{\Sigma_u[-\ln(1-p)]^{1/\beta}}{\Gamma(1+1/\beta)}. \quad (26)$$

It could be checked that Σ_u is

$$\Sigma_u = \int_0^1 \sigma_u(p)\,dp = \langle\hat{\sigma}_u\rangle$$

such that it plays the role of a parameter that defines the mesoscale complete failure, that is, the stress at which all sliders become active, and is equal to the average of all the constituents' plastic threshold.

Contrary to the common assumption of the suitability of the Weibull distribution in describing the failure of materials, there is no apparent evidence, at least that we are aware of, suggesting such a dependency of the elastic moduli. For this reason let us assume constant elastic stiffness

$$c(p) = C_0 \quad (27)$$

suggesting uniform instantaneous elastic moduli C_0 in the SVE.

The two inverse cumulative distribution functions of Equations (26) and (27) are plotted qualitatively in Figure 6. In this figure the shaded area represents the contribution of the microstresses to balance the applied mesostress. Mathematically this could be expressed
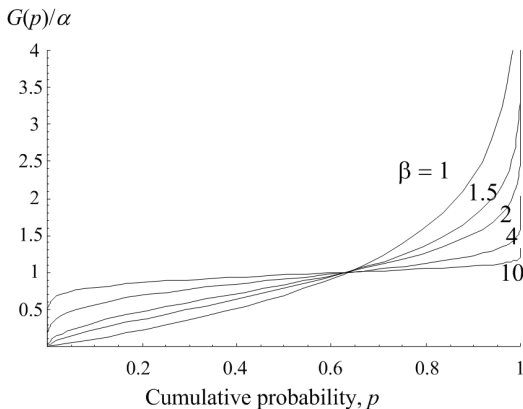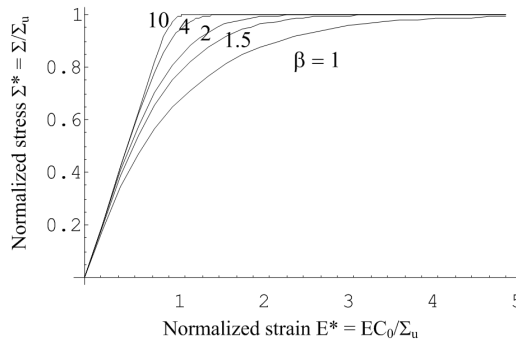
Figure 5. Normalized inverse cdf for different shape parameter β of the Weibull distribution.

$$\Sigma = \partial\psi(E, e_p(p))/\partial E$$
$$= \int_0^1 \sigma(p)\,dp$$
$$= \Sigma_1 + \Sigma_2 \tag{28}$$
$$= \int_0^{p^*} \sigma_u(p)\,dp + \int_{p^*}^1 c(p)e\,dp$$
$$= \Sigma_u\left(1 - \frac{\gamma(\omega, -\ln(1-p^*))}{\Gamma(\omega)}\right) + (1-p^*)C_0E,$$
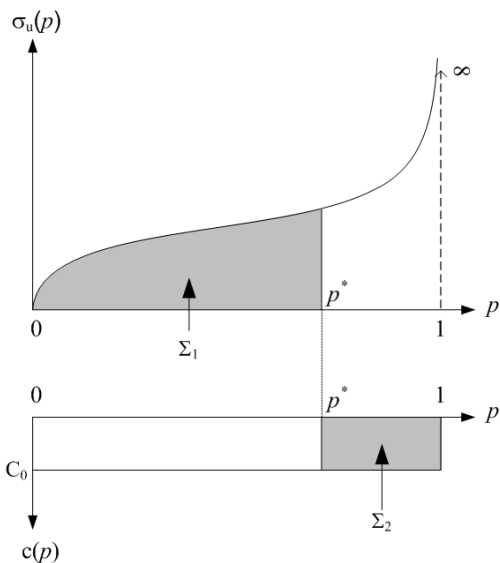
Figure 6. Inverse cdf for the micro thermomechanical one-dimensional plasticity model. (a) microscale strength; (b) microscale elastic modulus.

Figure 7. Analytical stress-strain curves for monotonic loading of the one-dimensional randomly distributed plasticity model based on Weibull statistics (in correspondence with Figure 5).

where we use $\omega = 1 + 1/\beta$; Σ_1 and Σ_2 designates the stress contribution from elements on yield or in elastic state; $\gamma(x_1, x_2) = \int_{x_2}^{\infty} \mu^{x_1 - 1} \exp(-\mu) \, d\mu$ is the incomplete gamma function; and $p = p*$ denotes the transition point between those elements. At the transition point, $p = p*$, both Equations (4) and (25) must be satisfied. Since we seek a solution for proportional monotonic loading conditions $e_p(p \equiv p^*) = 0$ and $C_0 E = \sigma_u(p^*)$ such that

$$p^* = 1 - \exp\left[-\left(\frac{\Gamma(\omega) C_0 E}{\Sigma_u} \right)^{1/\beta} \right],$$

which upon substitution into Equation (28) gives the analytical solution for monotonic loading conditions of the conceptual one-dimensional model for heterogeneous materials with Weibull's distribution of strength

$$\frac{\Sigma(E^*)}{\Sigma_u} = 1 - \frac{\gamma\left(\omega, (E^* \Gamma(\omega))^{\beta} \right)}{\Gamma(\omega)} + E^* \exp[-(E^* \Gamma(\omega))^{1/\beta}], \tag{29}$$

where we use $E^* = C_0 E / \Sigma_u$. Figure 7 presents the changes in the normalised stress-strain curves resulting from variations in the Weibull's shape parameter β (corresponding to Figure 5), which decreases with increasing variability in strength. It is clearly shown how a decrease in the strength variability is accompanied with a stronger curvature in the stress-strain curve which seems only logical to expect.

5.2. One-directional cyclic loading of the one-dimensional basic model. The results above were derived for one-directional monotonic loading conditions and analytic expressions were given. However, the model could be reformulated in a numerical form for cyclic loads realisation according to Section 4.4. For this particular model the solution for the n-th nonnegative multiplier takes a rather simple form

$$\tilde{\lambda}_n = \Theta(\sigma_n \dot{E}) |\dot{E}|,$$

where $\Theta(x) = 1$ if $x > 0$, and $\Theta(x) = 0$ if $x \leq 0$. Then according to Equation (17)

$$\dot{\Sigma} = |\dot{E}| \sum_{n=1}^{N} c(p_n) \omega, \quad \omega = \text{sgn}(\dot{E}) - \Theta(\sigma_n \dot{E}) \, \text{sgn}(\sigma_n).$$
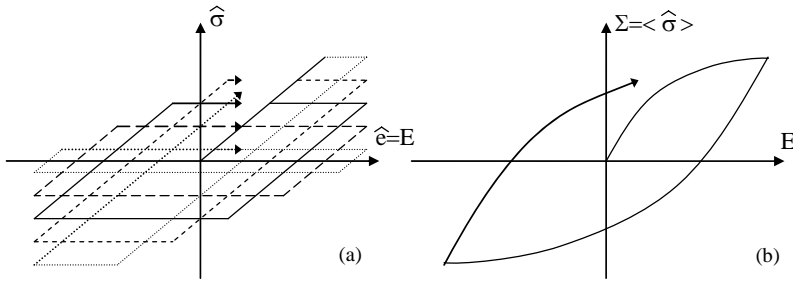
Figure 8. Micro and meso stress-strain curves under cyclic loading conditions of the one-dimensional model.

The last equation (see also a schematic diagram in Figure 8) proves that the model presents the well known Masing hysteretic rules as the microconstituent's local stiffness multiplier is $\omega = 0$, 1, or -1 (for microyield, microelastic loading, or microelastic unloading conditions). The meso stress-strain curve of Figure 8b is defined by integrating the micro stress-strain curves of Figure 8a. Each individual micro stress-strain curve is typical for an elasto-perfectly plastic element, described by a single elastic modulus and a single plastic threshold. Their assembly produces a smooth hysteretic macrocurve without incorporating any kinematic hardening parameter. This model, known as the Masing-Iwan model, could be generalized as we do in the next section.

5.3. *Micro thermomechanical von Mises model (with linear elasticity).* The previous example model has dealt with the reaction of heterogeneous materials that are subjected to the action of one-directional compression loading. However, the theory can facilitate in defining complete constitutive models that can accommodate any direction of loading. To demonstrate this aspect a conceptual micro thermomechanical von Mises model is derived.

5.3.1. *Classical (homogeneous) linear elasto-perfectly plastic von Mises model.* The stored elastic energy within linear isotropic elasticity in homogeneous materials is expressed directly by the mesoscopic elastic strains

$$\Psi = \tfrac{1}{2}\big(K \cdot \mathrm{tr}(\boldsymbol{E}_e)^2 + 2G \boldsymbol{E}_e^d : \boldsymbol{E}_e^d\big), \tag{30}$$

where K and G are the bulk and shear moduli; $\mathrm{tr}(\bullet) = \bullet : \mathbf{1}$ is the trace of a second order tensor "$\bullet$" while $\mathbf{1}$ is the second order identity tensor; and we have used $\bullet^d = \bullet - \tfrac{1}{3}\mathrm{tr}(\bullet)\mathbf{1}$ to denote the distortional (deviatoric) part of the tensor.

The rate of dissipation potential of perfectly plastic von Mises model for homogeneous materials is expressed directly by the mesoscopic plastic strain rates

$$\tilde{\Phi}(\dot{\boldsymbol{E}}_p) = k\sqrt{2\dot{\boldsymbol{E}}_p^d : \dot{\boldsymbol{E}}_p^d} \geq 0, \tag{31}$$

where k is the simple shear strength. Using the degenerate case Legendre transformation together with $\chi = \Sigma$ resulting from the structure of Equation (30) this potential gives the classical von Mises yield function [Collins and Houlsby 1997]

$$y(\Sigma) = \Sigma^d : \Sigma^d - 2k^2 \leq 0. \tag{32}$$

5.3.2. *Von Mises model for randomly distributed heterogeneous materials.* It is possible to extend the above homogeneous model within the micro thermomechanics framework. First let us rewrite Equation (30) as a local energy density

$$\psi = \psi_1 = \tfrac{1}{2}\big(K_m(p)\cdot\mathrm{tr}(\boldsymbol{e}_e(p))^2 + 2G_m(p)\boldsymbol{e}_e^d(p):\boldsymbol{e}_e^d(p)\big)$$

thus the global Helmholtz free energy potential is

$$\Psi = \frac{1}{2}\int_0^1 \Big(K_m(p)\cdot\mathrm{tr}\big(\boldsymbol{E}-\boldsymbol{e}_p(p)\big)^2 + 2G_m(p)\big(\boldsymbol{E}^d - \boldsymbol{e}_p^d(p)\big):\big(\boldsymbol{E}^d - \boldsymbol{e}_p^d(p)\big)\Big)dp, \qquad (33)$$

where $K_m(p)$ and $G_m(p)$ are the microscale bulk and shear moduli. It follows that

$$\sigma^d(p) = 2G_m(p)\boldsymbol{e}_e^d(p), \qquad\qquad\qquad \mathrm{tr}(\sigma(p)) = 3K_m(p)\,\mathrm{tr}(\boldsymbol{e}_e(p)),$$

$$\Sigma^d = \int_0^1 \sigma^d(p)\,dp = 2\int_0^1 G_m(p)\boldsymbol{e}_e^d(p)\,dp, \qquad \mathrm{tr}(\Sigma) = 3\int_0^1 K_m(p)\,\mathrm{tr}(\boldsymbol{e}_e(p))\,dp.$$

Let us also rewrite the rate of dissipation potential from Equation (31) in local density form

$$\tilde{\phi}(\dot{\boldsymbol{e}}_p(p), p) = k_m(p)\sqrt{2\dot{\boldsymbol{e}}_p^d(p):\dot{\boldsymbol{e}}_p^d(p)} \geq 0,$$

where $k_m(p)$ is the simple shear microscale strength. Thus the global potential is

$$\tilde{\Phi}(\dot{\boldsymbol{e}}_p(p)) = \int_0^1 k_m(p)\sqrt{2\dot{\boldsymbol{e}}_p^d(p):\dot{\boldsymbol{e}}_p^d(p)}\,dp.$$

Whenever $\dot{\boldsymbol{e}}_p^d(p):\dot{\boldsymbol{e}}_p^d(p) > 0$, the microscale deviatoric stress at point p could also be defined using Equation (17)

$$\sigma^d(p) = 2k_m^2(p)\dot{\boldsymbol{e}}_p^d(p)/\tilde{\phi}\big(\dot{\boldsymbol{e}}_p(p), p\big),$$

such that $\sigma^d(p):\sigma^d(p) = 2k_m^2(p)$ and we recover the p-th von Mises yield function in the microscale stress-space

$$y(\sigma(p), p) = \sigma^d(p):\sigma^d(p) - 2k_m^2(p) \leq 0$$

which in the mesoscale strain-space is written by

$$y(\boldsymbol{E}, \boldsymbol{e}_p(p), p) = 2G^2(p)\boldsymbol{e}_e^d(p):\boldsymbol{e}_e^d(p) - k_m^2(p) = 2G^2(p)\big(\boldsymbol{E}^d - \boldsymbol{e}_p^d(p)\big):\big(\boldsymbol{E}^d - \boldsymbol{e}_p^d(p)\big) - k_m^2(p) \leq 0.$$

Instantaneous elasticity. From (23), (24) and (33) the instantaneous macro shear and bulk moduli is

$$G = \int_0^1 G_m(p)\,dp = \langle\hat{G}\rangle, \quad K = \int_0^1 K_m(p)\,dp = \langle\hat{K}\rangle.$$

Terminal mesoscale yielding. Let us define terminal mesoscale yielding when all the subelements constituents yield, that is, when $\sigma^d(p):\sigma^d(p) = 2k_m^2(p)$ for any p. The solution for the microscale deviatoric stress is in the form

$$\sigma^d(p) = \sqrt{2}k_m(p)\boldsymbol{n}', \quad \text{where } \boldsymbol{n}':\boldsymbol{n}' = 1, \text{ and } \boldsymbol{n}':\mathbf{1} = 0. \qquad (34)$$

If $\sigma^d(p) : \sigma^d(p) = 2k_m^2(p)$ is satisfied for any p, its integral form is satisfied as well, thus

$$\int_0^1 \sqrt{\sigma^d(p) : \sigma^d(p)}\, dp = \langle \sqrt{\hat{\sigma}^d : \hat{\sigma}^d} \rangle = \sqrt{2}\bar{k},$$

where we designate the constant $\bar{k} = \int_0^1 k_m(p)\, dp$. A question arrises as to whether $\bar{k}$ agrees with the constant k of the conventional (homogeneous) von Mises model. From Equation (32) upon yielding the conventional von Mises model predicts

$$\sqrt{\Sigma^d : \Sigma^d} = \sqrt{\langle \hat{\sigma}^d \rangle : \langle \hat{\sigma}^d \rangle} = \sqrt{2}k,$$

which with Equation (34) proves that $\bar{k} = k$, thus the overall mesoscale simple shear strength is given by the average over the microscale simple shear strengths in the SVE

$$k = \int_0^1 k_m(p)\, dp = \langle \hat{k}_m \rangle.$$

6. Evaluation of the probabilistic approach

In the previous sections the different properties in the modelling approach were physically interpreted. The suitability of this interpretation is dependent on the validity of the probabilistic concepts adopted in Section 2. For that purpose this section presents a short numerical study. This study includes several finite difference (FD) experiments using the commercial code FLAC of Itasca [FLAC 2000], which are compared with the analytical solution of the same problem based on the micro thermomechanics framework. The advantages of the use of FLAC for such analyses was recently noticed by Ostoja-Starzewski [2005], who have performed similar calculations for rigid-perfectly-plastic two-phase randomly distributed medium. This paper will concern itself with materials with finite rigidity that are presented for continuous phased Weibull media.

The FD models in our calculations involve a 50×50 element mesh that represents 2500 von Mises subelements in a single RVE. The large number of elements used for the analyses was chosen such that the simulation will satisfy, as close as possible, the criterion of $\delta = L/l = 50 \to \infty$ in order to be able to consider results from a point statistics view point. As a result we can practically view the RVE as a SVE with the weaker form of nondimensional length scales. According to Ostoja-Starzewski [2005], when δ tends to infinity, results for constant applied displacement or constant applied traction boundary conditions tend to merge to a unique solution for a given deterministic spatial arrangement of a randomly distributed material. Thus the following calculations will be based only on applying constant displacement boundary conditions. The bulk modulus received a significantly large value insuring that the calculation will simulate as close as possible the behaviour of incompressible material. This condition insures that a plane strain FD model with constant vertical and horizontal displacements but with opposite signs acting on the horizontal and vertical boundaries will not produce a stress reaction perpendicular to the plane. This point was validated during the calculation by averaging the in-plane stresses in all the subelements and validating that the result is negligible compared to the other stress components. The mesoscale vertical and horizontal stresses acting on the horizontal and vertical boundaries were calculated by summing the unbalanced forces along the corresponding boundaries and dividing them by their lengths. The mesoscale vertical strain was calculated simply by dividing the vertical relative
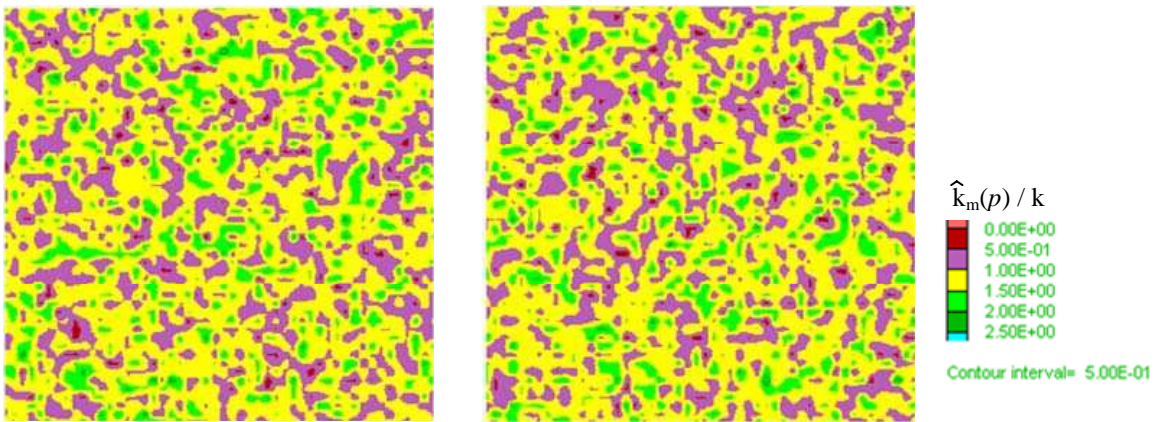
Figure 9. Contours of the normalized von Mises strength distribution ($\hat{k}_m / k$) within two randomly based 50*50 elements FLAC experiments generated by the Weibull inverse cdf.

displacement between the horizontal boundaries by their distance. The opposite operation gave the mesoscale horizontal strain.

6.1. *Monotonic loads on Weibullian random elasto-plastic von Mises media.* Weibull's statistics is most appropriate in describing the spatial variations in the compression strength of materials (for example as demonstrated by McDowell and Bolton [1998] for sands) and it is not so clear whether such a distribution may also be appropriate in describing variations in the shear strength. However, our main purpose is to assess the theoretical assumptions and this could be more easily done by randomly varying the shear strength coefficients between the (von Mises) subelements. To this end using a modification to Equation (26)) Weibull's inverse cdf is used for generating spatial variations in the simple shear strength $k_m(p) = k[-\ln(1-p)]^{1/\beta}/\Gamma(1+1/\beta)$, while the shear and bulk stiffness moduli $G_m(p) = G$ and $K_m(p) = K \gg G$ were homogeneous. In the analyses the range of $\beta = 1.5, 3, 10$ will be used to cover ideal materials ranging from strongly ($\beta = 1.5$, typical low value for silica sand [Nakata et al. 1999]) to weakly heterogeneous materials ($\beta = 10$, typical for ceramics [Espinosa et al. 2003]). Each ideal material will be analyzed based on two deterministic fields thus giving a total of 6 analyses. This means that the two FD calculations for the same β material are essentially different in their geometrical configuration. This is illustrated in Figure 9, describing the contours of two different deterministic fields of the normalized microscale von-Mises strength within the first and second FLAC calculations for the same $\beta = 3$ randomly distributed material.

Our aim is to show that the results from the finite difference calculations do not change practically if we use the same random distribution to obtain a different deterministic arrangement. This is carried out to validate the proposition of the MPR. The results from the 6 different FLAC calculations are presented in Figure 10. It is clearly shown that the responses are repetitive. The minor discrepancies between the lines can be largely attributed to the fact that only 2500 subelements were used, while point statistic requires essentially infinite number.
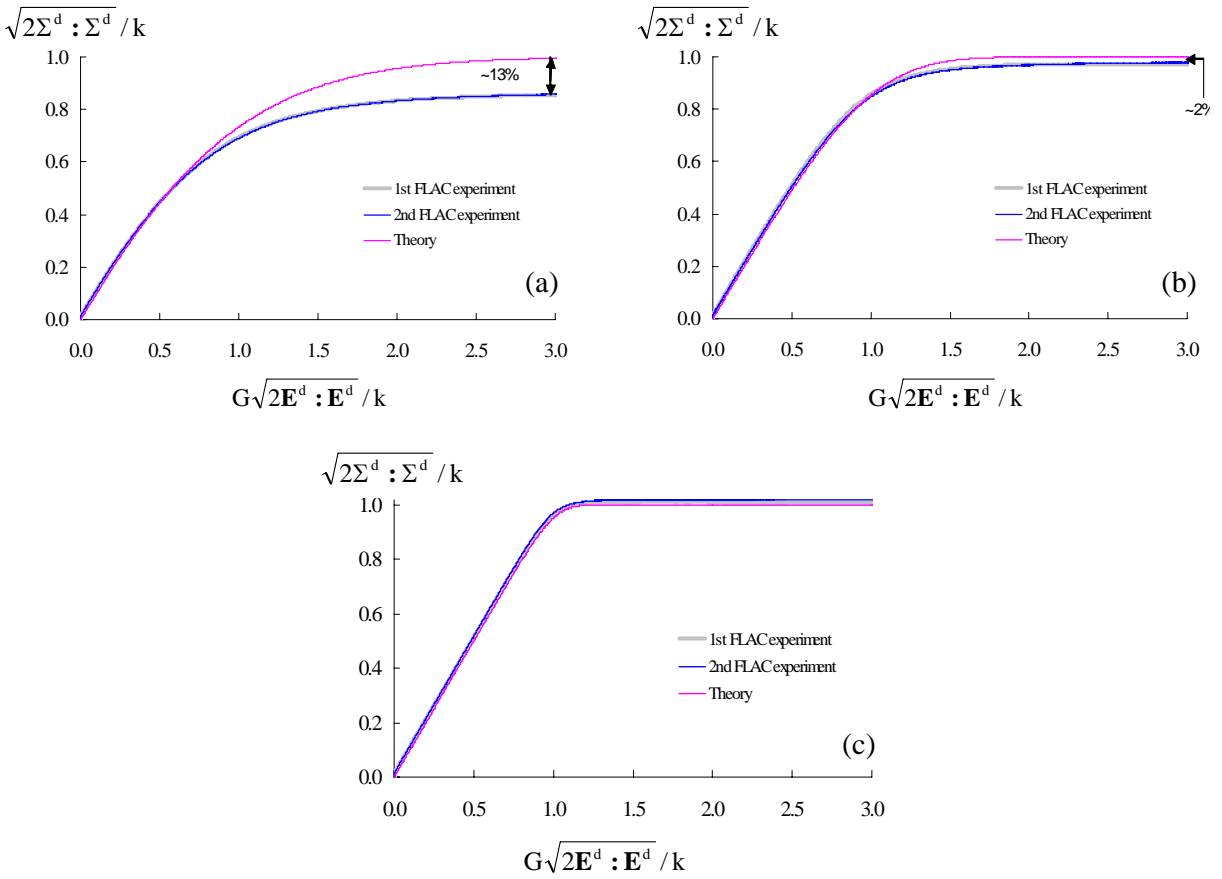
Figure 10. Comparison between 2 different deterministic FLAC experiments and the theoretical expression for (a) $\beta = 1.5$, (b) $\beta = 3$, and (c) $\beta = 10$ materials.

Next, we will evaluate the ability of the theoretical framework to predict the same results. Applying the back-bone curve of the one-dimensional model given Equation (29) to the general Von Mises model for randomly distributed heterogeneous materials suggests that in the current loading condition

$$J^*_1 = 1 - \frac{\Gamma\big(\omega, (J^*_2\Gamma(\omega))^\beta\big)}{\Gamma(\omega)} + J^*_2 \exp[-(J^*_2\Gamma(\omega))^{1/\beta}],$$

where

$$J^*_2 = \frac{G\sqrt{2\boldsymbol{E}' : \boldsymbol{E}'}}{k} \quad \text{and} \quad J^*_1 = \frac{\sqrt{\frac{1}{2}\Sigma' : \Sigma'}}{k}.$$

The predictions from the above equation are compared with the 2500 elements FD calculations; these are given in the Figure 10. The agreement is quantitatively very good and qualitatively excellent. Nevertheless it should be mentioned that the analytical solution gives a stiffer response. The difference is reduced as the degree of heterogeneity is reduced from approximately 13% difference in the highly heterogeneous case of $\beta = 1.5$ down as β increases. When $\beta = 10$ the numerical prediction is even
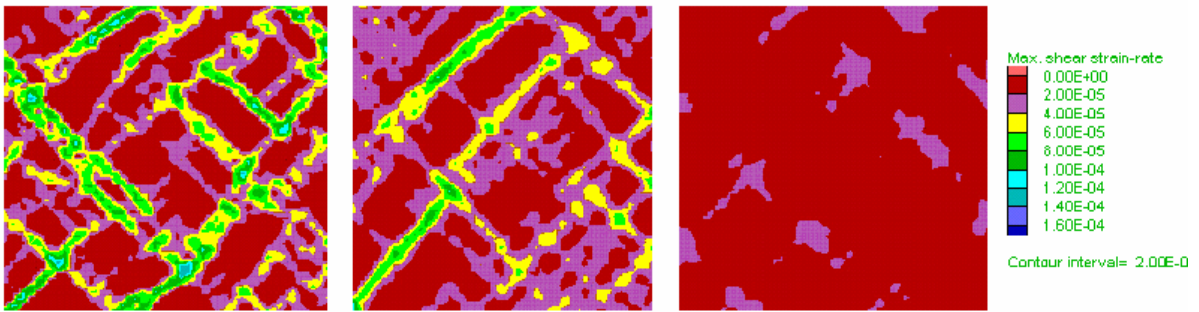
Figure 11. Internal patterning of deformations (maximum shear strain-rate) for a single deterministic calculation using $\beta = 1.5$, 3, and 10 materials.

showing a fractionally stiffer response, but this is attributed to dynamical wave propagation numerical drift in FLAC due to a shock in the early beginning of the calculation. This shock was eliminated as much as possible by ramping the load slowly.

In order to reduce the deviation of the theory from the true solution future improvements should include better estimates than the uniform strain assumption. This issue is highlighted when examining the internal patterning of deformations by plotting the maximum shear strain rate contours. As is shown in Figure 11 scattered shear bands appears in a random fashion. As expected those bands are deviated 45° from the horizon with some noise due to the randomality of the field. Theoretically, if the subelement size l was reduced to infinitesimal normalized size compared with L, those bands should tend to be infinitesimally thin slip lines as suggested by Ostoja-Starzewski and Ilies [1996]. Based on Figure 11 it can also be observed that as the degree of heterogeneity is reduced, the average distance between the slip lines is increasing. One possibility for further improvements would be to introduce an additional (normalized) length scale denoting the average distance between the slip lines. Alternatively, possibly a better option could be to introduce additional distribution function denoting the probability of a particular subelement to be within a slip line.

6.2. *Cyclic loads on Weibullian random elasto-plastic von Mises media.* Next the same FD model is examined under cyclic loading conditions (for the $\beta = 3$ case only). After applying deviatoric load in a similar manner to the previous section, the direction of the boundary displacements is reversed followed by another (re)loading phase. This cyclic loading test requires a very careful numerical procedure in which a sinusoidal type of ramping is applied minimizing the numerical dynamics waves as much as possible. The response of the detailed FD model is compared against the prediction of the simple micro thermomechanical von Mises constitutive model in Figure 12. The response of the simple model could be derived either by utilising the numerical discretisation method or simply by applying Masing rules on the approximating analytical formula (1). It is shown that the simple constitutive model agrees rather well with the detailed numerical FD model.
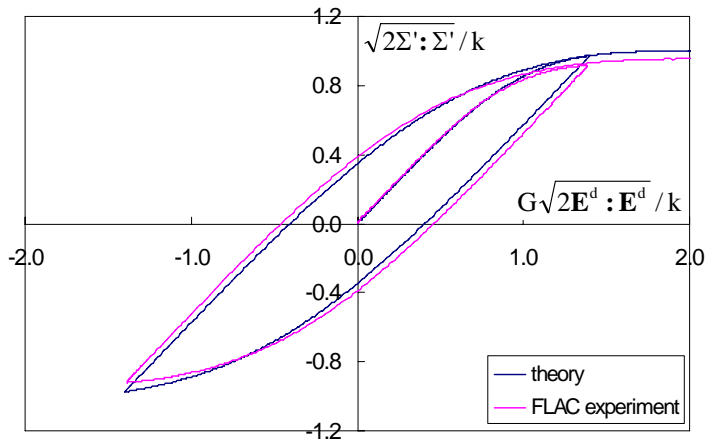
Figure 12. Comparison between the FLAC experiment and the performance of the constitutive model under unidirectional cyclic load for $\beta = 3$.

7. Summary

A theory for modelling heterogeneous randomly distributed elastic-plastic materials was presented. A conventional thermomechanical elasto-plastic constitutive modelling framework is proposed but one that allows an effective physical interpretation of the micromechanical internal variables and inherent parameters in a RVE. The main points behind this work are as follow

1. The paper demonstrates a micro thermomechanical constitutive modelling methodology that allows deriving estimates for the response of random elasto-plastic material under monotonic, cyclic and multidirectional loads. This particular property of the framework enables to capture memory features that are intrinsic within plastic material.

2. The method of probabilistic rearrangement (MPR) is suggested and verified against the finite Difference program of FLAC. By applying the MPR conventional constitutive modelling frameworks could be linked directly to the statistical distribution of the elasto-plastic material properties within the RVE or a SVE. The MPR enables to estimate effective properties within the SVE such that mesoscopic as well as microscopic field variables could be evaluated using localisation-homogenisation analytical procedure. An important point is that the MPR allows accounting for the gradual yielding that occurs within the SVE; a fact that could not be accounted for if the set of infinite plastic internal variables are replaced by a single average plastic internal variable.

3. The MPR facilitated in recovering analytical approximating formula to monotonic loading conditions of the full probabilistic boundary value problem. Under one-directional cyclic loading conditions, the approximating analytical formula could be extended using the famous Masing rules to provide the estimate of the micro thermomechanical constitutive model to the full probabilistic boundary value problem. For the more complicated scenarios of general multidirectional cyclic loading conditions a simple numerical procedure is suggested.

4. The results for the cyclic loading case show how hysteresis behavior of random materials could be realized directly by describing the physical heterogeneities in the material properties without the need to incorporate any kinematic hardening parameters.

8. Acknowledgments

References

[Adams et al. 1989] B. L. Adams, G. R. Canova, and A. Molinari, "A statistical formulation of viscoplastic behaviour in heterogeneous polycrystals", *Textures Microstruct.* **11** (1989), 57–71.

[Chaboche 2003] J. L. Chaboche, "Thermodynamics of local state: overall aspects and micromechanics based constitutive relations", pp. 113–129 in *Technische Mechanik*, Manuskripteingang, 11. Juni 2003 2003. Band 23, Heft 2-4.

[Chang and Ma 1991] C. S. Chang and L. Ma, "A micromechanically-based micropolar theory for deformation of granular solids", *Int. J. Solids Struct.* **28**:1 (1991), 67–86.

[Collins 2005a] I. F. Collins, "Elastic/plastic models for soils and sands", *Int. J. Mech. Sci.* **47** (2005a), 493–508.

[Collins 2005b] I. F. Collins, "The concept of "stored plastic work" or "frozen elastic energy" in soil mechanics", *Geotechnique* **55**:5 (2005b), 373–382.

[Collins and Hilder 2002] I. F. Collins and P. A. Hilder, "A theoretical framework for constructing elastic/plastic constitutive models of triaxial tests", *Geotechnique* **52**:7 (2002), 507–518.

[Collins and Houlsby 1997] I. F. Collins and G. T. Houlsby, "Application of thermomechanical principles to the modeling of geomaterials", *Proc. R. Soc. Lon. Ser-A* **453** (1997), 1975–2001.

[Collins and Kelly 2002] I. F. Collins and P. A. Kelly, "A thermomechanical analysis of a family of soil models", *Geotechnique* **52**:7 (2002), 507–518.

[Collins and Muhunthan 2003] I. F. Collins and B. Muhunthan, "On the relationship between stress-dilatancy, anisotropy, and plastic dissipation for granular materials", *Geotechnique* **53**:7 (2003), 611–618.

[Cundall and Strack 1979] P. A. Cundall and O. D. L. Strack, "A discrete model for granular assemblies", *Geotechnique* **29**:7 (1979), 47–65.

[Doghri 2000] I. Doghri, *Mechanics of deformable solids. Linear, nonlinear, analytical and computational aspects*, Springer, Berlin, 2000.

[Drescher and de Josselin de Jong 1972] A. Drescher and G. de Josselin de Jong, "Photoelastic verification of a mechanical model for the flow of a granular material", *J. Mech. Phys. Solids* **20** (1972), 337–351.

[Einav 2002] I. Einav, *Applications of thermodynamical approaches to mechanics of soils*, PhD. Thesis, Technion- Israel Institute of Technology, Haifa, 2002.

[Einav 2005] I. Einav, "A second look at strain space plasticity and latest applications", pp. 225–231 in *18th Australiasian conference on the mechanics of structures and materials (ACMSM)*, vol. 1, Perth, 1–3 December 2005.

[Einav and Puzrin 2004] I. Einav and A. M. Puzrin, "Continuous hyperplastic critical state (CHCS) model: derivation", *Int. J. Solids Struct.* **41**:1 (2004), 199–226.

[Espinosa and Zavattieri 2003] H. D. Espinosa and P. D. Zavattieri, "A grain level model for the study of failure initiation and evolution in polycrystalline brittle materials. Part I: theory and numerical implementation", *Mech. Mater.* **35** (2003), 333–364.

[Espinosa et al. 2003] H. D. Espinosa, B. Peng, B. C. Prorok, N. Moldovan, O. Auciello, J. A. Carlisle, D. M. Gruen, and D. C. Mancini, "Fracture strength of ultrananocrystalline diamond thin films- identification of Weibull parameters", *J. Appl. Phys.* **94**:9 (2003), 6076–6084.

[FLAC 2000] *FLAC (Fast Lagrangian Analysis of Continua) User's Manual*, Itasca Consulting Group, Inc., Minneapolis Minnesota: Itasca, 2000. Ver. 4.0.

[Frantziskonis 1998] G. Frantziskonis, "Stochastic modelling of heterogeneous materials- A process for the analysis and evaluation of alternative formulations", *Mech. Mater.* **27**:3 (1998), 165–175.

[Garmestani et al. 1988] H. Garmestani, S. Lin, and B. L. Adams, "Statistical continuum theory for inelastic behaviour of a two-phase medium", *Int. J. Plasticity* **14**:8 (1988), 719–731.

[Gurtin 2000] M. E. Gurtin, "On the plasticity of single crystals: free energy, microforces, plastic-strain gradients", *J. Mech. Phys. Solids* **48** (2000), 989–1036.

[Hill 1963] R. Hill, "Elastic properties of reinforced solids: some theoretical principles", *J. Mech. Phys. Solids* **11** (1963), 357–372.

[Houlsby and Puzrin 2000] G. T. Houlsby and A. M. Puzrin, "A thermomechanical framework for constitutive models for rate-independent dissipative materials", *Int. J. Plasticity* **16**:9 (2000), 1017–1047.

[Houlsby and Sharma 1999] G. T. Houlsby and R. S. Sharma, "A conceptual model for the yielding and consolidation of clays", *Geotechnique* **49**:4 (1999), 491–502.

[Maugin 1992] G. A. Maugin, *The thermomechanics of plasticity and fracture*, Cambridge University Press, 1992.

[McDowell and Bolton 1998] G. R. McDowell and M. D. Bolton, "On the micro mechanics of crushable aggregates", *Geotechnique* **48**:5 (1998), 667–679.

[Nakata et al. 1999] Y. Nakata, A. F. L. Hyde, M. Hyodo, and H. Murata, "A probablistic approach to sand particle crushing in the triaxial test", *Geotechnique* **49**:5 (1999), 567–583.

[Ostoja-Starzewski 2002] M. Ostoja-Starzewski, "Microstructural randomness versus representative volume element in thermomechanics", *J. Appl. Mech. (Trans. ASME)* **69** (2002), 25–35.

[Ostoja-Starzewski 2005] M. Ostoja-Starzewski, "Scale effects in plasticity of random media: status and challenges", *Int. J. Plasticity* **21** (2005), 1119–1160.

[Ostoja-Starzewski and Ilies 1996] M. Ostoja-Starzewski and H. Ilies, "The Cauchy and characteristic boundary value problems of random rigid-perfectly plastic media", *Int. J. Solids Struct.* **33**:8 (1996), 1119–1136.

[Pasternak and Mühlhaus 2005] E. Pasternak and H.-B. Mühlhaus, "Generalised homogenisation procedures for granular materials", *J. Eng. Math.* **52**:1 (2005), 199–229(31).

[Ponte Castañeda 1996] P. Ponte Castañeda, "Exact second-order estimates for the effective mechanical properties of nonlinear composite materials", *J. Mech. Phys. Solids* **44**:6 (1996), 827–862.

[Puzrin and Houlsby 2001] A. M. Puzrin and G. T. Houlsby, "A thermomechanical framework for rate-independent dissipative materials with internal functions", *Int. J. Plasticity* **17** (2001), 1147–1165.

[Puzrin et al. 2001] A. M. Puzrin, G. T. Houlsby, and J. B. Burland, "Thermomechanical formulation of a small strain model for overconsolidated clays", *Proc. R. Soc. Lon. Ser-A* **457**:2006 (February 2001), 425–440. ISSN 1364-5021.

[Rice 1971] J. R. Rice, "Inelastic constitutive relations for solids: an internal variable theory and its application to metal plasticity", *J. Mech. Phys. Solids* **19** (1971), 433–455.

[Satake 1978] M. Satake, "New formulation of graph-theoretical approach in the mechanics of granular materials", *Mechanics of Materials* **16(1-2)** (1978), 65–72.

[Suquet 1987] P. M. Suquet, "Elements of homogenization for inelastic solid mechanics", pp. 194–271 in *Proc. Homogenisation Techniques for Composite Media, Udine, Italy 1985*, 272, Part IV, Springer-Verlag, 1987. Lecture Notes in Physics.

[Tordesillas et al. 2004] A. Tordesillas, S. D. C. Walsh, and B. Gardiner, "Bridging the length scales: micromechanics of granular media", *BIT Numerical Mathematics* **44** (2004), 539–556.

[Ulm and Coussy 2003] F.-J. Ulm and O. Coussy, *Mechanics and durability of solids*, vol. 1, Prentice Hall, New Jersey, 2003.

[Vardoulakis 1983] I. Vardoulakis, "Rigid granular plasticity model and bifurcation in the triaxial test", *Acta Mech.* **49** (1983), 57–79.

[Vardoulakis and Sulem 1995] I. Vardoulakis and J. Sulem, *Bifurcation analysis in geomechanics*, Blackie Academic and Professional, 1995.

[Walsh and Tordesillas 2004] S. D. C. Walsh and A. Tordesillas, "A thermomechanical approach to the development of microp-
olar constitutive models for granular media", *Acta Mech.* **167**:3-4 (2004), 145–169.

[Walton 1987] K. Walton, "The effective elastic moduli of a random packing of spheres", *J. Mech. Phys. Solids* **35**:2 (1987),
213–226.

[Weibull 1951] W. Weibull, "A statistical distribution function of wide applicability", *J. Appl. Mech. (Trans. ASME)* **18** (1951),
293–297.

[Ziegler 1977] H. Ziegler, *An introduction to thermomechanics*, 2nd edition: 1983 ed., North Holland, Amsterdam, 1977.

ITAI EINAV: I.Einav@civil.usyd.edu.au
School of Civil Engineering, The University of Sydney, Sydney, NSW 2006, Australia

IAN F. COLLINS: i.collins@auckland.ac.nz
Department of Engineering Science, The University of Auckland, Auckland 1142, New Zealand

A CRACKED BEAM FINITE ELEMENT FOR ROTATING SHAFT DYNAMICS AND STABILITY ANALYSIS

SABER EL AREM AND HABIBOU MAITOURNAM

In this paper, a method for the construction of a cracked beam finite element is presented. The additional flexibility due to the cracks is identified from three-dimensional finite element calculations taking into account the unilateral contact conditions between the crack lips. Based on this flexibility, which is distributed over the entire length of the element, a cracked beam finite element stiffness matrix is deduced. Considerable gain in computing efforts is reached compared to the nodal representation of the cracked section when dealing with the numerical integration of differential equations in structural dynamics. The stability analysis of a cracked shaft is carried out using the Floquet theory.

1. Introduction

Because of the increasing need for energy, the plants installed by electricity supply utilities throughout the world are becoming larger and more highly stressed. Thus, the risk of turbogenerator shaft cracking is increasing also. Rotating shafts are omnipresent in aeronautics, aerospace, automobile industries, and in particular in the energy sector which is vital for any economic development. Fatigue cracks is an important form of rotor damage which can lead to catastrophic failures unless detected early. They can have detrimental effects on the reliability of rotating shafts. According to [Bently and Muszynska 1986], in the 1970s and till the beginning of the 1980s, at least 28 shaft failures due to cracks were recorded in the US energy industry. Thus, since the 1980s, the interest of researchers to characterize structures containing cracks has grown remarkably. Between the beginning of the 1970s and the end of the 1990s, more than 500 articles concerning the cracked structures were published [Dimarogonas 1996; Bachschmid and Pennacchi 2008].

The problem of determining the behavior of cracked structures has been worked on for a long time. The fact that a crack presence or a local defect in a structural member introduces a local flexibility that affects its vibration response was known long ago. This local flexibility is related to the strain energy concentration in the vicinity of the crack.

The study of cracked turbine rotors began in the American energy industry with the works of Dimarogonas [1970; 1971]. In Europe, the first works appeared only some years later in papers by Gasch [1976], Mayes and Davies [1976], and Henry and Okah-Avae [1976]. These authors considered a simple model to account for the crack breathing mechanism to which we often refer to as the *switching crack model* or the *hinge crack model* where the crack is totally opened or totally closed.

The vibration analysis of cracked beams or shafts is a problem of great interest due to its practical importance. In fact, vibration measurements offer a nondestructive, inexpensive, and fast means to detect and locate cracks. Thus, vibration behavior analysis and monitoring of cracked rotors has received

considerable attention in the last three decades [Gudmundson 1982; Gudmundson 1983]. It has, perhaps, the greatest potential since it can be carried out without dismantling any part of the machine and usually done online thus avoiding the costly downtime of turbomachinery.

Zuo [1992] and Zuo and Curnier [1994] also used a bilinear model to characterize the vibrational response of a cracked shaft with the aim of developing an online cracks detection method. They first examined the one degree of freedom system and then studied the behavior of a system with two degrees of freedom. By extending the Rosenberg normal mode notion for smooth and symmetric nonlinear systems to bilinear systems, they defined the nonlinear modes of the bilinear system which were calculated numerically, and in certain simple cases, analytically. The application of this method to systems with high number of degrees of freedom is complicated and would lead to high computation costs.

Bachschmid and his coworkers [Bachschmid et al.1984; 2002; 2004a] examined the effects of the presence of a crack on the vibratory response of a rotor or a pump axis. Experimental and numerical models were proposed, the thermal effects on the crack breathing mechanism were taken into account [Bachschmid et al. 2004a]. It was reported that the temperature distribution is not influenced by the presence of the crack unlike those of the stresses and deformations.

A comparison of various cracked beams models was presented by Friswell and Penny [2002]. The authors showed that in the low frequencies domain, simple models of the crack breathing mechanism and beam type elements are adequate to monitor structures health. However, the approach of modeling based on a bilinear dynamic system, which still acts as a reference, remains a simplistic approach which leads to some reservations about the quality of the quantitative results stemming from its exploitation.

A good review on the most relevant analytical, experimental and numerical works conducted in the last three decades and related to the cracked structures behavior were reported in [Dimarogonas and Paipetis 1983; Entwistle and Stone 1990; Dimarogonas 1996; Wauer 1990; Gasch 1993; El Arem 2006].

Today, most of the works on the cracked shafts vibration analysis are concerned with more detailed investigations of certain particular points such as the phase of acceleration or deceleration of the shaft and the passage through the critical speed or the coupling between diverse modes of vibrations to highlight parameters facilitating the online cracks detection when dealing with machines monitoring. These works such as those of Darpe et al. [2004], those of Jun et al. [1992] and those of Sinou and Lees [2005; 2007] where we find numerical and experimental results of their investigations on certain aforementioned points remain faithful to the theoretical principles formalized in the 70s in some reference papers. In the other hand, remarkable and continuous progress of the computational tools allows the realization of successful three-dimensional models. So it becomes possible to envisage an identification of the constitutive equations of a cracked shaft section (breathing mechanism description) which eliminates certain simplifying hypotheses and approximations made until now; this without degrading the costs of the calculations of the vibrational response.

The main objective of this work is the presentation of a method of construction of a cracked beam finite element. The stiffness variation of the element is deduced from three-dimensional finite element computations accounting for the unilateral contact between the crack lips. Based on an energy approach, this method could be applied to cracks of any shape. The validation of the approach on a case of a cracked rotating shaft is then presented and its stability analysis is carried using Floquet theory. The work of El Arem and Maitournam [2007] is used to show the general form of the stiffness matrix of the finite element and then facilitate the approximation of its terms.

2. Cracked rotors modeling: State of the art

The analysis of rotating machinery shafts behavior is a complex structural problem. For a relevant description, it requires a fine and precise modeling of the rotor and cracks in order to allow the identification and calculation of the parameters characterizing their presence.

Researchers dealing with the problem of a rotating cracked beam recognize its two main features: the determination of the local flexibility of the beam cracked section, and the consideration of the crack breathing mechanism responsible of the system nonlinearity (the stiffness of the system is dependent on the cracked section's position).

Most researchers agree with the application of the linear fracture mechanics theory to evaluate the local flexibility introduced by the crack [Gross and Srawley 1965; Anifantis and Dimarogonas 1983; Dimarogonas and Paipetis 1983; Dimarogonas 1996; Papadopoulos and Dimarogonas 1987a; 1987b; 1987c; Papadopoulos 2004]. Obviously, the first work was done in the early 1970s by Dimarogonas [1970; 1971] and Pafelias [1974] at the General Electric Company. There has been different attempts to quantify local effects introduced by cracks. The analysis of the local flexibility of a cracked region of a structural element was quantified in the 1950s by Irwin [1957a; 1957b], Bueckner [1958] , and Westmann and Yang [1967] by relating it to the stress intensity factors (SIF). Afterwards, the efforts to calculate the SIF for different cracked structures with simple geometry and loading was duplicated [Tada et al. 1973; Bui 1978].

For an elastic structure, the additional displacement $\boldsymbol{u}$ due to the presence of a straight crack of depth a under the generalized loading $\boldsymbol{P}$ is given by the Castigliano theorem

$$\boldsymbol{u} = \frac{\partial}{\partial \boldsymbol{P}} \int_0^a \boldsymbol{G}(a) \, da.$$

$\boldsymbol{G}$ is the energy release rate defined in fracture mechanics and related to the SIF by the Irwin formula [Irwin 1957a]. Then, the local flexibility matrix coefficients are obtained by

$$c_{ij} = \frac{\partial^2}{\partial P_i \partial P_j} \int_0^a \boldsymbol{G}(a) \, da, \quad 1 \le i, j \le 6.$$

Extra diagonal terms of this matrix are responsible for longitudinal and lateral vibrations coupling that can be of great interest when dealing with cracks detection.

In two technical notes from NASA, Gross and Srawley [1964; 1965] computed the local flexibility corresponding to tension and bending including their coupling terms. This coupling effect was observed by Rice and Levy [1972] in their study of cracked elastic plates for stress analysis.

Dimarogonas and his coworkers introduced the full (6×6) flexibility matrix of a cracked section [Dimarogonas 1982; 1987; 1988; Dimarogonas and Paipetis 1983; Anifantis and Dimarogonas 1983]. They noted the presence of extra diagonal terms which indicate the coupling between the longitudinal and lateral vibrations. Papadopoulos and Dimarogonas [1987a; 1987b; 1987c], and Ostachowicz and Krawwczuk [1992] computed all the (6×6) flexibility matrices of a Timoshenko beam cracked section for any loading case.

However, there are no results for the SIF for cracks on a cylindrical shaft. Thus, Dimarogonas and Paipetis [1983] have developed a procedure which is commonly used in FEM software: the shaft was considered as an assembly of elementary rectangular strips where an approximation of the SIF using

fracture mechanics results remains possible. The SIF are obtained by integration of the energy release rate on the crack tip. Although it offers the advantage of being easily applicable in a numerical algorithm, this method remains an approximation whose convergence remains to be checked. In fact, some numerical problems were noted when the depth of the crack exceeds the section radius [Abraham et al. 1994; Dimarogonas 1994]. Moreover, generalization of this method to any geometry of cracked section is complex, even impossible in the case of nonconnate multiple cracks affecting the same transverse section.

An original method for deriving a lumped cracked section beam model was proposed by Varé and Andrieux [2000; 2002]. The procedure was designed by starting from three-dimensional computations and incorporating more realistic behavior on the cracks than the previous models, namely the unilateral contact conditions on the crack lips and the breathing mechanism of the cracks under variable loading. The approach was validated experimentally by Audebert and Voinis [2000] and applied for the study of real cracked structures especially turbines.

The cracked element of Figure 1 is submitted to an end moment $M_{2L} = (M_x(2L), M_y(2L))$ at $z = 2L$. Andrieux [2000] has demonstrated certain properties of the problem elastic energy, W^*, leading to a considerable gain in three-dimensional calculus needed for the identification of the constitutive law. In particular, for a linear elastic material, under the assumption of small displacements and small deformations, and in the absence of friction on the crack lips, the energy function could be written by distinguishing the contribution of the cracked section from that of the uncracked element as

$$W^*(M_{2L}) = W^*(M) = W_s^*(M) + w^*(M) = \frac{L}{EI}\|M\|^2(1 + s(\Phi)), \tag{1}$$

where $M = (M_x, M_y)$ is the resulting couple of flexural moments at the cracked section, $W_s^*(M)$ is the total elastic energy of the uncracked element submitted to the flexural moment M, and $w^*(M)$ is the additional elastic energy due to the presence of the cracked section. The loading direction angle is defined by $\Phi = \arctan(M_y/M_x)$, E is the Young modulus, and I is the quadratic moment of inertia.

In this framework, the nonlinear constitutive law of the discrete element modeling of the cracked section is obtained by differentiating the function $w^*(M)$ with respect to M. We obtain

$$[\boldsymbol{\theta}] = \begin{pmatrix} [\theta_x] \\ [\theta_y] \end{pmatrix} = \frac{2L}{EI} \begin{pmatrix} s(\Phi) & -\frac{1}{2}s'(\Phi) \\ \frac{1}{2}s'(\Phi) & s(\Phi) \end{pmatrix} \begin{pmatrix} M_x \\ M_y \end{pmatrix}, \quad \text{with } s'(\Phi) = \frac{ds(\Phi)}{d\Phi}.$$

However, for finite element computational codes in rotordynamics, the compliance function $s(\Phi)$ is of low interest and a nonlinear relation of the form $[\boldsymbol{\theta}] = f(M)$ is to be integrated in transient computations.
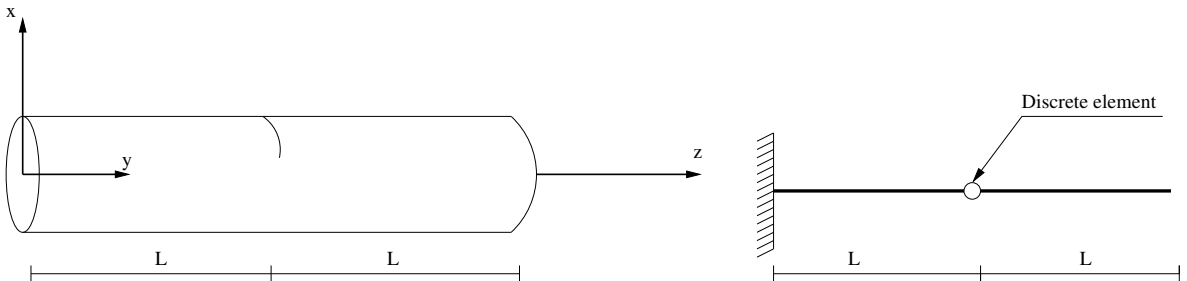
Figure 1. The cracked beam element modeling. Left: Three-dimensional model; right: beam model.

Andrieux and Varé [2002] introduced some properties of the additional strain energy due to the cracked section, $w([\boldsymbol{\theta}])$. Thus, w could be written as a quadratic function of the rotations jumps as

$$w([\theta_x], [\theta_y]) = \frac{EI}{4L} k(\varphi) \|[\boldsymbol{\theta}]\|^2, \quad \text{with } \varphi = \arctan \frac{[\theta_y]}{[\theta_x]}.$$

By using the Légendre–Fenchel transform to establish the relation between the two energy functions $w^*(\boldsymbol{M})$ and $w([\boldsymbol{\theta}])$, the stiffness function $k(\varphi)$ is obtained from the compliance function $s(\Phi)$ identified from three-dimensional calculus. As described in [Andrieux and Varé 2002], the behavior law is finally deduced from differentiation of $w([\boldsymbol{\theta}])$ with respect to $[\theta]$ as

$$\begin{pmatrix} M_x \\ M_y \end{pmatrix} = \frac{EI}{2L} \begin{pmatrix} k(\varphi) & -\frac{1}{2}k'(\varphi) \\ \frac{1}{2}k'(\varphi) & k(\varphi) \end{pmatrix} \begin{pmatrix} [\theta_x] \\ [\theta_y] \end{pmatrix}, \quad \text{with } k'(\varphi) = \frac{dk(\varphi)}{d\varphi}.$$

3. A cracked beam finite element construction

There are two procedures to introduce the local flexibility generated by a cracked section when dealing with the numerical integration of differential equations in dynamics. The first technique considers the construction of a stiffness matrix exclusively for the cracked section by computing the inverse of the flexibility matrix. However, for small cracks, the additional flexibility is very small and consequently the corresponding stiffness coefficient is extremely large leading to high numerical integration costs and convergence problems [El Arem 2006].

The second procedure, adopted here, consists of constructing a cracked finite element stiffness matrix which is later assembled with the other uncracked elements of the system. Thus, the elastic energy due to the cracks is distributed over the entire length of the cracked element. This method has been used in [Bachschmid et al. 2004b] and [Saavedra and Cuitino 2001].

The studies of Verrier and El Arem [2003], El Arem et al. [2003], Varé and Andrieux [2005], and El Arem [2006] showed that the shear effects on the breathing mechanism of the cracks is insignificant and will be neglected in this study.

Consider the cracked finite element of length $2L_e$, circular transverse section of diameter D and quadratic moment of inertia I; see Figure 2. First, we clamp all the displacements of node A and establish a relation of the form $\boldsymbol{u} = \mathcal{S}(\boldsymbol{f}) \cdot \boldsymbol{f}$, where $\boldsymbol{f} = \{T_{x_2}, T_{y_2}, M_{x_2}, M_{y_2}\}^t$ and $\boldsymbol{u} = \{u_{x_2}, u_{y_2}, \theta_{x_2}, \theta_{y_2}\}^t$ denote, respectively, the loading and displacements vectors at the end section ($z = 2L_e$), and $\mathcal{S}(\boldsymbol{f})$ represents
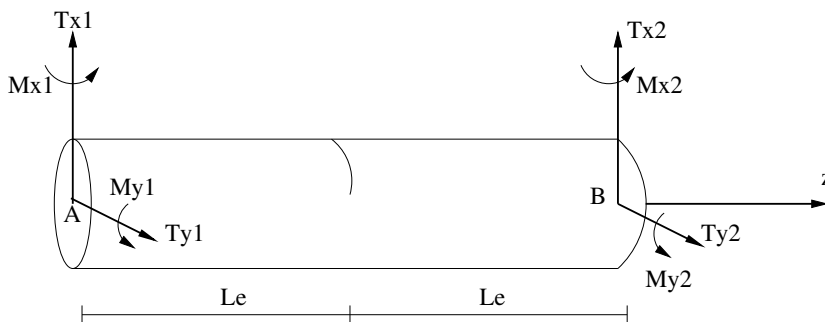

Figure 2. The cracked beam finite element.

the compliance matrix of the structure. At the cracked section $(z = L_e)$, the internal forces are given by

$$T_x = T_{x_2}, \quad T_y = T_{y_2}, \quad M_x = M_{x_2} - L_e T_y, \quad M_y = M_{y_2} + L_e T_x. \tag{2}$$

The breathing mechanism of the cracks is governed by the flexural moment direction $\Phi = \arctan(M_y/M_x)$ at the cracked section. The elastic energy of the cracked element could be written as

$$W^*(\boldsymbol{f}) = W_s^*(\boldsymbol{f}) + w^*(\boldsymbol{M}) = W_s^*(\boldsymbol{f}) + \frac{L}{EI}\|\boldsymbol{M}\|^2 s(\Phi), \tag{3}$$

where $W_s^*(\boldsymbol{f})$ denotes the elastic energy of the uncracked finite element of the same geometry and submitted to the same loading conditions. By using Equation (1), the additional elastic energy due to the cracked section is given by

$$w^*(\boldsymbol{M}) = \frac{L}{EI}\|\boldsymbol{M}\|^2 s(\Phi), \tag{4}$$

where L is the half length of the three-dimensional element used to identify the compliance function $s(\Phi)$ as described below. The nonlinear relation between the applied forces and the resulting displacements at the end section $(z = 2L_e)$ are obtained by differentiating W^* with respect to $\boldsymbol{f}$. Using (2), we get

$$\boldsymbol{u} = \mathcal{S}(\boldsymbol{f}) \cdot \boldsymbol{f} = \mathcal{S}(\Phi) \cdot \boldsymbol{f}, \tag{5}$$

where

$$\mathcal{S}(\Phi) = \mathcal{S}_0 + \frac{2L}{EI}\begin{pmatrix} L_e^2 s(\Phi) & -\frac{1}{2}L_e^2 s'(\Phi) & \frac{1}{2}L_e s'(\Phi) & L_e s(\Phi) \\ \frac{1}{2}L_e^2 s'(\Phi) & L_e^2 s(\Phi) & -L_e s(\Phi) & \frac{1}{2}L_e s'(\Phi) \\ -\frac{1}{2}L_e s'(\Phi) & -L_e s(\Phi) & s(\Phi) & -\frac{1}{2}s'(\Phi) \\ L_e s(\Phi) & -\frac{1}{2}L_e s'(\Phi) & \frac{1}{2}s'(\Phi) & s(\Phi) \end{pmatrix}.$$

Here $\mathcal{S}_0$ denotes the compliance matrix of an uncracked beam element of length $2L_e$. Let us consider $\{u_{B/A}\}$ the relative displacement of node B in relation to node A. It satisfies the relation

$$\{T_{x_2}, T_{y_2}, M_{x_2}, M_{y_2}\}^t = (\mathcal{S}(\Phi))^{-1}\{u_{B/A}\}. \tag{6}$$

From equilibrium conditions of the element of Figure 2, the internal forces in B can be expressed in terms of those in A as $T_{x_1} = -T_{x_2}$, $T_{y_1} = -T_{y_2}$, $M_{x_1} = -M_{x_2} + 2L_e T_{y_2}$, $M_{y_1} = -M_{y_2} - 2L_e T_{x_2}$, or, written in matrix form,

$$\{T_{x_1}, T_{y_1}, M_{x_1}, M_{y_1}, T_{x_2}, T_{y_2}, M_{x_2}, M_{y_2}\}^t = \boldsymbol{\Pi_1}\{T_{x_2}, T_{y_2}, M_{x_2}, M_{y_2}\}^t \tag{7}$$

with

$$\boldsymbol{\Pi_1} = \begin{pmatrix} -1 & 0 & 0 & 0 \\ 0 & -1 & 0 & 0 \\ 0 & 2L_e & -1 & 0 \\ -2L_e & 0 & 0 & -1 \\ 1 & 0 & 0 & 0 \\ 0 & 1 & 0 & 0 \\ 0 & 0 & 1 & 0 \\ 0 & 0 & 0 & 1 \end{pmatrix}. \tag{8}$$

In addition, writing $\{u_{B/A}\}$ as $\{u_{B/A}\} = \{u^1_{B/A}, u^2_{B/A}, u^3_{B/A}, u^4_{B/A}\}$, we obtain $u_{x_2} = u^1_{B/A} + u_{x_1} + 2L_e\theta_{y_1}$, $u_{y_2} = u^2_{B/A} + u_{y_1} - 2L_e\theta_{x_1}$, $\theta_{x_2} = u^3_{B/A} + \theta_{x_1}$, $\theta_{y_2} = u^4_{B/A} + \theta_{y_1}$, or, in a matrix form

$$\{u_{B/A}\} = \mathbf{\Pi_2}\{u_{x_1}, u_{y_1}, \theta_{x_1}, \theta_{y_1}, u_{x_2}, u_{y_2}, \theta_{x_2}, \theta_{y_2}\}^t, \tag{9}$$

where

$$\mathbf{\Pi_2} = \begin{pmatrix} -1 & 0 & 0 & -2L_e & 1 & 0 & 0 & 0 \\ 0 & -1 & 2L_e & 0 & 0 & 1 & 0 & 0 \\ 0 & 0 & -1 & 0 & 0 & 0 & 1 & 0 \\ 0 & 0 & 0 & -1 & 0 & 0 & 0 & 1 \end{pmatrix}. \tag{10}$$

Comparing with (8), we see that $\mathbf{\Pi_2} = \mathbf{\Pi_1^t}$. Moreover, the cracked beam finite element stiffness matrix $\mathbf{K_{ef}}$ satisfies

$$\{T_{x_1}, T_{y_1}, M_{x_1}, M_{y_1}, T_{x_2}, T_{y_2}, M_{x_2}, M_{y_2}\}^t = \mathbf{K_{ef}}\{u_{x_1}, u_{y_1}, \theta_{x_1}, \theta_{y_1}, u_{x_2}, u_{y_2}, \theta_{x_2}, \theta_{y_2}\}^t. \tag{11}$$

Substituting (7) into (11) gives

$$\mathbf{\Pi_1}\{T_{x_2}, T_{y_2}, M_{x_2}, M_{y_2}\}^t = \mathbf{K_{ef}}\{u_{x_1}, u_{y_1}, \theta_{x_1}, \theta_{y_1}, u_{x_2}, u_{y_2}, \theta_{x_2}, \theta_{y_2}\}^t. \tag{12}$$

Then, substituting (6) into (12) results in

$$\mathbf{\Pi_1}(\mathcal{S}(\Phi))^{-1}\{u_{B/A}\} = \mathbf{K_{ef}}\{u_{x_1}, u_{y_1}, \theta_{x_1}, \theta_{y_1}, u_{x_2}, u_{y_2}, \theta_{x_2}, \theta_{y_2}\}^t$$

Finally, using (9) leads to

$$\mathbf{K_{ef}} = \mathbf{\Pi_1}(\mathcal{S}(\Phi))^{-1}\mathbf{\Pi_1^t}. \tag{13}$$

In this relation, the stiffness matrix appears as depending on the applied moments represented by angle Φ. However, in a finite element code, it is preferable to express relation (13) as a function of the problem's unknowns, that is, the nodal displacements. By writing

$$(\mathcal{S}(\Phi))^{-1} = \mathcal{K}(\varphi_e) = \mathcal{K}_0 - \mathbf{K}_e(\varphi_e) \tag{14}$$

and using (13), we distinguish the stifness matrix of an uncracked element, $\mathbf{\Pi_1}\mathcal{K}_0\mathbf{\Pi_1^t}$, from the matrix modeling the cracked section, $\mathbf{\Pi_1}\mathbf{K}_e(\varphi_e)\mathbf{\Pi_1^t}$. Here φ_e is the angle given by

$$\varphi_e = \arctan\left(\frac{\theta_{y_2} - \theta_{y_1}}{\theta_{x_2} - \theta_{x_1}}\right) \quad \text{and} \quad \mathcal{K}_0 = \mathcal{S}_0^{-1} = \frac{EI}{2L_e(1+a)} \begin{pmatrix} \dfrac{3}{L_e^2} & 0 & 0 & -\dfrac{3}{L_e} \\ 0 & \dfrac{3}{L_e^2} & \dfrac{3}{L_e} & 0 \\ 0 & \dfrac{3}{L_e} & 4+a & 0 \\ -\dfrac{3}{L_e} & 0 & 0 & 4+a \end{pmatrix},$$

(see Lalanne and Ferraris [1990]) where $a = 12EI/(4\mu k SL_e^2)$ is the shearing effect coefficient. For an

Euler–Bernoulli beam element, a is zero. Equation (14) leads to

$$\mathbf{K_e}(\varphi_e) = \mathcal{K}_0 - (\mathcal{S}(\Phi))^{-1} = \frac{EI}{2L} \begin{pmatrix} 0 & 0 & 0 & 0 \\ 0 & 0 & 0 & 0 \\ 0 & 0 & k_{xx}(\varphi_e) & k_{xy}(\varphi_e) \\ 0 & 0 & k_{yx}(\varphi_e) & k_{yy}(\varphi_e) \end{pmatrix}, \tag{15}$$

where

$$k_{xx}(\varphi_e) = k_{yy}(\varphi_e) = \frac{L^2(4L_e s(\Phi) + 4Ls^2(\Phi) + Ls'^2(\Phi))}{L_e(4L_e^2 + 8LL_e s(\Phi) + 4L^2 s^2(\Phi) + L^2 s'^2(\Phi))},$$

$$k_{xy}(\varphi_e) = -k_{yx}(\varphi_e) = -\frac{2L^2 s'(\Phi)}{4L_e^2 + 8LL_e s(\Phi) + 4L^2 s^2(\Phi) + L^2 s'^2(\Phi)}.$$

When $L = L_e$, we obtain

$$k_{xx}(\varphi_e) = k_{yy}(\varphi_e) = \frac{4s(\Phi) + 4s^2(\Phi) + s'^2(\Phi)}{4 + 8s(\Phi) + 4s^2(\Phi) + s'^2(\Phi)}, \quad k_{xy}(\varphi_e) = -k_{yx}(\varphi_e) = -\frac{2s'(\Phi)}{4 + 8s(\Phi) + 4s^2(\Phi) + s'^2(\Phi)}.$$

Using the three-dimensional calculus conducted on the cracked element of Figure 1, we identify the compliance function $s(\Phi)$ as described previously. Then, we determine the stiffness matrix $\mathbf{K_e}(\varphi_e)$ terms by using relation (15).

We have noticed that $k_{xy}(\varphi_e) = -\frac{1}{2}k'_{xx}(\varphi_e)$. Thus, $\mathbf{K_e}(\varphi_e)$ can be written in the form

$$\mathbf{K_e}(\varphi_e) = \frac{EI}{2L} \begin{pmatrix} 0 & 0 & 0 & 0 \\ 0 & 0 & 0 & 0 \\ 0 & 0 & k_{xx}(\varphi_e) & -\frac{1}{2}k'_{xx}(\varphi_e) \\ 0 & 0 & \frac{1}{2}k'_{xx}(\varphi_e) & k_{xx}(\varphi_e) \end{pmatrix}.$$

For a straight crack of depth $a = D/2$, these terms are shown by Figure 3. We notice small variations in the interval $[0, \pi/2]$. However, in $[\pi/2, 2\pi]$, these variations becomes important but remain regular. The crack is totally closed when $\varphi_e = \pi/2$, image of $\Phi = \pi/2$. It opens totally at $\varphi_e = 3\pi/2$, the image of $\Phi = 3\pi/2$. Here Φ is the angle defined in Section 2 by $\Phi = \arctan(M_y/M_x)$.
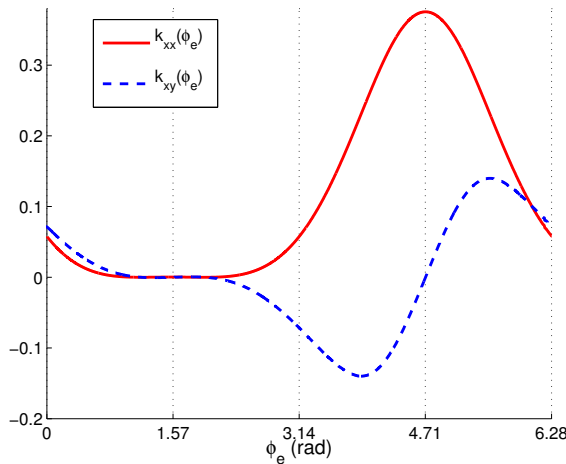

Figure 3. $\mathbf{K_e}(\varphi_e)$ terms for a straight crack of depth $a = D/2$, $L_e = L = 2D$.
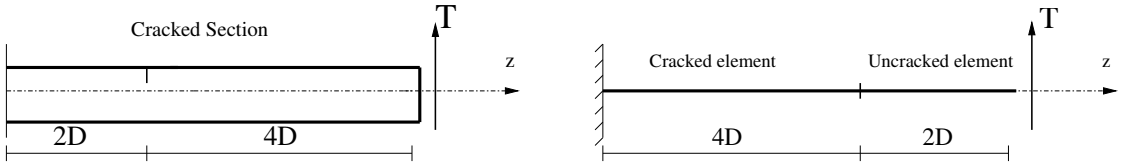
Figure 4. Three-dimensional and beam modeling of the system. Left: three-dimensional model; right: beam model.

4. Validation of the approach

In order to validate the stiffness beam finite element matrix construction method presented above, we propose to compare the three-dimensional modeling calculus results to those obtained using a beam modeling of the cracked structure of Figure 4. The cylinder element, of axis $0z$, diameter $D = 0.5$ m, and total length $L_t = 3$ m, is clamped at its end $z = 0$ and submitted at the other end to the force vector $\mathbf{T}$ ($T_x = \cos\alpha$, $T_y = \sin\alpha$), with $\alpha \in [0, 2\pi[$. The cracked section is located at $z = 1$ m. The crack is straight with depth $a = 0.5D$; see Figure 4, left. The three-dimensional finite element calculus take into account the unilateral contact conditions between the crack lips. The beam model consists of two beam finite elements: the first is a cracked beam finite element of length 2 m, and the second is a classic beam finite element of length 1 m (Figure 4, right). Figure 5 shows excellent agreement for the results.
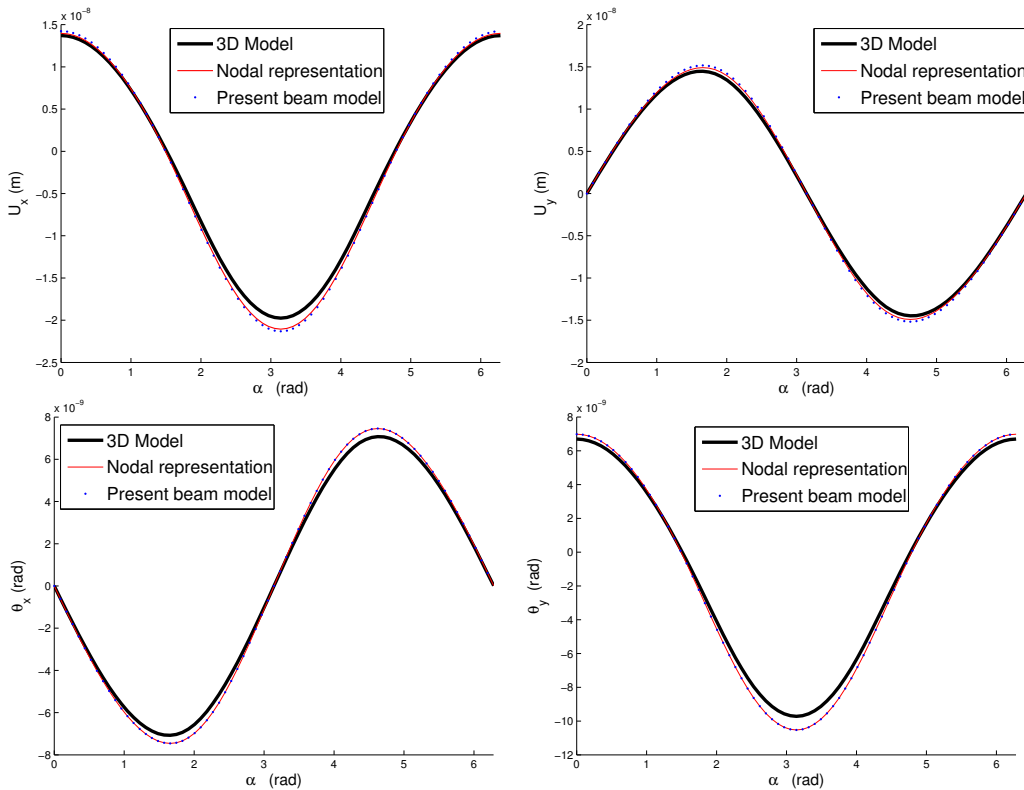
**Figure 5.** Model comparison to three-dimensional results and nodal modeling, $a/D = 0.50$.

5. Vibratory response of a cracked shaft

This section is devoted to exploring the vibratory response of a shaft with a cracked section under the effect of own weight. The system is composed of a beam of distributed mass m, circular section S, and diameter $D = 0.20$ m. The cracked section is located at mid-span. The structure is simply supported at node 1 and node 6 and submitted to the effects of its own weight. The shaft is rotating at the frequency Ω about the (oz) axis. The system is divided into five elements of length $l = 4D$; see Figure 6. The elements 1–2, 2–3, 4–5 and 5–6 represent the structure's uncracked parts. Element 3–4 is a cracked beam finite element.

At $t = 0$, the crack is totally open; see Figure 6, right. We suppose that the stiffness matrix remains constant between two instants $t_n = nh$ and $t_{n+1} = (n+1)h$, where h is the time step used for the numerical integration of the dynamical system. For the validity of this approximation, the time steps should be relatively small compared to the excitation period $(1/\Omega)$. In the low frequency domain, this difficulty is easily overcome. Thus, the stiffness matrix is updated at the end of each integration step. The HHT method is adopted for the numerical integration of the obtained system [Hilber et al. 1977] with $\alpha = \frac{1}{3}$, $\gamma = \frac{1}{2} + \alpha$, and $\beta = \frac{1}{4}(1+\alpha)^2$ which corresponds, in the linear analysis, to an unconditionally stable scheme with maximum precision.

With this modeling, the unilateral contact conditions between the crack lips are taken into account exactly. In fact, when the crack is totally closed, we obtain $\mathbf{K_e}(\varphi_e) = \mathbf{0}$ and the cracked element stiffness matrix is the one of an uncracked element. Furthermore, the time step used here is $\sim 10^{-3}$ s, which is at least 20 to 100 times smaller than the ones used for a penalization-implicit approach when the cracked section is modeled by a nodal element (element of length zero). In this later approch, the time step depends on the value given to the penalization constant and it is always less than $\sim 10^{-5}$ s to ensure calculus convergence.

The vibratory response shows superharmonic resonance phenomena when the rotating frequency passes through submultiples of the critical speed w_1; that is, for $\xi \approx w_1/n$, the shaft orbit and the phase diagram are composed of n interlaced loops (see Figure 7, where the viscous damping d is 5%). The vibration amplitude of the n-fold harmonic reaches higher levels at this rotating frequency (Figure 8).
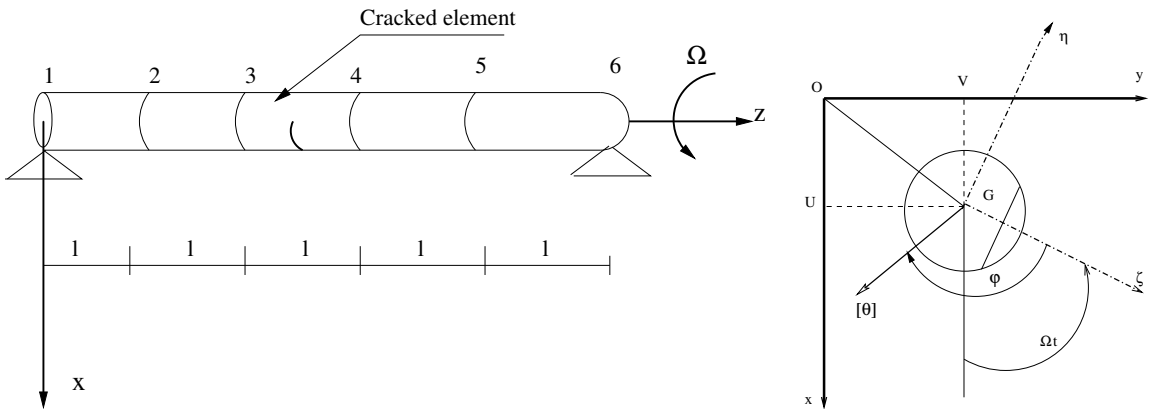
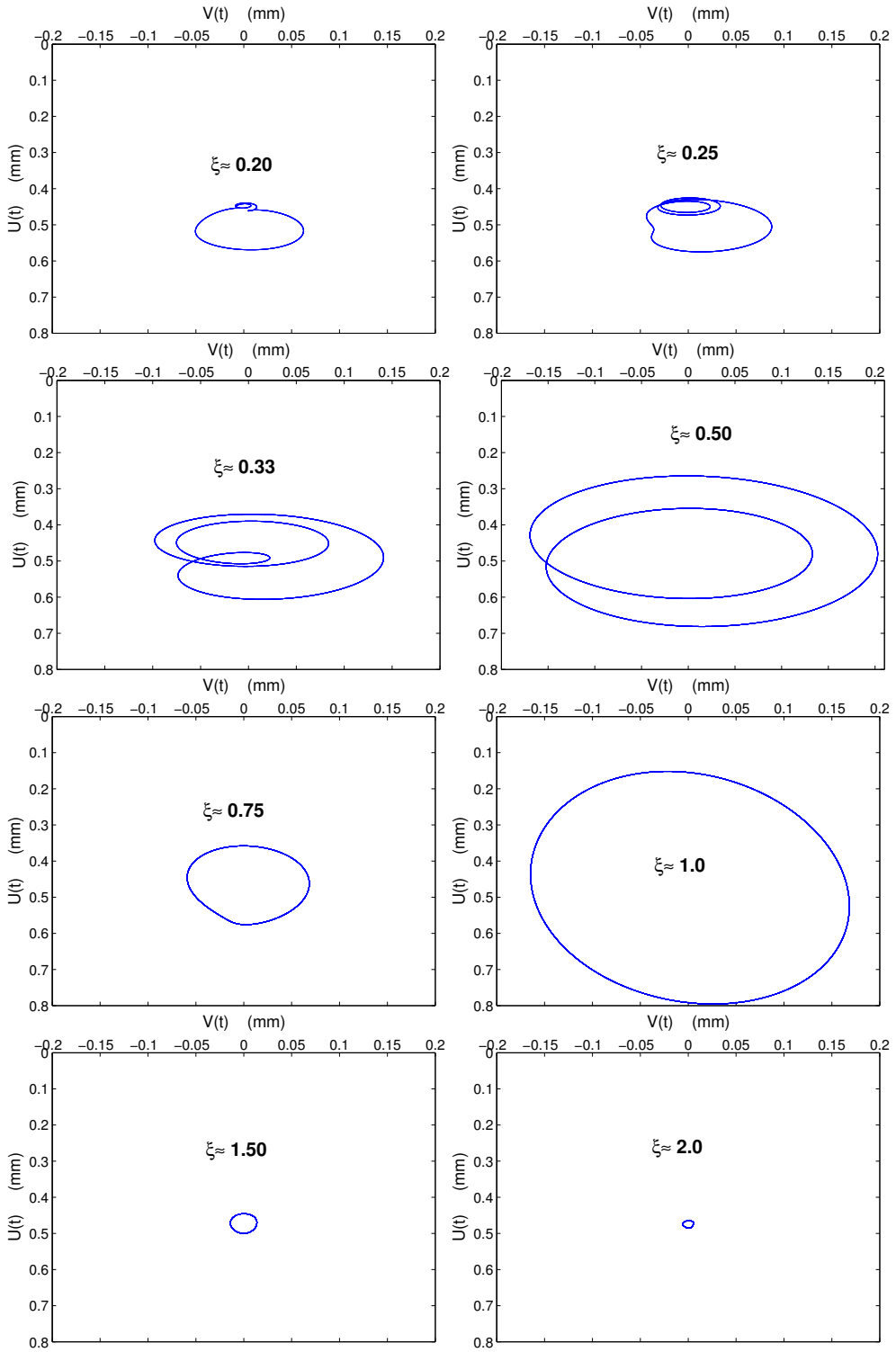**Figure 6.** Finite element modeling of the cracked shaft (left) and the cracked section (right).
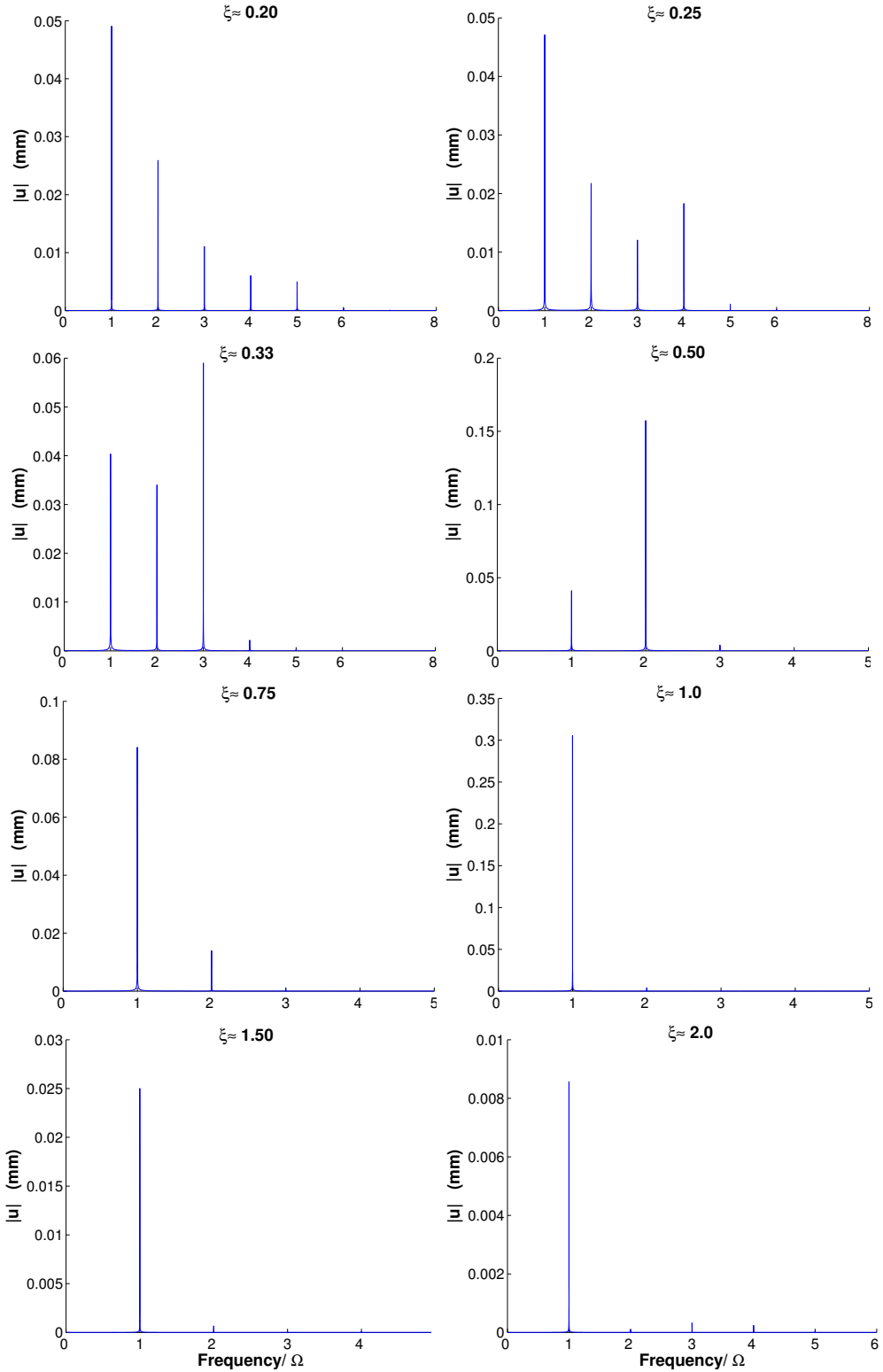
Figure 7. Examples of node 2 orbits, $a/D = 0.50$, $d = 0.05$.

Figure 8. Examples of node 3 $u(t)$ amplitude spectra, $a/D = 0.50$, $d = 0.05$.

6. Stability analysis

The stability of a cracked shaft is analyzed using the Floquet method [Floquet 1879; Nayfeh and Mook 1979; Nayfeh and Balachandran 1994]. This method was used by Gasch [1976], Meng and Gasch [2000], and El Arem and Nguyen [2006] for the stability analysis of a two parameter cracked rotating shaft. The first step of this section consists of approximating the $\mathbf{K_e}(\varphi_e)$ terms by a classical function of the crack depth a and angle φ_e. We have noticed that the function $k_{xx}(\varphi_e)$ for different straight tip crack depths shows that it could be approximated by

$$k_{xx}(\varphi_e) \approx k_{max} \sin^4\left(\frac{\varphi_e}{2} - \frac{\pi}{4}\right) \exp\left(\sin\left(\frac{\varphi_e}{2} - \frac{\pi}{4}\right)\right)^4,$$

where k_{max} is given by $k_{max} \approx 3.43(a/D)^{2.73}$. These approximations remain satisfactory for cracks of depth going up to 30% of the diameter of the shaft; see Figure 9.

By using the Floquet theory, we have investigated, numerically, the stability of a cracked rotating shaft with a straight tip crack at mid-span; see Figure 6. The results, shown in Figure 10, show three principal areas of instability. The first corresponds to a $(0 < \xi < 0.5)$ superharmonic resonance phenomenon. The second is located around the exact resonance $(\xi = 1)$ and the third area (around $\xi = 2$) corresponds to a subharmonic resonance. It is important to note that even for weak viscous damping $(d \approx 1\%)$ the stability of the cracked shaft is only slightly affected. The zones of instabilities appear for Ω near the first critical speed $(\xi \approx 1)$ and twice the critical speed $(\xi \approx 2)$ and correspond to deep cracks $(\frac{a}{D} > 25\%)$.

7. Conclusions

A method for the construction of a cracked beam finite element is presented. The crack breathing phenomenon is finely described since the flexibility due to the presence of the cracks is deduced from three-dimensional finite element calculations taking into account the conditions of unilateral contact between
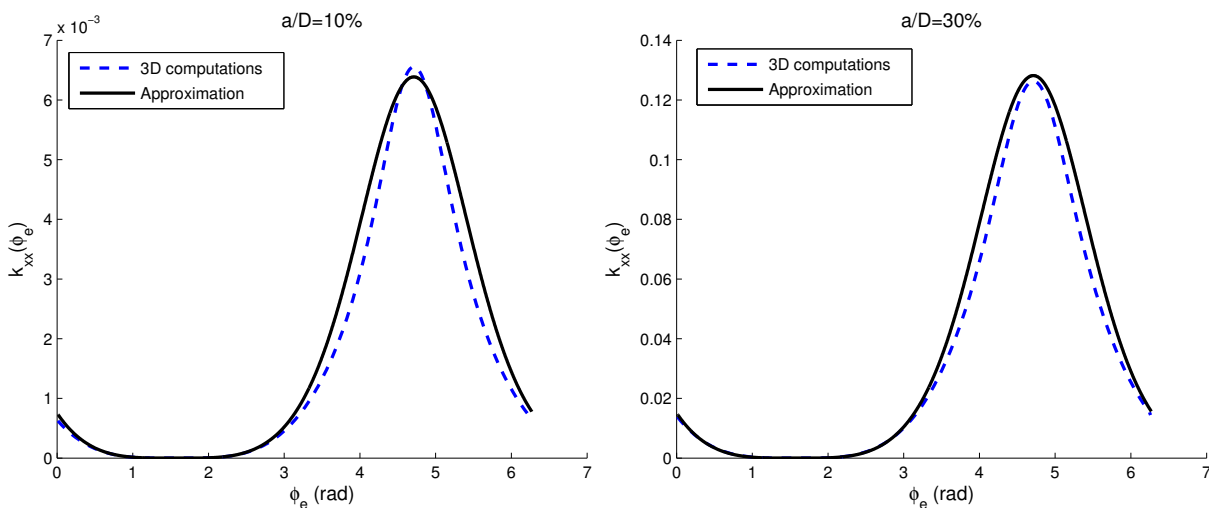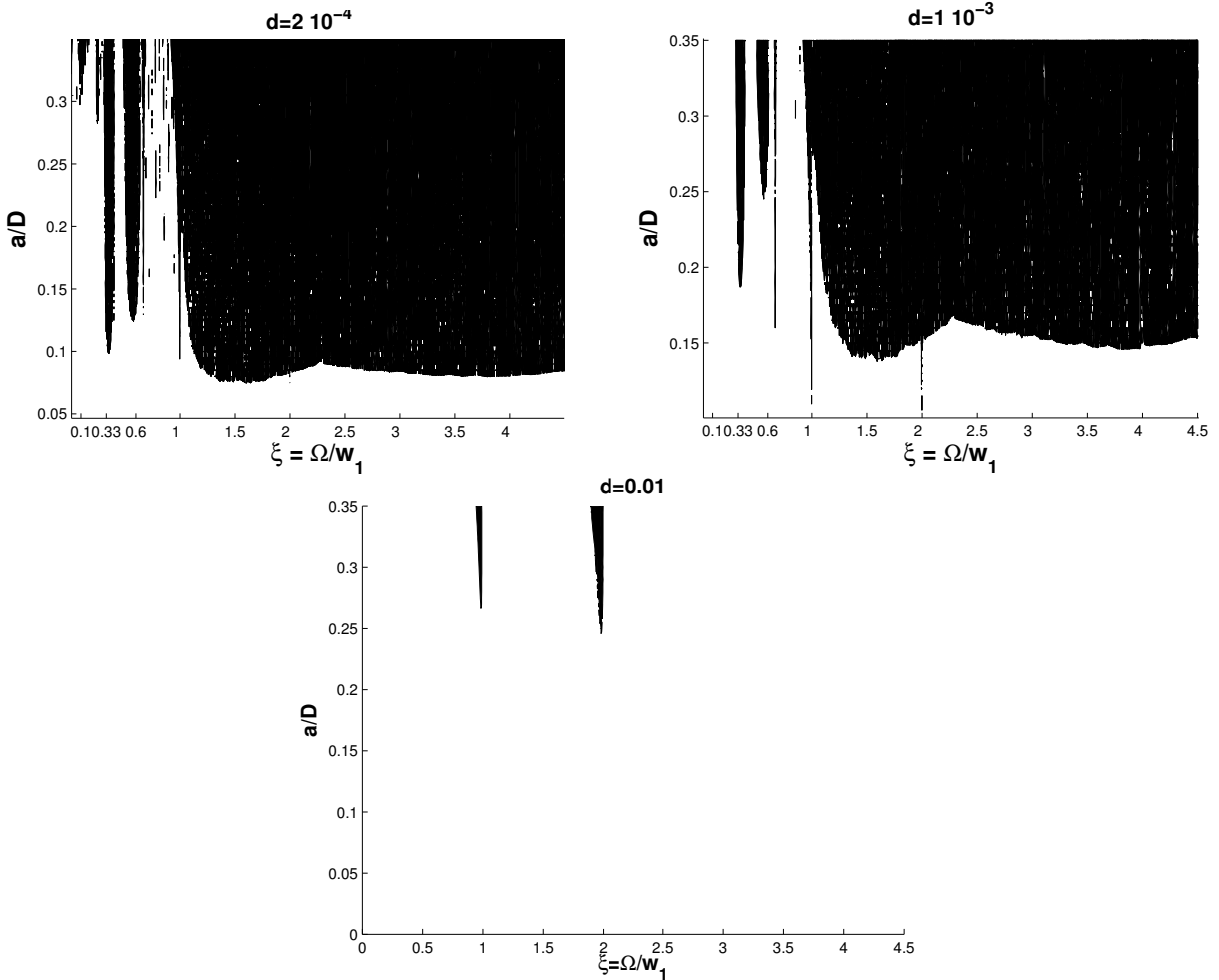

Figure 9. $k_{xx}(\varphi_e)$ approximation for different straight crack depths.

Figure 10. Stable and unstable (hatched) regions.

the crack lips as originally developed by Andrieux and Varé [2002]. The precise descriptions of the loss of stiffness and of the progressive closure or opening of the cracks are of fundamental importance.

The approach is quite simple and comprehensive and can be applied to any geometry of cracks. It is important to note the considerable gain in computational efforts when compared with the use of the technique of penalization.

Indeed this technique, when used when the cracked section is modeled by a nodal element [El Arem 2006], leads to the appearance of very high numerical frequencies (without physical significance). The time steps considered for the temporal numerical integration of the dynamic system are then very small and the computation costs are, consequently, very important. When considering the conditions of contact between the crack lips, this model has the following advantages compared to the nodal representation of the cracked section and the technique of penalization:

- It takes into account in an exact way the phenomenon of cracks breathing mechanism.
- It reduces the calculation costs by 20 to 100 times.

To reduce the difficulty of the problem in the study of cracked shafts, researchers often assumed that the amplitude of the vibrations due to the presence of cracks is weak compared to those of the vibrations due to permanent loads [El Arem and Nguyen 2006; Gasch 1976; Mayes and Davies 1976; 1980; Davies and Mayes 1984; Henry and Okah-Avae 1976; Gasch 1993]. The present model is more general and allows us to overcome the limitations of such an assumption.

The stability analysis of the cracked shaft of Figure 6 was carried out using the Floquet theory. Figure 10 shows stable and unstable zones in the $(\xi, a/D)$ plane for different viscous damping coefficients. We have noticed that the instability zones disappear for $d \geq 3\%$. For real turbines shafts, where the viscous damping is about 3% to 4% [Lalanne and Ferraris 1990], it can be deduced that the effects of a cracked section at mid-span on the stability of the structure is negligible when a/D is less than 35% .

Acknowledgements

References

[Abraham et al. 1994] O. N. L. Abraham, J. A. Brandon, and A. M. Cohen, "Remark on the determination of compliance coefficients at the crack section of a uniform beam with circular cross section", *J. Sound Vib.* **169**:2 (1994), 570–574.

[Andrieux 2000] S. Andrieux, "Détermination de la loi de comportement en flexion bi-axée d'une poutre fissurée avec prise en compte du contact sur les fissures", rapport interne HP-50/99/018/A, EDF-DER, 2000.

[Andrieux and Varé 2002] S. Andrieux and C. Varé, "A 3D cracked beam model with unilateral contact: Application to rotors", *European Journal of Mechanics, A/Solids* **21** (2002), 793–810.

[Anifantis and Dimarogonas 1983] N. Anifantis and A. D. Dimarogonas, "Identification of peripheral cracks in cylindrical shells", pp. Paper 83–WA/DE–14 in *ASME Winter Annual Meeting* (Boston), 1983.

[Audebert and Voinis 2000] S. Audebert and P. Voinis, "Comportement dynamique de rotors avec fissuration transverse: modélisation et validation expérimentale", in *13ème colloque vibrations, chocs et bruits* (Lyon, France), 2000.

[Bachschmid and Pennacchi 2008] N. Bachschmid and P. Pennacchi, "Crack effects in rotordynamics", *Mechanical Systems and Signal* **22**:4 (2008), 761–762.

[Bachschmid et al. 1984] N. Bachschmid, N. Diana, and B. Pizzigoni, "The influence of unbalance on cracked rotors", pp. 193–198 in *3rd international conference on vibrations in rotating machinery*, Institution of Mechanical Engineers, London, 1984.

[Bachschmid et al. 2002] N. Bachschmid, P. Pennacchi, and A. Vania, "Identification of multiple faults in rotor systems", *Journal of Sound and Vibration* **254**:2 (2002), 327–366.

[Bachschmid et al. 2004a] N. Bachschmid, P. Pennacchi, E. Tanzi, and S. Audebert, "Transverse crack modeling and validation in rotor systems including thermal effects", *Int. J. of Rotat. Mach.* **10**:4 (2004), 253–263.

[Bachschmid et al. 2004b] N. Bachschmid, P. Pennacchi, E. Tanzi, and A. Vania, "Cracks in rotating shafts: experimental behaviour, modelling and identification", in *SURVEILLANCE 5: Fifth international conference on acoustical and vibratory surveillance methods and diagnostic techniques* (Senlis, France), 2004.

[Bently and Muszynska 1986] D. E. Bently and A. Muszynska, "Detection of rotor cracks", pp. 129–39 in *Proceedings of the 15th Turbomachinery Symposium* (Corpus Christi, TX), Texas A&M University, Texas, 1986.

[Bueckner 1958] H. F. Bueckner, "The propagation of cracks and the energy of elastic deformation", *Trans. ASME* **80** (1958), 1225–1229.

[Bui 1978] H. D. Bui, *Mécanique de la rupture fragile*, Masson, Paris, 1978.

[Darpe et al. 2004] A. K. Darpe, K. Gupta, and A. Chawla, "Transient response and breathing behaviour of a cracked Jeffcott rotor", *J. Sound Vib.* **272** (2004), 207–243.

[Davies and Mayes 1984] W. G. R. Davies and I. W. Mayes, "The vibrational behaviour of multi-shaft, multi-bearing system in the presence of the propagating transverse crack", *J. Vib. Acous. Stress Reliab. Design* **106** (1984), 146–153.

[Dimarogonas 1970] A. D. Dimarogonas, "Dynamic response of cracked rotors", Internal report, General Electric Co., Schenectady NY, 1970.

[Dimarogonas 1971] A. D. Dimarogonas, "Dynamics of cracked shafts", Internal report, General Electric Co., Schenectady NY, 1971.

[Dimarogonas 1982] A. D. Dimarogonas, "Crack identification in aircraft structures", pp. 11–22 in *First national aircraft conference*, Athens, 1982.

[Dimarogonas 1987] A. D. Dimarogonas, *EXPERTS: A fuzzy logic neutral network structured expert system shell for diagnosis and prognosis — user's manual*, Clayton Laboratories, St Louis, MO, 1987.

[Dimarogonas 1988] A. D. Dimarogonas, *RODYNA: A general purpose rotor dynamic analysis program — user's manual*, Clayton Laboratories, St Louis, MO, 1988.

[Dimarogonas 1994] A. D. Dimarogonas, "Author's reply", *J. Sound and Vibration* **169** (1994), 575–576.

[Dimarogonas 1996] A. D. Dimarogonas, "Vibration of cracked structures: A state of the art review", *Engineering Fracture Mechanics* **55**:5 (1996), 831–857.

[Dimarogonas and Paipetis 1983] A. D. Dimarogonas and S. A. Paipetis, *Analytical methods in rotor dynamics*, Applied Science Publishers, 1983.

[El Arem 2006] S. El Arem, *Vibrations non-linéaires des structures fissurées: application aux rotors de turbines*, Ph.D. thesis, Ecole Nationale des Ponts et Chaussées, 2006.

[El Arem and Maitournam 2007] S. El Arem and H. Maitournam, "Un élément fini de poutre fissurée: application à la dynamique des arbres tournants", *European Journal of Computational Mechanics* **16**:5 (2007), 643–663.

[El Arem and Nguyen 2006] S. El Arem and Q. S. Nguyen, "A simple model for the dynamical behavior of a cracked rotor", pp. 393–398 in *Advances in Geomaterials and Structures*, Hammamet, 2006.

[El Arem et al. 2003] S. El Arem, S. Andrieux, C. Varé, and P. Verrier, "Loi de comportement en flexion d'une section de poutre fissurée avec prise en compte des effets de cisaillement", pp. 223–230 in *6ème colloque nationale en calcul des structures*, vol. II, Giens, 2003.

[Entwistle and Stone 1990] R. D. Entwistle and B. J. Stone, "Survey of the use of vibration methods in the assessment of component geometry", *Vib. and Noise Meas. Pred. and Cont., Inst. engineers, Australia* **90** (1990), 210–217.

[Floquet 1879] G. Floquet, "Sur les équations différentielles linéaires à coefficients périodiques", *Ann. Scien. Ecole Nor. Sup. 2ème série* (1879), 3–132.

[Friswell and Penny 2002] M. I. Friswell and J. E. T. Penny, "Crack modelling for structural health monitoring", *International Journal of Structural Health Monitoring* **1**:2 (2002), 139–148.

[Gasch 1976] R. Gasch, "Dynamical behavior of a simple rotor with a cross-sectional crack", pp. 123–128 in *Vibrations in rotating machinery*, I. Mech. E. Conference, London, 1976.

[Gasch 1993] R. Gasch, "A survey of the dynamic behavior of a simple rotating shaft with a transverse crack", *J. Sound and vibration* **160** (1993), 313–332.

[Gross and Srawley 1964] B. Gross and J. E. Srawley, "Stress intensity factors for a single-edge-notch tension specimen by boundary collocation of a stress function", Tech. Note D-2395, NASA, 1964.

[Gross and Srawley 1965] B. Gross and J. E. Srawley, "Stress intensity factors for a single-edge-notch specimen in bending or combined bending and tension by boundary collocation of a stress function", Tech. Note D-2603, NASA, 1965.

[Gudmundson 1982] P. Gudmundson, "Eigenfrequency changes of structures due to cracks, notches or other geometrical changes", *J. Mech. Phys. Solids* **30**:5 (1982), 339–353.

[Gudmundson 1983] P. Gudmundson, "The dynamical behavior of slender structures with cross-sectional cracks", *J. Mech. Phys. Solids* **31** (1983), 329–345.

[Henry and Okah-Avae 1976] T. A. Henry and Okah-Avae, "Vibrations in cracked shafts", pp. 15–19 in *Vibrations in rotating machinery*, Inst. Mech. E. Conference, London, 1976.

[Hilber et al. 1977] H. M. Hilber, T. J. R. Hughes, and R. L. Taylor, "Improved numerical dissipation for time integration algorithms in structural dynamics", *Earthquake Engneering and Structural Dynamics* **5** (1977), 283–293.

[Irwin 1957a] G. R. Irwin, "Analysis of stresses and strains near the end of a cracktraversing a plate", *J. App. Mech.* **24** (1957), 361–364.

[Irwin 1957b] G. R. Irwin, "Relation of stresses near a crack to the crack extension force", in *Proc. 9th Cong. App. Mech.* (Brussels, 1956), 1957.

[Jun et al. 1992] O. S. Jun, H. J. Eun, Y. Y. Earmme, and C. W. Lee, "Modelling and vibration analysis of a simple rotor with a breathing crack", *J. Sound and Vibration* **155**:2 (1992), 273–290.

[Lalanne and Ferraris 1990] M. Lalanne and G. Ferraris, *Rotordynamics Prediction in Engineering*, John Wiley & Sons, England, 1990.

[Mayes and Davies 1976] I. W. Mayes and W. G. R. Davies, "The vibrational behaviour of a rotating shaft system containing a transverse crack", pp. 53–65 in *Vibrations in rotating machinery*, Inst. Mech. E. Conference, London, 1976.

[Mayes and Davies 1980] I. W. Mayes and W. G. R. Davies, "A method of calculating the vibrational behaviour of coupled rotating shafts containning a transverse crack", pp. 17–27 in *Vibrations in rotating machinery*, Inst. Mech. E. Conference, London, 1980.

[Meng and Gasch 2000] G. Meng and R. Gasch, "Stability ans stability degree of a cracked flexible rotor supported on journal bearings", *J. Vibration and Acoustics, Transactions of ASME* **122** (2000), 116–125.

[Nayfeh and Balachandran 1994] A. H. Nayfeh and B. Balachandran, *Applied nonlinear dynamics*, Wiley series in nonlinear science, 1994.

[Nayfeh and Mook 1979] A. H. Nayfeh and D. T. Mook, *Nonlinear oscillations*, John Wiley & Sons, 1979.

[Ostachowicz and Krawwczuk 1992] W. M. Ostachowicz and M. Krawwczuk, "Coupled torsional and bending vibrations of a rotor with an open crack", *Arch. App. Mech.* **62** (1992), 191–201.

[Pafelias 1974] T. Pafelias, "Dynamic response of a cracked rotor", Technical Information Series DF-74-LS-79, General Electric Co., 1974.

[Papadopoulos 2004] C. A. Papadopoulos, "Coupling of bending and torsional vibration of a cracked Timoshenko beam", *J. Sound and Vibration* **278** (2004), 1205–1211.

[Papadopoulos and Dimarogonas 1987a] C. A. Papadopoulos and A. D. Dimarogonas, "Coupled longitudinal and bending vibrations of a rotating shaft with an open crack", *J. Sound vibration* **117** (1987), 81–93.

[Papadopoulos and Dimarogonas 1987b] C. A. Papadopoulos and A. D. Dimarogonas, "Coupling of bending and torsional vibration of a cracked Timoshenko beam", *Ing. Arch.* **57** (1987), 496–505.

[Papadopoulos and Dimarogonas 1987c] C. A. Papadopoulos and A. D. Dimarogonas, "Stability of cracked rotors in the coupled vibration mode", pp. 25–34 in *ASME-11th Bien. Conf. Mech. Vib. Noise*, Boston, Mass., USA, 1987.

[Rice and Levy 1972] J. R. Rice and N. Levy, "The part-through surface crack in an elastic plate", *J. App. Mech.* **39** (1972), 185–194.

[Saavedra and Cuitino 2001] P. N. Saavedra and L. A. Cuitino, "Crack detection and vibrational behavior of cracked beams", *Comput. Struct.* **79** (2001), 1451–1459.

[Sinou and Lees 2005] J. J. Sinou and A. W. Lees, "The influence of cracks in rotating shafts", *J. Sound Vib.* **285** (2005), 1015–1037.

[Sinou and Lees 2007] J. J. Sinou and A. W. Lees, "A non-linear study of a cracked rotor", *European Journal of Mechanics-A/Solids* **26** (2007), 152–170.

[Tada et al. 1973] H. Tada, P. Paris, and G. Irwin, *The stress analysis of cracks handbook*, Del Research Corporation, Hellertown, PA, 1973.

[Varé and Andrieux 2000] C. Varé and S. Andrieux, "Modélisation d'une section de poutre fissurée-Application aux rotors de turbine", *Revue Française de Mécanique* **2000**:2 (2000), 91–97.

[Varé and Andrieux 2005] C. Varé and S. Andrieux, "Modélisation d'une section de poutre fissurée en flexion: prise en compte des efforts tranchants", pp. 29–34 in *7ème colloque nationale en calcul des structures*, vol. II, Giens, 2005.

[Verrier and El Arem 2003] P. Verrier and S. El Arem, "Calcul d'un modèle de rotor fissuré avec prise en compte de l'effort tranchant-cas de la flexion plane", rapport interne HT-65/03/009/A, EDF-DER, 2003.

[Wauer 1990] J. Wauer, "On the dynamics of cracked rotors: A literature survey", *Applied Mechanical Reviews* **43**:1 (1990), 13–17.

[Westmann and Yang 1967] R. A. Westmann and W. H. Yang, "Stress analysis of cracked rectangular beams", *J. App. Mech.* **32** (1967), 639–701.

[Zuo 1992] L. Zuo, *Etude du comportement dynamique des systèmes linéaires par morceaux- contribution à la détection des fissures dans les arbres de machines tournantes*, Ph.D. thesis, EPFL, 1992.

[Zuo and Curnier 1994] L. Zuo and A. Curnier, "Nonlinear real and complex modes of conewise linear systems", *J. Sound and Vib.* **174**:3 (1994), 289–313.

SABER EL AREM: saber.el-arem@polytechnique.edu
Laboratoire de Mécanique des Solides CNRS (UMR 7649), Ecole Polytechnique, 91128 Palaiseau Cedex, France

HABIBOU MAITOURNAM: maitournam@lms.polytechnique.fr
Laboratoire de Mécanique des Solides CNRS (UMR 7649), Ecole Polytechnique, 91128 Palaiseau Cedex, France
http://www.lms.polytechnique.fr/annuaire_nom.php?id=49

ANISOTROPY IN HYPOELASTIC SOFT-TISSUE MECHANICS, I: THEORY

Alan David Freed

A hypoelastic constitutive theory is derived with an eye towards modeling the passive response of soft anisotropic biological tissues. Anisotropy is handled through a material tensor whose construction is independent of the constitutive formulation. Anisotropy tensors are provided for tissues that have a single dominant fiber family with an elliptic fiber projection onto the transverse plane, and their limiting cases. The tissue is comprised of two constituents: a matrix phase and a fiber phase. The theory is derived in the polar configuration, for ease of handling the derivatives, and then mapped into the commonly used Eulerian configuration. Kirchhoff stress and its conjugate strain-rate are the state variables.

1. Introduction

In a landmark paper for the field of biomechanics, Fung [1967] empirically fit the tensile load-deflection curve of rabbit mesentery with the linear, first-order, differential equation

$$\frac{d\sigma}{d\lambda} = \alpha + \beta\sigma \quad \text{or equivalently} \quad \frac{d\sigma}{dt} = (\alpha + \beta\sigma)\frac{d\lambda}{dt}, \tag{1}$$

where σ denotes stress, λ denotes stretch, and α and β represent material constants. This is Fung's law. The second formula, which follows from the first via the chain rule, is in the format of a hypoelastic constitutive equation. Although originally expressed as a differential equation, Fung's law is almost always referred to in its integrated form

$$\sigma = \frac{\alpha}{\beta}(e^{\beta\epsilon} - 1), \tag{2}$$

where $\epsilon = \lambda - 1$ denotes strain.

Since then, numerous constitutive formulae have been put forward by various researchers in the field of biomechanics in an effort to extend Fung's one-dimensional law to three dimensions; see Fung's textbook [1993] and the literature reviews [Humphrey 2002; Sacks 2000; Viidik 1973; Weiss and Gardiner 2001]. These three-dimensional theories have been derived as hyperelastic constitutive expressions, in spite of the fact that Fung's original one-dimensional formulation was hypoelastic in construction [Fung 1967]. Even Fung's own three-dimensional extension of Equation (1) was a hyperelastic theory [Fung 1973], that is,

$$\sigma_{ij} + pI_{ij} = C'_{ijkl}\epsilon_{kl} + \exp(aJ_1 + bJ_2)C_{ijkl}\epsilon_{kl}, \tag{3}$$

where σ_{ij} are components of stress, ϵ_{ij} are components of strain, J_1 and J_2 are the first and second strain invariants, a and b are constants, C'_{ijkl} and C_{ijkl} are elastic moduli, and p is a Lagrange multiplier that forces an isochoric response. The only nonhyperelastic theory that has been put forward for soft

tissues was derived by Criscione et al. [2003a], where hyper- and hypoelastic models were combined to describe glutaraldehyde fixed bovine pericardial sacs [Criscione et al. 2003b]. They demonstrated that a hyperelastic material model, alone, is not capable of describing this tissue, because the work done *does* depend upon the path taken.

A *hyperelastic material* defines stress through some potential function in strain or deformation [Ogden 1984]. This potential function has its origin in thermodynamics and produces a theory where the value of stress depends only on the current state of strain and not on the path traversed to reach that state. A *hypoelastic material* defines stress-rate as some *linear* function of strain-rate [Truesdell 1955], where various objective rates have been used in the literature. Hypoelastic materials have the potential of reaching states of stress that do depend upon the path of strain taken. Noll (see Truesdell [1955]) proved a theorem that states: "Every isotropic elastic body is also an isotropic hypoelastic body." Hypoelasticity is therefore a generalization of hyperelasticity. In contrast, Criscione et al. [2003a] state: "Together they (hyperelasticity and hypoelasticity) define all elastic-type relations, yet they are mutually exclusive." Obviously, these two statements are inconsistent. The word *hypoelastic* is being used differently in these manuscripts. We will use the term *hypoelastic* in the sense of Truesdell.

This paper provides a rational extension of Fung's law (1) through an application of Truesdell's hypoelastic theory [1955] to a class of anisotropic materials that potentially includes soft biological tissues. The theory is also novel in the method by which anisotropy is introduced into it and by the choice of strain rate that is used as its independent variable.

1.1. *Preliminaries.*

Scalars are typeset in italics, for example, y. Vectors are typeset in lower-case bold italics, for example, $y = y_i e_i$. And tensors are typeset in upper-case bold italics, for example, $Y = Y_{ij} e_i \otimes e_j$, wherein $\otimes$ signifies a tensor product. Components y_i and Y_{ij} are also typeset in italics, and they are quantified in a rectangular Cartesian basis $\{e_1, e_2, e_3\}$. Exceptions to this notation are minimal, but they do arise, both from the use of conventional notations and from the need to introduce multiple variables of similar nature. Components map from one set of coordinates $\{e_1, e_2, e_3\}$ into another set of coordinates $\{\tilde{e}_1, \tilde{e}_2, \tilde{e}_3\}$ according to the transformation rules $\tilde{y}_i = Q_{ia} y_a$ and $\tilde{Y}_{ij} = Q_{ia} Q_{jb} Y_{ab}$ with $Q_{ik} Q_{jk} = Q_{ki} Q_{kj} = \delta_{ij}$, where δ_{ij} is the Kronecker delta function. Repeated indices are summed from 1 to 3 in accordance with Einstein's summation convention.

The identity tensor $I = \delta_{ij} e_i \otimes e_j = e_i \otimes e_i$ maps vectors into themselves, for example, $y = I \cdot y$ with the dot denoting a contraction over a pair of indices such that $y_i = \delta_{ij} y_j$. Dot notation is used whenever two vectors are contracted together, for example, when defining the vector norm $\|y\|_2^2 = y \cdot y = y_i y_i$. However, dot notation is suppressed whenever a tensor contracts with a vector, for example, $y = I y$, or whenever two tensors are contracted together, for example, $Y Z = Y_{ik} Z_{kj} e_i \otimes e_j$. Here contractions are implicit.

The tensor $Y = Y_{ij} e_i \otimes e_j$ has a transpose $Y^T = Y_{ji} e_i \otimes e_j$ and an inverse $Y^{-1} = Y_{ij}^{-1} e_i \otimes e_j$, whenever it exists, such that $Y Y^{-1} = Y^{-1} Y = I$ where $Y_{ij}^{-1} \neq (Y_{ij})^{-1}$. The symmetric tensor operator, $\text{sym } Y = \frac{1}{2}(Y_{ij} + Y_{ji}) e_i \otimes e_j$, and the antisymmetric tensor operator, $\text{skew } Y = \frac{1}{2}(Y_{ij} - Y_{ji}) e_i \otimes e_j$, satisfy $Y = \text{sym } Y + \text{skew } Y$. The trace operator $\text{tr } Y = Y_{ii}$ is the diagonal sum. And, from of the Cayley-Hamilton theorem, the determinant obeys the identity $\det Y = \frac{1}{3}(\text{tr } Y^3 - \frac{3}{2} \text{tr } Y \text{tr } Y^2 + \frac{1}{2}(\text{tr } Y)^3)$.

Any modern textbook that addresses the mechanics of continuous media can be used as a reference. A particularly good text has been written by Holzapfel [2000].

2. Kinematics

Consider a mass point in a Cartesian coordinate frame $(1, 2, 3)$ with unit vectors $\{e_1, e_2, e_3\}$ whose original location in some reference configuration κ_0 affiliated with time $t = 0$, say, is given by a position vector $X = X_i e_i$. Let its current location in configuration κ, which is affiliated with time t, be given by another position vector $x = x_i e_i$ that moves with a velocity of $v = v_i e_i$ wherein $v_i = \dot{x}_i = \partial x_i / \partial t$.

It is supposed that the motion of this mass point through space can be described by a one-parameter family (in time) of locations $x = \chi_i(X, t) e_i$ that is considered to be continuous and sufficiently differentiable (in space) to allow a deformation gradient to be defined according to $F = F_{ij} e_i \otimes e_j$ wherein $F_{ij} = \partial \chi_i(X, t) / \partial X_j$. The inverse to the deformation gradient F^{-1} exists because $J = \det F > 0$ from the conservation of mass.

Because the tensor $F F^T$ is positive-definite, F has a polar decomposition of

$$F = VR = RU, \tag{4}$$

with properties $V = V^T$, $U = U^T$, $R^{-1} = R^T$ such that $\det R = +1$, where R is a proper orthogonal tensor, and where V and U are commonly referred to as the left (or Eulerian) and right (or Lagrangian) stretch tensors, respectively, which are symmetric positive-definite. Also associated with the deformation gradient are the left B [Finger 1894] and right C [Green 1841] deformation tensors quantified by $B = F F^T = V^2$ and $C = F^T F = U^2$, which are symmetric positive-definite with components $B_{ij} = F_{ik} F_{jk}$ and $C_{ij} = F_{ki} F_{kj}$.

An infinitesimal material vector dX is pushed forward into an infinitesimal spatial vector dx according to the mapping

$$dx = F dX \quad \text{so that} \quad dS^2 = dX \cdot dX \quad \text{and} \quad ds^2 = dx \cdot dx = dX \cdot C dX, \tag{5}$$

where dS and ds are the Euclidean norms of vectors dX and dx, respectively, both of which are positive. It is apparent from the last formula of the above expression that tensor C plays the role of a metric quantifying the deformation that occurs at a mass point, expressed in the Lagrangian viewpoint.

Akin to the deformation gradient tensor F is the velocity gradient tensor $L = L_{ij} e_i \otimes e_j$ with components $L_{ij} = \partial v_i / \partial x_j$, so that $L = \dot{F} F^{-1}$. Its symmetric and antisymmetric parts, $D = \operatorname{sym} L$ and $W = \operatorname{skew} L$, are called the stretching D and vorticity W tensors, respectively, with W quantifying the rate of rotation occurring about the principal axes of D. In the literature tensor D is also referred to as either the strain-rate tensor or the rate-of-deformation tensor.

2.1. *Polar fields*. By selecting what Dienes [1987; 2003] calls the *polar configuration* $\bar{\kappa}$, a material modeler can construct constitutive equations that depend only on stretch and its rate; not on rotation or its rate. This is advantageous when developing mathematical models suitable for finite deformation analysis. All constitutive equations in the PRONTO two-dimensional and three-dimensional finite-element codes [Flanagan and Taylor 1987], for example, are solved in the polar configuration $\bar{\kappa}$, and then mapped into the spatial configuration κ for the displaying of results.

Dienes [1987; 2003] refers to any spatial field, for example, vector y or tensor Y, that is mapped into $\bar{\kappa}$ (by means of the rotation tensor R defined in Equation (4)) as a *polar* field; specifically,

$$\bar{y} = R^T y \quad \text{and} \quad \bar{Y} = R^T Y R. \tag{6}$$
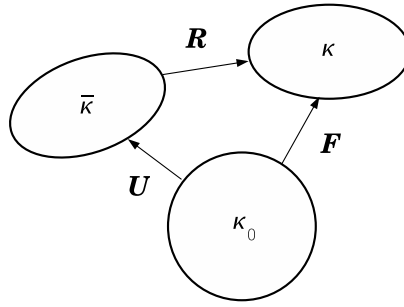
Figure 1. Mappings between the reference κ_0, polar $\bar{\kappa}$, and current κ configurations of a body.

Dienes [1979; 1986] distinguishes polar fields, for example, $\bar{\boldsymbol{y}}$ and $\bar{\boldsymbol{Y}}$, from their Eulerian counterparts, that is, $\boldsymbol{y}$ and $\boldsymbol{Y}$, with a bar — a notation that we adopt. A direct consequence of his definition is that $\boldsymbol{e}_1 = \boldsymbol{R}\bar{\boldsymbol{e}}_1$, $\boldsymbol{e}_2 = \boldsymbol{R}\bar{\boldsymbol{e}}_2$, and $\boldsymbol{e}_3 = \boldsymbol{R}\bar{\boldsymbol{e}}_3$, where rotation $\boldsymbol{R}$ maps *polar axes* $\{\bar{\boldsymbol{e}}_1, \bar{\boldsymbol{e}}_2, \bar{\boldsymbol{e}}_3\}$ into *spatial axes* $\{\boldsymbol{e}_1, \boldsymbol{e}_2, \boldsymbol{e}_3\}$. How the three configurations κ_0, $\bar{\kappa}$, and κ relate to one another is depicted in Figure 1.

Material derivatives of polar fields are described by [Dienes 1979]

$$\dot{\bar{\boldsymbol{y}}} = \boldsymbol{R}^T \hat{\boldsymbol{y}} \text{ wherein } \hat{\boldsymbol{y}} = \dot{\boldsymbol{y}} - \boldsymbol{\Omega}\boldsymbol{y}, \quad \text{and} \quad \dot{\bar{\boldsymbol{Y}}} = \boldsymbol{R}^T \hat{\boldsymbol{Y}} \boldsymbol{R} \text{ wherein } \hat{\boldsymbol{Y}} = \dot{\boldsymbol{Y}} - \boldsymbol{\Omega}\boldsymbol{Y} + \boldsymbol{Y}\boldsymbol{\Omega}, \tag{7}$$

where $\dot{\boldsymbol{y}} = \partial \boldsymbol{y}/\partial t + \nabla \boldsymbol{y} \cdot \boldsymbol{v}$ defines the material derivative of spatial field $\boldsymbol{y}$, which contains partial derivatives in both time $\partial \boldsymbol{y}/\partial t = (\partial y_i/\partial t)\boldsymbol{e}_i$ and space $\nabla \boldsymbol{y} = \frac{\partial y_i}{\partial x_j}\boldsymbol{e}_i \otimes \boldsymbol{e}_j$, and where $\boldsymbol{\Omega} = \dot{\boldsymbol{R}}\boldsymbol{R}^T$ is the spin tensor, which is the rate of rigid-body rotation about a material point that, like $\boldsymbol{W}$, is antisymmetric. The spatial derivatives $\hat{\boldsymbol{y}}$ and $\hat{\boldsymbol{Y}}$ are objective rates with $\hat{\boldsymbol{Y}}$ being commonly called the Green-Naghdi rate [Green and Naghdi 1965]. Instead, following the naming convention of Dienes [1987; 2003], we shall call $\dot{\bar{\boldsymbol{Y}}}$ the *material rate of polar tensor* $\bar{\boldsymbol{Y}}$, and $\hat{\boldsymbol{Y}}$ the *polar rate of spatial tensor* $\boldsymbol{Y}$. Freed and Diethelm [2007] have recently extended this class of mappings to include integrals and derivatives of fractional (noninteger) order, which they then used in the construction of a viscoelastic model for isotropic tissues.

There are a variety of objective time derivatives that have been used in constitutive modeling (see Atluri [1984] for a review). Physical reasons for selecting the polar rate over other objective rates and, in particular, over the Jaumann rate $\dot{\boldsymbol{Y}} - \boldsymbol{W}\boldsymbol{Y} + \boldsymbol{Y}\boldsymbol{W}$, has been the topic of many research papers [Atluri 1984; Dienes 1979; 1979; 1986; 1987; 2003; Flanagan and Taylor 1987; Freed and Diethelm 2007; Johnson and Bammann 1984; Szabó and Balla 1989].

Remark 1. In accordance with Equations (4), (6), and (7), Dienes [1979; 1986; 1987; 2003] argues that there is in fact just one *physical* stretch tensor, it being $\boldsymbol{V}$, since $\bar{\boldsymbol{V}} = \boldsymbol{R}^T \boldsymbol{V} \boldsymbol{R} \equiv \boldsymbol{U}$ and $\dot{\bar{\boldsymbol{V}}} = \boldsymbol{R}^T \hat{\boldsymbol{V}} \boldsymbol{R} \equiv \dot{\boldsymbol{U}}$, wherein

$$\hat{\boldsymbol{V}} = \dot{\boldsymbol{V}} - \boldsymbol{\Omega}\boldsymbol{V} + \boldsymbol{V}\boldsymbol{\Omega} \quad \text{with evolution} \quad \dot{\boldsymbol{V}} = \boldsymbol{L}\boldsymbol{V} - \boldsymbol{V}\boldsymbol{\Omega} \quad \text{so that} \quad \hat{\boldsymbol{V}} = (\boldsymbol{D} + \boldsymbol{Z})\boldsymbol{V}. \tag{8}$$

In other words, the right-stretch tensor $\boldsymbol{U}$ and the polar stretch tensor $\bar{\boldsymbol{V}}$ are synonyms for the same tensor field. Similarly, Dienes argues that there is just one *physical* deformation tensor, it being $\boldsymbol{B}$, since $\bar{\boldsymbol{B}} = \boldsymbol{R}^T \boldsymbol{B} \boldsymbol{R} \equiv \boldsymbol{C}$ and $\dot{\bar{\boldsymbol{B}}} = \boldsymbol{R}^T \hat{\boldsymbol{B}} \boldsymbol{R} \equiv \dot{\boldsymbol{C}}$, wherein

$$\hat{\boldsymbol{B}} = \dot{\boldsymbol{B}} - \boldsymbol{\Omega}\boldsymbol{B} + \boldsymbol{B}\boldsymbol{\Omega} \quad \text{with evolution} \quad \dot{\boldsymbol{B}} = \boldsymbol{L}\boldsymbol{B} + \boldsymbol{B}\boldsymbol{L}^T \quad \text{so that} \quad \hat{\boldsymbol{B}} = (\boldsymbol{D} + \boldsymbol{Z})\boldsymbol{B} + \boldsymbol{B}(\boldsymbol{D} - \boldsymbol{Z}), \tag{9}$$

or equivalently, $\hat{\boldsymbol{B}} = 2\boldsymbol{V}\boldsymbol{D}\boldsymbol{V}$. Consequently the right-deformation tensor $\boldsymbol{C}$ and the polar deformation tensor $\bar{\boldsymbol{B}}$ are synonyms for the same tensor field.

We have introduced another antisymmetric tensor in Equations (8) and (9), it being $\boldsymbol{Z} = \boldsymbol{W} - \boldsymbol{\Omega}$, which we call *swirl*. It is the actual vorticity that occurs within a material element, that is, the rigid-body spin $\boldsymbol{\Omega}$ has been removed from the overall rotation of vortex $\boldsymbol{W}$. Its influence can be neglected when analyzing most engineered materials, because they cannot sustain finite deformations, but soft tissues can.

In light of Remark 1, we will hereafter break with traditional notation and terminology, somewhat, and adopt the notation and terminology of Dienes when addressing the polar configuration $\bar{\kappa}$. We will, however, retain conventional usage whenever a particular field or equation applies to the Lagrangian configuration κ_0. In this regard, a concerted effort has been made herein to distinguish between tensor equations defined on κ_0 from those that are defined on $\bar{\kappa}$.

3. Conjugate stress-strain pairs

The rate at which work is being done on a material element of unit volume, when expressed in either the Eulerian κ or Lagrangian κ_0 configuration, is well-known and given by the respective formulae [Holzapfel 2000; Ogden 1984]

$$\dot{W} = \operatorname{tr}(\boldsymbol{T}\boldsymbol{D}) = \tfrac{1}{2}\operatorname{tr}(\boldsymbol{S}\dot{\boldsymbol{C}}), \tag{10}$$

where $\boldsymbol{T}$ is the Kirchhoff stress of the Eulerian frame, and $\boldsymbol{S}$ is the second Piola-Kirchhoff stress of the Lagrangian frame, which relate to the true stress of Cauchy $\boldsymbol{\sigma}$ via the well-known identities $\boldsymbol{T} = J\boldsymbol{\sigma}$ and $\boldsymbol{S} = J\boldsymbol{F}^{-1}\boldsymbol{\sigma}\boldsymbol{F}^{-T}$, recalling that $J = \det\boldsymbol{F}$.

Upon inserting the polar decomposition of $\boldsymbol{F}$, that is, $\boldsymbol{R}\bar{\boldsymbol{V}}$, into the work expression for the κ_0 configuration, noting that $\boldsymbol{S} = \boldsymbol{F}^{-1}\boldsymbol{T}\boldsymbol{F}^{-T} \equiv \bar{\boldsymbol{V}}^{-1}\boldsymbol{R}^T\boldsymbol{T}\boldsymbol{R}\bar{\boldsymbol{V}}^{-1}$ and $\dot{\boldsymbol{C}} = \boldsymbol{U}\dot{\boldsymbol{U}} + \dot{\boldsymbol{U}}\boldsymbol{U} \equiv \bar{\boldsymbol{V}}\dot{\bar{\boldsymbol{V}}} + \dot{\bar{\boldsymbol{V}}}\bar{\boldsymbol{V}}$ because $\boldsymbol{C} = \boldsymbol{U}^2$, one can reexpress Equation (10) for the $\bar{\kappa}$ configuration as

$$\dot{W} = \tfrac{1}{2}\operatorname{tr}\bigl(\bar{\boldsymbol{V}}^{-1}\boldsymbol{R}^T\boldsymbol{T}\boldsymbol{R}\bar{\boldsymbol{V}}^{-1}(\bar{\boldsymbol{V}}\dot{\bar{\boldsymbol{V}}} + \dot{\bar{\boldsymbol{V}}}\bar{\boldsymbol{V}})\bigr) = \operatorname{tr}\bigl(\boldsymbol{R}^T\boldsymbol{T}\boldsymbol{R}\tfrac{1}{2}(\dot{\bar{\boldsymbol{V}}}\bar{\boldsymbol{V}}^{-1} + \bar{\boldsymbol{V}}^{-1}\dot{\bar{\boldsymbol{V}}})\bigr)$$
$$= \operatorname{tr}\bigl(\bar{\boldsymbol{T}}\dot{\bar{\boldsymbol{E}}}\bigr) = \operatorname{tr}\bigl(\bar{\boldsymbol{T}}\operatorname{sym}\dot{\bar{\mathcal{E}}}\bigr) \equiv \operatorname{tr}\bigl(\bar{\boldsymbol{T}}\dot{\bar{\mathcal{E}}}\bigr), \tag{11}$$

where the symmetric *polar stress* $\bar{\boldsymbol{T}}$ and its rate $\dot{\bar{\boldsymbol{T}}}$ obey the mappings

$$\bar{\boldsymbol{T}} = \boldsymbol{R}^T\boldsymbol{T}\boldsymbol{R} \quad\text{and}\quad \dot{\bar{\boldsymbol{T}}} = \boldsymbol{R}^T\hat{\boldsymbol{T}}\boldsymbol{R},$$

the *nonsymmetric polar strain* $\bar{\mathcal{E}}$ and its rate $\dot{\bar{\mathcal{E}}} = \dot{\bar{\boldsymbol{V}}}\bar{\boldsymbol{V}}^{-1}$ obey the mappings

$$\bar{\mathcal{E}} = \boldsymbol{R}^T\mathcal{E}\boldsymbol{R} \quad\text{and}\quad \dot{\bar{\mathcal{E}}} = \boldsymbol{R}^T\widehat{\mathcal{E}}\boldsymbol{R},$$

with $\operatorname{sym}\widehat{\mathcal{E}} = \boldsymbol{D}$ and $\operatorname{skew}\widehat{\mathcal{E}} = \boldsymbol{Z}$, so that

$$\bar{\mathcal{E}} = \int_0^t \boldsymbol{R}^T(0, \tau)(\boldsymbol{L} - \boldsymbol{\Omega})(\tau)\boldsymbol{R}(0, \tau)\mathrm{d}\tau = \int_0^t \boldsymbol{R}^T(0, \tau)(\boldsymbol{D} + \boldsymbol{Z})(\tau)\boldsymbol{R}(0, \tau)\mathrm{d}\tau$$

and

$$\mathcal{E} = \int_0^t \boldsymbol{R}(\tau, t)(\boldsymbol{L} - \boldsymbol{\Omega})(\tau)\boldsymbol{R}^T(\tau, t)\mathrm{d}\tau = \int_0^t \boldsymbol{R}(\tau, t)(\boldsymbol{D} + \boldsymbol{Z})(\tau)\boldsymbol{R}^T(\tau, t)\mathrm{d}\tau,$$

because $\boldsymbol{R}(0, t) = \boldsymbol{R}(\tau, t)\boldsymbol{R}(0, \tau)^1$, while the *symmetric polar strain* $\bar{\boldsymbol{E}}$ and its rate $\dot{\bar{\boldsymbol{E}}}$ obey the mappings[2]

$$\bar{\boldsymbol{E}} = \boldsymbol{R}^T \boldsymbol{E} \boldsymbol{R} \quad \text{and} \quad \dot{\bar{\boldsymbol{E}}} = \boldsymbol{R}^T \hat{\boldsymbol{E}} \boldsymbol{R} \equiv \boldsymbol{R}^T \boldsymbol{D} \boldsymbol{R}, \tag{12}$$

so that

$$\bar{\boldsymbol{E}} = \int_0^t \boldsymbol{R}^T(0, \tau) \boldsymbol{D}(\tau) \boldsymbol{R}(0, \tau) \mathrm{d}\tau \quad \text{and} \quad \boldsymbol{E} = \int_0^t \boldsymbol{R}(\tau, t) \boldsymbol{D}(\tau) \boldsymbol{R}^T(\tau, t) \mathrm{d}\tau. \tag{13}$$

In summary, $\bar{\boldsymbol{E}} = \operatorname{sym}\bar{\mathcal{E}}$, $\dot{\bar{\boldsymbol{E}}} = \operatorname{sym}\dot{\bar{\mathcal{E}}}$, $\boldsymbol{E} = \operatorname{sym}\mathcal{E}$, and $\hat{\boldsymbol{E}} = \operatorname{sym}\hat{\mathcal{E}}$. The polar rate of strain $\hat{\mathcal{E}} = \boldsymbol{L} - \boldsymbol{\Omega}$ has symmetric and antisymmetric parts that are described by $\operatorname{sym}\hat{\mathcal{E}} = \boldsymbol{D}$ and $\operatorname{skew}\hat{\mathcal{E}} = \boldsymbol{Z}$.

The above development demonstrates that $\{\bar{\boldsymbol{T}}, \bar{\boldsymbol{E}}\}$, $\{\bar{\boldsymbol{T}}, \bar{\mathcal{E}}\}$, $\{\boldsymbol{T}, \boldsymbol{E}\}$, and $\{\boldsymbol{T}, \mathcal{E}\}$ are admissible conjugate pairs for stress and strain in the polar $\bar{\kappa}$ and spatial κ configurations, and that they are associated with the respective strain rates of $\dot{\bar{\boldsymbol{E}}}$, $\dot{\bar{\mathcal{E}}} = \dot{\bar{\boldsymbol{V}}}\bar{\boldsymbol{V}}^{-1}$, $\hat{\boldsymbol{E}} \equiv \boldsymbol{D}$, and $\hat{\mathcal{E}} = \boldsymbol{L} - \boldsymbol{\Omega} \equiv \boldsymbol{D} + \boldsymbol{Z}$. None of these pairs are found in Farahani and Naghdabadi [2003], who recently reviewed the literature of conjugate stress-strain pairs in κ_0.

3.1. *Updating polar stress.* When constructing numerical algorithms for solving constitutive equations in the polar configuration $\bar{\kappa}$, it becomes necessary to establish a means for pushing the polar stress forward from the polar configuration $\bar{\kappa}_N$ of the N-th step, say, into the polar configuration $\bar{\kappa}_{N+1}$ of the $N + 1$-st step. This process is most easily understood via the diagram presented in Figure 2. Found in this diagram are three, well-known, polar decompositions: $\boldsymbol{F}_N = \boldsymbol{R}_N \boldsymbol{U}_N$, $\boldsymbol{F}_{N+1} = \boldsymbol{R}_{N+1} \boldsymbol{U}_{N+1}$, and $\boldsymbol{F}_{N+1} = \boldsymbol{F}_{N+1}^N \boldsymbol{F}_N$, wherein $\boldsymbol{F}_{N+1}^N$ represents the deformation gradient between κ_N and κ_{N+1}. Also present is the polar decomposition $\boldsymbol{F}_{N+1}^N = \boldsymbol{R}_{N+1}^N \boldsymbol{U}_{N+1}^N$ that leads to $\boldsymbol{U}_{N+1}^N = \boldsymbol{R}_N \boldsymbol{U}_{N+1} \boldsymbol{U}_N^{-1} \boldsymbol{R}_N^T$ because $\boldsymbol{R}_{N+1} = \boldsymbol{R}_{N+1}^N \boldsymbol{R}_N$.

Given a state of polar stress $\bar{\boldsymbol{T}}_N$ for the $\bar{\kappa}_N$ configuration that has been stored for later use by an integrator affixed to the $\bar{\kappa}_{N+1}$ configuration, for example, the retrieved stress must first be pushed forward from $\bar{\kappa}_N$ into $\bar{\kappa}_{N+1}$ before it can be utilized in this new configuration. This is achieved via the mapping

$$\bar{\boldsymbol{T}}_{N+1}^N = \bar{\boldsymbol{G}}_{N+1}^N \bar{\boldsymbol{T}}_N (\bar{\boldsymbol{G}}_{N+1}^N)^T \quad \text{wherein} \quad \bar{\boldsymbol{G}}_{N+1}^N = \boldsymbol{U}_{N+1} \boldsymbol{U}_N^{-1} \equiv \bar{\boldsymbol{V}}_{N+1} \bar{\boldsymbol{V}}_N^{-1} \approx \bar{\boldsymbol{I}} + \Delta t\, \dot{\bar{\mathcal{E}}}_N, \tag{14}$$

where $\bar{\boldsymbol{T}}_{N+1}^N$ represents the polar stress $\bar{\boldsymbol{T}}$ of state $\bar{\kappa}_N$ pushed forward into state $\bar{\kappa}_{N+1}$. This mapping is akin to the well-known mapping that pushes the second Piola-Kirchhoff stress $\boldsymbol{S}$ forward into the Kirchhoff stress $\boldsymbol{T}$ via $\boldsymbol{T} = \boldsymbol{F}\boldsymbol{S}\boldsymbol{F}^T$. The difference between this scheme and the updated-Lagrangian scheme is that Equation (14) maps the polar stress $\bar{\boldsymbol{T}}$ from $\bar{\kappa}_N$ into $\bar{\kappa}_{N+1}$; whereas the updated-Lagrangian method maps the Kirchhoff stress $\boldsymbol{T}$ from κ_N into κ_{N+1} as $\boldsymbol{T}_{N+1}^N = \boldsymbol{F}_{N+1}^N \boldsymbol{T}_N (\boldsymbol{F}_{N+1}^N)^T$ [Belytschko et al. 2000]. The approximation for $\bar{\boldsymbol{G}}$ in the above formula follows from a Taylor expansion of $\bar{\boldsymbol{V}}$ about t_N with $\Delta t = t_{N+1} - t_N$, while recalling that $\dot{\bar{\mathcal{E}}} = \dot{\bar{\boldsymbol{V}}}\bar{\boldsymbol{V}}^{-1}$ and noting that $\bar{\boldsymbol{I}} = \boldsymbol{R}^T \boldsymbol{I} \boldsymbol{R} = \boldsymbol{R}^T \boldsymbol{R} = \boldsymbol{I}$.

---

[1]Any material rotation $\boldsymbol{R}(0, t)$ from κ_0 to κ can be decomposed into two sequential rotations: the first rotation $\boldsymbol{R}(0, \tau)$ goes from κ_0 to κ_τ, while the second rotation $\boldsymbol{R}(\tau, t)$ goes from κ_τ to κ with $0 \le \tau \le t$ and $\boldsymbol{R}(\tau, \tau) = \boldsymbol{I}$ for all τ. The product $\boldsymbol{R}(\tau, t)\boldsymbol{R}(0, \tau)$ of two orthogonal tensors is another orthogonal tensor; however, $\boldsymbol{R}(\tau, t)\boldsymbol{R}(0, \tau) \ne \boldsymbol{R}(0, \tau)\boldsymbol{R}(\tau, t)$, that is, matrix multiplication does not commute between orthogonal tensors.

[2]Definitions for $\bar{\boldsymbol{E}}$ and $\boldsymbol{E}$ first appeared in Freed and Diethelm [2007]. Earlier, Hill [1968] proved that $\dot{\bar{\boldsymbol{E}}}$ approximates Hencky's definition for strain rate whenever $\|\boldsymbol{E}_G \dot{\bar{\boldsymbol{E}}} \boldsymbol{E}_G\|$ is sufficiently small with $\boldsymbol{E}_G = \frac{1}{2}(\boldsymbol{C} - \boldsymbol{I})$ being the Green strain.
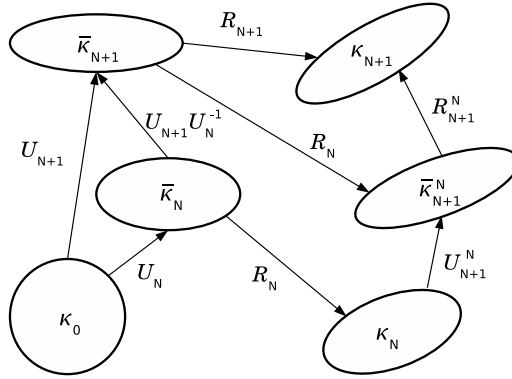
Figure 2. Mappings between the Lagrangian κ_0, updated Lagrangian κ_N, and Eulerian κ_{N+1} configurations, and their relationships to the polar configurations $\bar{\kappa}_N$, $\bar{\kappa}_{N+1}$, and $\bar{\kappa}_{N+1}^N$ that associate with the updated Lagrangian and Eulerian configurations, and the incremental advancement between them, respectively.

4. Simple shear

To demonstrate that the symmetric polar strain $\bar{E}$ and its spatial counterpart E are tractable strain measures, let us consider a simple shear flow whose deformation history is described by

$$\chi_1 = X_1 + \gamma X_2, \quad \chi_2 = X_2, \quad \text{and} \quad \chi_3 = X_3,$$
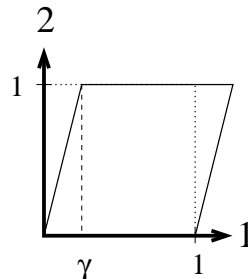
leading to a deformation gradient with components

$$F = \begin{bmatrix} 1 & \gamma & 0 \\ 0 & 1 & 0 \\ 0 & 0 & 1 \end{bmatrix} \quad \text{so that} \quad F^{-1} = \begin{bmatrix} 1 & -\gamma & 0 \\ 0 & 1 & 0 \\ 0 & 0 & 1 \end{bmatrix},$$

wherein γ quantifies the extent of shear, as shown in Figure 3. Simple shear is isochoric, that is, $\det F = 1$ independent of material constitution.

This deformation gradient is affiliated with a material rotation of

$$R = \frac{1}{\sqrt{4+\gamma^2}} \begin{bmatrix} 2 & \gamma & 0 \\ -\gamma & 2 & 0 \\ 0 & 0 & \sqrt{4+\gamma^2} \end{bmatrix},$$

Figure 3. Simple shear of a unit (dotted) square sheared by γ into a (solid) parallelogram.

which satisfies the required identity that det $\boldsymbol{R} = 1$. Utilizing this description for $\boldsymbol{R}$, derived by Ogden [1984], leads to simpler expressions for fields described in terms of $\boldsymbol{R}$ than one would otherwise arrive at if sines and cosines were used, as appear in classic rotation matrices [Dienes 1979; Flanagan and Taylor 1987].

The velocity gradient $\boldsymbol{L} = \dot{\boldsymbol{F}}\boldsymbol{F}^{-1}$ and stretching $\boldsymbol{D} = \operatorname{sym}\boldsymbol{L}$ tensors have components

$$\boldsymbol{L} = \begin{bmatrix} 0 & \dot{\gamma} & 0 \\ 0 & 0 & 0 \\ 0 & 0 & 0 \end{bmatrix} \quad \text{and} \quad \boldsymbol{D} \equiv \hat{\boldsymbol{E}} = \frac{\dot{\gamma}}{2} \begin{bmatrix} 0 & 1 & 0 \\ 1 & 0 & 0 \\ 0 & 0 & 0 \end{bmatrix},$$

while the vorticity $\boldsymbol{W} = \operatorname{skew}\boldsymbol{L}$, spin $\boldsymbol{\Omega} = \dot{\boldsymbol{R}}\boldsymbol{R}^{T}$, and swirl $\boldsymbol{Z} = \boldsymbol{W} - \boldsymbol{\Omega}$ tensors have components

$$\boldsymbol{W} = \frac{\dot{\gamma}}{2} \begin{bmatrix} 0 & 1 & 0 \\ -1 & 0 & 0 \\ 0 & 0 & 0 \end{bmatrix}, \quad \boldsymbol{\Omega} = \frac{2\dot{\gamma}}{4+\gamma^2} \begin{bmatrix} 0 & 1 & 0 \\ -1 & 0 & 0 \\ 0 & 0 & 0 \end{bmatrix}, \quad \text{and} \quad \boldsymbol{Z} = \frac{\gamma^2\dot{\gamma}}{2(4+\gamma^2)} \begin{bmatrix} 0 & 1 & 0 \\ -1 & 0 & 0 \\ 0 & 0 & 0 \end{bmatrix},$$

where $\boldsymbol{W}$ and $\boldsymbol{\Omega}$ are seen to be equal only when $\gamma = 0$, while $\boldsymbol{Z}$ approaches $\boldsymbol{W}$ and $\boldsymbol{\Omega}$ approaches $\boldsymbol{0}$ with increasing values of $|\gamma|$.

The symmetric, polar, strain rate $\dot{\bar{\boldsymbol{E}}}$ defined in Equation (12) is therefore given by

$$\dot{\bar{\boldsymbol{E}}} = \frac{\dot{\gamma}}{2(4+\gamma^2)} \begin{bmatrix} -4\gamma & 4-\gamma^2 & 0 \\ 4-\gamma^2 & 4\gamma & 0 \\ 0 & 0 & 0 \end{bmatrix} \equiv \begin{bmatrix} \dot{\bar{\varepsilon}} & \dot{\bar{\theta}} & 0 \\ \dot{\bar{\theta}} & -\dot{\bar{\varepsilon}} & 0 \\ 0 & 0 & 0 \end{bmatrix},$$

where, to simplify notation, we have introduced terms

$$\dot{\bar{\theta}} = \frac{4-\gamma^2}{2(4+\gamma^2)}\dot{\gamma} \quad \text{and} \quad \dot{\bar{\varepsilon}} = \frac{-2\gamma}{4+\gamma^2}\dot{\gamma}.$$

Integrating from 0 to γ produces

$$\bar{\boldsymbol{E}} = \begin{bmatrix} \bar{\varepsilon} & \bar{\theta} & 0 \\ \bar{\theta} & -\bar{\varepsilon} & 0 \\ 0 & 0 & 0 \end{bmatrix}, \quad \text{wherein} \quad \bar{\varepsilon} = \ln\left(\frac{4}{4+\gamma^2}\right) \text{ and } \bar{\theta} = 2\tan^{-1}\left(\frac{\gamma}{2}\right) - \frac{\gamma}{2}, \tag{15}$$

which quantifies the polar strain $\bar{\boldsymbol{E}}$ for simple shear. By rotating the polar strain tensor of Equation (15) into the Eulerian frame, according to Equation (12), one gets the physical strain measure

$$\boldsymbol{E} = \begin{bmatrix} \varepsilon & \theta & 0 \\ \theta & -\varepsilon & 0 \\ 0 & 0 & 0 \end{bmatrix} \quad \text{wherein} \quad \varepsilon = \frac{1}{4+\gamma^2}\big((4-\gamma^2)\bar{\varepsilon}+4\gamma\bar{\theta}\big) \text{ and } \theta = \frac{1}{4+\gamma^2}\big((4-\gamma^2)\bar{\theta}-4\gamma\bar{\varepsilon}\big). \tag{16}$$

No other strain field, that we are aware of, has these components for simple shear. Having said this, the isotropic hypoelastic material considered by Dienes [1979] has a stress response in simple shear that is proportional to the strain components listed in Equation (16), with the shear modulus being the constant of proportionality. However, Dienes [1986] does not define polar strain as we have done in Equation (13); rather, he advocates using Signorini-strain, that is, $\boldsymbol{E}_S = \frac{1}{2}(\boldsymbol{B} - \boldsymbol{I})$ [Signorini 1930]. Other differences

Polar Components of Strain in Simple Shear
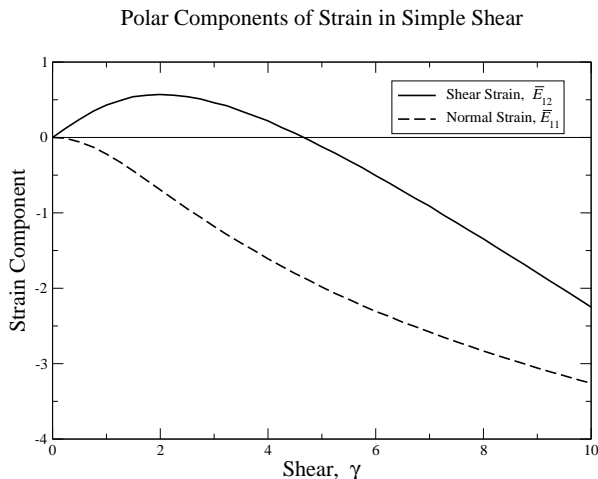
Figure 4. Polar components of strain in simple shear, where $\bar{E}_{12} = \bar{\theta}$ and $\bar{E}_{11} = \bar{\varepsilon}$.

between Dienes' formulae and ours for simple shear originate with the different, but equivalent, ways that we assign components to the rotation tensor $\boldsymbol{R}$.

The polar strain components for simple shear are plotted in Figure 4, while their associated spatial components are plotted in Figure 5. Of these, the curves for ε and θ presented in Figure 5 represent physical components, while those for $\bar{\varepsilon}$ and $\bar{\theta}$ presented in Figure 4 are nonphysical in nature. The two normal strains $\bar{\varepsilon}$ and ε are even functions of shear γ, while the two shear strains $\bar{\theta}$ and θ are odd functions of γ. Accordingly, only the right half of the response plane needs to be shown. The shear strain E_{12} is seen to dip below $\gamma/2$ over much of the range plotted in Figure 5, yet it asymptotes with $\gamma/2$ at both small and large values of shear strain; essentially whenever $|\gamma| < 0.5$ or $|\gamma| > 100$. In contrast, the normal strain E_{11} grows very slow at large values of γ, for example, whenever $|\gamma| > 100$, giving it a local appearance of having reached an asymptote.

Spatial Components of Strain in Simple Shear
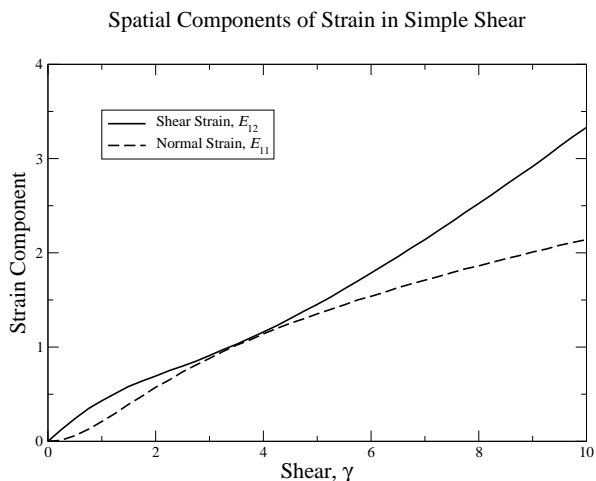
Figure 5. Spatial components of strain in simple shear, where $E_{12} = \theta$ and $E_{11} = \varepsilon$.

5. Material anisotropy

The fibrous structures of biological tissues are not strongly aligned; rather, they are dispersed over angles of splay [Finlay et al. 1995]. The use of a distribution density function for the handling of fiber splay in connective tissues was introduced by Lanir [1983]. Since then single-family fiber splays have been adopted by Hurschler et al. [1997] for tendon and ligament, Billiar and Sacks [2000] and Freed et al. [2005] for heart valves, and Usyk et al. [2000] for ventricular myofibers; double-family fiber splays have been adopted by Gasser et al. [2006] for arteries; and triple-family fiber splays have been adopted by Nash and Hunter [2000] for myocardial laminae. In the papers by Freed et al. [2005] and Gasser et al. [2006], the distribution function describing anisotropy was extracted from the overall constitutive formulation yielding a material or structural tensor. In what follows, this material tensor is given additional physical insight through a derivation based on Riemannian Geometry.

In Equation (5), the symmetric positive-definite Lagrangian tensor $\boldsymbol{C}$ is shown to be a metric tensor that quantifies deformation. In what follows, a new symmetric positive-semidefinite tensor, call it $\boldsymbol{C}^f$, is introduced that can be thought of as being a metric-like tensor that quantifies just the anisotropic contributions of deformation caused by fiber reinforcement, that is, the isotropic contributions to deformation are removed.

Let us begin by postulating the existence of a masking tensor $\boldsymbol{M} = M_{ij}\boldsymbol{e}_i \otimes \boldsymbol{e}_j$ defined in κ_0 (it is a material tensor; hence it does not change over time) that strips away all isotropic contributions otherwise present in $\mathrm{d}\boldsymbol{X}$ by scaling only those components of a displacement that align with the material directions of anisotropy in κ_0, as defined by the transformation law

$$\mathrm{d}\boldsymbol{\Xi} = \boldsymbol{M}\mathrm{d}\boldsymbol{X} \quad \text{with} \quad \mathrm{d}\Sigma^2 = \mathrm{d}\boldsymbol{\Xi} \cdot \mathrm{d}\boldsymbol{\Xi} = \mathrm{d}\boldsymbol{X} \cdot \boldsymbol{A}_0 \mathrm{d}\boldsymbol{X} \quad \text{wherein} \quad \boldsymbol{A}_0 = \boldsymbol{M}^T \boldsymbol{M}, \tag{17}$$

where $\mathrm{d}\Sigma$ is some nonnegative fraction of $\mathrm{d}S$ that quantifies the relative anisotropic stiffening in material direction $\mathrm{d}\boldsymbol{X}$, that is, $0 \leq \mathrm{d}\Sigma \leq \mathrm{d}S$. Consequently, the *anisotropy tensor* $\boldsymbol{A}_0 = A_{ij}^0 \boldsymbol{e}_i \otimes \boldsymbol{e}_j$ is symmetric positive-semidefinite with components $A_{ij}^0 = M_{ki}M_{kj}$. The lower bound of $\mathrm{d}\Sigma = 0$ occurs in those directions $\mathrm{d}\boldsymbol{X}$ where a material has no anisotropic stiffening. Here its stiffness is considered to be due solely to its isotropic constituents. The upper bound of $\mathrm{d}\Sigma = \mathrm{d}S$ occurs in those directions $\mathrm{d}\boldsymbol{X}$ where the material has its greatest anisotropic stiffening. Here its stiffness is considered to be due solely to its anisotropic constituents. All other directions, that is, where $0 < \mathrm{d}\Sigma < \mathrm{d}S$, are considered to have a mixture of isotropic and anisotropic stiffening effects with the anisotropic contribution scaling according to ratio $\mathrm{d}\Sigma/\mathrm{d}S \in (0, 1)$.

Because the masking tensor $\boldsymbol{M}$ is a material tensor defined in the reference configuration κ_0, it maps into the current configuration κ through a simple rotation such that

$$\mathrm{d}\boldsymbol{\xi} = \boldsymbol{R}\boldsymbol{M}\boldsymbol{R}^T\mathrm{d}\boldsymbol{x} \quad \text{with} \quad \mathrm{d}\sigma^2 = \mathrm{d}\boldsymbol{\xi} \cdot \mathrm{d}\boldsymbol{\xi} = \mathrm{d}\boldsymbol{X} \cdot \boldsymbol{C}^f \mathrm{d}\boldsymbol{X} \quad \text{wherein} \quad \boldsymbol{C}^f = \boldsymbol{U}\boldsymbol{A}_0\boldsymbol{U},$$

and, in doing so, analogous to $\mathrm{d}\Sigma$, $\mathrm{d}\sigma$ is bound to the interval $0 \leq \mathrm{d}\sigma \leq \mathrm{d}s$. Here we see that the anisotropy tensor $\boldsymbol{A}_0$ now takes on the role of a geometric metric within $\boldsymbol{C}^f$, making $\boldsymbol{C}^f$ a metric of the anisotropic deformation. Tensor $\boldsymbol{C}^f$ possesses the property that $\boldsymbol{C}^f \to \boldsymbol{C}$ whenever $\boldsymbol{A}_0 \to \boldsymbol{I}$, which occurs at all isotropic barriers.

Remark 2. The fact that $d\Sigma/dS \in [0, 1]$ requires that the maximum eigenvalue of tensor A_0 be 1. This physical constraint is equivalent to the mathematical constraint that

$$\|A_0\|_2 = 1, \tag{18}$$

where $\|A_0\|_2$ is the L_2 norm of A_0.

5.1. *Transverse isotropy.* Materials described by a unit vector a_0 that aligns with a single fiber orientation in some reference configuration κ_0 have an anisotropy tensor that is given by[3] Spencer [1972]

$$A_0 = a_0 \otimes a_0, \tag{19}$$

which satisfies the constraint listed in Equation (18), because $\|a_0\|_2 = 1$ by definition. The eigenvalues for this material tensor A_0 are $\{1, 0, 0\}$. Highly aligned fiber orientations, as implied by transverse isotropy, are intentionally designed into many man-made materials; whereas fiber architectures in biological tissues usually have splayed or distributed fiber orientations.

5.1.1. *Conic splay.* Gasser et al. [2006] derived an anisotropy tensor from a statistical assessment of fiber splay, where a projection of the fibers onto the transverse plane is uniformly distributed by angle (the fiber distribution is a cone of orientation vectors) with unit vector a_0 denoting their mean orientation. Their anisotropy tensor has the form

$$A_0 = \delta I + (1 - \delta)a_0 \otimes a_0, \tag{20}$$

where our presentation of their formula has been normalized so that $\|A_0\|_2 = 1$. Our δ relates to their $\kappa = \frac{1}{4} \int_0^\pi \rho(\Theta) \sin^3(\Theta) d\Theta$ via the formula $\delta = \kappa/(1-2\kappa)$, where $\rho(\Theta)$ is an orientation density function for fiber splay, with $\kappa \in [0, 1/3]$ and therefore $\delta \in [0, 1]$. The dispersion parameter δ is bound from below by transverse isotropy (that is, the limiting case of $\delta = 0$, which simplifies Equation (20) to Equation (19)), and it is bound from above by isotropy in 3-space (that is, whenever $\delta = 1$). The eigenvalues for this material tensor A_0 are $\{1, \delta, \delta\}$.

The dispersion parameter δ is to be regarded as a phenomenological material constant. It is a material property derived from a statistical assessment of fiber distribution, just like the shear modulus μ is a material property derived from a statistical assessment of the spatial geometry of the molecular backbone in elastomers [Treloar 1975]. No specific knowledge pertaining to the statistical underpinnings of either δ or μ is required for their use in applications.

5.1.2. *Fan splay.* Freed et al. [2005] derived another anisotropy tensor from a different statistical assessment of fiber dispersion. Here splay was considered to occur as a two-dimensional fan contained within 3-space whose planar normal aligns with unit vector b_0. Fibers reside within this plane with a mean orientation of a_0. Hence, by definition, $a_0 \cdot b_0 = 0$ and $\|a_0\|_2 = \|b_0\|_2 = 1$. The anisotropy tensor for this geometry, when their formula has been normalized so that $\|A_0\|_2 = 1$, can be rewritten as

$$A_0 = \delta I + (1 - \delta)a_0 \otimes a_0 - \delta b_0 \otimes b_0, \tag{21}$$

---

[3]Ateshian [2007] has extended transverse isotropy to address the fact that thin filaments can only carry tensile loads. His adaptation into this framework lies beyond the scope of this paper.

where, like Equation (20), the dispersion parameter δ is bound from below by transverse isotropy; see Equation (19). However, unlike Equation (20), δ is now bound from above by an isotropy in 2-space. The eigenvalues for this material tensor A_0 are $\{1, \delta, 0\}$.

5.1.3. *Orthotropic splay.* As alluded to in Freed et al. [2005], the two cases of conic and fan splay can be unified into an orthotropic anisotropy tensor for a single dispersed fiber family given by

$$A_0 = \delta I + (1 - \delta)a_0 \otimes a_0 + (\epsilon - \delta)b_0 \otimes b_0,$$

where $0 \leq \epsilon \leq \delta \leq 1$. Here the projection of fibers onto the transverse plane about a_0 produces an ellipse whose minor axis is in the direction of b_0 with a length of ϵ, and whose major axis is in the direction of $a_0 \times b_0$ with a length of δ. The limiting case of $\epsilon = 0$ reduces to fan splay (Equation (21)); the limiting case of $\epsilon = \delta$ reduces to conic splay (Equation (20)); and the limiting case of $\epsilon = \delta = 0$ reduces to transverse isotropy (Equation (19)). The eigenvalues for this material tensor A_0 are $\{1, \delta, \epsilon\}$.

These are but a few of the possible anisotropy tensors that can be derived and utilized within the framework of the following proposition. The above cases apply whenever a single family of fibers exists whose geometric interpretation of anisotropy can be described with an elliptic projection onto the transverse plane.

6. Hypothesis

Proposition 1. *The isotropic constituent* (*for example*, *the ground substance **matrix***) *and the anisotropic constituent* (*for example*, *the collagen **fiber***) *that comprise soft tissues are considered to be cohabitant, in a continuum sense, at every mass point throughout a tissue. In these materials, the Kirchhoff stress T is considered to be a sum of fiber and matrix stresses governed by the rule of mixtures*

$$T + \wp I = \phi T^f + (1 - \phi)T^m, \tag{22}$$

while the metric for deformation C is considered to decompose according to the sum

$$C = U^2 = U A_0 U + U(I - A_0)U, \tag{23}$$

which is given the notation

$$C = C^f + C^m, \quad wherein \quad C^f = U A_0 U \quad and \quad C^m = U(I - A_0)U, \tag{24}$$

where C^f and T^f are the deformation and stress tensors associated with the anisotropic fibers, C^m and T^m are the deformation and stress tensors associated with the isotropic matrix, and A_0 is the anisotropy tensor of (17) — *all five of these tensors are symmetric* — *and where ϕ is the volume fraction occupied by the anisotropic constituents, and $\wp$ is a Lagrange multiplier used to enforce an isochoric constraint, that is,* $\det C = 1$.

Regarding stresses, Equation (22) is the well-known rule-of-mixtures formula from composites theory [Spencer 1972]. It is adopted here for the same reason that Humphrey and Rajagopal [2002] adopted it; specifically, to make boundary value problems tractable. Formula (22) enables residual stresses to be assigned to the fiber and matrix phases via initial conditions, for example, as T_0^f and $T_0^m = \frac{-\phi}{1-\phi} T_0^f$, so that $T_0 = 0$ at time $t = 0$.

However, regarding deformations, the above proposition differs from all existing hypotheses known to the author. There are two commonly used kinematic splits found in the literature. They are the multiplicative decompositions of the deformation gradient tensor (elastic-plastic theories that originate with Lee [1969]) and the mass-weighted sums of constituent velocity vectors (mixture theories that originate with Truesdell [1957]), respectively. In contrast, here the geometric metric, which we take to be I because Cartesian tensor fields are used, is additively split into two parts, that is, isotropic and anisotropic, so that the positive-definite metric of deformation C becomes a sum of two positive-semidefinite tensors C^f and C^m defined according to Equation (24).

Remark 3. Because the anisotropy tensor A_0 is a material tensor, its mapping from κ_0 into $\bar{\kappa}$ is not affected by stretch U, and one has $\bar{A} \equiv A_0$. However, it is affected by rotation R when mapped from either κ_0 or $\bar{\kappa}$ into κ, wherein the anisotropy tensor becomes $A = R\bar{A}R^T \equiv RA_0R^T$. In other words, unlike metals, for example, anisotropy in soft tissues is not considered to be deformation induced.

6.1. *Polar representation.* In general tensor analysis the deformation tensor is given by the formula $C = F^T g F$, wherein g is the geometric metric tensor of κ [Sokolnikoff 1964]. The deformation metric can be rewritten as $C \equiv \bar{B} = \bar{V}R^T g R\bar{V} = \bar{V}\bar{g}\bar{V}$ for $\bar{\kappa}$, where $\bar{g} = R^T g R$ defines a polar metric. Tensors $\bar{I} - \bar{A} \equiv I - A_0$ and $\bar{A} \equiv A_0$ in Equation (23) are analogous to metric $\bar{g}$; however, they are not true metric tensors, like $\bar{g}$ is, in the sense that $\bar{I} - \bar{A}$ and $\bar{A}$ are not positive definite; they are only positive semidefinite. If the base vectors $\{\bar{e}_1, \bar{e}_2, \bar{e}_3\}$ happen to be affiliated with a curvilinear coordinate system, then C^m would become $\bar{V}(\bar{g} - \bar{A})\bar{V}$ and $\bar{A} \to \bar{g}$ at isotropic barriers, with the Riemannian metric $\bar{g}$ now replacing the Cartesian metric $\bar{I}$. But, in this document, Cartesian tensors are used.

Isotropic and anisotropic contributions to the polar strain-rates $\dot{\bar{\mathcal{E}}}$ and $\dot{\bar{E}}$ can be readily constructed by replacing $\dot{C}$ with $\dot{C}^m$ and $\dot{C}^f$ in Equation (10), recalling that tensor $A_0 \equiv \bar{A}$ is temporally constant, and then recasting these expressions, as was done in the derivation within Equation (11), which leads to

$$\dot{\bar{\mathcal{E}}} = \dot{\bar{\mathcal{E}}}^f + \dot{\bar{\mathcal{E}}}^m, \quad \text{wherein} \quad \dot{\bar{\mathcal{E}}}^f = \bar{A}\dot{\bar{\mathcal{E}}} \quad \text{and} \quad \dot{\bar{\mathcal{E}}}^m = (\bar{I} - \bar{A})\dot{\bar{\mathcal{E}}}, \tag{25}$$

and therefore

$$\dot{\bar{E}} = \dot{\bar{E}}^f + \dot{\bar{E}}^m, \quad \text{wherein} \quad \dot{\bar{E}} = \operatorname{sym}\dot{\bar{\mathcal{E}}}, \quad \dot{\bar{E}}^f = \operatorname{sym}\dot{\bar{\mathcal{E}}}^f, \quad \text{and} \quad \dot{\bar{E}}^m = \operatorname{sym}\dot{\bar{\mathcal{E}}}^m, \tag{26}$$

while the isotropic and anisotropic contributions to polar stress obey $\bar{T} + \wp\bar{I} = \phi\bar{T}^f + (1 - \phi)\bar{T}^m$, which follows straightaway from Equations (6) and (22).

7. Hypoelasticity

We begin our discussion of general hypoelasticity by considering an isotropic material and finish our discussion by extending that construction into a simple anisotropic material model that has potential in the modeling of the passive response of soft biological tissues.

7.1. *Isotropic materials.* An analytic expression for the polar strain $\bar{E}(\bar{V})$, as suggested by Equation (12), does not currently exist, to the best of our knowledge; nevertheless, this does not preclude one from using its rate $\dot{\bar{E}}$ as the primitive kinematic variable in constitutive formulations. Specifically, instead of the more common hyperelastic constitutive constructions [Holzapfel 2000; Ogden 1984], constitutive

equations for elasticity can be cast in rate form, whose formulae belong to the material class[4] [Dienes 1979]

$$\hat{T} = \psi(T, D) = \psi(R\bar{T}R^T, R\dot{\bar{E}}R^T) = R\psi(\bar{T}, \dot{\bar{E}})R^T \quad \text{or equivalently} \quad \dot{\bar{T}} = \psi(\bar{T}, \dot{\bar{E}}). \qquad (27)$$

A hypoelastic solid, in the sense of Truesdell [1955], is that subset to this material class which restricts the tensor-valued material function ψ to be a linear function in strain rate; here, either D or $\dot{\bar{E}}$ depending on one's choice of reference frame. Flanagan and Taylor [1987] have published an algorithm that can be used to solve constitutive formulae belonging to the material class $\dot{\bar{T}} = \psi(\bar{T}, \dot{\bar{E}})$.

Leonov [2000] derived a theorem that states: Hypoelastic constitutive equations are physically meaningful (that is, they obey the second law of thermodynamics) if, and only if, they admit a potential. Consequently, Equation (27) becomes physically meaningful if, and only if, $\psi = \partial\Psi/\partial\dot{\bar{E}}$ so that

$$\dot{\bar{T}} = \frac{\partial\Psi(\bar{T}, \dot{\bar{E}})}{\partial\dot{\bar{E}}}. \qquad (28)$$

It necessarily follows that the potential function Ψ must now be quadratic in $\dot{\bar{E}}$ in order for the response to be hypoelastic (that is, stress-rate is linear in strain-rate). In this regard, Ψ is not so different from a conventional hyperelastic strain-energy potential.

Any material that is an isotropic function of two symmetric tensor fields, as in Equation (28), can be expressed as a function of ten scalar invariants [Spencer 1972]; specifically: $\mathrm{tr}(\bar{T})$, $\mathrm{tr}(\bar{T}\bar{T})$, $\mathrm{tr}(\bar{T}\bar{T}\bar{T})$, $\mathrm{tr}(\dot{\bar{E}})$, $\mathrm{tr}(\dot{\bar{E}}\dot{\bar{E}})$, $\mathrm{tr}(\dot{\bar{E}}\dot{\bar{E}}\dot{\bar{E}})$, $\mathrm{tr}(\bar{T}\dot{\bar{E}})$, $\mathrm{tr}(\bar{T}\dot{\bar{E}}\bar{T})$, $\mathrm{tr}(\dot{\bar{E}}\bar{T}\dot{\bar{E}})$, and $\mathrm{tr}(\bar{T}\dot{\bar{E}}\bar{T}\dot{\bar{E}})$. Imposing the hypoelastic constraint that Ψ be quadratic in $\dot{\bar{E}}$, while also assuming that Ψ be at most linear in $\bar{T}$, in accordance with Fung's law (Equation (1)), allows one to write down a general potential function that has merit for modeling biological tissues; it being,

$$\Psi = \tfrac{1}{2}\left(\alpha_1 \mathrm{tr}(\dot{\bar{E}})^2 + \alpha_2 \mathrm{tr}(\dot{\bar{E}}\dot{\bar{E}}) + \alpha_3 \mathrm{tr}(\bar{T})\mathrm{tr}(\dot{\bar{E}})^2 + \alpha_4 \mathrm{tr}(\bar{T})\mathrm{tr}(\dot{\bar{E}}\dot{\bar{E}}) + 2\alpha_5 \mathrm{tr}(\bar{T}\dot{\bar{E}})\mathrm{tr}(\dot{\bar{E}}) + \alpha_6 \mathrm{tr}(\dot{\bar{E}}\bar{T}\dot{\bar{E}})\right), \qquad (29)$$

wherein the $\alpha_1, \ldots, \alpha_6$ are material constants, thereby resulting in the general constitutive equation

$$\dot{\bar{T}} = \left((\alpha_1 + \alpha_3 \mathrm{tr}\,\bar{T})\mathrm{tr}\,\dot{\bar{E}} + \alpha_5 \mathrm{tr}(\bar{T}\dot{\bar{E}})\right)\bar{I} + (\alpha_2 + \alpha_4 \mathrm{tr}\,\bar{T})\dot{\bar{E}} + \alpha_5 \mathrm{tr}(\dot{\bar{E}})\bar{T} + \alpha_6 \mathrm{sym}(\bar{T}\dot{\bar{E}}), \qquad (30)$$

whose structure Truesdell [1955] calls a "hypoelastic material of grade one". For isochoric flows and for materials whose bulk modulus greatly exceeds its shear modulus, like soft tissues [Fung 1973], this potential function can be further simplified to

$$\Psi = \mu \mathrm{tr}(\dot{\bar{E}}\dot{\bar{E}}) + \frac{\alpha}{3}\mathrm{tr}(\bar{T})\mathrm{tr}(\dot{\bar{E}}\dot{\bar{E}}) + \beta \mathrm{tr}(\dot{\bar{E}}\bar{T}\dot{\bar{E}}) - \wp(\mathrm{tr}\,\dot{\bar{E}} - 0), \qquad (31)$$

because $\mathrm{tr}\,\dot{\bar{E}} \equiv \mathrm{tr}\,D = 0$, which in turn produces the constitutive equation

$$\dot{\bar{T}} + \wp\bar{I} = 2(\mu - \alpha p)\dot{\bar{E}} + 2\beta \mathrm{sym}(\bar{T}\dot{\bar{E}}), \qquad (32)$$

---

[4]Truesdell [1955] used the upper-convected derivative of Oldroyd [1950] for establishing stress rate in his original formulation of hypoelasticity, although no mention was made by Truesdell of Oldroyd's pioneering work in the field.

where μ is the shear modulus, α and β are dimensionless material constants, $p = -\frac{1}{3} \operatorname{tr} \bar{T}$ is the hydrostatic pressure, and $\dot{\wp}$ is a Lagrange multiplier that is distinct from pressure p. This Lagrange multiplier is a workless constraint, that is, $\operatorname{tr} \dot{\bar{E}} = 0$, whose value is indeterminate, and can only be fixed after a boundary value problem has been specified.

Equations (30) and (32) rotate into the Eulerian frame κ by premultiplying them with R, and postmultiplying them with R^T, thereby producing

$$\hat{T} = \big((\alpha_1 + \alpha_3 \operatorname{tr} T) \operatorname{tr} D + \alpha_5 \operatorname{tr}(TD)\big) I + (\alpha_2 + \alpha_4 \operatorname{tr} T) D + \alpha_5 \operatorname{tr}(D) T + \alpha_6 \operatorname{sym}(TD) \qquad (33)$$

and

$$\hat{T} + \dot{\wp} I = 2(\mu - \alpha p) D + 2\beta \operatorname{sym}(TD), \qquad (34)$$

respectively, where now $p = -\frac{1}{3} \operatorname{tr} T \equiv -\frac{1}{3} \operatorname{tr} \bar{T}$. Equations (32) and (34) are isotropic three-dimensional generalizations of Fung's one-dimensional law (Equation (1)) for the $\bar{\kappa}$ and κ configurations, respectively.

Remark 4. By assigning $\alpha \equiv \beta$, the material model listed in Equations (32) and (34) for the $\bar{\kappa}$ and κ configurations, respectively, predicts the same stiffening ratios for α ($\beta \equiv \alpha$) and μ as the neo-Hookean solid does for its shear modulus μ [Treloar 1975], as they pertain to differences between the experiments of uniaxial and equibiaxial extension (that is, the modulus coefficients are 3 and 6, respectively).

7.2. Soft tissues. Existing elastic material models for soft tissues are predominantly *hyperelastic* in construction, and typically consider the stress carried by collagen fibers to be modeled as some generalization of an integrated Fung-like solid (see the review articles of Humphrey [2002], Sacks [2000], Viidik [1973], and Weiss and Gardiner [2001]). In particular, stress is taken to be proportional to some deformation tensor, for example, B, with its coefficient of proportionality being a scalar-valued measure of strain written as a Fung-like exponential, as in Equation (2), whose argument is expressed in terms of various components or invariants of strain, as in Equation (3). A notable exception to these theories is the theory of Criscione et al. [2003a] who derived a transversely isotropic pseudo-elastic model for describing the passive response of biomembranes.

In this paper, we break with this longstanding tradition by extending Truesdell's [1955] isotropic, *hypoelastic*, constitutive theory into an anisotropic constitutive theory that is capable of modeling the passive response of soft tissues. Specifically, we consider a class of materials whose anisotropic and isotropic constituents are governed by the respective constitutive formulae

$$\dot{\bar{T}}^f = \frac{\partial \Psi^f (\bar{T}^f, \dot{\bar{E}}^f)}{\partial \dot{\bar{E}}^f} \quad \text{and} \quad \dot{\bar{T}}^m = \frac{\partial \Psi^m (\bar{T}^m, \dot{\bar{E}}^m)}{\partial \dot{\bar{E}}^m}, \qquad (35)$$

with there being no coupling between the arguments of the two material functions Ψ^f and Ψ^m. Consequently, results from the prior section addressing isotropic hypoelastic materials can be applied straightaway, because of Prop. 1, to that of an anisotropic solid which belongs to this class of materials.

In accordance with the constitutive assumption in Equation (35), and assuming an isochoric response, one obtains the general potential

$$\Psi^i = \mu_i \operatorname{tr}(\dot{\bar{E}}^i \dot{\bar{E}}^i) + \frac{\alpha_i}{3} \operatorname{tr}(\bar{T}^i) \operatorname{tr}(\dot{\bar{E}}^i \dot{\bar{E}}^i) + \beta_i \operatorname{tr}(\dot{\bar{E}}^i \bar{T}^i \dot{\bar{E}}^i), \quad i \in \{f, m\},$$

that leads to the constitutive formulation

$$\dot{\bar{T}}^i = 2\big(\mu_i + \frac{\alpha_i}{3}\,\mathrm{tr}\,\bar{T}^i\big)\dot{\bar{E}}^i + 2\beta_i\,\mathrm{sym}(\bar{T}^i\,\dot{\bar{E}}^i),\quad i\in\{f,m\}, \tag{36}$$

each of which has three parameters: μ_i has units of stress and is the small-strain shear modulus of phase i, while α_i and β_i are dimensionless parameters that govern the rate of exponential growth in stress with increasing strain in phase i, wherein α_i is a bulk-like parameter in that it accounts for influences caused by variations in phase pressure. Combining these formulae, in accordance with Prop. 1, implies that the overall polar stress is governed by the differential equation

$$\dot{\bar{T}} + \dot{\wp}\bar{I} = \phi\dot{\bar{T}}^f + (1-\phi)\dot{\bar{T}}^m, \tag{37}$$

where $\dot{\wp}$ is a Lagrange multiplier used to enforce the constraint $\mathrm{tr}\,\dot{\bar{E}}=0$, and where ϕ is the fiber volume fraction.

As with isotropic materials, one can rotate this polar equation for hypoelastic, soft, biological tissues, Equation (36), into the spatial frame κ, resulting in

$$\hat{T}^i = 2\big(\mu_i + \frac{\alpha_i}{3}\,\mathrm{tr}\,T^i\big)\hat{E}^i + 2\beta_i\,\mathrm{sym}(T^i\hat{E}^i),\quad i\in\{f,m\},$$

while Equation (37) maps into κ as

$$\hat{T} + \dot{\wp}I = \phi\hat{T}^f + (1-\phi)\hat{T}^m,$$

wherein, from Equations ((6), (25) and (26)) and Remark 3, the various polar rates of strain obey

$$\hat{E} = \hat{E}^f + \hat{E}^m \equiv D \text{ with } \hat{E}^f = \tfrac{1}{2}\big(A(L-\Omega)+(L^T+\Omega)A\big) \equiv \tfrac{1}{2}\big(A(D+Z)+(D-Z)A\big),$$

and therefore $\hat{E}^m = D - \hat{E}^f$ recalling that $A = R\bar{A}R^T \equiv RA_0R^T$ from Remark 3.

Applications of this theory to specific tissues will follow in future papers.

8. Summary

A constitutive theory designed for modeling the passive behavior of soft biological tissues has been derived. It contains several novel features. Foremost, a hypoelastic construction has been adopted, as in Fung's original one-dimensional model, instead of the hyperelastic constructions that pervade the literature. Anisotropy has been introduced as a geometric property separate from constitutive construction, and a measure for strain rate that arises naturally from the work potential has been used as the independent variable of the theory. The theory was derived in the polar configuration to ensure objectivity, and then mapped into the spatial (Eulerian) configuration.

9. Acknowledgment

References

[Ateshian 2007] G. A. Ateshian, "Anisotropy of fibrous tissues in relation to the distribution of tensed and buckled fibers", *J. Biomech. Eng. (Trans. ASME)* **129** (2007), 240–249.

[Atluri 1984] S. N. Atluri, "On constitutive relations at finite strain: hypo-elasticity and elasto-plasticity with isotropic or kinematic hardening", *Comput. Methods Appl. Mech. Eng.* **43** (1984), 137–171.

[Belytschko et al. 2000] T. Belytschko, W. K. Liu, and B. Moran, *Nonlinear finite elements for continua and structures*, Wiley, Chichester, 2000.

[Billiar and Sacks 2000] K. L. Billiar and M. S. Sacks, "Biaxial mechanical properties of the native and glutaraldehyde-treated aortic valve cusp–part II: a structural constitutive model", *J. Biomech. Eng. (Trans. ASME)* **122** (2000), 327–335.

[Criscione et al. 2003a] J. C. Criscione, M. S. Sacks, and W. C. Hunter, "Experimentally tractable, pseudo-elastic constitutive law for biomembranes: I. theory", *J. Biomech. Eng. (Trans. ASME)* **125** (2003), 94–99.

[Criscione et al. 2003b] J. C. Criscione, M. S. Sacks, and W. C. Hunter, "Experimentally tractable, pseudo-elastic constitutive law for biomembranes: II. application", *J. Biomech. Eng. (Trans. ASME)* **125** (2003), 100–105.

[Dienes 1979] J. K. Dienes, "On the analysis of rotation and stress rate in deforming bodies", *Acta Mech.* **32** (1979), 217–232.

[Dienes 1986] J. K. Dienes, "A discussion of matrial rotation and stress rate", *Acta Mech.* **65** (1986), 1–11.

[Dienes 1987] J. K. Dienes, "Theory of deformation: Part 1, kinematics", Technical Report LA–11063–MS Vol. 1, Los Alamos National Laboratory, December 1987.

[Dienes 2003] J. K. Dienes, "Finite deformation of materials with an ensemble of defects", Technical Report LA–13994–MS, Los Alamos National Laboratory, January 2003.

[Farahani and Naghdabadi 2003] K. Farahani and R. Naghdabadi, "Basis free relations for the conjugate stresses of the strains based on the right stretch tensor", *Int. J. Solids Struct.* **40** (2003), 5887–5900.

[Finger 1894] J. Finger, "Über die allgemeinsten beziehungen zwischen endlichen deformationen und den zugehörigen spannungen in aeolotropen und isotropen substanzen", *Sitzungsberichte der Akademie der Wissenschaften Wien* **103** (1894), 1073–1100.

[Finlay et al. 1995] H. M. Finlay, L. McCullough, and P. B. Canham, "Three-dimensional collagen organization of human brain arteries at different transmural pressures", *J. Vasc. Res.* **32** (1995), 301–312.

[Flanagan and Taylor 1987] D. P. Flanagan and L. M. Taylor, "An accurate numerical algorithm for stress integration with finite rotations", *Comput. Methods Appl. Mech. Eng.* **62** (1987), 305–320.

[Freed and Diethelm 2007] A. D. Freed and K. Diethelm, "Caputo derivatives in viscoelasticity: a non-linear finite-deformation theory for tissue", *Fractional Calculus and Applied Analysis* **10**:3 (2007), 219–248.

[Freed et al. 2005] A. D. Freed, D. R. Einstein, and I. Vesely, "Invariant formulation for dispersed transverse isotropy in aortic heart valves: an efficient means for modeling fiber splay", *Biomech. Model. Mechanobiol.* **4** (2005), 100–117.

[Fung 1967] Y. C. Fung, "Elasticity of soft tissues in simple elongation", *Am. J. Physiol.* **28** (1967), 1532–1544.

[Fung 1973] Y.-C. Fung, "Biorheology of soft tissues", *Biorheology* **10** (1973), 139–155.

[Fung 1993] Y. C. Fung, *Biomechanics: mechanical properties of living tissues*, second edition ed., Springer-Verlag, New York, 1993.

[Gasser et al. 2006] T. C. Gasser, R. W. Ogden, and G. A. Holzapfel, "Hyperelastic modelling of arterial layers with distributed collagen fibre orientations", *J. Roy. Soc. Interface* **3** (2006), 15–35.

[Green 1841] G. Green, "On the propagation of light in crystallized media", *Trans. Cambridge Philos. Soc.* **7** (1841), 121–140.

[Green and Naghdi 1965] A. E. Green and P. M. Naghdi, "A general theory of an elastic-plastic continuum", *Arch. Rational Mech. Anal.* **18** (1965), 251–281.

[Hill 1968] R. Hill, "On constitutive inequalites for simple materials–I", *J. Mech. Phys. Solids* **16** (1968), 229–242.

[Holzapfel 2000] G. A. Holzapfel, *Nonlinear solid mechanics: A continuum approach for engineering*, Wiley, Chichester, 2000.

[Humphrey 2002] J. D. Humphrey, "Continuum biomechanics of soft biological tissues", *P. Roy. Soc. Lond.* **A-459** (2002), 3–46.

[Humphrey and Rajagopal 2002] J. D. Humphrey and K. R. Rajagopal, "A constrained mixture model for growth and remodeling of soft tissues", *Math. Mod. Meth. Appl. S.* **12** (2002), 407–430.

[Hurschler et al. 1997] C. Hurschler, B. Loitz-Ramage, and R. J. Vanderby, "A structurally based stress-stretch relationship for tendon and ligament", *J. Biomech. Eng. (Trans. ASME)* **119** (1997), 392–399.

[Johnson and Bammann 1984] G. C. Johnson and D. J. Bammann, "A discussion of stress rates in finite deformation problems", *Int. J. Solids Struct.* **20** (1984), 725–737.

[Lanir 1983] Y. Lanir, "Constitutive equations for fibrous connective tissues", *J. Biomech.* **16** (1983), 1–12.

[Lee 1969] E. H. Lee, "Elastic-plastic deformation at finite strains", *J. Appl. Mech.* **36** (1969), 1–6.

[Leonov 2000] A. Leonov, "On the conditions of potentiality in finite elasticity and hypo-elasticity", *Int. J. Solids Struct.* **37** (2000), 2565–2576.

[Nash and Hunter 2000] M. P. Nash and P. J. Hunter, "Computational mechanics of the heart: from tissue structure to ventricular function", *J. Elasticity* **61** (2000), 113–141.

[Ogden 1984] R. W. Ogden, *Non-linear elastic deformations*, John Wiley, New York, 1984. Republished by Dover Publications, Mineola, NY, 1997.

[Oldroyd 1950] J. G. Oldroyd, "On the formulation of rheological equations of state", *P. Roy. Soc. Lond.* **200** (1950), 523–541.

[Sacks 2000] M. S. Sacks, "Biaxial mechanical evaluation of planar biological materials", *J. Elasticity* **61** (2000), 199–246.

[Signorini 1930] A. Signorini, "Sulle deformazioni thermoelastiche finite", pp. 80–89 in *Proceedings of the 3rd international congress for applied mechanics*, vol. 2, edited by C. W. Oseen and W. Weibull, Ab. Sveriges Litografiska Tryckerier, Stockholm, 1930.

[Sokolnikoff 1964] I. S. Sokolnikoff, *Tensor analysis: theory and applications to geometry and mechanics of continua*, second edition ed., Applied Mathematics Series, Wiley, New York, 1964.

[Spencer 1972] A. J. M. Spencer, *Deformations in fibre-reinforced materials*, Oxford Science Research Papers, Clarendon Press, Oxford, 1972.

[Szabó and Balla 1989] L. Szabó and M. Balla, "Comparison of some stress rates", *Int. J. Solids Struct.* **25** (1989), 279–297.

[Treloar 1975] L. R. G. Treloar, *The physics of rubber elasticity*, third edition ed., Clarendon Press, Oxford, 1975.

[Truesdell 1955] C. Truesdell, "Hypoelasticity", *J. Rational Mech. Anal.* **4** (1955), 83–133.

[Truesdell 1957] C. Truesdell, "Sulle basi della thermomeccanica", *Rendiconti Lincei* **22**:8 (1957), 33–38, 158–166.

[Usyk et al. 2000] T. P. Usyk, R. Mazhari, and A. D. McCulloch, "Effect of laminar orthotropic myofiber architecture on regional stress and strain in the canine left ventricle", *J. Elasticity* **61** (2000), 143–164.

[Viidik 1973] A. Viidik, "Functional properties of collagenous tissues", *Int. Rev. Connect. Tiss.* **6** (1973), 127–215.

[Weiss and Gardiner 2001] J. A. Weiss and J. C. Gardiner, "Computational modeling of ligament mechanics", *Crit. Rev. Biomed. Eng.* **29** (2001), 303–371.

ALAN DAVID FREED: adfreed@svsu.edu
202 Pioneer Hall, Saginaw Valley State University, University Center, MI 48710, United States

SPLINE-BASED INVESTIGATION OF NATURAL VIBRATIONS OF ORTHOTROPIC RECTANGULAR PLATES OF VARIABLE THICKNESS WITHIN CLASSICAL AND REFINED THEORIES

YAROSLAV M. GRIGORENKO, ALEXANDER YA. GRIGORENKO AND TATYANA L. EFIMOVA

A spline-collocation approach is proposed for studying the natural vibrations of orthotropic rectangular plates of variable thickness. The approach is based on the spline-approximation method and the method of discrete orthogonalization coupled with the step-by-step search method. The study is carried out within the framework of the classical and refined theories of plates. The dynamic response of the plates is studied depending on the variation of the plate thickness, the mechanical parameters, and the type of boundary conditions.

1. Introduction

Plates, as rational structural elements, are widely used in some fields using modern techniques (mainly aircraft construction and shipbuilding). In connection with the wide application of composite materials and structural peculiarities, studying the mechanical behavior of anisotropic plates of varying thickness is currently of great importance. The essential point in securing the reliability of plate-shaped elements is the determination of the natural frequencies and modes with high accuracy. Such knowledge is needed in order to describe the response of the plates to operating conditions. For plates with constant thickness and hinged opposite edges, the solution can be constructed in closed form [Graff 1991; Varvak and Ryabov 1971]. The natural vibrations of orthotropic plates with other boundary conditions have been studied quite actively and are the subject of a number of publications [Leissa 1969; 1981; 1987].

Solutions for forced and natural vibrations of orhotropic plates were obtained in [Sakata and Hosokawa 1988] in the form of double trigonometric series. Lagrangian multipliers were used in [Ramkumar et al. 1987] to solve a similar problem, with allowance being made for shear strains in the first several modes. The superposition method was used in [Gorman 1990] to tabulate natural frequencies for a certain range of stiffness ratios. In [Yu and Cleghorn 1993], the superposition method and affine transformations were used to determine the natural frequencies of partially clamped and partially simply supported orthotropic plates. The Kantorovich method was used in [Bercin 1996] to study the natural vibrations of clamped plates. The natural vibrations of complex anisotropic plates were studied in [Bhat 1985; Kurpa and Chistilina 2003] using variational methods and the R-function method. The natural vibrations of rectangular plates of varying thickness were addressed by many authors. For example, the papers [Chen 1976; 1977] are concerned with the general natural-vibration problem for plates of varying thickness. The transverse vibrations of plates with exponentially varying thickness are studied in [Bhat 1987] and inhomogeneous rectangular plates with parabolically varying thickness in [Tomar et al. 1982]. The natural vibrations

of simply supported plates with linearly varying thickness were investigated in [Appl and Bayers 1965; Bhat 1985; Bhat et al. 1990; Nog and Araar 1989].

The natural vibrations of rectangular plates with varying thickness were studied using Mindlin's theory with lesser activity than in similar investigations fulfilled within the framework of the classical theory of plates. Let us note some works, such as [Mindlin 1951; Mizusava 1993; Mizusava and Condo 2001; Roufacil and Dawe 1980], dedicated to this scientific trend. The collocation method based on orthogonal polynomials was used in [Mikami and Yoshimura 1984] to analyze vibrations of a plate with linearly varying thickness. In [Al-Kaabi and Aksu 1958; Bercin 1996], a method based on the variational procedure in combination with the finite-difference method was used to solve the problems for plates with linearly and parabolically varying thickness. To study the natural vibrations of wedge-like plates with varying thickness, some variants of the spline-element method were used. Note that the above-mentioned publications are devoted to isotropic plates.

The analysis presented allows us to conclude that there is a variety of different approximate approaches to the study of natural vibrations of rectangular plates with boundary conditions, which do not allow us to obtain the solutions in closed form. Recently, computational mathematics, mathematical physics, and mechanics have employed spline widely functions to solve such problems. This is due to the following advantages of the spline-approximation method over other ones: stability of splines against local perturbations, that is, the behavior of a spline in the neighborhood of a point does not affect the overall behavior of the spline (as do, for example, polynomial approximations); better convergence of spline-interpolation compared with polynomial interpolation; and simple and convenient computer implementation of spline algorithms. The use of spline functions in variational, projective, and other discrete-continuous methods allows us to obtain appreciable results compared to the use of classical polynomials and substantially simplify their numerical implementation, leading to highly accurate solutions.

In [Mizusava 1993; Mizusava and Condo 2001], in order to solve one-dimensional boundary-value problems or those reduced to them, which describe bending, stability, and vibrations of plates and shells, the solution is approximated by splines of the third or fifth power and the problem is reduced to a system of algebraic equations. This is more advantageous than other methods from the viewpoint of calculation time and accuracy. In a number of two-dimensional problems concerning the stress-strain state and vibrations of plates and shells under certain boundary conditions, the problem is reduced to a one-dimensional one by using some variational or projective method. Such a problem can be solved by the spline-approximation method.

To solve a two-dimensional linear boundary-value problem and boundary-value problem for eigenvalues, the approach, based on a reduction of a two-dimensional problem to a one-dimensional one by the spline-collocation method in one coordinate direction or by other stable numerical method, has an effective application, along with the above-mentioned approaches to solve the problems in the theory of plates and shells. Here we extend the spline-collocation method proposed in [Grigorenko and Trigubenko 1990] to study the natural vibrations of rectangular orthotropic plates of varying thickness with complex boundary conditions within the framework of different models. The spline-collocation method was used previously in [Grigorenko and Yaremchenko 2004; Grigorenko and Zakhariichenko 2003; 2004].

2. Basic relations and constitutive equations

We will solve the natural-vibration problem for a rectangular orthotropic plate with thickness $h(x, y)$, varying along two coordinate directions, in a rectangular coordinate system (the coordinate plane xOy is the mid-surface of the plate, $0 \le x \le a$, $0 \le y \le b$, $-h/2 \le z \le h/2$).

2A. *Formulation of the problem within the framework of Kirchhoff theory.* We assume that normals to the plate mid-surface under deformation remain straight and perpendicular to this surface and that the normal stresses on elemental areas, which are parallel to the mid-surface, are small and can be neglected. Then, the equations of motion can be written [Lekhnitskii 1957; Varvak and Ryabov 1971] as

$$\frac{\partial Q_x}{\partial x} + \frac{\partial Q_y}{\partial y} = \rho h \frac{\partial^2 w}{\partial t^2}, \quad \frac{\partial M_x}{\partial x} + \frac{\partial M_{xy}}{\partial y} = Q_x, \quad \frac{\partial M_y}{\partial y} + \frac{\partial M_{xy}}{\partial x} = Q_y, \tag{2-1}$$

where x, y are the Cartesian coordinates ($0 \le x \le a$, $0 \le y \le b$), t is time, w is the deflection of the plate, ρ is the density of a material, and Q_x and Q_y are shear forces. The moments M_x, M_y, M_{xy} satisfy the relations

$$M_x = -\left(D_{11}\frac{\partial^2 w}{\partial x^2} + D_{12}\frac{\partial^2 w}{\partial y^2}\right), \quad M_y = -\left(D_{12}\frac{\partial^2 w}{\partial x^2} + D_{22}\frac{\partial^2 w}{\partial y^2}\right), \quad M_{xy} = -2D_{66}\frac{\partial^2 w}{\partial x \partial y}, \tag{2-2}$$

where the stiffness characteristics D_{ij} of the plate are defined by $D_{ij} = B_{ij}h^3(x, y)/12$. Here $B_{11} = E_1/(1 - v_1 v_2)$, $B_{12} = v_2 E_1/(1 - v_1 v_2) = v_1 E_2/(1 - v_1 v_2)$, $B_{22} = E_2/(1 - v_1 v_2)$, $B_{66} = G_{12}$, where E_1, E_2, v_1, and v_2 are the elastic and shear moduli and Poisson's ratios.

The system of equations in (2-1) and (2-2) yields an equivalent differential equation for the deflection:

$$D_{11}\frac{\partial^4 w}{\partial x^4} + D_{22}\frac{\partial^4 w}{\partial y^4} + 2(D_{12} + 2D_{66})\frac{\partial^4 w}{\partial x^2 \partial y^2} + 2\frac{\partial D_{11}}{\partial x}\frac{\partial^3 w}{\partial x^3} + 2\frac{\partial D_{22}}{\partial y}\frac{\partial^3 w}{\partial y^3}$$

$$+ 2\frac{\partial}{\partial y}(D_{12} + 2D_{66})\frac{\partial^3 w}{\partial x^2 \partial y} + 2\frac{\partial}{\partial x}(D_{12} + 2D_{66})\frac{\partial^3 w}{\partial x \partial y^2}$$

$$+ \left(\frac{\partial^2 D_{11}}{\partial x^2} + \frac{\partial^2 D_{12}}{\partial y^2}\right)\frac{\partial^2 w}{\partial x^2} + \left(\frac{\partial^2 D_{12}}{\partial x^2} + \frac{\partial^2 D_{22}}{\partial y^2}\right)\frac{\partial^2 w}{\partial y^2} + 4\frac{\partial^2 D_{66}}{\partial x \partial y}\frac{\partial^2 w}{\partial x \partial y} + \rho h\frac{\partial^2 w}{\partial t^2} = 0. \tag{2-3}$$

It is assumed that all points of the plate vibrate harmonically with a frequency ω, that is, $w(x, y, t) = \hat{w}(x, y)e^{i\omega t}$ (the symbol $\hat{}$ is omitted hereafter).

Let us rearrange Equation (2-3) to the form

$$\frac{\partial^4 w}{\partial x^4} = a_1\frac{\partial^3 w}{\partial x^3} + a_2\frac{\partial^4 w}{\partial x^2 \partial y^2} + a_3\frac{\partial^3 w}{\partial x^2 \partial y} + a_4\frac{\partial^2 w}{\partial x^2} + a_5\frac{\partial^3 w}{\partial x \partial y^2}$$

$$+ a_6\frac{\partial^2 w}{\partial x \partial y} + a_7\frac{\partial^4 w}{\partial y^4} + a_8\frac{\partial^3 w}{\partial y^3} + a_9\frac{\partial^2 w}{\partial y^2} + a_{10}w, \tag{2-4}$$

where the coefficients $a_i = a_i(x, y)$, $i = 1, \ldots, 9$, $a_{10} = a_{10}(x, y, \omega)$ are defined by

$$a_1 = -\frac{2}{D_{11}}\frac{\partial D_{11}}{\partial x}, \quad a_2 = -\frac{2}{D_{11}}(D_{12} + 2D_{66}), \quad a_3 = -\frac{2}{D_{11}}\left(\frac{\partial D_{12}}{\partial y} + 2\frac{\partial D_{66}}{\partial y}\right),$$

$$a_4 = -\frac{2}{D_{11}}\left(\frac{\partial^2 D_{11}}{\partial x^2} + \frac{\partial^2 D_{12}}{\partial y^2}\right), \quad a_5 = -\frac{2}{D_{11}}\left(\frac{\partial D_{12}}{\partial x} + 2\frac{\partial D_{66}}{\partial x}\right), \quad a_6 = -\frac{4}{D_{11}}\frac{\partial^2 D_{66}}{\partial x \partial y},$$

$$a_7 = -\frac{D_{22}}{D_{11}}, \quad a_8 = -\frac{2}{D_{11}}\frac{\partial D_{22}}{\partial y}, \quad a_9 = -\frac{2}{D_{11}}\left(\frac{\partial^2 D_{12}}{\partial x^2} + \frac{\partial^2 D_{22}}{\partial y^2}\right), \quad a_{10} = \frac{\rho}{D_{11}}h(x, y)\omega^2.$$

Let us specify the boundary conditions expressed in terms of the deflection at the edges as $x = 0$, $x = a$, $y = 0$, $y = b$. We will consider the following boundary conditions:

i) All edges are clamped (boundary conditions of type A):

$$w = 0, \frac{\partial w}{\partial y} = 0 \text{ at } y = 0, y = b, \quad w = 0, \frac{\partial w}{\partial x} = 0 \text{ at } x = 0, x = a. \tag{2-5}$$

ii) Three edges are clamped and the fourth one is simply supported (boundary conditions of type B):

$$w = 0, \frac{\partial w}{\partial y} = 0 \text{ at } y = b, \quad w = 0, \frac{\partial w}{\partial x} = 0 \text{ at } x = 0, x = a, \quad w = 0, \frac{\partial^2 w}{\partial y^2} = 0 \text{ at } y = 0,$$

or boundary conditions of type C:

$$w = 0, \frac{\partial w}{\partial y} = 0 \text{ at } y = 0, y = b, \quad w = 0, \frac{\partial w}{\partial x} = 0 \text{ at } x = 0, \quad w = 0, \frac{\partial^2 w}{\partial x^2} = 0 \text{ at } x = a.$$

iii) Two edges are clamped and two are simply supported (boundary conditions of type D):

$$w = 0, \frac{\partial w}{\partial y} = 0 \text{ at } y = 0, \quad w = 0, \frac{\partial^2 w}{\partial y^2} = 0 \text{ at } y = b,$$

$$w = 0, \frac{\partial w}{\partial x} = 0 \text{ at } x = 0, \quad w = 0, \frac{\partial^2 w}{\partial x^2} = 0 \text{ at } x = a, \tag{2-6}$$

or boundary conditions of type E:

$$w = 0, \frac{\partial w}{\partial y} = 0 \text{ at } y = 0, y = b, \quad w = 0, \frac{\partial^2 w}{\partial x^2} = 0 \text{ at } x = 0, x = a,$$

or boundary conditions of type G:

$$w = 0, \frac{\partial w}{\partial x} = 0 \text{ on } x = 0, x = a, \quad w = 0, \frac{\partial^2 w}{\partial x^2} = 0 \text{ on } y = 0, y = b. \tag{2-7}$$

2B. *Formulation of the problem within the framework of Mindlin's theory.* We suppose that the element, which is initially normal to a coordinate surface in the undeformed state, remains rectilinear but perpendicular to the deformable surface of the plate and turns by some angle keeping its length unchanged. Also, the initial forces caused by the deflection of the element of the coordinate surface and by the turn of

the normal element are taken into account. In keeping with this hypothesis, the displacements u_x, u_y, u_z can be written as

$$u_x(x, y, z) = u(x, y) + z\psi_x(x, y), \quad u_y(x, y, z) = v(x, y) + z\psi_y(x, y), \quad u_z(x, y, z) = w(x, y). \quad (2\text{-}8)$$

Here u, v, w are the displacements of the point of a median surface in the x, y, z-directions, respectively, and ψ_x, ψ_y are the full rotation angles of the rectangular element. Then the relations for strains will be defined by

$$e_x(x, y, z) = \varepsilon_x(x, y) + z\varkappa_x(x, y), \quad e_y(x, y, z) = \varepsilon_y(x, y) + z\varkappa_y(x, y),$$
$$e_{xy}(x, y, z) = \varepsilon_{xy}(x, y) + 2z\varkappa_{xy}(x, y), \quad e_{xz}(x, y, z) = \gamma_x(x, y), \quad e_{yz}(x, y, z) = \gamma_y(x, y), \quad (2\text{-}9)$$

where

$$\varepsilon_x = \frac{\partial u}{\partial x}, \quad \varepsilon_y = \frac{\partial v}{\partial y}, \quad \varepsilon_{xy} = \frac{\partial u}{\partial y} + \frac{\partial v}{\partial x}, \quad \varkappa_x = \frac{\partial \psi_x}{\partial x}, \quad \varkappa_y = \frac{\partial \psi_y}{\partial y}, \quad 2\varkappa_{xy} = \frac{\partial \psi_x}{\partial y} + \frac{\partial \psi_y}{\partial x},$$
$$\gamma_x = \psi_x - \theta_x, \quad \gamma_y = \psi_y - \theta_y, \quad \theta_x = -\frac{\partial w}{\partial x}, \quad \theta_y = -\frac{\partial w}{\partial y}. \quad (2\text{-}10)$$

In equations (2-9) and (2-10), $\varepsilon_x, \varepsilon_y, \varepsilon_{xy}$ are tangential strains of a median surface, $\varkappa_x, \varkappa_y, \varkappa_z$ are bending strains, θ_x, θ_y are rotation angles of the normal without considering the transversal shears, and γ_x, γ_y are rotation angles of the normal caused by the transversal shears.

The equations describing natural bending vibrations of the plate can be written as follows:

$$\frac{\partial Q_x}{\partial x} + \frac{\partial Q_y}{\partial y} = \rho h \frac{\partial^2 w}{\partial t^2}, \quad \frac{\partial M_x}{\partial x} + \frac{\partial M_{xy}}{\partial y} - Q_x = \rho \frac{h^3}{12} \frac{\partial^2 \psi_x}{\partial t^2}, \quad \frac{\partial M_y}{\partial y} + \frac{\partial M_{xy}}{\partial x} - Q_y = \rho \frac{h^3}{12} \frac{\partial^2 \psi_y}{\partial t^2}. \quad (2\text{-}11)$$

It is assumed that all points of the plate vibrate harmonically with a frequency ω that is $w(x, y, t) = \hat{w}(x, y)e^{i\omega t}, \psi_x(x, y, t) = \hat{\psi}_x(x, y)e^{i\omega t}, \psi_y(x, y, t) = \hat{\psi}_y(x, y)e^{i\omega t}$ (the symbol ˆ is omitted hereafter). in (2-11) ρ is the density of a material, $h = h(x, y)$ is the plate thickness. The moments M_x, M_y, M_z and shear forces Q_x and Q_y satisfy the elasticity relations

$$M_x = D_{11}\varkappa_x + D_{12}\varkappa_y, \quad M_y = D_{22}\varkappa_y + D_{12}\varkappa_x, \quad M_{xy} = 2D_{66}\varkappa_{xy}, \quad Q_x = K_1\varkappa_x, \quad Q_y = K_1\varkappa_y, \quad (2\text{-}12)$$

which are valid for the orthotropic plate whose orthotropy axes coincide with coordinate axes. In (2-12), the stiffness characteristics K_i and D_{ij} are defined by the formulas

$$K_1 = \tfrac{5}{6}h(x, y)G_{13}, \quad K_2 = \tfrac{5}{6}h(x, y)G_{23}, \quad D_{ij} = \frac{B_{ij}h^3(x, y)}{12}, \quad B_{11} = \frac{E_1}{1 - \nu_1\nu_2},$$
$$B_{12} = \frac{\nu_2 E_1}{1 - \nu_1\nu_2} = \frac{\nu_1 E_2}{1 - \nu_1\nu_2}, \quad B_{22} = \frac{E_2}{1 - \nu_1\nu_2}, \quad B_{66} = G_{12}.$$

Here E_i, G_{ij}, and ν_i are the Young's and shear moduli and Poisson's ratios, respectively. Having introduced the notation $\tilde{w} = \partial w/\partial x, \tilde{\psi}_x = \partial \psi_x/\partial x$, and $\tilde{\psi}_y = \partial \psi_y/\partial x$, we can write the resolving equations

for functions w, $\tilde{w}$, ψ_x, $\tilde{\psi}_x$, ψ_y, and $\tilde{\psi}_y$ as

$$\frac{\partial w}{\partial x} = \tilde{w}, \quad \frac{\partial \psi_x}{\partial x} = \tilde{\psi}_x, \quad \frac{\partial \psi_y}{\partial x} = \tilde{\psi}_y,$$

$$\frac{\partial \tilde{w}}{\partial x} = a_{11} w + a_{12} \frac{\partial w}{\partial y} + a_{13} \frac{\partial^2 w}{\partial y^2} + a_{14} \tilde{w} + a_{15} \psi_x + a_{16} \tilde{\psi}_x + a_{17} \psi_y + a_{18} \frac{\partial \psi_y}{\partial y},$$

$$\frac{\partial \tilde{\psi}_x}{\partial x} = a_{21} \tilde{w} + a_{22} \psi_x + a_{23} \frac{\partial \psi_x}{\partial y} + a_{24} \frac{\partial^2 \psi_x}{\partial y^2} + a_{25} \tilde{\psi}_x + a_{26} \frac{\partial \psi_y}{\partial y} + a_{27} \psi_y + a_{28} \frac{\partial \tilde{\psi}_y}{\partial y},$$

$$\frac{\partial \tilde{\psi}_x}{\partial x} = a_{31} \frac{\partial w}{\partial y} + a_{32} \frac{\partial \psi_x}{\partial y} + a_{33} \tilde{\psi}_x + a_{34} \frac{\partial \tilde{\psi}_x}{\partial y} + a_{35} \psi_y + a_{36} \frac{\partial \psi_y}{\partial y} + a_{37} \frac{\partial^2 \psi_y}{\partial y^2} + a_{38} \tilde{\psi}_y.$$

$$(2\text{-}13)$$

The coefficients a_{ij} in system (2-13) are

$$a_{11} = -\frac{\rho h \omega^2}{K_1}, \quad a_{12} = a_{17} = -\frac{1}{K_1} \frac{\partial K_2}{\partial y}, \quad a_{13} = a_{18} = -\frac{K_2}{K_1}, a_{14} = a_{15} = -\frac{1}{K_1} \frac{\partial K_1}{\partial x}, \quad a_{16} = -1,$$

$$a_{21} = \frac{K_1}{D_{11}}, \quad a_{22} = \frac{1}{D_{11}} \Big(K_1 - \rho \frac{h^3}{12} \omega^2\Big), \quad a_{23} = a_{27} = -\frac{1}{D_{11}} \frac{\partial D_{66}}{\partial y},$$

$$a_{24} = -\frac{D_{66}}{D_{11}}, \quad a_{25} = -\frac{1}{D_{11}} \frac{\partial D_{11}}{\partial x}, \quad a_{26} = -\frac{1}{D_{11}} \frac{\partial D_{12}}{\partial x}, \quad a_{28} = -\Big(\frac{D_{12} + D_{66}}{D_{11}}\Big),$$

$$a_{31} = \frac{K_2}{D_{66}}, \quad a_{32} = a_{38} = -\frac{1}{D_{66}} \frac{\partial D_{66}}{\partial x}, \quad a_{33} = -\frac{1}{D_{66}} \frac{\partial D_{12}}{\partial y}, \quad a_{34} = -\Big(\frac{D_{12} + D_{66}}{D_{66}}\Big),$$

$$a_{35} = \frac{1}{D_{66}} \Big(K_2 - \rho \frac{h^3}{12} \omega^2\Big), \quad a_{36} = -\frac{1}{D_{66}} \frac{\partial D_{22}}{\partial y}, \quad a_{37} = -\frac{D_{22}}{D_{66}}.$$

The resolving equations should be supplemented with boundary conditions at the plate edges $x = 0$, $x = a$, $y = 0$, and $y = b$. We will consider the following boundary conditions:

i) All edges are clamped (boundary conditions of type A):

$$w = 0, \psi_x = 0, \psi_y = 0 \text{ at } y = 0, y = b, x = 0, x = a. \qquad (2\text{-}14)$$

ii) Three edges are clamped, the fourth is simply supported (boundary conditions of type B):

$$w = 0, \psi_x = 0, \psi_y = 0 \text{ at } y = 0, y = b, x = 0, \quad w = 0, \frac{\partial \psi_x}{\partial x} = 0, \psi_y = 0 \text{ at } x = a. \qquad (2\text{-}15)$$

iii) Two edges are clamped, the other two are simply supported (boundary conditions of type C):

$$w = 0, \psi_x = 0, \psi_y = 0 \text{ at } x = 0, x = a, \quad w = 0, \psi_x = 0, \frac{\partial \psi_y}{\partial y} = 0 \text{ at } y = 0, y = b. \qquad (2\text{-}16)$$

iv) All edges are simply supported (boundary conditions of type D):

$$w = 0, \frac{\partial \psi_x}{\partial x} = 0, \psi_y = 0 \text{ at } x = 0, x = a, \quad w = 0, \psi_x = 0, \frac{\partial \psi_y}{\partial y} = 0 \text{ at } y = 0, y = b. \qquad (2\text{-}17)$$

3. Solution method

To solve problems (2-4) and (2-13) with the corresponding boundary conditions, the spline-collocation, discrete-orthogonalization, and step-by-step search methods were used.

3A. *Spline-approximation.* We will search for the solution of Equation (2-4) by the Kirchhoff theory in the form

$$w = \sum_{i=0}^{N} w_i(x)\psi_i(y), \tag{3-1}$$

where $w_i(x)$ $(i = 1, \ldots, N)$ are unknown functions and $\psi_i(y)$ are the functions constructed using quintic B-splines $(N > 6)$.

The functions $\psi_i(y)$ are selected in order to satisfy the boundary conditions for $y = const$ using the linear combinations of B-splines

$$\psi_0(y) = \alpha_{11} B_5^{-2}(y) + \alpha_{12} B_5^{-1}(y) + B_5^0(y),$$

$$\psi_1(y) = \alpha_{21} B_5^{-1}(y) + \alpha_{22} B_5^0(y) + B_5^1(y),$$

$$\psi_2(y) = \alpha_{31} B_5^{-2}(y) + \alpha_{32} B_5^0(y) + B_5^2(y),$$

$$\psi_i(y) = B_5^i(y), \quad i = 3, 4, \ldots, N-3,$$

$$\psi_{N-2}(y) = \beta_{31} B_5^{N+2}(y) + \beta_{32} B_5^N(y) + B_5^{N+2}(y),$$

$$\psi_{N-1}(y) = \beta_{21} B_5^{N+1}(y) + \beta_{22} B_5^N(y) + B_5^{N-1}(y),$$

$$\psi_N(y) = \beta_{11} B_5^{N+2}(y) + \beta_{12} B_5^{N+1}(y) + B_5^N(y),$$

where $\psi_i(y) = B_5^i(y)$ $(i = -2, \ldots, N+2, i$ is the spline number) are splines constructed on a uniform mesh Δ with a spacing h_y: $y_{-5} < y_{-4} < \ldots < y_N < y_{N+5} < \ldots < y_{N+5}$, $y_0 = 0$, $y_N = b$,

$$B_5^i(y) = \frac{1}{120} \begin{cases} 0 & \text{at } -\infty < y < y_{i-3}, \\ z^5 & \text{at } y_{i-3} \le y < x_{i-2}, \\ -5z^5 + 5z^4 + 10z^3 + 10z^2 + 5z + 1 & \text{at } y_{i-2} \le y < y_{i-1}, \\ 10z^5 - 20z^4 - 20z^3 + 20z^2 + 50z + 26 & \text{at } y_{i-1} \le y < y_i, \\ -10z^5 + 30z^4 - 60z^2 + 66 & \text{at } y_i \le y < y_{i+1}, \\ 5z^5 - 20z^4 + 20z^3 + 20z^2 - 50z + 26 & \text{at } y_{i+1} \le y < y_{i+2}, \\ (1-z)^5 & \text{at } y_{i+2} \le y < y_{i+3}, \\ 0 & \text{at } y_{i+3} \le y < \infty, \end{cases}$$

where $z = (y - y_k)/h_y$ on the interval $[y_k, y_{k+1}]$, $k = \overline{i-3, i+2}$, $i = \overline{-3, N+2}$, $h_y = y_{k+1} - y_k = const$, α_{ij}, and β_{ij} $(i = 1, 2, 3, j = 1, 2)$ are constant coefficients that depend on the specified boundary conditions at $y = 0$ and $y = b$, respectively.

Let

$$A_\alpha = \begin{bmatrix} \alpha_{11} & \alpha_{12} \\ \alpha_{21} & \alpha_{22} \\ \alpha_{31} & \alpha_{32} \end{bmatrix}, \, A_\beta = \begin{bmatrix} \beta_{11} & \beta_{12} \\ \beta_{21} & \beta_{22} \\ \beta_{31} & \beta_{32} \end{bmatrix}.$$

Then, for edges $y = 0$, $y = b$ we have

$$A_\alpha = A_\beta = \begin{bmatrix} \frac{165}{4} & -\frac{33}{8} \\ 1 & -\frac{26}{33} \\ 1 & -\frac{1}{33} \end{bmatrix}$$

if the edges $y = 0$ and $y = b$ are clamped,

$$A_\alpha = A_\beta = \begin{bmatrix} 12 & -3 \\ -1 & 0 \\ -1 & 0 \end{bmatrix}$$

if those edges are simply supported, and

$$A_\alpha = \begin{bmatrix} \frac{165}{4} & -\frac{33}{8} \\ 1 & -\frac{26}{33} \\ 1 & -\frac{1}{33} \end{bmatrix}, \quad A_\beta = \begin{bmatrix} 12 & -3 \\ -1 & 0 \\ -1 & 0 \end{bmatrix}$$

if the edge $y = 0$ is clamped and the edge $y = b$ is simply supported. Now we rewrite Equation (2-4) as

$$\frac{\partial^4 w}{\partial x^4} = a_1 \frac{\partial^3 w}{\partial x^3} + a_2 \frac{\partial^4 w}{\partial x^2 \partial y^2} + a_3 \frac{\partial^3 w}{\partial x^2 \partial y} + a_4 \frac{\partial^2 w}{\partial x^2}$$

$$+ a_5 \frac{\partial^3 w}{\partial x \partial y^2} + a_6 \frac{\partial^2 w}{\partial x \partial y} + a_7 \frac{\partial^4 w}{\partial y^4} + a_8 \frac{\partial^3 w}{\partial y^3} + a_9 \frac{\partial^2 w}{\partial y^2} + a_{10} w, \quad (3\text{-}2)$$

where $a_i = a_i(x, y)$, $i = 1, 2, \ldots, 9$, $a_{10} = a_{10}(x, y, \omega)$.

Substituting (3-1) into (3-2), we will require that the equation should be satisfied at given collocation points $\xi_k \in [0, b]$ for $k = 0, N$. Let us consider the case where the number of mesh nodes is even, that is, $N = 2n + 1$, $(n \geq 3)$, and the collocation nodes satisfy the conditions $\xi_{2i} \in [y_{2i}, y_{2i+1}]$, $\xi_{2i+1} \in [y_{2i}, y_{2i+1}]$ with $i = 0, 1, \ldots, n$. The interval $[y_{2i}, y_{2i+1}]$ has two collocation points and the adjacent intervals $[y_{2i+1}, y_{2i+2}]$ do not have such points. Within the intervals $[y_{2i+1}, y_{2i+2}]$, the collocation points are selected as follows: $\xi_{2i} = x_{2i} + z_1 h_y$, $\xi_{2i+1} = y_{2i} + z_2 h_y$ with $i = 0, 1, 2, \ldots, n$, where z_1 and z_2 are the roots of the quadratic Legendre polynomial, equal to $z_1 = 1/2 - \sqrt{3}/6$, $z_2 = 1/2 + \sqrt{3}/6$ on the interval $[0, 1]$. Such collocation points are optimal and the accuracy of the approximation substantially increases. As a result, we obtain a system of $N + 1$ linear differential equations for w_i. If $\Psi_j = [\psi_i^{(j)}(\xi_k)]$ with $k, i = 0, \ldots, N$, $j = 0, \ldots, 4$, $\bar{w} = \{w_0, w_1, \ldots, w_N\}^T$, $\bar{a}_r^T = \{a_r(x, \xi_0), a_r(x, \xi_1), \ldots, a_r(x, \xi_N)\}$ for $r = 1, \ldots, 9$, $\bar{a}_{10}^T = \{a_{10}(x, \xi_0, \omega), a_{10}(x, \xi_1, \omega), \ldots, a_{10}(x, \xi_N, \omega)\}$, and $\bar{c} * A$ denotes the matrix $[c_i a_{ij}]$, where vector $\bar{c} = \{c_0, c_1, \ldots, c_N\}^T$ and $A = [a_{ij}]$ with $i, j = 0, \ldots, N$, then the system of differential equations becomes

$$\bar{w}^{IV} = \Psi_0^{-1}(\bar{a}_7 \Psi_4 + \bar{a}_8 \Psi_3 + \bar{a}_9 \Psi_2 + \bar{a}_{10} \Psi) \bar{w} + \Psi_0^{-1}(\bar{a}_5 \Psi_2 + \bar{a}_6 \Psi_1) \bar{w}'$$

$$+ \Psi_0^{-1}(\bar{a}_2 \Psi_3 + \bar{a}_3 \Psi_1 + \bar{a}_4 \Psi_0) \bar{w}'' + \Psi_0^{-1}(\bar{a}_1 \Psi_0) \bar{w}'''.$$

This system can be normalized:

$$\frac{d\bar{Y}}{dx} = A(x, \omega) \bar{Y} \quad (0 \leq x \leq a), \tag{3-3}$$

where

$$\bar{Y} = \left\{ w_1, w_2, \ldots, w_{N+1}, w'_1, w'_2, \ldots, w'_{N+1}, w''_1, w''_2, \ldots, w''_{N+1}, w'''_1, w'''_2, \ldots, w'''_{N+1} \right\}^T,$$

where $w_K^{(I)} = w^{(I)}(x, \xi_K)$ with $K = 1, \ldots, N+1$, $I = 1, 2, 3$ and $A(x, \omega)$ is the square matrix of order $(N+1) \times (N+1)$.

The boundary conditions for this system can be expressed as

$$B_1 \bar{Y}(0) = \bar{0}, \quad B_2 \bar{Y}(a) = \bar{0}. \tag{3-4}$$

To solve the problem using Mindlin's theory, we will present the resolving functions in the form:

$$w(x, y) = \sum_{i=0}^{N} w_i(x)\varphi_{1i}(y), \quad \psi_x = \sum_{i=0}^{N} \psi_{xi}(x)\varphi_{1i}(y), \quad \psi_y = \sum_{i=0}^{N} \psi_{yi}(x)\varphi_{2i}(y), \tag{3-5}$$

where w_i, ψ_{xi}, ψ_{yi} are the searched functions of the variable X and $\varphi_{ij}(y)$ with $j = 1, 2$, $i = 0, 1, \ldots, N$ are the linear combinations of B-splines on the uniform mesh Δ: $0 = y_0 < y_1 < \ldots < y_N = b$ with allowance for boundary conditions at $y = 0$ and $y = b$. The system (2-13) includes derivatives of the resolving functions with respect to the coordinate y not greater than the second order. Thus, approximation by spline functions of the third power can be employed, leading to

$$B_3^i(y) = \frac{1}{6} \begin{cases} 0 & \text{at } -\infty < y < y_{i-2}, \\ z^3 & \text{at } y_{i-2} \leq y < y_{i-1}, \\ -3z^3 + 3z^2 + 3z + 1 & \text{at } y_{i-1} \leq y < y_i, \\ 3z^3 - 6z^2 + 4 & \text{at } y_i \leq y < y_{i+1}, \\ (1-z)^3 & \text{at } y_{i+1} \leq y < y_{i+2}, \\ 0 & \text{at } y_{i+2} \leq y < \infty, \end{cases} \tag{3-6}$$

where $z = (y - y_k)/h_y$ on the interval $[y_k, y_{k+1}]$, $k = \overline{i-2, i+1}$, $i = \overline{-1, N+1}$, $h_y = y_{k+1} - y_k = \text{const}$. In this case, the functions $\varphi_{ji}(y)$ are formed as follows:

i) If the resolving function is equal to zero, then

$$\varphi_{j0}(y) = -4B_3^{-1}(y) + B_3^0(y), \quad \varphi_{j1}(y) = B_3^{-1}(y) - \tfrac{1}{2}B_3^0(y) + B_3^1(y),$$
$$\varphi_{ji}(y) = B_3^i(y), \quad (i = 2, 3, \ldots, N-2). \tag{3-7}$$

ii) If the derivative of the resolving function with respect to y is zero, then

$$\varphi_{j0}(y) = B_3^0(y), \quad \varphi_{j1}(y) = B_3^{-1}(y) - \tfrac{1}{2}B_3^0(y) + B_3^1(y), \quad \varphi_{ji}(y) = B_3^i(y), (i = 2, 3, \ldots, N-2). \tag{3-8}$$

Similar formulas hold for the functions $\varphi_{j,N-1}(y)$ and $\varphi_{j,N}(y)$.

Functions $\varphi_{1i}(y)$ (to define $w(x, y)$ and $\psi_x(x, y)$), as applied to the boundary conditions at the plate edges $y = 0$, $y = b$ being considered in the present paper, were selected in accordance with relation (3-6), because for hinge supporting and clamping $w = \psi_x = 0$. In this case, the function $\varphi_{2i}(y)$ was chosen depending on the type of specified boundary conditions or in the form of linear combination of B-splines (3-6) or (3-7).

Substituting (3-5) into equations (2-13), we will require that they are satisfied at the prescribed collocation points $\xi_k \in [0, b]$ for $k = 0, N$. The selection of the collocation points $\xi_{2i} \in [y_{2i}, y_{2i+1}]$,

$\xi_{2i+1} \in [y_{2i}, y_{2i+1}]$, $(i = 0, 1, \ldots, n)$ in the form $\xi_{2i} = y_{2i} + z_1 h_y$, $\xi_{2i+1} = y_{2i} + z_2 h_y$ with $i = 0, 1, 2, \ldots, n$, where $z_1 = 1/2 - \sqrt{3}/6$ and $z_2 = 1/2 + \sqrt{3}/6$ are the roots of the second-order Legendre polynomials in the segment $[0, 1]$, is optimal. Due to this selection the accuracy of the approximation increases essentially. As a result, we obtain the system of $6(N + 1)$ linear differential equations with respect to functions w_i, $\tilde{w}_i$, ψ_{xi}, $\check{\psi}_{xi}$, ψ_{yi}, $\check{\psi}_{yi}$ with $i = 0, \ldots, N$. Having adopted the notations

$$\Phi_j = [\varphi_{ji}(\xi_k)], \quad k, i = 0, \ldots, N, \, j = 1, 2,$$

$$\bar{w} = \{w_0, w_1, \ldots, w_N\}^T, \quad \bar{\tilde{w}} = \{\tilde{w}_0, \tilde{w}_1, \ldots, \tilde{w}_N\}^T,$$

$$\bar{\psi}_x = \{\psi_{x0}, \psi_{x1}, \ldots, \psi_{xN}\}^T, \quad \bar{\check{\psi}}_x = \{\check{\psi}_{x0}, \check{\psi}_{x1}, \ldots, \check{\psi}_{xN}\}^T,$$

$$\bar{\psi}_y = \{\psi_{y0}, \psi_{y1}, \ldots, \psi_{yN}\}^T, \quad \bar{\check{\psi}}_y = \{\check{\psi}_{y0}, \check{\psi}_{y1}, \ldots, \check{\psi}_{yN}\}^T,$$

$$\bar{a}_{kl}^T = \{a_{kl}(x, \xi_0), a_{kl}(x, \xi_1), \ldots, a_{kl}(x, \xi_N)\},$$

$$(k, l) \in \{(k, l) \mid k = 1, 2, 3; l = 1, \ldots, 8\} \setminus \{(1, 1), (2, 2), (3, 5)\},$$

$$\bar{a}_{11}^T = \{a_{11}(x, \xi_0, \omega), a_{11}(x, \xi_1, \omega), \ldots, a_{11}(x, \xi_N, \omega)\},$$

$$\bar{a}_{22}^T = \{a_{22}(x, \xi_0, \omega), a_{22}(x, \xi_1, \omega), \ldots, a_{22}(x, \xi_N, \omega)\},$$

$$\bar{a}_{35}^T = \{a_{35}(x, \xi_0, \omega), a_{35}(x, \xi_1, \omega), \ldots, a_{35}(x, \xi_N, \omega)\},$$

as well as $\bar{c} * A = [c_i a_{ij}]$ for an $N \times N$ matrix $A = [a_{ij}]$ and a vector $\bar{c} = \{c_0, c_1, \ldots, c_N\}^T$, we can express the system of ordinary differential equations with respect to $\bar{w}$, $\bar{\tilde{w}}$, $\bar{\psi}_x$, $\bar{\check{\psi}}_x$, $\bar{\psi}_y$, $\bar{\check{\psi}}_y$ as

$$\frac{d\bar{w}}{dx} = \bar{\tilde{w}}, \quad \frac{d\bar{\psi}_x}{dx} = \bar{\check{\psi}}_x, \quad \frac{d\bar{\psi}_y}{dy} = \bar{\check{\psi}}_y,$$

$$\frac{d\bar{\tilde{w}}}{dx} = \Phi_1^{-1}(\bar{a}_{11}\Phi_1 + \bar{a}_{12}\Phi_1' + \bar{a}_{13}\Phi_1'' + \bar{a}_{14}\Phi_1)\bar{w} + \Phi_1^{-1}(\bar{a}_{15}\Phi_1)\bar{\psi}_x$$
$$+ \Phi_1^{-1}(\bar{a}_{16}\Phi_1)\bar{\check{\psi}}_x + \Phi_1^{-1}(\bar{a}_{17}\Phi_2 + \bar{a}_{18}\Phi_2')\bar{\psi}_y,$$

$$\frac{d\bar{\check{\psi}}_x}{dx} = \Phi_1^{-1}(\bar{a}_{21}\Phi_1)\bar{\tilde{w}} + \Phi_1^{-1}(\bar{a}_{22}\Phi_1 + \bar{a}_{23}\Phi_1' + \bar{a}_{24}\Phi_1'')\bar{\psi}_x + \Phi_1^{-1}(\bar{a}_{25}\Phi_1)\bar{\check{\psi}}_x$$
$$+ \Phi_1^{-1}(\bar{a}_{26}\Phi_2')\bar{\psi}_y + \Phi_1^{-1}(\bar{a}_{27}\Phi_2 + \bar{a}_{28}\Phi_2')\bar{\check{\psi}}_y,$$

$$\frac{d\bar{\check{\psi}}_y}{dy} = \Phi_2^{-1}(\bar{a}_{31}\Phi_1')\bar{w} + \Phi_2^{-1}(\bar{a}_{32}\Phi_1')\bar{\psi}_x + \Phi_2^{-1}(\bar{a}_{33}\Phi_1 + \bar{a}_{34}\Phi_1')\bar{\check{\psi}}_x$$
$$+ \Phi_2^{-1}(\bar{a}_{35}\Phi_2 + \bar{a}_{36}\Phi_2' + \bar{a}_{37}\Phi_2'')\bar{\psi}_y + \Phi_2^{-1}(\bar{a}_{38}\Phi_2)\bar{\check{\psi}}_y,$$

and can be written in the form

$$\frac{d\bar{Y}}{dx} = A(x, \omega)\bar{Y}, \tag{3-9}$$

where $\bar{Y} = \{w_0, \ldots w_N, \tilde{w}_0, \ldots, \tilde{w}_N, \psi_{x0}, \ldots, \psi_{xN}, \check{\psi}_{xo}, \ldots, \check{\psi}_{xN}, \psi_{y0}, \ldots, \psi_{yN}, \check{\psi}_{y0}, \ldots, \check{\psi}_{yN}\}^T$ is a vector function of x and $A(x, \omega)$ is a $6(N+1) \times 6(N+1)$ quadratic matrix. The boundary conditions for this system can be written as

$$B_1\bar{Y}(0) = \bar{0}, \quad B_2\bar{Y}(a) = \bar{0}. \tag{3-10}$$

To solve the eigenvalue problems for the systems of ordinary differential equations with variable coefficients (3-3), (3-4), (3-9), and (3-10), we will use the stable numerical method of discrete-orthogonalization coupled with the step-by-step search method, which makes it possible to obtain the desired solutions with a high degree of accuracy [Grigorenko et al. 1986]. Let us consider in detail the basic principles of the method of discrete orthogonalization.

3B. *Method of discrete orthogonalization.* Let us consider the linear system of differential equations in the Cauchy normal form

$$\frac{d\bar{Y}}{dx} = A(x, \omega)\bar{Y}(x), \quad 0 \le x \le a \tag{3-11}$$

with boundary conditions

$$B_1\bar{Y}(0) = \bar{0}, \tag{3-12}$$

$$B_2\bar{Y}(a) = \bar{0}, \tag{3-13}$$

where $\bar{Y} = \{y_1, y_2, \ldots, y_n\}^T$ is the vector-column, $A(x, \omega)$ is the n-order quadratic matrix, and B_1 and B_2 are matrixes of the order $k \times n$ and $(n - k) \times n$ ($k < n$), respectively.

The boundary-value problem (3-11)–(3-13) was solved by the step-by-step search method coupled with the method of discrete orthogonalization. At the fixed frequency ω the solution of the problem is reduced to the form

$$\bar{Y}(x) = \sum_{j=1}^{m} C_j\bar{Y}_j(x), \tag{3-14}$$

where $m = \min\{k, n - k\}$ (for the sake of definiteness $m = n - k$), $\bar{Y}_j$ are the solutions of the Cauchy problems for the system of equations (3-11) with initial conditions which satisfy the boundary condition (3-12) on the left end of the interval $[0, a]$, and m is the number of boundary conditions on the right end of the interval of integration.

Let us present the boundary conditions (3-12) at the point $x = 0$ in detail:

$$\begin{aligned} b_{11}y_1 + b_{12}y_2 + \cdots + b_{1k}y_k + b_{1,k+1}y_{k+1} + \cdots + b_{1n}y_n &= 0, \\ b_{21}y_1 + b_{22}y_2 + \cdots + b_{2k}y_k + b_{2,k+1}y_{k+1} + \cdots + b_{2n}y_n &= 0, \\ &\vdots \\ b_{k1}y_1 + b_{k2}y_2 + \cdots + b_{kk}y_k + b_{k,k+1}y_{k+1} + \cdots + b_{kn}y_n &= 0. \end{aligned} \tag{3-15}$$

Assuming that the coefficients of the first k columns in (3-15) form a nonsingular matrix, we transfer the rest of the columns to the right-hand side. Then conditions (3-15) take the form

$$\begin{aligned} b_{11}y_1 + b_{12}y_2 + \cdots + b_{1k}y_k &= -b_{1,k+1}y_{k+1} - \cdots - b_{1n}y_n, \\ b_{21}y_1 + b_{22}y_2 + \cdots + b_{2k}y_k &= -b_{2,k+1}y_{k+1} - \cdots - b_{2n}y_n, \\ &\vdots \\ b_{k1}y_1 + b_{k2}y_2 + \cdots + b_{kk}y_k &= -b_{k,k+1}y_{k+1} - \cdots - b_{kn}y_n. \end{aligned} \tag{3-16}$$

Then, setting the components $y_{k+1}, y_{k+2}, \ldots, y_n$ equal to the columns of a unit matrix, we obtain the initial conditions for $\bar{Y}_j$ with $j = 1, 2, \ldots, m$. The Cauchy problems with corresponding initial conditions can be solved by the Runge–Kutta method, for example. The numerical integration is performed in combination with the orthonormalization of vectors $\bar{Y}_j$ ($j = 1, 2, \ldots, m$) at a finite number of points on the interval of change of argument that provides a stable calculation process.

Let us divide the interval $[0, a]$ by integration points x_s with $s = 0, 1, \ldots, N$ into small segments so that $x_0 = 0$ and $x_N = a$. Among these points we choose the points of orthogonalization X_i with $i = 0, 1, \ldots, M$. The choice of points of orthogonalization depends only on the necessary accuracy of the problem solution. Assume that solutions to the Cauchy problems, which we will designate as $\bar{Y}_r(X_i)$ with $r = 1, 2, \ldots, m$, have been obtained at the points X_i using some numerical method. We perform the orthonormalization of the vectors $\bar{Y}_r(X_i)$ at the points X_i and denote the resulting vectors by $\bar{Z}_r(X_i)$. We have

$$\bar{Z}_r = \frac{1}{w_{rr}}\left(\bar{Y}_r - \sum_{j=1}^{r-1} w_{rj}\,\bar{Z}_j\right), \quad r = 1, 2, \ldots, m, \tag{3-17}$$

where

$$w_{rj} = (\bar{Y}_r, \bar{Z}_j)\ (j < r), \quad w_{rr} = \sqrt{(\bar{Y}_r, \bar{Z}_r) - \sum_{j=1}^{r-1} w_{rj}^2}.$$

According to (3-17), at $x = X_i$ we have

$$w_{11}\bar{Z}_1 = \bar{Y}_1, \quad w_{22}\bar{Z}_2 = \bar{Y}_2 - w_{21}\bar{Z}_1, \quad \ldots \quad w_{mm}\bar{Z}_m = \bar{Y}_m - w_{m1}\bar{Z}_1 - w_{m2}\bar{Z}_2 - \cdots - w_{m,m-1}\bar{Z}_{m-1}. \tag{3-18}$$

Having transformed (3-18), we obtain the matrix equality

$$\begin{bmatrix} \bar{Y}_1(X_i) \\ \bar{Y}_2(X_i) \\ \vdots \\ \bar{Y}_m(X_i) \end{bmatrix} = \Omega_i \begin{bmatrix} \bar{Z}_1(X_i) \\ \bar{Z}_2(X_i) \\ \vdots \\ \bar{Z}_m(X_i) \end{bmatrix}, \tag{3-19}$$

where

$$\Omega_i = \Omega(X_i) = \begin{bmatrix} w_{11}(X_i) & 0 & 0 & 0 & \ldots & 0 \\ w_{21}(X_i) & w_{22}(X_i) & 0 & 0 & \ldots & 0 \\ w_{31}(X_i) & w_{32}(X_i) & w_{33}(X_i) & 0 & \ldots & 0 \\ \vdots & \vdots & \vdots & \vdots & & \vdots \\ w_{m-1,1}(X_i) & w_{m-1,2}(X_i) & w_{m-1,3}(X_i) & w_{m-1,4}(X_i) & \ldots & 0 \\ w_{m1}(X_i) & w_{m2}(X_i) & w_{m3}(X_i) & w_{m4}(X_i) & \ldots & w_{mm}(X_i) \end{bmatrix}. \tag{3-20}$$

The vectors $\bar{Z}_r(X_i)$, with $r = 1, 2, \ldots, m$, are the initial values of the Cauchy problems for the system of differential equations (3-11) on the interval $X_i \leq x \leq X_{i+1}$.

Solutions of the system (3-11), which satisfy the boundary conditions on the left end of the interval (3-12), can be written at each point X of discrete orthogonalization in the form of two expressions: prior

to orthogonalization

$$\bar{Y}(X_i) = \sum_{j=1}^{m} C_j^{(i-1)} \bar{Y}_j(X_i), \tag{3-21}$$

and upon orthogonalization

$$\bar{Y}(X_i) = \sum_{j=1}^{m} C_j^{(i)} \bar{Z}_j(X_i). \tag{3-22}$$

We represent the solution of system (3-11) on the interval $X_i \leq X \leq X_{i+1}$ as

$$\bar{Y}(x) = \sum_{j=1}^{m} C_j^{(i)} \bar{Z}_j(x). \tag{3-23}$$

Having integrated the initial system of equations on the last interval $X_{M-1} \leq X \leq X_M$ and having performed the orthogonalization at point X_M by formula (3-17), we obtain

$$\bar{Y}(X_M) = \sum_{j=1}^{m} C_j^{(M)} \bar{Z}_j(X_M). \tag{3-24}$$

Satisfying the boundary conditions on the right end of the integration interval, that is, substituting equation (3-24) into (3-13), we obtain the uniform system of m linear algebraic equations relative to $C_j^{(M)}$ with $j = 1, 2, \ldots, m$. In order for the nontrivial solution of the boundary-value problem (3-11) and (3-12) to exist, it is necessary and sufficient to set the determinant $D(\omega)$ of the system,

$$B_2 \sum_{j=1}^{m} C_j^{(M)} \bar{Z}_j(X_M) = 0, \tag{3-25}$$

equal to zero, that is,

$$D(\omega) = 0. \tag{3-26}$$

In this case, the determinant may be calculated, for example, by the Gauss method. Condition (3-26) is nonlinear with respect to the parameter ω. Because the solution of the boundary-value problem is a continuous function, the dependency $D(\omega)$ is also a continuous function. To solve the nonlinear equation (3-26), we can use, for example, Newton's method or the method of chords. However, these methods may be inefficient, if the initial approximation is chosen improperly. In this case, the use of the step-by-step method for searching the interval of the change in sign of function $D(\omega)$ would be more advantageous. Having determined the interval where the sign changes, we can find the frequency with the necessary accuracy using, for instance, the method of chords or a binary search. To determine the eigenmodes, it is necessary to define the approximate value of C_j^M using the largest minor of the matrix of the system of linear equations.

In what follows, the values of C_j^{i-1} may be determined by values C_j^i with $j = 1, 2, \ldots, m$ beginning with $i = M$. To this end, we equate the right-hand sides of (3-22) and (3-23):

$$\sum_{j=1}^{m} C_j^{(i-1)} \bar{Y}_j(X_i) = \sum_{j=1}^{m} C_j^{(i-1)} \bar{Z}_j(X_i). \tag{3-27}$$

Substituting $\bar{Y}_j$ from (3-19) for $x = X_i$ we find

$$C_1^{(i-1)}w_{11}\bar{z}_1 + C_2^{(i-1)}(w_{21}\bar{z}_1 + w_{22}\bar{z}_2) + C_3^{(i-1)}(w_{31}\bar{z}_1 + w_{32}\bar{z}_2 + w_{33}\bar{z}_3) + \cdots$$
$$\ldots + C_m^{(i-1)}(w_{m1}\bar{z}_1 + w_{m2}\bar{z}_2 + \cdots + w_{mm}\bar{z}_m) = C_1^{(i)}\bar{z}_1 + C_2^{(i)}\bar{z}_2 + \cdots + C_m^{(i)}\bar{z}_m. \quad (3\text{-}28)$$

Equating of the coefficients for vectors $\bar{Z}_j$ for $j = 1, 2, \ldots, m+1$ in (3-28), we obtain

$$\Omega'_i \bar{C}^{(i-1)} = \bar{C}^{(i)}, \quad (i = 1, 2, \ldots, M)$$

or

$$\bar{C}^{(i-1)} = [\Omega'_i]^{-1}\bar{C}^{(i)}, \quad (3\text{-}29)$$

where Ω'_i is the transposed matrix (3-20), $\bar{C}^{(i)}$ is the vector-column with components $C_1^{(i)}, C_2^{(i)}, \ldots, C_m^{(i)}$. So, using Equation (3-29), we may find $C_j^{(i)}$ at all points beginning with $i = M$. The eigenshapes of $\bar{Y}(X_i)$ can be obtained using the formula (3-23) as a solution of the boundary-value problem.

4. Analysis of results

Based on the proposed techniques, the natural vibrations of square and rectangular plates of varying thickness were investigated under different boundary conditions at the edges.

4A. *Investigation of the natural vibrations of plates using Kirchhoff theory.* Let's analyze the natural vibrations of a square plate whose thickness varies as $h(x) = [\alpha(6x^2 - 6x + 1) + 1]h_0$ (Figure 1).

The plate material is orthotropic glass-fabric-reinforced plastic with Young's moduli $E_1 = 4.76 \cdot 10^4$ MPa and $E_2 = 2.07 \cdot 10^4$ MPa, shear modulus $G_{12} = 0.531 \cdot 10^4$ MPa, and Poisson's ratios $\nu_1 = 0.149$, $\nu_2 = 0.0647$. The dimensionless frequencies $\bar{\omega} = \omega a^2 (\rho h_0/D_0)^{1/2}$ with $D_0 = h_0^3/12 \cdot 10^4$ MPa of the clamped plate as determined by Kirchhoff theory with different numbers of collocation points ($N = 10, 12, 14, 16, 18, 20, 22$) differ a little (Table 1).
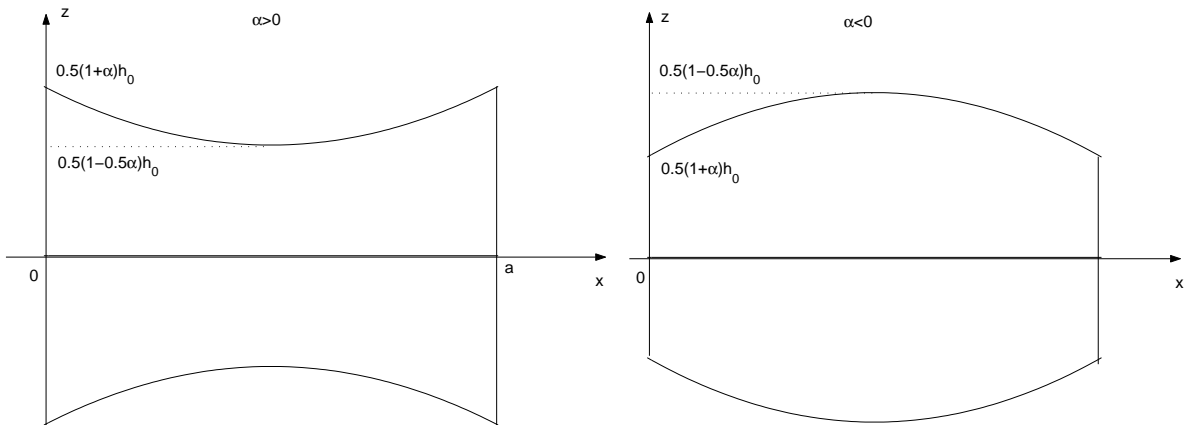
Figure 1. Plate cross-sections for $\alpha > 0$ (left) and $\alpha < 0$ (right).

Tables 2 and 3 collect the dimensionless frequencies ($i = 1, 2, 3$) (ordered by value) of an orthotropic square plate (Kirchhoff theory) for $\alpha \leq 0$ and $\alpha > 0$, respectively, under the boundary conditions (2-5)–(2-7). The number of collocation points is $N = 10$.

α	$\bar{\omega}_i$	N						
		10	12	14	16	18	20	22
0	$\bar{\omega}_1$	61.139	61.132	61.129	61.127	61.127	61.127	61.127
0	$\bar{\omega}_2$	107.188	107.066	107.016	106.994	106.982	106.976	106.972
0	$\bar{\omega}_3$	142.550	142.537	142.532	142.530	142.529	142.528	142.528
0.3	$\bar{\omega}_1$	62.108	62.102	62.099	62.099	62.098	62.098	62.098
0.3	$\bar{\omega}_2$	97.737	97.637	97.598	97.580	97.570	97.566	97.562
0.3	$\bar{\omega}_3$	145.289	145.276	145.271	145.269	145.268	145.268	145.267

Table 1. Values of the dimensionless frequency parameter $\bar{\omega} = \omega a^2 (\rho h_0 / D_0)^{1/2}$, $D_0 = (h_0^3/12) \cdot 10^4$ MPa for a clamped orthotropic square plate with different number of collocation points.

Boundary condition	$\bar{\omega}_i$	α					
		-0.5	-0.4	-0.3	0.2	-0.1	0
A	$\bar{\omega}_1$	58.375	59.012	59.605	60.159	60.674	61,139
	$\bar{\omega}_2$	121.526	119.010	116.240	113.311	110.281	107.188
	$\bar{\omega}_3$	124.339	129.656	134.030	137.585	140.405	142.550
B	$\bar{\omega}_1$	50.227	51.605	52.905	54.129	55.270	56.320
	$\bar{\omega}_2$	102.334	100.723	98.953	97.083	95.147	93.166
	$\bar{\omega}_3$	121.396	126.863	131.384	135.083	138.045	140.330
C	$\bar{\omega}_1$	52.733	52.211	51.624	50.995	50.337	49.659
	$\bar{\omega}_2$	109.151	112.403	110.490	107.334	104.080	100.783
	$\bar{\omega}_3$	116.222	113.496	114.497	116.613	117.777	118.403
D	$\bar{\omega}_1$	43.939	44.009	43.998	43.923	43.790	43.607
	$\bar{\omega}_2$	97.299	95.178	92.905	90.549	88.155	85.755
	$\bar{\omega}_3$	105.958	109.322	111.879	113.750	115.019	115.748
E	$\bar{\omega}_1$	48.701	47.412	46.059	44.676	43.289	41.918
	$\bar{\omega}_2$	95.664	97.177	97.994	98.235	97.985	96.671
	$\bar{\omega}_3$	113.313	110.306	107.049	103.676	100.170	97.306
F	$\bar{\omega}_1$	45.045	49.929	48.698	50.354	51.893	53.306
	$\bar{\omega}_2$	85.738	85.046	84.248	83.378	82.453	81.479
	$\bar{\omega}_3$	119.425	124.989	129.605	133.396	136.448	138.819

Table 2. Effect of thickness variation on the frequency parameter of the Kirchhoff square plate with different boundary conditions ($\alpha \leq 0$).

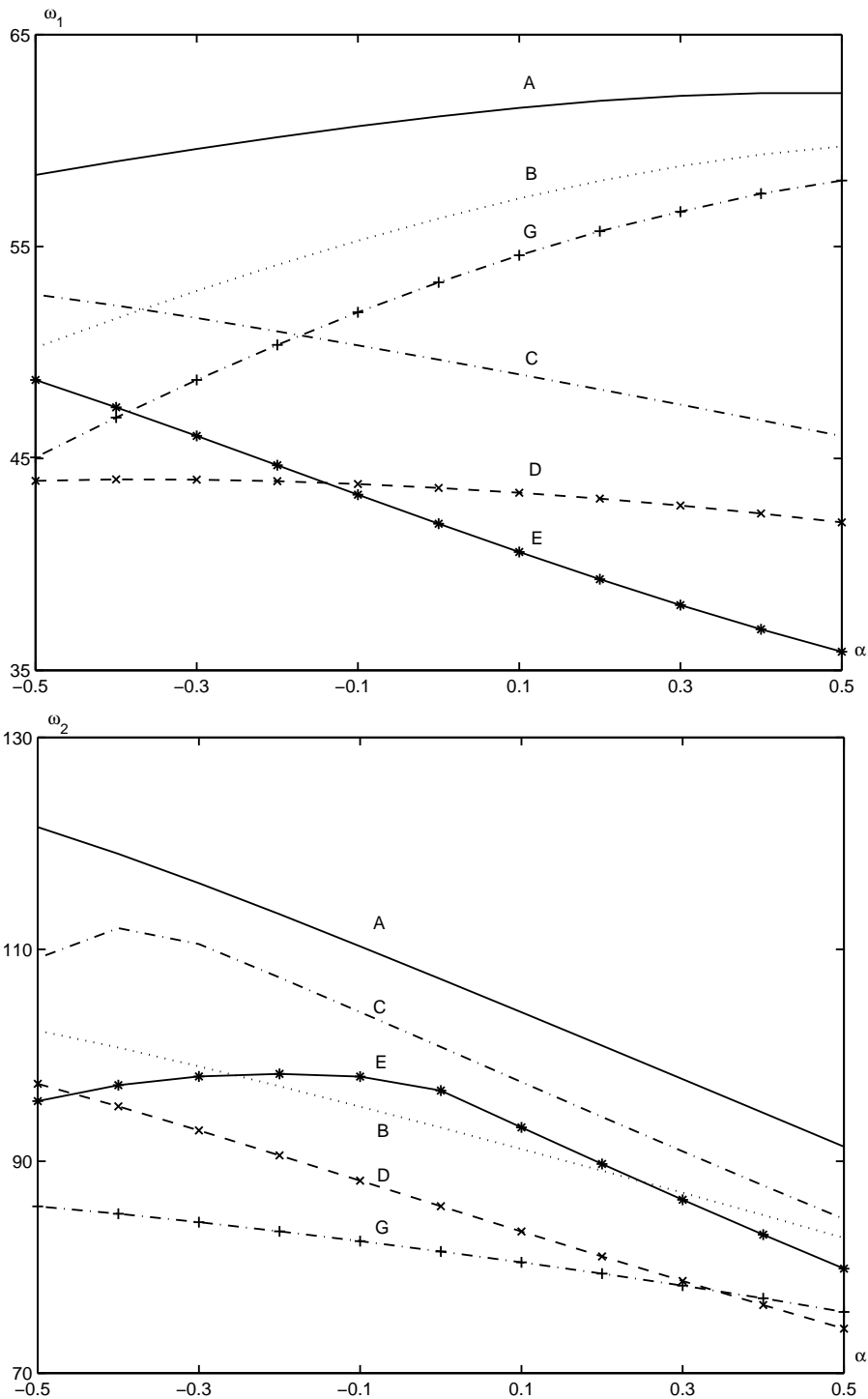| Boundary condition	$\bar{\omega}_i$	α					
		0	0.1	0.2	0.3	0.4	0.5
A	$\bar{\omega}_1$	61.139	61.542	61.871	62.108	62.237	62.238
	$\bar{\omega}_2$	107.188	104.058	100.904	97.737	94.557	91.364
	$\bar{\omega}_3$	142.550	144.062	144.968	145.289	145.035	144.212
B	$\bar{\omega}_1$	56.320	57.266	58.095	58.791	59.339	59.724
	$\bar{\omega}_2$	93.166	91.149	89.104	87.026	84.911	82.749
	$\bar{\omega}_3$	140.330	141.977	143.017	143.469	138.723	131.720
C	$\bar{\omega}_1$	49.659	48.965	48.257	47.535	46.801	46.05
	$\bar{\omega}_2$	100.783	97.477	94.187	90.928	87.713	84.546
	$\bar{\omega}_3$	118.403	118.535	118.208	117.477	116.269	114.688
D	$\bar{\omega}_1$	43.607	43.376	43.098	42.774	42.402	41.982
	$\bar{\omega}_2$	85.755	83.369	81.013	78.694	76.420	74.190
	$\bar{\omega}_3$	115.748	115.981	115.752	115.085	113.998	112.506
E	$\bar{\omega}_1$	41.918	40.583	39.297	38.077	36.933	35.878
	$\bar{\omega}_2$	96.671	93.185	89.743	86.364	83.065	79.858
	$\bar{\omega}_3$	97.306	96.249	94.852	93.149	91.160	88.934
G	$\bar{\omega}_1$	53.306	54.586	55.718	56.642	57.495	58.109
	$\bar{\omega}_2$	81.479	80.460	79.389	78.258	77.055	75.765
	$\bar{\omega}_3$	138.819	140.291	134.815	129.283	123.717	118.135

Table 3. Effect of thickness variation on the frequency parameter of square Kirchhoff plates with different boundary conditions ($\alpha > 0$).

Figure 2 on the next two pages shows the dimensionless vibration frequencies $\bar{\omega}_i$ of a square orthotropic plate with different boundary conditions as a function of the parameter α. The maximum and minimum frequencies $\bar{\omega}_2$ and $\bar{\omega}_3$ correspond to a reorganization of the vibration modes. The frequency of the clamped plate is maximal among all frequencies computed for different boundary conditions and values of α. The first frequency for the boundary conditions of type D changes weakly in comparison with other boundary conditions. The modes of the natural vibrations of a plate with boundary conditions of type G are presented in Figure 3.

4B. *Studying the natural vibrations of plates based on Mindlin's theory.* To evaluate the accuracy of the technique proposed, we analyze the dimensionless vibration frequencies $\bar{\omega} = (\omega a^2/\pi^2)\sqrt{\rho h_0/D}$ of an isotropic square constant-thickness plate, collected in Table 4, for the edge length a, $\nu = 0.3$, $h_0/a = 0.1$. Here the results calculated by Mindlin's and the three-dimensional theories [Liew and Teo 1999] using the various approaches of determining the frequencies as applied to the simply supported edges $y = 0$, $y = a$ are presented. In the case of Mindlin's theory, we used the proposed approach with 16 collocation points. The solution is searched for by application of the trigonometric functions

$$w = \hat{w}(x) \sin \frac{m\pi y}{a}, \qquad \psi_x = \hat{\psi}_x(x) \sin \frac{m\pi y}{a}, \qquad \psi_y = \hat{\psi}_y(x) \cos \frac{m\pi y}{a}, \qquad (4\text{-}1)$$

Figure 2. Dimensionless vibration frequencies $\bar{\omega}_1$ (top) and $\bar{\omega}_2$ (bottom) for the Kirchhoff square orthotropic plate with different boundary conditions as a function of α. The corresponding graphs for $\bar{\omega}_3$ are shown on the next page.
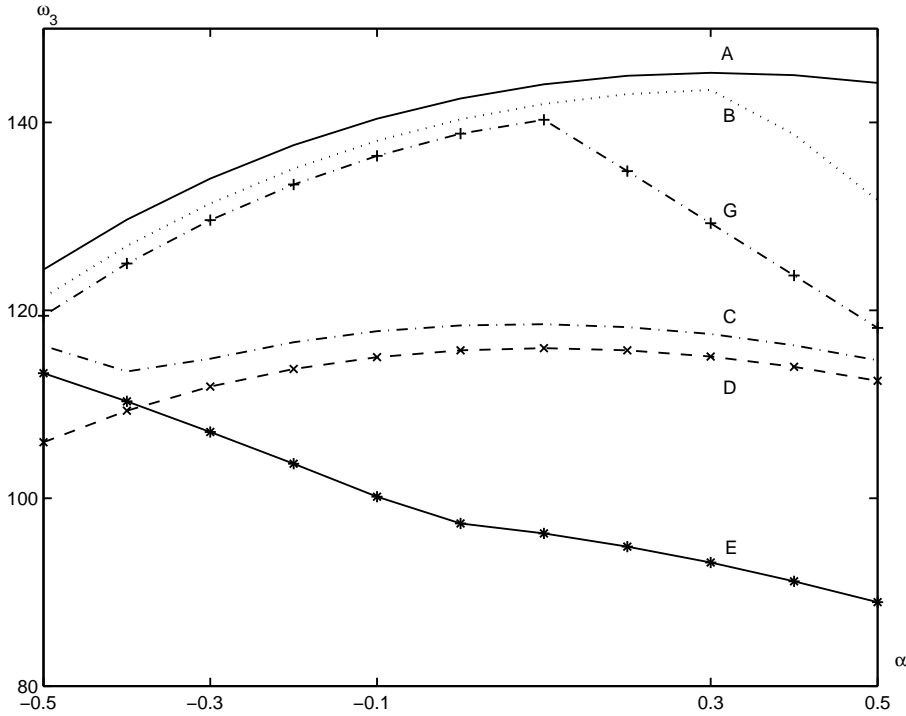
Figure 2, continued.

followed by the discrete-orthogonalization method. Application of the proposed technique yields small differences between the second and third frequencies corresponding to one half-wave in one coordinate direction and two half-waves in the other. Mindlin's theory gives lower frequencies in comparison with those obtained by the spatial theory.

Based on Mindlin's theory and the proposed technique, we studied the spectrum of natural vibrations of a square ($0 \leq x \leq a$, $0 \leq y \leq a$) orthotropic plate (the material is a glass-fabric-reinforced composite with Young's moduli $E_1 = 4.76 \cdot 10^4$ MPa and $E_2 = 2.07 \cdot 10^4$ MPa, shear modulus $G_{12} = 0.531 \cdot 10^4$ MPa, $G_{13} = 0.501 \cdot 10^4$ MPa, $G_{23} = 0.434 \cdot 10^4$ MPa and Poisson's ratios $\nu_1 = 0.149$, $\nu_2 = 0.0647$) for a

$\bar{\omega}$	Three-dimensional theory [Bhat et al. 1990]	Mindlin's theory	
		Spline-collocation method	By expansion (4-1)
$\bar{\omega}_1$	1.9342	1.9320	1.9320
$\bar{\omega}_2$	4.6222	4.6073	4.6073
$\bar{\omega}_3$	4.6222	4.6074	4.6073
$\bar{\omega}_4$	7.1030	7.0818	7.0717
$\bar{\omega}_5$	8.6617	8.6153	8.6153

Table 4. Comparison of frequency parameters calculated for the isotropic square plate of constant thickness with simply supported edges using different theories and methods.
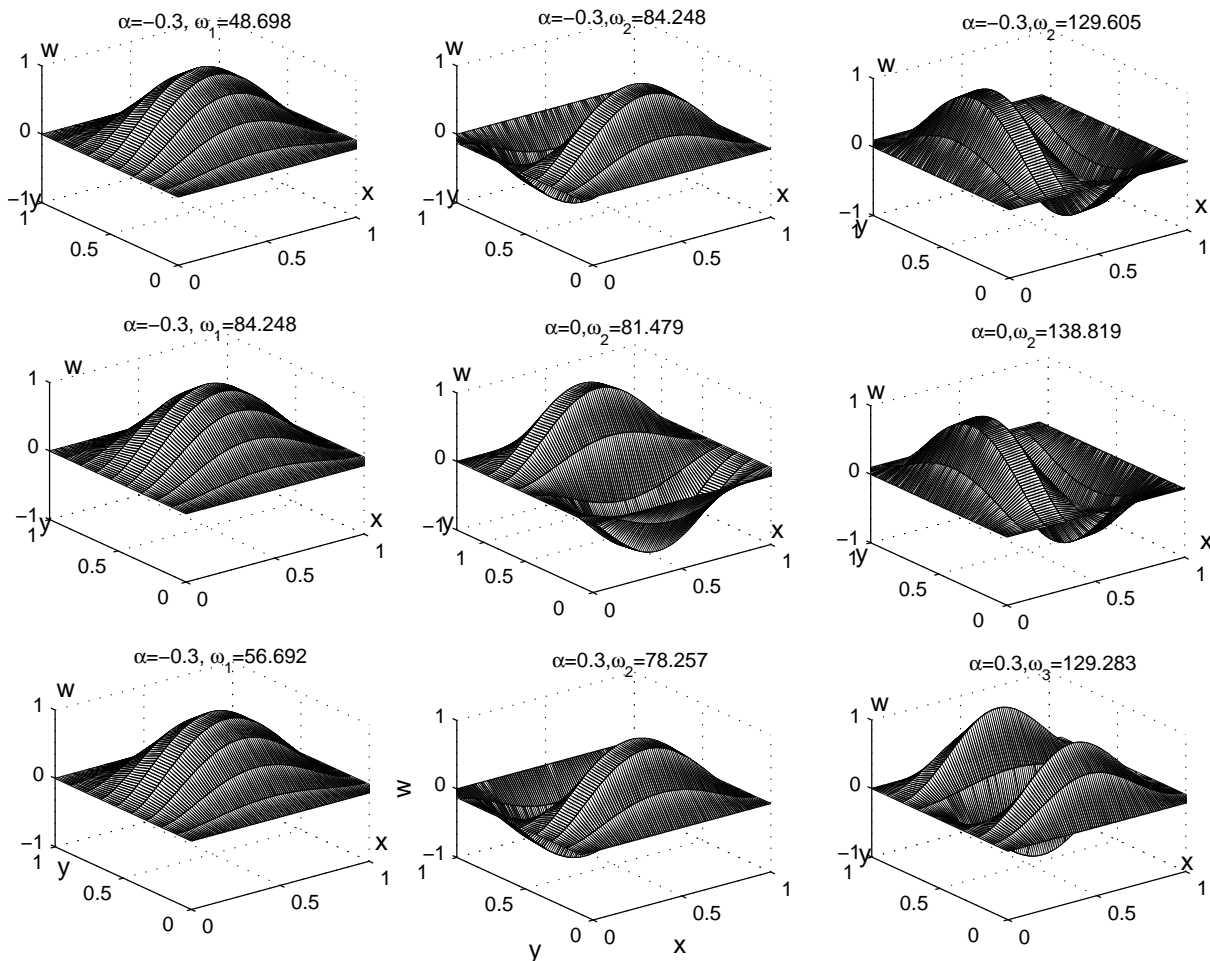
Figure 3. Natural vibration modes of the Kirchhoff orthotropic plate with boundary conditions of type G.

thickness given by the law

$$h(x) = \left[\alpha\left(6\frac{x^2}{a^2} - 6\frac{x}{a} + 1\right) + 1\right]h_0. \tag{4-2}$$

In this case the weight of the plate is independent of α.

To evaluate the accuracy of the proposed technique as applied to plates of varying thickness, we will consider the plate with the boundary conditions (2-7). In this case the solution of the problem may be presented in the form of Equations (4-1). Table 5 collects the values of dimensionless vibration frequencies $\bar\omega = \omega a_0^2(\rho h_0/D_0)^{1/2}$ ($D_0 = h_0^3 \cdot 10^4$ MPa, $h_0 = a_0 = 1$ m) for an orthotropic plate with $h_0/a = 0.1$, $\alpha = 0.4$ with and without the use of splines for different numbers of collocation points. It should be noted that the convergence of the method is faster for modes with one half-wave in the OY-direction ($\bar\omega_1$, $\bar\omega_3$). To reach the desired accuracy, if the number of half-waves increases ($\bar\omega_2$, $\bar\omega_5$ are two half-waves, $\bar\omega_4$ is three half-waves), it is necessary to increase the number of collocation points.

$\bar{\omega}$	Without splines	Using splines					
		$N=9$	$N=11$	$N=13$	$N=15$	$N=17$	$N=19$
$\bar{\omega}_1$	0.1469	0.1469	0.1469	0.1469	0.1469	0.1469	0.1469
$\bar{\omega}_2$	0.2039	0.2065	0.2052	0.2046	0.2043	0.2041	0.2040
$\bar{\omega}_3$	0.2959	0.2959	0.2959	0.2959	0.2959	0.2959	0.2959
$\bar{\omega}_4$	0.3218	0.3356	0.3286	0.3255	0.3240	0.3232	0.3227
$\bar{\omega}_5$	0.3405	0.3419	0.3411	0.3408	0.4307	0.3406	0.3405

Table 5. Comparison of frequency parameters calculated for the isotropic square plate of constant thickness with and without splines for various numbers of collocation points.

Table 6 presents the three first vibration frequencies of a square orthotropic plate ($h/a = 0.1$) for the above-mentioned stiffness coefficients and the law of thickness distribution (4-2) for different values of the parameter α and boundary conditions (2-6)–(2-8) at the ends. The results were obtained from Mindlin's theory. The frequency of plates with all edges being clamped is largest for the boundary conditions under consideration and different values of α. The computations we carried out make it possible to analyze the effect of variance in thickness (with the weight of the plate being constant) and the type of boundary conditions on the distribution of dynamic characteristics of the orthotropic plate within the framework of the applied theory.

Table 7 collects vibration frequencies $\bar{\omega} = a^2\omega\sqrt{\rho h_0/D_0}$, $D_0 = h_0^3 \cdot 10^4$ MPa for a square plate, calculated by Kirchhoff's theory and Mindlin's theory. The plate made from an orthotropic material with the parameters mentioned above and thickness varying according to (4-2).

Boundary condition	$\bar{\omega}_i$	α				
		-0.2	-0.1	0	0.1	0.2
A	$\bar{\omega}_1$	0.1304	0.1393	0.1482	0.1572	0.1665
	$\bar{\omega}_2$	0.2422	0.2445	0.2469	0.2496	0.2525
	$\bar{\omega}_3$	0.2798	0.2855	0.2907	0.2956	0.3002
B	$\bar{\omega}_1$	0.1112	0.1192	0.1275	0.1360	0.1449
	$\bar{\omega}_2$	0.2327	0.2344	0.2364	0.2386	0.2412
	$\bar{\omega}_3$	0.2561	0.2607	0.2651	0.2693	0.2753
C	$\bar{\omega}_1$	0.1200	0.1245	0.1289	0.1333	0.1379
	$\bar{\omega}_2$	0.2016	0.2020	0.2024	0.2029	0.2034
	$\bar{\omega}_3$	0.2718	0.2770	0.2817	0.2859	0.2896
D	$\bar{\omega}_1$	0.0847	0,0841	0.0836	0.0829	0.0823
	$\bar{\omega}_2$	0.1826	0.1807	0.1787	0.1768	0.1750
	$\bar{\omega}_3$	0.2266	0.2273	0.2271	0.2264	0.2249

Table 6. Effect of thickness variation on the frequency parameter of square Mindlin plates with different boundary conditions.

Kirchhoff's theory	Mindlin's theory						
	$a=10h_0$	$a=15h_0$	$a=20h_0$	$a=25h_0$	$a=30h_0$	$a=35h_0$	$a=40h_0$
$\alpha = 0$							
17.943	14.819	16.308	16.976	17.388	17.577	17.754	17.920
$\alpha = 0.2$							
18.834	15.430	17.550	17.840	18.250	18.630	18.811	18.865

Table 7. Comparison of frequency parameter $\bar{\omega} = a^2\omega\sqrt{\rho h_0/D_0}$, $(D_0 = h_0^3 \cdot 10^4 \, \text{MPa})$ calculated for square clamped orthotropic plate by Kirchhoff's and Mindlin's theories.

Table 8 collects the first frequencies $\bar{\omega} = a_0^2\omega\sqrt{\rho h_0/D_0}$, $(D_0 = h_0^3 \cdot 10^4 \, \text{MPa})$ for the orthotropic rectangular plate with the stiffness parameters identical to those already mentioned, and edges $a = a_0 \cdot \beta$, $b = a_0/\beta$, $h_0/a_0 = 0.05$ for different boundary conditions (2-6)–(2-8) at the plate ends. (For this selection of geometrical parameters of the weight of the plate is independent of edge length.)

	β	α						
		-0.3	-0.2	-0.1	0	0.1	0.2	0.3
A	1	0.03987	0.04075	0.04167	0.04261	0.04359	0.04461	0.04565
	2	0.09002	0.08888	0.08719	0.08513	0.08281	0.08026	0.07754
	1/2	0.10105	0.10637	0.11163	0.11686	0.12204	0.12719	0.13234
	5/4	0.04426	0.04396	0.04366	0.04338	0.04311	0.04286	0.04253
	4/5	0.04783	0.04999	0.05219	0.05439	0.05659	0.05880	0.06102
B	1	0.03530	0.03436	0.03541	0.03547	0.03553	0.03559	0.03566
	2	0.08769	0.08765	0.08664	0.08486	0.08266	0.08018	0.07749
	1/2	0.08189	0.08398	0.08588	0.08758	0.08909	0.09040	0.09150
	5/4	0.04223	0.04164	0.04105	0.04045	0.04987	0.03930	0.03876
	4/5	0.03932	0.04003	0.04071	0.04133	0.04190	0.04241	0.04288
C	1	0.03262	0.03407	0.03552	0.03695	0.03842	0.03987	0,04133
	2	0.04571	0.04483	0.04385	0.04279	0.04169	0.04053	0.03933
	1/2	0.10077	0.10061	0.11141	0.11660	0.12185	0.12701	0.13217
	5/4	0.02787	0.02852	0.02908	0.02966	0.03026	0.03087	0.3150
	4/5	0.04525	0.04766	0.05005	0.05244	0.05480	0.05717	0.05954
D	1	0.02238	0.02220	0.02200	0.02179	0.02158	0.02140	0.02125
	2	0.04443	0.04367	0.04279	0.04185	0.04083	0.03975	0.03861
	1/2	0.06379	0.06296	0.06188	0.06057	0.05906	0.05738	0.05555
	5/4	0.02151	0.02162	0.02166	0.02200	0.02165	0.02158	0.02148
	4/5	0.02840	0.02811	0.02774	0.02732	0.02687	0.02639	0.02491

Table 8. Effect of thickness variation on the frequency parameter $\bar{\omega} = a^2\omega\sqrt{\rho h_0/D_0}$ $(D_0 = h_0^3 \cdot 10^4 \, \text{MPa}, h_0/a_0 = 0.05, a = a_0 \cdot \beta, b = a_0/\beta)$ for the orthotropic rectangular plate with different boundary conditions.
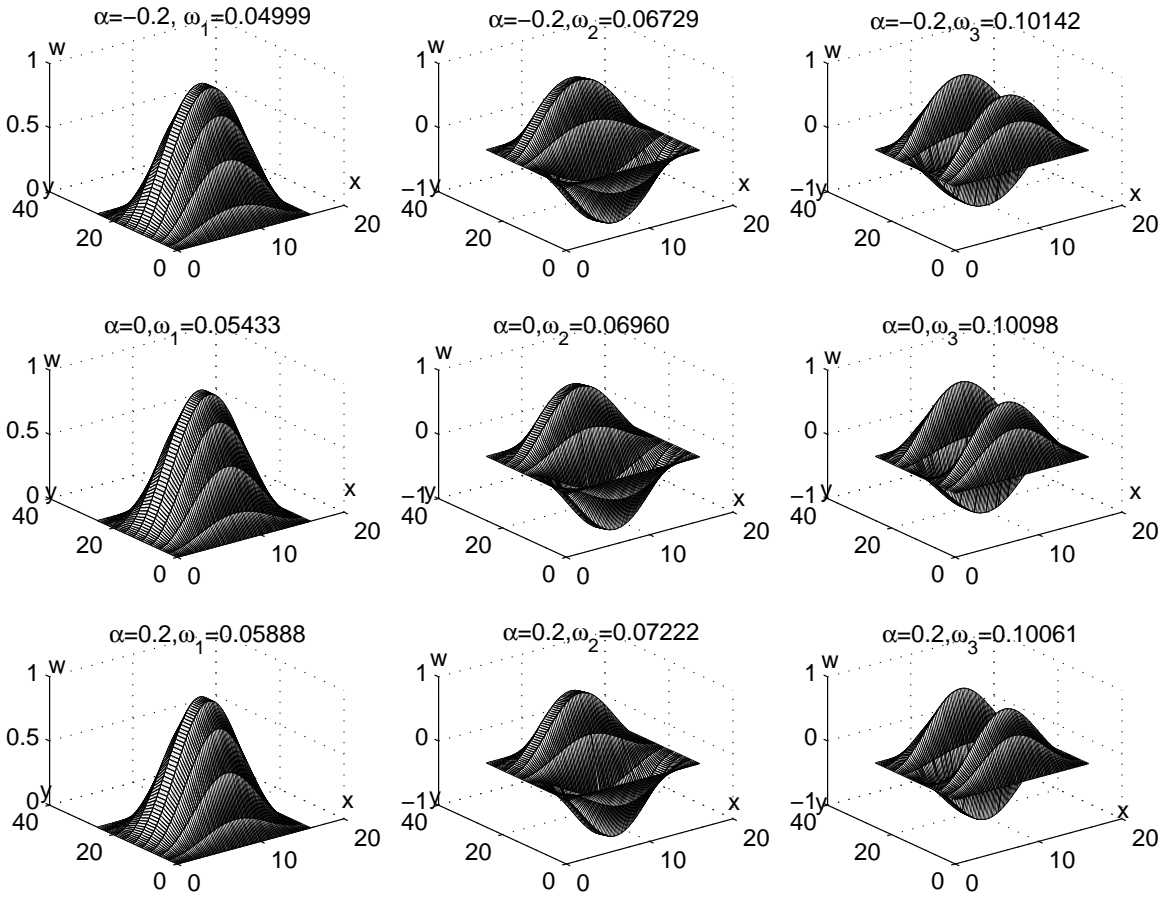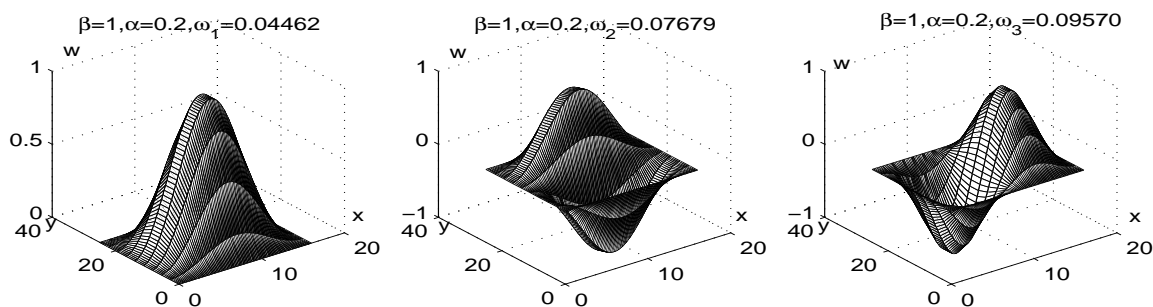
Figure 4. Natural vibration modes of a Mindlin orthotropic rectangular plate with $\beta = 0.8$, $h_0/a_0 = 0.05$ and boundary conditions of type A.

Figure 4 shows forms of deflection for vibrations of a rectangular ($\beta = 0.8$) orthotropic plate with clamped edges and various values of the parameter α. The corresponding graphs for a square plane with $\alpha = 0.2$ are shown in Figure 5. Note that for the third mode the number of half-waves changes along two coordinate directions in the case of square ($m = 2$, $n = 1$) and rectangular ($m = 1$, $n = 3$) plates with insignificant variation of the plate geometry.

5. Conclusions

The paper proposes a spline-collocation approach to study the natural vibrations of orthotropic rectangular variable-thickness plates within the framework of classical (of Kirchhoff's type) and refined (of Timoshenko-Mindlin's type) theory of plates. The approach includes two stages. At the first stage an initial eigenvalue problem for the systems of partial differential equations is reduced to an eigenvalue problem for the system of high-order ordinary differential equations by representing the desired solution in the form of truncated series of spline-collocations and choosing collocation points for the domain under consideration. Application of the spline-approximation makes it possible to satisfy boundary conditions

Figure 5. Natural vibration modes of a Mindlin orthotropic square plate with $\beta = 0.8$, $h_0/a_0 = 0.05$ and boundary conditions of type A.

at the plate edges exactly. The one-dimensional eigenvalue problems obtained are solved by the stable numerical discrete-orthogonalization method in combination with the step-by-step search method that provides a highly accurate solution. The reliability of the results obtained is estimated. Some new problems for natural vibrations of rectangular plates with varying thickness under different boundary conditions at plate edges are solved. The dynamic response of the plate is studied within the framework of different plate theories depending on the law of thickness variation.

References

[Al-Kaabi and Aksu 1958] S. A. Al-Kaabi and G. Aksu, "Free vibration analysis of Mindlin plates with parabolically varying thickness", *Comput. Struct.* **34** (1958), 395–399.

[Appl and Bayers 1965] F. C. Appl and N. R. Bayers, "Fundamental frequency of simply supported rectangular plates with linearly varying thickness", *Trans. ASME Ser. E. J. Mech.* **32** (1965), 163–168.

[Bercin 1996] A. N. Bercin, "Free vibration solution for clamped orthotropic plates using the Kantorovich method", *J. Sound Vibr.* **196** (1996), 243–247.

[Bhat 1985] R. B. Bhat, "Natural frequencies of rectangular plates using characteristic orthogonal polynomials in Rayleigh–Ritz method", *J. Sound Vibr.* **102** (1985), 493–499.

[Bhat 1987] R. B. Bhat, "Flexural vibration of polygonal plates using characteristic orthogonal polynomials in two variables", *J. Sound Vibr.* **114** (1987), 65–71.

[Bhat et al. 1990] R. B. Bhat, P. A. Laura, R. G. Gutierrez, V. N. Cortinez, and H. C. Sanzi, "Numerical experiments on the determination of natural frequencies of transverse vibrations of rectangular plates of non-uniform thickness", *J. Sound Vibr.* **138** (1990), 205–219.

[Chen 1976] S. H. Chen, "Bending and vibration of plates of variable thickness", *Trans. ASME. Ser. B. J. Eng. Industry* **98** (1976), 16–170.

[Chen 1977] S. H. Chen, "Bending and vibration of plates of variable thickness", *Trans. ASME. Ser. B. J. Eng. Industry* **98** (1977), 157–158.

[Gorman 1990] D. J. Gorman, "Accurate free vibration analysis of clamped orthotropic plates by the method of superposition", *J. Sound Vibr.* **140** (1990), 391–411.

[Graff 1991] K. F. Graff, *Wave motion in elastic solids*, Dover, New York, 1991.

[Grigorenko and Trigubenko 1990] A. Y. Grigorenko and T. V. Trigubenko, "Numerical and experimental analysis of natural vibration of rectangular plates with variable thickness", *Int. Appl. Mech.* **36** (1990), 268–270.

[Grigorenko and Yaremchenko 2004] Y. M. Grigorenko and S. N. Yaremchenko, "Stress analysis of orthotropic noncircular cylindrical shells of variable thickness in refined formulation", *Int. Appl. Mech.* **40** (2004), 266–274.

[Grigorenko and Zakhariichenko 2003] Y. M. Grigorenko and L. I. Zakhariichenko, "Studying the effect of the spatial frequency and amplitude of corrugation on the stress-strain state of cylindrical shells", *Int. Appl. Mech.* **39** (2003), 1429–1435.

[Grigorenko and Zakhariichenko 2004] Y. M. Grigorenko and L. I. Zakhariichenko, "Stress-strain analysis of elliptic cylindrical shells under local loads", *Int. Appl. Mech.* **40** (2004), 1157–1163.

[Grigorenko et al. 1986] Y. M. Grigorenko, E. I. Bespalova, A. B. Kitaigorodskii, and A. I. Shinkar, Свободные колебания элементов оболочечных конструкций, Naukova Dumka, Kiev, 1986.

[Kurpa and Chistilina 2003] L. V. Kurpa and A. V. Chistilina, "Investigation of free vibrations of multilayer shallow shells and plates of complex shape in plan", *Probl. Prochn.* **35**:2 (2003), 112–123. In Russian; translated in *Strength Mat.* **35**:2 (2003), 183-191.

[Leissa 1969] A. W. Leissa, "Vibration of plates", technical report SP-160, 1969, Available at http://www.vibrationdata.com/Leissa.htm.

[Leissa 1981] A. W. Leissa, "Plate vibration research: 1976-1980", *Shock Vibr. Digest* **10** (1981), 19–36.

[Leissa 1987] A. W. Leissa, "Recent studies in plate vibrations", *Shock Vibr. Digest* **19** (1987), 10–24.

[Lekhnitskii 1957] S. G. Lekhnitskii, Анизотропные пластинки, Gostekhizdat, Moscow, 1957.

[Liew and Teo 1999] K. M. Liew and T. M. Teo, "Tree-dimensional vibration analysis of rectangular plates based on differential quadrature method", *J. Sound Vibr.* **220** (1999), 577–599.

[Mikami and Yoshimura 1984] T. Mikami and J. Yoshimura, "Application of the collocation method to vibration analysis of rectangular Mindlin plates", *Comput. Struct.* **18** (1984), 425–431.

[Mindlin 1951] R. D. Mindlin, "Influence of rotatory inertia and shear on flexural motion of isotropic elastic plates", *J. Appl. Mech.* **18** (1951), 31–38.

[Mizusava 1993] T. Mizusava, "Vibration of rectangular Mindlin plates with tapered thickness by the spline trip method", *Comput. Struct.* **46** (1993), 451–463.

[Mizusava and Condo 2001] T. Mizusava and Y. Condo, "Application of the spline element method to analyze vibration of skew Mindlin plates", *J. Sound Vibr.* **241** (2001), 495–501.

[Nog and Araar 1989] S. F. Nog and Y. Araar, "Free vibration and buckling analysis of clamped rectangular plates of variable thickness by the Galerkin method", *J. Sound Vibr.* **135** (1989), 263–274.

[Ramkumar et al. 1987] R. L. Ramkumar, P. C. Chen, and W. J. Sanders, "Free vibration solution for clamped orthotropic plates using Lagrangian multiplier technique", *Amer. Inst. Aeronaut. Astronaut.* **25** (1987), 146–151.

[Roufacil and Dawe 1980] O. L. Roufacil and D. J. Dawe, "Vibration analysis of rectangular Mindlin plates by the finite strip method", *Comput. Struct.* **12** (1980), 833–842.

[Sakata and Hosokawa 1988] T. Sakata and K. Hosokawa, "Vibration of clamped orthotropic rectangular plates", *J. Sound Vibr.* **125** (1988), 429–439.

[Tomar et al. 1982] J. S. Tomar, D. C. Gupta, and N. C. Jain, "Vibration of nonhomogeneous plates of variable thickness", *J. Acous. Soc. Amer.* **72** (1982), 851–855.

[Varvak and Ryabov 1971] P. M. Varvak and A. F. Ryabov (editors), Справочник по теории упругости (для инженеров-строителей), Budivel'nyk, Kiev, 1971.

[Yu and Cleghorn 1993] S. D. Yu and W. I. Cleghorn, "Generic free vibration of orthotropic rectangular plates with clamped and simply supported edges", *J. Sound Vibr.* **163** (1993), 439–450.

YAROSLAV M. GRIGORENKO: ayagrigorenko@yandex.ru
S. P. Timoshenko Institute of Mechanics of NAS of Ukraine, Nesterov Street 3, Kiev 03057, Ukraine

ALEXANDER YA. GRIGORENKO: grigyam@yandex.ru
S. P. Timoshenko Institute of Mechanics of NAS of Ukraine, Nesterov Street 3, Kiev 03057, Ukraine

TATYANA L. EFIMOVA: efimovatl@yandex.ru
S. P. Timoshenko Institute of Mechanics of NAS of Ukraine, Nesterov Street 3, Kiev 03057, Ukraine

EFFECTIVE PROPERTIES OF SHEAR BAND STRUCTURES IN ROCK AT DIFFERENT LENGTH SCALES

JOHN NAPIER

Failure localization in rock is observed ubiquitously on geological scales in the form of fault or earthquake damage structures. Similar failure processes are observed in confined compression tests carried out on laboratory-scale rock samples. At an intermediate scale, seismic activity is often associated with the formation of so-called burst fractures that are intermittently formed and exposed in the vicinity of deep level mining operations. Computational modeling can assist the understanding of the complex nature of these failure processes. The present study investigates the question of how the properties of macroscopic shear band features are controlled by microscopic constitutive behavior. The computational approach that is used is to consider the formation of shear band structures by selectively mobilizing members of an assembly of randomly oriented cracks that are modeled as displacement discontinuity elements. Particular issues that are addressed are the question of whether the microscopic failure processes are self-similar to the macroscopic processes, and how the density of the discontinuity assembly affects the localization patterning. It appears that the use of slip or tension-weakening constitutive models yields equivalent "macro" results that are independent of the "micro" mesh density for a given mesh type. If the intrinsic junction coordination of the mesh is altered, it is found that the equivalent macro dilation angle is changed. This has important implications in determining whether a particular distinct element or lattice model with an intrinsic junction structure is capable of replicating the observed failure behavior of a given rock type. A dimensionless parameter group is suggested as a measure of the intrinsic coordination number for a random crack model of rock micro structure.

1. Introduction

Computational modeling of rock failure processes is of great practical value in determining the onset and consequences of stress changes induced by earthquakes, by mining operations, and by the construction of large structures such as dams. This requires the quantitative evaluation of the interactive nature of tectonic loading and of excavation or construction steps and the attendant mobilization of discontinuities and possible fracture of intact rock. A comprehensive review of numerical modeling procedures has been compiled by Jing [2003]. However, the formulation of appropriate constitutive models to use in numerical simulations of rock failure processes is very difficult. Consequently, many computational schemes have been designed to solve discrete assemblies of interacting blocks, bonded particles, or other simple lattice structures that can be assembled to represent macroscopically complex failure patterns. The pioneering development of the so-called Distinct Element Method (DEM) [Cundall 1988; Hart et al. 1988; Potyondy and Cundall 2004] is of particular interest. Numerous applications of distinct element and other lattice models have been applied towards the simulation of granular and quasibrittle material failure in rock, concrete structures, and large-scale fault systems. Representative examples of

these applications are reported in [Lockner and Madden 1991a; 1991b; Bolander et al. 1996; Chiaia et al. 1997; Morgan and Boettcher 1999; Morgan 1999; Budhu et al. 1999; Jefferson et al. 2002; Kuhn 2005; Rechenmacher 2006]. In these examples, failure is initiated by selected breakage or slippage of bonds or linkages within a simulated lattice structure or particle assembly. Individual bonds, interfaces, and internal linkages are assigned simple failure rules and the entire system is allowed to evolve under selected loading steps. Consequent micro fracture sequences are tracked during the simulation and macro coalescence and localization mechanisms are noted. The approach can be applied as well to the study of rock fracture by selecting crack elements sequentially from a random assembly of potential crack positions and evaluating the stress and displacement movements induced by the mobilized cracks using the displacement discontinuity boundary element method; see, for example, [Napier and Peirce 1995; Napier and Malan 1997; Sellers and Napier 1997].

It is apparent that the distinct element and other lattice models are very fruitful in gaining some appreciation of the complex fracture patterning and sequencing that may arise from the incremental loading or straining of particular problem configurations. A number of troublesome issues, though, are not addressed generally. These include the following basic questions:

– Does the characteristic size of the underlying lattice element (for example, particle size, block size, crack length, spring element) affect the emergent failure pattern?

– How should the intrinsic failure rules that are assigned to the micro structure components be assigned or calibrated?

– Do these micro structures have to bear a direct relationship to the actual material micro properties (for example, pore sizes, micro cracks, grain boundaries) and at what length scale should this correspondence be established?

– Can macro failure mechanisms, such as shear bands, be represented by appropriate macro geometric objects, such as individual slip lines, and can the equivalent constitutive properties of the macro objects be deduced from the assigned micro element properties?

– How many micro-macro hierarchical scales should be considered in modeling the material behavior at a given scale of interest?

This paper attempts to address some of these questions by considering a random fracture network simulation of shear failure through an intact bridge region between two adjacent sliding discontinuities. The problem is restricted initially to plane strain conditions. Micro-level failure is assumed to be initiated from a random assembly of crack elements that are at least an order of magnitude smaller than the bridge width. The resulting failure mechanism is then compared to the simulation of the rock bridge as an equivalent slip line linking the adjacent sliding discontinuities. An important property of the fine-scale micro system is identified which appears to control the effective behavior of the macro slip line. This property is related to the connectivity of the random mesh structure at each mesh junction point in terms of the number of potential mesh segments that are attached to each junction and can be thought of as a junction coordination number. It is demonstrated that this topological property of the mesh controls the macro strain behavior of the equivalent slip line failure mechanism and may, in general, determine whether any particular lattice model is intrinsically suitable to simulate failure in a given bonded/disordered material such as rock.

2. Rock failure simulation model

The displacement discontinuity boundary element method (see, for example, [Crouch and Starfield 1983]) is used in the present study to formulate a lattice-type failure model comprising multiple interacting crack segments. It is assumed that loading rates are sufficiently slow that inertial (wave propagation) effects can be neglected. Similar results can, in principle, be obtained by using any computational framework that can represent the interaction of multiple intersecting crack discontinuities in a continuous elastic host medium. Suitable numerical models would include the Distinct Element approach of Cundall [1988], and Finite Element codes having appropriate joint element features (see also [Jing 2003]). The displacement discontinuity boundary element method (DDBEM) does offer a number of useful advantages in terms of computational efficiency when the problem can be considered to comprise multiple crack structures that are embedded within an "infinite" region as only the significant crack surfaces are modeled. The main disadvantages of the DDBEM approach are the necessary assumptions of a fundamental influence function solution for the host medium. These issues are of secondary importance in the context of the present study. Some selected examples of the application of the DDBEM to the study of fracture interaction and propagation processes are reported by [Scavia 1992; Napier and Hildyard 1992; Bobet and Einstein 1998] and [Allodi et al. 2003].

A series of numerical experiments were performed to simulate shear-driven failure between two preexisting sliding discontinuities labeled AB and CD respectively as shown in Figure 1. The dimension, R, of the rock bridge between points B and C in Figure 1 is set to 10 units of length, and the sliding discontinuities are each 50 units in length. These units may be considered nominally to be millimeters although the length scale is actually implied by the ratio of the material shear modulus to the slip-weakening parameter used in the failure model that is described later. A random mesh of potential micro crack segments is superimposed on the rectangular region covering the inner tips of the sliding discontinuities as depicted in Figure 1. Remote compressive principal stress loading components P_1 and P_2 are applied at an oblique angle of 22.5 degrees to the preexisting discontinuities to induce sliding movements and consequent fracturing in the random mesh region. In the present case, P_1 is increased in a series of 24 incremental steps from 20 MPa to 135 MPa, and P_2 is held fixed at a value of 5 MPa. Within
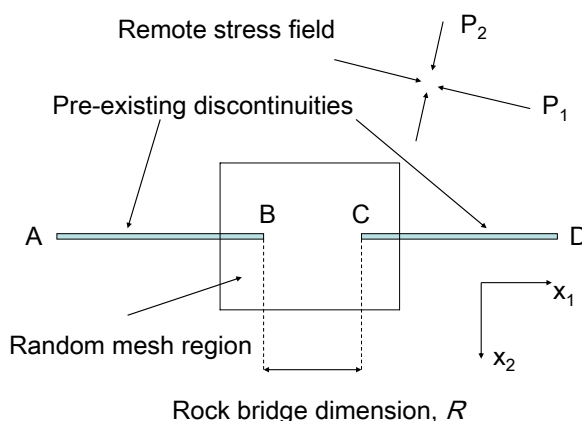
Figure 1. Geometry, principal loading, and dimensions for the numerical experiments.

each load increment, fractures are activated in sequence from the random mesh region according to a defined failure priority. Each activated crack element is assumed to be a straight line segment. The shear slip and crack opening displacement discontinuity components can be defined with respect to a local x-y coordinate system that is centered on each crack element. Suppose that a particular crack element falls in the region $-b \leq x \leq b$ on the x-axis. Define the shear and normal components of the displacement discontinuity vector at the point $x = \eta$ to be $D_x(\eta)$ and $D_y(\eta)$, respectively, where, for each component k,

$$D_k(\eta) = u_k^+(\eta) - u_k^-(\eta) \tag{1}$$

represents the difference in the displacement vector components between the positive $(+)$ and negative $(-)$ sides of the crack with respect to the direction of the positive normal to the crack line.

Define the complex valued discontinuity vector $\Delta(\eta) = D_x(\eta) + i D_y(\eta)$, where $i = \sqrt{-1}$. It can then be shown (see, for example, [Linkov and Mogilevskaya 1994; Mogilevskaya 2000]) that the induced in-plane stress tensor components σ_{xx}, σ_{xy}, and σ_{yy}, are given by the integral relationships

$$\sigma_{xx} + \sigma_{yy} = \frac{iG}{2\pi(1-\nu)} \int_{-b}^{b} \left\{ \frac{\bar{\Delta}(\eta)}{(\bar{Z}-\eta)^2} - \frac{\Delta(\eta)}{(Z-\eta)^2} \right\} d\eta, \tag{2}$$

$$\sigma_{yy} - \sigma_{xx} + 2i\sigma_{xy} = \frac{iG}{2\pi(1-\nu)} \int_{-b}^{b} \left\{ \frac{(\bar{\Delta}(\eta) - \Delta(\eta))}{(Z-\eta)^2} + \frac{2(\bar{Z}-\eta)}{(Z-\eta)^3} \right\} d\eta, \tag{3}$$

where G is the shear modulus, ν is Poisson's ratio, and $Z = x + iy$ is the field point at which the stress components are evaluated. (Note also that the following relationships hold: $\bar{\Delta} = D_x - i D_y$ and $\bar{Z} = x - iy$). In the present study, it is assumed that each of the displacement discontinuity components $D_k(\eta)$, for $k = x$ or y, has a linear variation along the element of the form

$$D_k(\eta) = p_k + q_k \eta, \tag{4}$$

where p_k and q_k are constants that are chosen to ensure that the stress tensor components satisfy local equilibrium boundary conditions at two collocation points located within each element. In this case, the integral expressions in Equations (2) and (3) can be determined from the evaluation of simple integrals of the form

$$I_j(Z) = \int_{-b}^{b} \frac{\eta^j d\eta}{(Z-\eta)}, \quad j = 0 \text{ and } 1 \tag{5}$$

and

$$I_0(Z) = \ln\left[\frac{Z+b}{Z-b}\right], \qquad I_1(Z) = Z I_0(Z) - 2b. \tag{6}$$

Additional expressions can be derived for higher order variation displacement discontinuity vector distributions and for special crack tip shapes, but these possibilities are not considered in the present study.

Each fracture simulation experiment is carried out in a series of incremental crack growth cycles. During each cycle the normal and shear stress traction vector components are evaluated at each collocation point of the current population of unmobilized crack elements that exist in the set of defined mesh segment positions. The normal and shear traction components are determined with respect to the local tangent and normal directions of each mesh segment. A choice is then made of the most likely element to fail according to the effective distance (in terms of the normal and shear traction components) from

a specified failure envelope. Once this choice has been made, the element is added to the population of active crack elements and the entire problem is solved again. The search procedure is continued until no additional crack elements are mobilized. The entire cycle is then repeated for the specified number of far field incremental loading steps. Further details of this approach have been reported in [Napier and Malan 1997].

Figure 2 illustrates the explicit form of the failure envelope and the definition of the stress distance in terms of the normal component σ_n and shear stress component τ acting at a point on a given crack segment. When the normal stress component is tensile (as in the case of point A in Figure 2), the failure envelope is assumed to follow a power law of the form

$$|\tau| = S_0(1 - \sigma_n/T_0)^\gamma, \tag{7}$$

where S_0 is the intact cohesive strength and T_0 is the intact tensile strength of the material at the collocation point. γ is a dimensionless exponent such that $0 < \gamma \leq 1$. The functional form of Equation (7) is chosen to ensure that the failure envelope is smooth in the tensile region and avoids the introduction of a corner point corresponding to a simple tension cut-off parameter. The distance from point A to the failure envelope is measured in the direction of the local origin as depicted in Figure 2. When the normal stress component is compressive ($\sigma_n < 0$), as for point B in Figure 2, the failure envelope is assumed to follow a linear Mohr–Coulomb relationship of the form

$$|\tau| = S_0 - \mu_0\sigma_n, \tag{8}$$

where μ_0 is the intact internal coefficient of friction of the material. The distance from point B to the failure envelope is assumed to be the vertical distance, parallel to the shear stress axis, as shown in Figure 2.

Once failure is initiated, the cohesive strength and tensile strength are assumed to reduce to zero as linear functions of the slip and crack opening displacements, D_x and D_y, respectively. The explicit
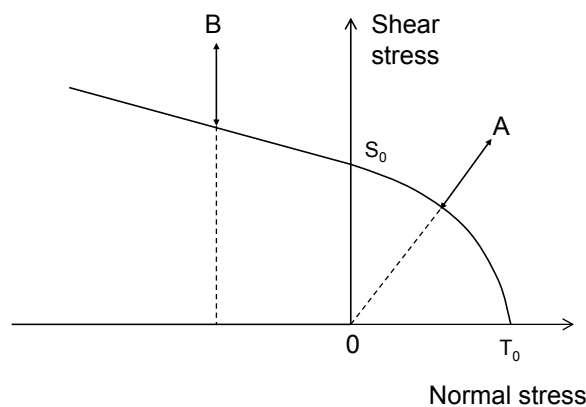
Figure 2. Schematic depiction of the assumed composite failure envelope and definition of the distance of a point from the envelope in terms of normal and absolute shear stress coordinates with respect to a local discontinuity segment line (the normal stress is assumed to be positive when it is tensile).

relationships that are assumed are of the form

$$S = S_0 - \alpha|D_x|, \tag{9}$$

$$T = T_0 - \beta D_y, \tag{10}$$

where S and T are the current values of the shear strength and the cohesion, and α and β are the shear and tension weakening parameters, respectively. The values of S and T are set to zero when the maximum slip and opening displacements implied by Equations (9) and (10) are exceeded. The composite failure envelope, shown in Figure 2, is updated progressively as failure continues by substituting the current values of S and T for S_0 and T_0 in Equations (7) and (8), respectively. It is further assumed that the progressive change in the failure envelope is such that S and T both reach zero simultaneously, and that the friction coefficient μ changes congruently from the intact value μ_0 to a specified residual value μ_f as these changes proceed. The failure envelopes in the tensile and compressive regions in Figure 2 are assumed to have the same slope when $\sigma_n = 0$. This, in turn, implies that the exponent γ must satisfy the relationship

$$\gamma = \mu T/S. \tag{11}$$

The slip-weakening concept [Palmer and Rice 1973; Uenishi and Rice 2003] has a number of important implications. In particular, the weakening behavior imposes an implicit length scale on the material (in some sense analogous to the mean particle size of a particle model) and also implies that numerical experiments of self-similar geometric configurations will exhibit size effects. In addition, it is important to note that the ratio of the host material shear modulus G to the shear weakening parameter α is proportional to an implicit slip nucleation length h_n for a single discontinuity [Uenishi and Rice 2003].

3. Effect of random mesh density

A series of three numerical experiments were performed to assess the consequences of changing the density of the random mesh in the rectangular failure region shown in Figure 1. Specific material strength parameters and slip and tension weakening parameters used in the numerical experiments are summarized in Table 1. These parameters were chosen to be appropriate for a failure region having a characteristic size that is nominally of the order of 10 millimeters. The length scale $\bar{g}$ of the micro flaws comprising the random mesh structure is assumed to be at least one order of magnitude smaller than the bridge dimension R between points B and C in Figure 1 (that is, $\bar{g} \leq 1$ mm). The mesh segment sizes were consequently also much smaller than the slip nucleation length, $h_n \sim G/\alpha = 6$ mm, implied by the parameters given in Table 1. The relative areas under the cohesion and tension weakening curves can be inferred from the parameters in Table 1 to have a ratio of about 15:1. This ratio can be considered, as well, to reflect the ratio of the intrinsic specific fracture energy required to mobilize shear micro cracks compared to the energy required to mobilize tensile micro cracks with an equivalent area.

Three different Delaunay mesh tessellations (designated as A, B, and C) were considered to determine the effect of the mesh density on the evolution of inelastic strain components in the rock bridge region. The size-frequency distribution of the mesh segments corresponding to each applied tessellation pattern is plotted in Figure 3. An approximate mesh density parameter, ρ, can be defined to be

$$\rho = L/\sqrt{A_T}, \tag{12}$$

Shear modulus	30000 MPa
Poisson's ratio	0.2
Cohesion, S_0	20.0 MPa
Tensile strength, T_0	8 MPa
Internal friction coefficient, μ_0	1.0
Residual friction coefficient, μ_f	0.577
Cohesion weakening slope, α	5000 MPa/mm
Tensile strength weakening slope, β	8000 MPa/mm

Table 1. Summary of material properties used in numerical experiments of shear fracture.

where L is the total length of all segments in the tessellation region, and A_T is the area of this region. The values of ρ corresponding to each mesh are included in Figure 3. The mean segment lengths, $\bar{g}$, for the cases A, B, and C are, respectively, equal to 1.023 mm, 0.525 mm, and 0.254 mm (see also, Table 3). Note that the coarsest mesh size, $\bar{g}_A = 1.023$ mm, for mesh A is chosen to be small relative to both the rock bridge dimension, R, and the slip nucleation length, h_n. (Specifically, $\bar{g}_A/R \sim 0.1$ and $\bar{g}_A/h_n \sim 0.17$). The finer mesh sizes for cases B and C were chosen to be approximately equal to one half and one quarter of the initial mesh, respectively, but no special significance is associated with these ratios. Figure 4 shows plots (with displacements magnified by a factor 10) of the fracture patterns developed in the rock bridge region after 24 load step increments of the far-field principal stress component P_1, for each mesh A, B, and C. The crack segments that are initiated in shear mode (that is, when the normal stress values in Figure 2 are negative) are depicted as thick (green) lines in contrast to the crack segments that are initiated under tension conditions (thin lines). It is apparent that both tension and shear failure
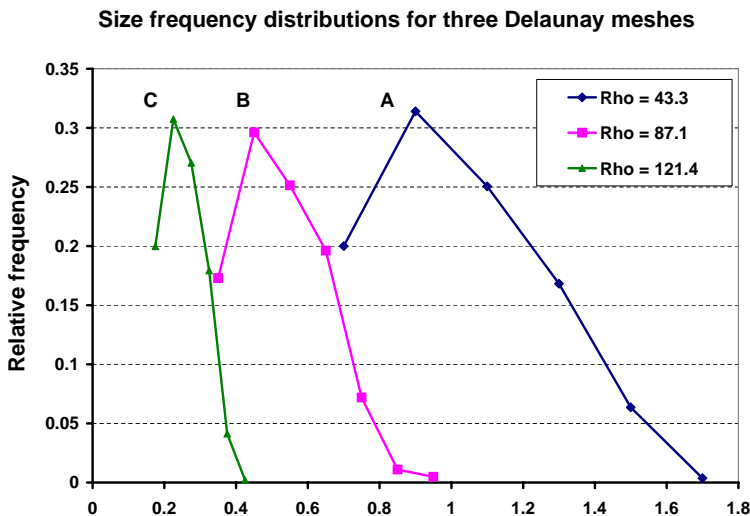
Figure 3. Size-frequency distributions of three Delaunay mesh grids used to simulate failure in the rock bridge region shown in Figure 1.

Fracture pattern - coarse Delaunay mesh

Fracture pattern - intermediate Delaunay mesh

Fracture pattern - fine Delaunay mesh
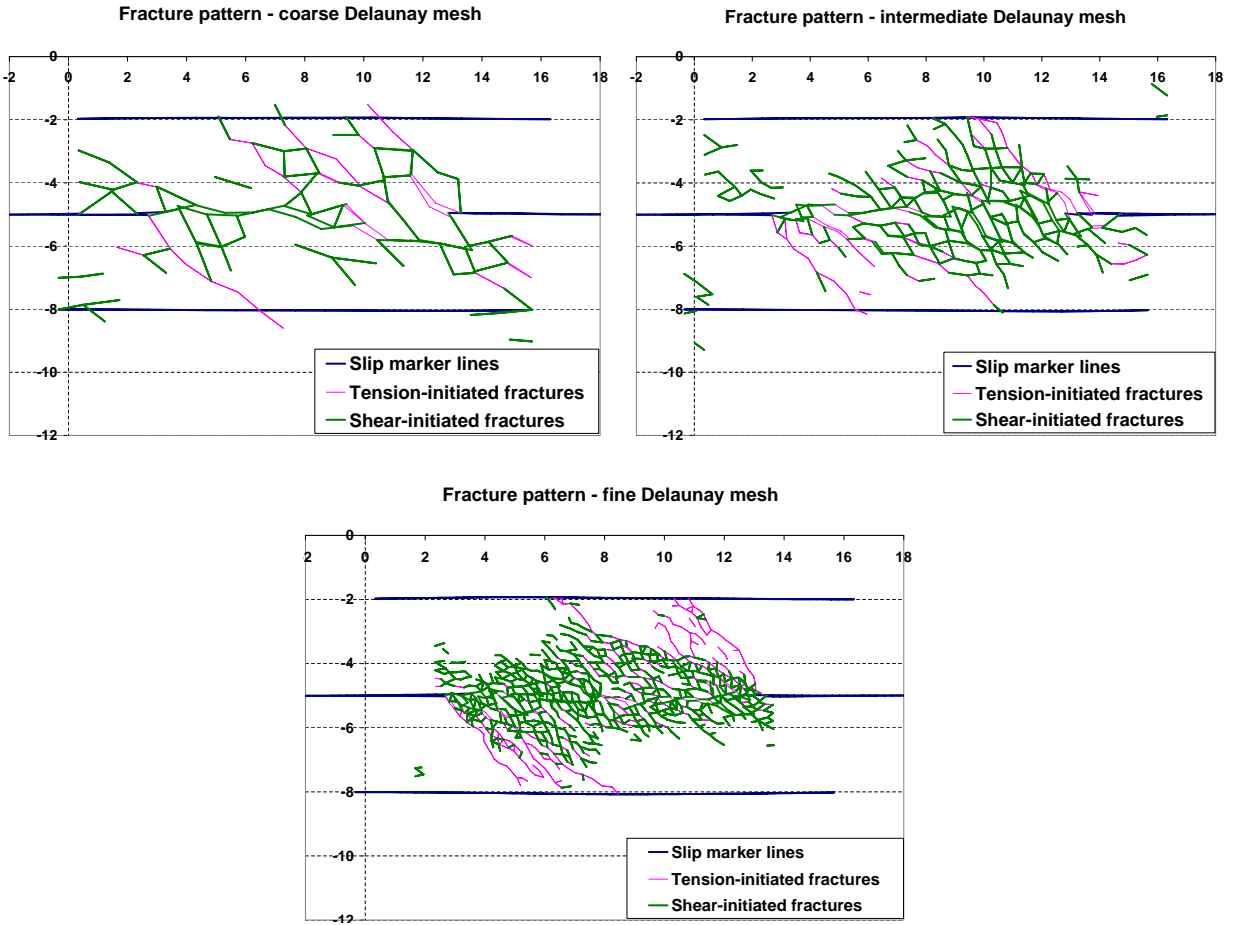
Figure 4. Fracture patterns developed for each Delaunay mesh after 24 load step increments: Coarse (top left), intermediate (top right), and fine (bottom) mesh density.

modes are important in establishing the overall fracture patterns shown in Figure 4. It is apparent as well that the total length of activated crack segments increases as the mesh density increases.

The average strain components, $\bar{\varepsilon}_{ij}$, within the rock bridge region (expressed in the global x_1-x_2 coordinate system shown in Figure 1), are computed for each mesh simulation using the following sum that is taken over all the elements, k, in the region with a total area A_T.

$$\bar{\varepsilon}_{ij} = \frac{1}{2A_T} \sum_k \left(\bar{D}_i^{(k)} n_j^{(k)} + \bar{D}_j^{(k)} n_i^{(k)} \right) g_k. \tag{13}$$

In Equation (13), $\bar{D}_i^{(k)}$ is the average value of component i of the discontinuity vector for element k, $n_i^{(k)}$ is the value of component i of the normal vector to element k, and g_k is the length of element k. The discontinuity and normal vector components are expressed in the global x_1-x_2 coordinate system. The average strain components $\bar{\varepsilon}_{11}$, $\bar{\varepsilon}_{12}$, and $\bar{\varepsilon}_{22}$ are plotted in Figure 5 for each mesh density. The nominal mesh segment sizes of 1 mm, 0.5 mm and 0.25 mm, shown in the legend in Figure 5, are associated with cases A, B, and C respectively. It can be seen from Figure 5 that the average values of each strain
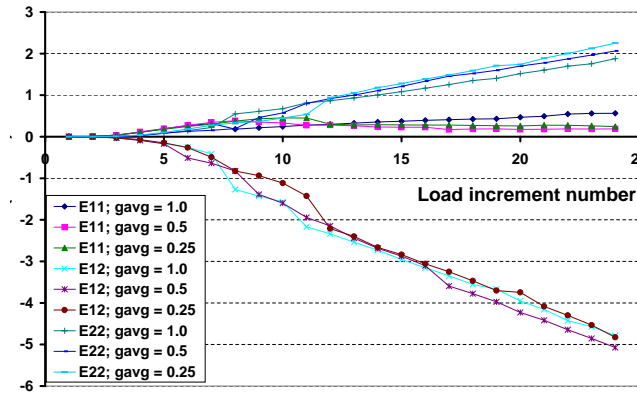
Figure 5. Evolution of average strain components for three Delaunay mesh simulations. For each strain component there are curves corresponding to coarse, intermediate, and fine mesh densities.

component are remarkably similar irrespective of the mesh density. It is observed as well that the values of the strain components, $\bar{\varepsilon}_{11}$, parallel to the direction of the shear sliding cracks are all relatively small. If this component is neglected, a measure of the effective dilation angle ψ in the control volume can be defined to be

$$\tan \psi \sim -\frac{\bar{\varepsilon}_{22}}{2\bar{\varepsilon}_{12}}. \tag{14}$$

The effective dilation angle ψ is plotted in Figure 6 for each mesh density case A, B, and C. It can be seen that as the shear fracture mechanism develops, the dilation angle for each mesh density tends asymptotically to similar constant values ranging approximately between 11 and 13 degrees. It is also observed in Figure 4 that the total length of the random mesh that is activated increases progressively as the mesh density is increased. The cumulative activated length, scaled by the bridge length R between points B and C in Figure 1 is plotted in Figure 7. This suggests that the plastic deformation developed in the fracture zone becomes increasingly "smeared" over increasing numbers of cracks as the underlying
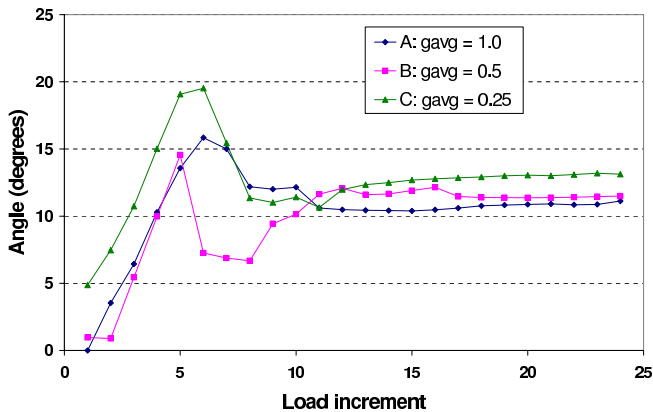
Figure 6. Cumulative dilation angle for three Delaunay mesh densities.
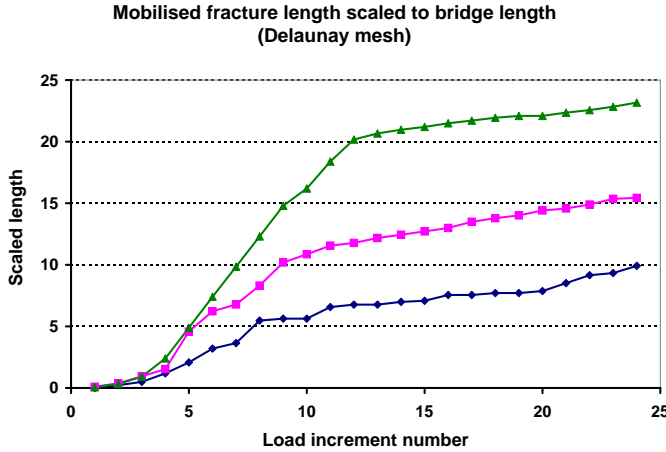
Figure 7. Cumulative fracture length scaled to bridge length for three Delaunay mesh densities. Curves are coded as in Figure 6.

mesh becomes finer. The cohesion loss in each mobilized segment will not necessarily be distributed uniformly. It is not clear at present whether this trend would persist if an even finer mesh were to be used. The current results suggest that the cumulative activated length is approximately proportional to the mesh density parameter, ρ, defined by Equation (12).

4. Topological characteristics of the tessellation mesh

The intrinsic connectivity of the mesh structure can play a significant role in determining the simulated fracture pattern. In order to investigate this, two additional numerical simulations (labeled D and E) were carried out using different intrinsic mesh connectivity properties. For case D, the mesh was constructed by subdividing each triangle of an existing Delaunay mesh as illustrated in Figure 8. The result is termed a *split* Delaunay mesh. It can be seen from the figure that the additional mesh segments will have the effect of doubling the number of segments connected to preexisting vertices $D1$, $D2$, $D3$, and $D4$. Additional vertices of the types labeled $C1$ and $C2$ in Figure 8 are also introduced. The representative vertex $C1$ has six segment connections, and representative vertex $C2$ has four.
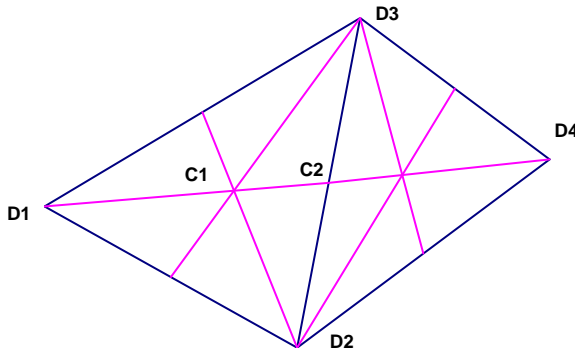
Figure 8. Additional mesh segments introduced into two adjacent Delaunay triangles to create a split Delaunay mesh structure.

A second mesh variation, Case E, was considered, where the mesh is generated as a classical Voronoi structure. Cases D and E were compared to case C, which corresponds to the finest scale Delaunay mesh discussed in the previous section. Table 2 summarizes the relative frequency of the number of segments joining each internal vertex (junction coordination number) of the meshes used in cases C, D, and E. It can be seen that case C (Delaunay mesh) and case E (Voronoi mesh) have a most frequent segment coordination number of 6 and 3 connections respectively. Case D (split Delaunay) is more complex, showing a mixture of doubled vertex coordinations derived from the parent mesh and new vertices with coordination numbers of 6 and 4 corresponding to the points $C1$ and $C2$ in Figure 8. A significant proportion of the vertices in case D have coordination numbers of 10, 12, and 14. A complete summary of the average mesh segment sizes, $\bar{g}$, total segment length, L, and mesh area, A_T, for all cases A to E is given in Table 3.

Coordination number	Relative frequency		
	C (Delaunay)	D (split Delaunay)	E (Voronoi)
3	0	0	0.8436
4	0.0116	0.5000	0.1416
5	0.2474	0	0.0148
6	0.5090	0.3350	0
7	0.2010	0	0
8	0.0296	0.0049	0
9	0.0013	0	0
10	0	0.0416	0
11	0	0	0
12	0	0.0733	0
13	0	0	0
14	0	0.0428	0
15	0	0	0
16	0	0.0024	0

Table 2. Mesh junction coordination frequencies for random mesh cases C, D. and E.

Mesh type	Mesh area, A_T	Grid size, $\bar{g}$	Mesh length, L	Density $\rho = L/\sqrt{A_T}$	Coordination $\lambda = \bar{g}L/A_T$
Delaunay (A)	160	1.023	547.6	43.3	3.50
Delaunay (B)	160	0.525	1101.9	87.1	3.61
Delaunay (C)	72	0.254	1029.9	121.4	3.63
Split Delaunay (D)	160	0.465	1602.1	126.7	4.66
Voronoi (E)	160	0.333	663.2	52.4	1.38

Table 3. Characteristic mesh parameters.
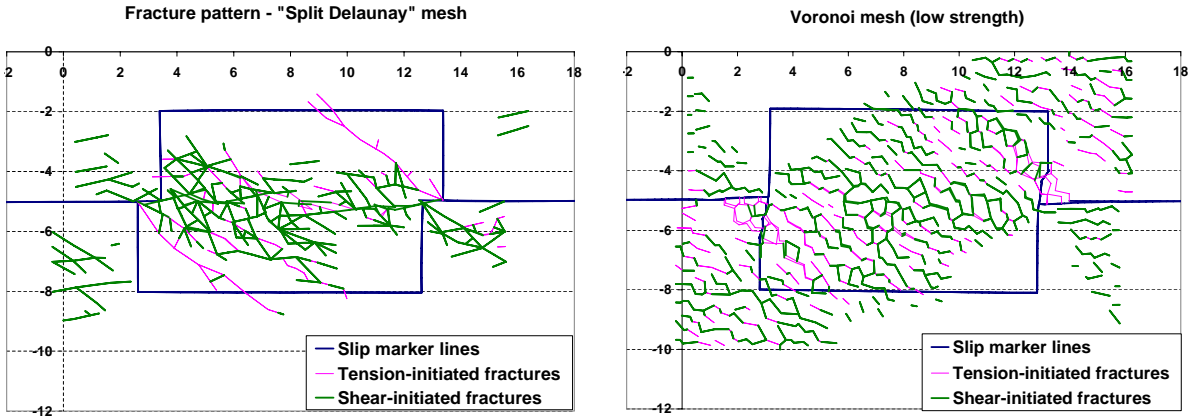
Figure 9. Fracture patterns resulting from two different mesh segment junction coordi-
nation models. Left: split Delaunay mesh; right, Voronoi mesh.

The loading experiments for cases D and E were repeated with the same orientation and number
of load increments used in cases A, B, and C. The material properties for case D were chosen to be
the same as those given in Table 1. However, in case E the cohesion value of 20 MPa and the tensile
strength of 8 MPa, given in Table 1, were reduced to 10 MPa and 4 MPa, respectively, to ensure that a
shear band mechanism was fully developed in the bridge region. The fracture patterns developed for
the split Delaunay and the Voronoi tessellation runs, D and E, are shown in Figure 9. A fixed marker
region around the rock bridge is included to indicate the general deformation pattern. The zone of
fracture activation can be seen to be more concentrated for the split Delaunay mesh than for the Voronoi
mesh. The mobilized fragments in case D appear to be more angular in character than the rounded
grains corresponding to the Voronoi mesh for case E. The effective dilation angles corresponding to the
simulations D and E are compared to case C in Figure 10. It can be seen that the mesh coordination
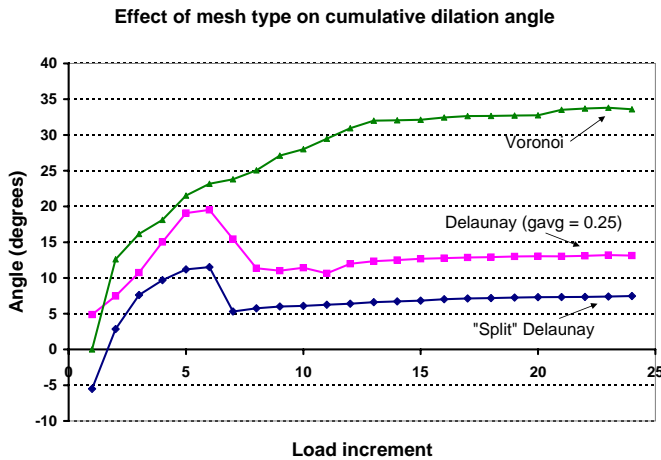
Figure 10. Effect of mesh segment coordination on the effective dilation angle for nu-
merical experiments with three distinct meshes.

structure plays a very significant role in determining the effective response of the bridge region. In particular, it is clear that as the average number of segments attached to each mesh junction decreases, the effective dilation angle increases. An equivalent macro model of the rock bridge deformation must therefore include the intrinsic dilation behavior associated with the properties of the micro mesh structure. A simple equivalent macro model for the rock bridge is to assume that it is represented by a single slip discontinuity line joining points B and C in Figure 1. In this case the asymptotic behavior of the macro model is determined by defining the following macro properties for the slip line in terms of the micro residual friction angle ϕ_f and the observed dilation angle ψ. Specifically,

$$\phi_{\text{macro}} = \psi + \phi_f, \tag{15}$$

$$\mu_f^{\text{macro}} = \tan(\psi + \phi_f). \tag{16}$$

Using the residual macroscopic friction coefficient given by Equation (16) and applying the dilation angles $\psi = 7°$ and $\psi = 33°$ implied by the asymptotic behavior of Figure 10 yields the equivalent average strain component evolution profiles shown in Figure 11. The plots there show that the macro slip line model is asymptotically equivalent to the corresponding average strain behavior of the underlying micro models after a significant numbers of load increments when the shear band mechanism is fully established. The main problem in applying the equivalent macro model is that it is unclear how the dilation angles of $\psi = 7°$ and $\psi = 33°$ can be deduced a priori from the intrinsic mesh structure.

It may be noted by examining the mesh properties reported in Table 3 that an intrinsic relationship can be established between the mean segment size, $\bar{g}$, the total length of the mesh segments, L, and the area of the tessellation mesh, A_T. Specifically, consider the dimensionless mesh coordination parameter, λ, defined by

$$\lambda = \bar{g}L/A_T. \tag{17}$$

The inferred values of λ are given in the last column of Table 3. It is interesting to note that in the case of the Delaunay mesh (cases A, B, and C), the values of λ are very similar (~ 3.6) irrespective of the mesh density, ρ. However, λ is distinctly different for the split Delaunay and Voronoi mesh cases D and E respectively. It appears that λ provides a relative measure of the intrinsic mesh coordination
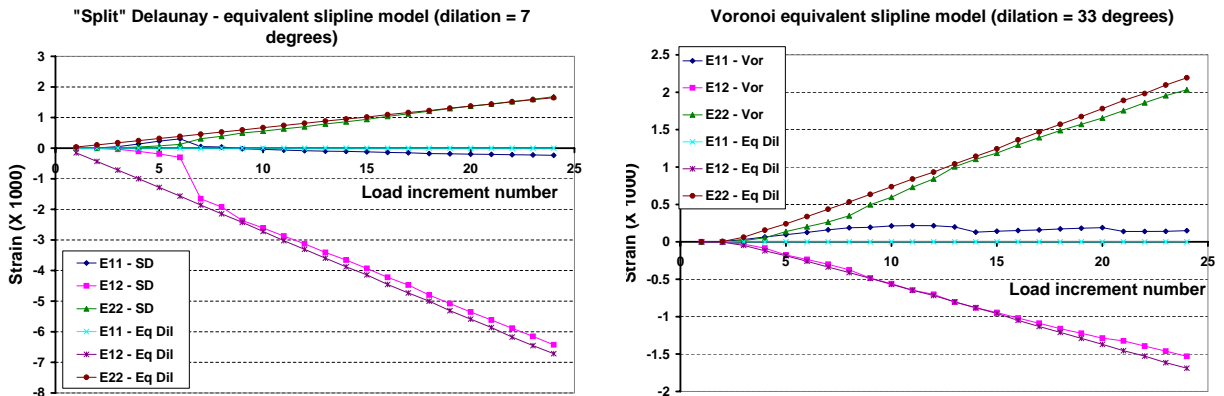
Figure 11. Equivalent slip line model asymptotic evolution of average strain in rock bridge region. Left: split Delaunay mesh; right, Voronoi mesh.
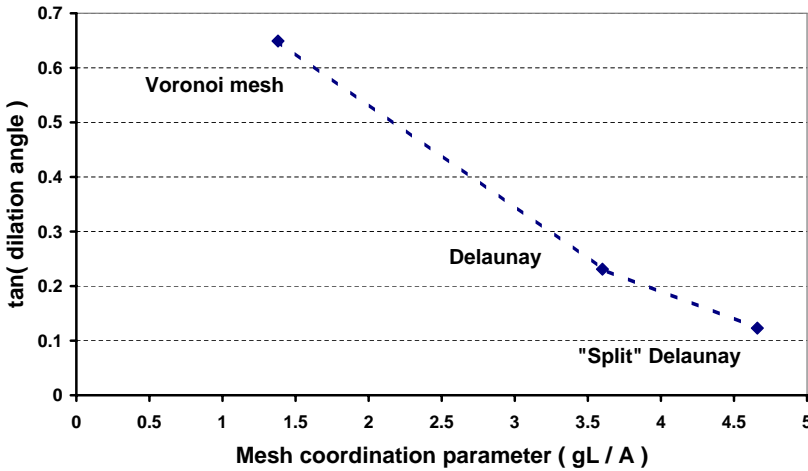
Figure 12. Effect of mesh coordination parameter on tangent of effective dilation angle.

topology that is essentially different from the mesh density, ρ. Figure 12 is a plot of the values of $\tan \psi$, inferred from Figure 9, against the coordination parameter λ. (Asymptotic values of ψ are inferred from Figure 9 to be equal to $13°$, $7°$, and $33°$ for cases C, D, and E respectively). Figure 12 suggests that it may, in fact, be possible to infer the appropriate macro dilation angle ψ from the intrinsic mesh coordination characteristics summarized by the dimensionless mesh coordination parameter λ. However, a more significant goal is to determine, eventually, whether λ can be determined by direct experimental observation of the actual microscopic fabric structures in rock specimens.

5. Conclusions

Numerical experiments have been carried out to determine the effect of a simulated micro structure on equivalent macro shear properties for a simple shear loading experiment relating to the failure of a rock bridge between two preexisting discontinuities. The study addresses only a single micro-to-macro hierarchical step change. It appears that the use of slip and tension-weakening failure parameters in the micro crack model does ensure that the observed macro average strain component evolution is substantially independent of the microscopic mesh density. Less satisfying is the observation of the extent of mesh mobilization associated with different mesh densities which appears to be dependent on the mesh density.

Interestingly, it is found that the intrinsic mesh coordination structure plays an essential role in determining the macro dilation properties of the failed region. This implies that, depending on the nature of a given lattice computational model, equivalent macro behavior (such as may be observed from the averaged results of a laboratory test) may or may not be able to be matched to observed physical behavior. In addition, it appears that some interpretation of the physical equivalent of the mesh junction coordination is required as an additional material parameter that may need to be measured to describe material fabric characteristics. This clearly warrants further investigation in cases of more general three dimensional failure.

The numerical experiments suggest, as well, that a simple dimensionless mesh coordination parameter could provide a useful measure of the effective intrinsic dilation behavior that may be expected to emerge from a selected random mesh crack model. Further studies are required to determine whether this proposed parameter grouping can be extended to a wider variety of computational lattice models.

Acknowledgements

References

[Allodi et al. 2003] A. Allodi, M. Castelli, S. Marello, and C. Scavia, "Shear band propagation in soft rocks: numerical simulation of experimental results", pp. 23–28 in *ISRM 2003 proceedings - technology roadmap for rock mechanics*, South African Institute of Mining and Metallurgy, 2003.

[Bobet and Einstein 1998] A. Bobet and H. H. Einstein, "Fracture coalescence in rock-type materials under uniaxial and biaxial compression", *Int. J. Rock. Mech. Min.* **35** (1998), 863–888.

[Bolander et al. 1996] J. E. Bolander, T. Shiraishi, and Y. Isogawa, "An adaptive procedure for fracture simulation in extensive lattice networks", *Eng. Fract. Mech.* **54** (1996), 325–334.

[Budhu et al. 1999] M. Budhu, S. Ramakrishnan, and G. Frantziskonis, "A lattice type model for particulate media", *Int. J. Numer. Anal. Meth. Geomech.* **23** (1999), 647–671.

[Chiaia et al. 1997] B. Chiaia, A. Vervuurt, and J. G. M. Van Mier, "Lattice model evaluation of progressive failure in disordered particle composites", *Eng. Fract. Mech.* **57** (1997), 301–318.

[Crouch and Starfield 1983] S. L. Crouch and A. M. Starfield, *Boundary element methods in solid mechanics*, George Allen & Unwin, London, 1983.

[Cundall 1988] P. A. Cundall, "Formulation of a three-dimensional distinct element model – Part I. A scheme to detect and represent contacts in a system composed of many polyhedral blocks", *Int. J. Rock. Mech. Min.* **25** (1988), 107–116.

[Hart et al. 1988] R. Hart, P. A. Cundall, and J. Lemos, "Formulation of a three-dimensional distinct element model – Part II. Mechanical calculations for motion and interaction of a system composed of many polyhedral blocks", *Int. J. Rock. Mech. Min.* **25** (1988), 117–125.

[Jefferson et al. 2002] G. Jefferson, G. K. Haritos, and R. M. McMeeking, "The elastic response of a cohesive aggregate – a discrete element model with coupled particle interaction", *J. Mech. Phys. Solids* **50** (2002), 2539–2575.

[Jing 2003] L. Jing, "A review of techniques advances and outstanding issues in numerical modelling for rock mechanics and rock engineering", *Int. J. Rock. Mech. Min.* **40** (2003), 283–353.

[Kuhn 2005] M. R. Kuhn, "Are granular materials simple? An experimental study of strain gradient effects and localization", *Mech. Mater.* **37** (2005), 607–627.

[Linkov and Mogilevskaya 1994] A. M. Linkov and S. G. Mogilevskaya, "Complex hypersingular integrals and integral equations in plane elasticity", *Acta Mech.* **105** (1994), 189–205.

[Lockner and Madden 1991a] D. A. Lockner and T. R. Madden, "A multiple-crack model of brittle fracture 1. Non-time-dependent simulations", *J. Geophys. Res.* **96**:B12 (1991), 19623–19642.

[Lockner and Madden 1991b] D. A. Lockner and T. R. Madden, "A multiple-crack model of brittle fracture 2. Time-dependent simulations", *J. Geophys. Res.* **96**:B12 (1991), 19643–19654.

[Mogilevskaya 2000] S. G. Mogilevskaya, "Complex hypersingular integral equation for the piece-wise homogeneous half-plane with cracks", *Int. J. Fract.* **102** (2000), 177–204.

[Morgan 1999] J. K. Morgan, "Numerical simulations of granular shear zones using the distinct element method - 2. Effects of particle size distribution and interparticle friction on mechanical behavior", *J. Geophys. Res.* **104**:B2 (1999), 2721–2732.

[Morgan and Boettcher 1999] J. K. Morgan and M. S. Boettcher, "Numerical simulations of granular shear zones using the distinct element method - 1. Shear zone kinematics and micromechanics of localization", *J. Geophys. Res.* **104**:B2 (1999), 2703–2719.

[Napier and Hildyard 1992] J. A. L. Napier and M. W. Hildyard, "Simulation of fracture growth around openings in highly stressed, brittle rock", *J. S. Afr. Inst. Min. Metall.* **92** (1992), 159–168.

[Napier and Malan 1997] J. A. L. Napier and D. F. Malan, "A viscoplastic discontinuum model of time-dependent fracture and seismicity effects in brittle rock", *Int. J. Rock. Mech. Min.* **34** (1997), 1075–1089.

[Napier and Peirce 1995] J. A. L. Napier and A. P. Peirce, "Simulation of extensive fracture formation and interaction in brittle materials", pp. 63–74 in *Proceedings of the second international conference on the mechanics of jointed and faulted rock*, edited by H. P. Rossmanith, Balkema, Rotterdam, 1995.

[Palmer and Rice 1973] A. C. Palmer and J. R. Rice, "The growth of slip surfaces in the progressive failure of over-consolidated clay", *Proc. Roy. Soc. Lond. A* **332** (1973), 527–548.

[Potyondy and Cundall 2004] D. O. Potyondy and P. A. Cundall, "A bonded-particle model for rock", *Int. J. Rock. Mech. Min.* **41** (2004), 1329–1364.

[Rechenmacher 2006] A. L. Rechenmacher, "Grain-scale processes governing shear band initiation and evolution in sands", *J. Mech. Phys. Solids* **54** (2006), 22–45.

[Scavia 1992] C. Scavia, "A numerical technique for the analysis of cracks subjected to normal compressive stresses", *Int. J. Numer. Methods Eng.* **33** (1992), 929–942.

[Sellers and Napier 1997] E. Sellers and J. A. L. Napier, "A comparative investigation of micro-flaw models for the simulation of brittle fracture in rock", *Comput. Mech.* **20** (1997), 164–169.

[Uenishi and Rice 2003] K. Uenishi and J. R. Rice, "Universal nucleation length for slip-weakening rupture instability under nonuniform fault loading", *J. Geophys. Res.* **108**:B1 (2003), ESE 17–1 – 17–13.

JOHN NAPIER: john.napier@pixie.co.za
School of Computational and Applied Mathematics, University of the Witwatersrand, Johannesburg, South Africa

STRAIN LOCALIZATION IN OPEN-CELL POLYURETHANE FOAMS: EXPERIMENTS AND THEORETICAL MODEL

Giampiero Pampolini and Gianpietro Del Piero

Confined compression tests performed by the authors on open-cell polyurethane foams reveal the presence of strain localization. After a brief description of the experiments, a theoretical model is proposed. In the model, the foam is represented as a chain of elastic springs with a two-phase strain energy density, and the strain localization is due to a progressive collapse of the springs. The collapse is a sort of continuum instability, which can be attributed to phase transition. An appropriate choice of the material constants leads to a close reproduction of the experimental force-elongation response curves.

1. Introduction

The rapidly increasing use of foam polymers, and of cellular materials in general, is due to a combination of some peculiar properties, such as lightness, easy packaging, and high energy absorption. Such properties come from the specific microstructure of the material, which consists of a complex network of ligaments and membranes. For a detailed description, see [Gibson and Ashby 1997]. Typical of such materials is the nonhomogeneous deformation exhibited in uniaxial compression tests. There is indeed experimental evidence that in a displacement-driven test the deformation is initially homogeneous, then localizes in transverse bands whose number grows with increasing deformation and eventually becomes again homogeneous, see, for example, [Lakes et al. 1993; Gioia et al. 2001; Wang and Cuitinho 2002; Gong and Kyriakides 2007], and the experiments made by the present authors described in the next section. This behavior determines a three-regime shape of the force-elongation response curve in which the central regime of strain localization corresponds to an almost horizontal plateau.

The same overall behavior was observed by Bart-Smith et al. [1998] and by Bastawros et al. [2000] in both open and closed-cell aluminium alloy foams. There is also a strong analogy with the response curves for shape memory alloy wires; see, for example, [Miyazaki and Otsuka 1989; Ortin 1992; Tanaka et al. 1996]. The analogy becomes even more interesting by the fact that for all such materials the loading-unloading tests exhibit hysteresis cycles of similar shapes [Tanaka et al. 1996; Bart-Smith et al. 1998; Bastawros et al. 2000; Gong et al. 2005].

To model the behavior of open-cell polymer foams, two main approaches are used: a numerical approach, directly reproducing the microstructure in the finite element scheme, and an analytical approach, based on the representation of the material as a continuum. In the numerical approach, the ligaments are usually represented as shear-deformable linear elastic beams, and strain localization is attributed to the buckling of the beams; see, for example, [Gent and Thomas 1963; Gibson and Ashby 1997; Warren and

Kraynik 1997]. In [Gong et al. 2005], the foam is modeled as a periodic structure whose basic element is a 14-sided polyhedron, called the Kelvin cell. In general, the numerical approach is computationally very demanding, due to the large number of unknowns and to difficulties in modeling the contact between beams in the post-buckling regime; see [Bardenhagen et al. 2005].

In the analytical approach, the material is considered to be a homogeneous hyperelastic continuum. Indeed, it was shown in [Ericksen 1975] that both strain localization and hysteretic behavior can be described within the elastic context, by assuming a nonconvex strain energy density of a special "double-well" shape. A model for foam polymers based on this simple idea was proposed in [Gioia et al. 2001].

In this paper we propose a discrete model whose origin traces back to a series of papers [Müller and Villaggio 1977; Fedelich and Zanzotto 1992; Puglisi and Truskinovsky 2000] in which Ericksen's problem is discretized by replacing a continuous bar by a finite chain of elastic springs with a double-well strain energy. The paper is divided into two parts. In the first part the test procedure and the experimental results are presented. In the second part the theoretical model is described and, by an appropriate identification of the constitutive constants, a close reproduction of the experimental force-elongation curves is obtained.

2. Experimental analysis

2.1. *Equipment and test procedure.* The compression tests were made using a load frame Instron 4467 with a 500 N load cell, located at the *Laboratorio di Materiali Polimerici* of the University of Ferrara. The specimens were parallelepipeds cut out from two sheets of commercial open-cell polyurethane foams, 10 and 50 mm thick, respectively. The cutting was done manually, using a ribbon saw. The cellular structures of the two sheets are shown in Figure 1, and their mass densities are 27 and 25 kg/m^3, respectively.

Ten specimens with base dimensions 100×100 mm, five for each of the thicknesses 10 and 50 mm, were tested in confined compression. Confinement was assured by a polystyrene box clamped to the load frame, of dimensions $101 \times 101 \times 60$ mm. The lower base of the samples was in contact with the bottom of the box, and the upper base was in contact with a steel plate fixed to the moving crosshead. Polystyrene,

(a) (b)

1 mm
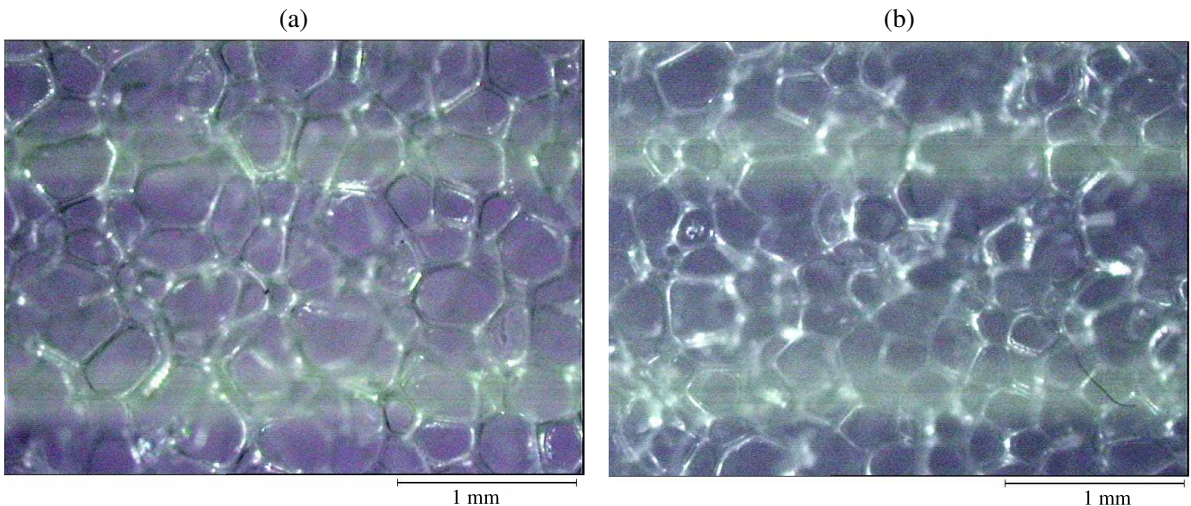
Figure 1. Cell structure of the polyurethane foams in the 50 mm (a) and 10 mm sheets (b).

Figure 2. The test equipment.

being transparent, allowed for optical control of the evolution of the deformation. Confinement was chosen to prevent lateral buckling, which was indeed observed in some collateral nonconfined tests. There were just slight differences between the response curves for confined and nonconfined tests. This led us to conclude that the effects of the friction between specimens and the lateral walls of the box were not important. Accordingly, we decided not to lubricate the walls of the box.

The testing equipment is shown in Figure 2. A preload of 2 to 3 N was applied to guarantee a full initial contact between plate and specimen. A crosshead speed of 1 mm/min was considered sufficiently slow to render negligible all rate-dependent effects. The test was stopped when the crosshead displacement reached 70 % of the specimen thickness, an elongation sufficient to capture all significant aspects of the force-elongation curve.

2.2. Results. Two experimental force-elongation curves are shown in Figure 3. They give the average responses of five tests made on 10 mm and 50 mm specimens, respectively. The figure shows the stress
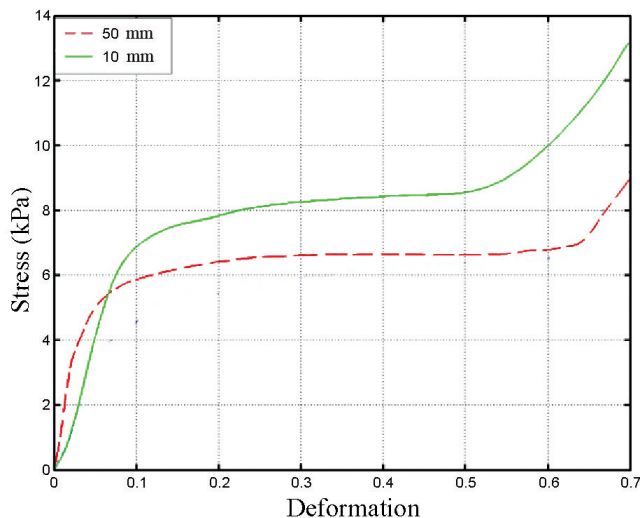
Figure 3. Comparison of the average force-elongation curves relative to five tests on 10 and 50 mm samples in confined compression.

(measured as axial force divided by the initial sample cross area) as a function of the deformation (measured as the crosshead displacement divided by the initial thickness of the specimen). The two curves are similar in shape. In particular, they exhibit the three-regime behavior mentioned in Section 1, characterized by a central plateau. The quantitative differences are significant. This means that the two commercial sheets from which the specimens were obtained have different mechanical properties. In the following, they will be considered as made of two different materials. From Figure 3, one sees that the initial slopes are about 110 and 145 kPa for the 10 mm and for the 50 mm specimens, respectively. The plateau occurs at a stress of about 6.5 kPa and 8.5 kPa, and ends at a deformation of about 55 % and 63 %, respectively.

To detect the strain localization, a rectangular grid was drawn on one of the specimens' sides. The progressive deformation of the grid under growing crosshead displacement is shown in Figure 4. As shown in Figure 4a, the deformation is initially homogeneous. Subsequently, a severe deformation occurs at the top layer of the specimen, Figure 4b. This deformation propagates to the underlying layers (Figures 4c, 4d), and after all layers have been reached, the deformation again becomes homogeneous, Figure 4e. The same qualitative evolution was observed in polyurethane low-density foams [Wang and Cuitinho 2002] and in aluminium alloy foams [Bart-Smith et al. 1998; Bastawros et al. 2000]. A very similar localization phenomenon was also observed in steel bars subjected to uniaxial tension [Froli and Royer-Carfagni 1997; 1999].

(a)   (b)   (c)

(d)   (e)
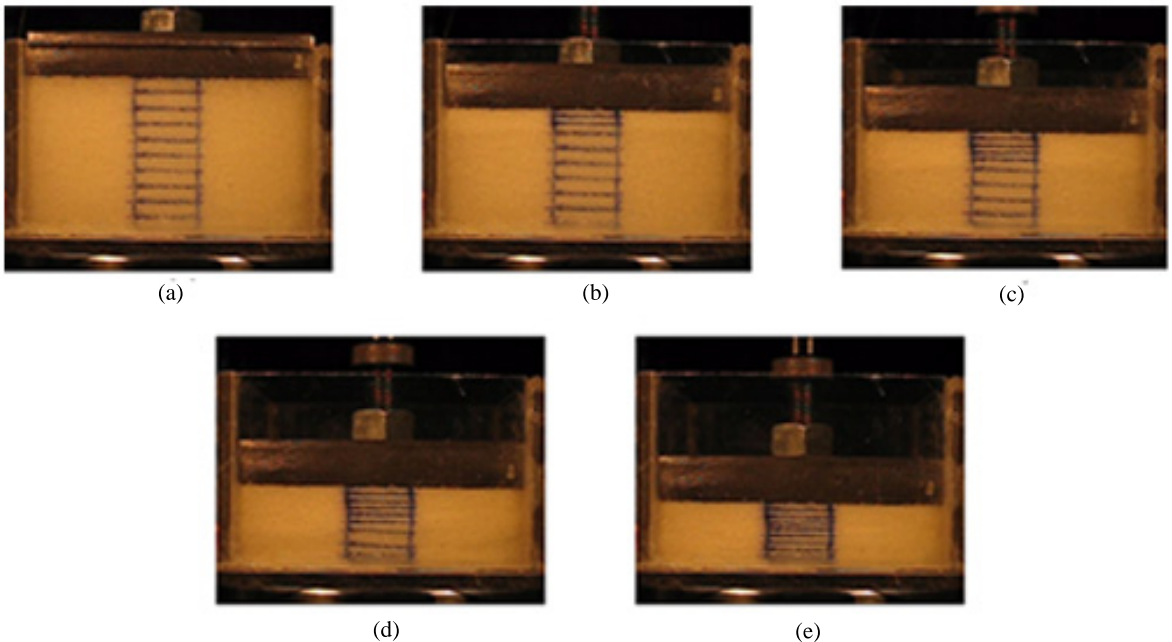
Figure 4. The deformation mechanism in confined compression test on the 50 mm thick samples: (a) the initial homogeneous deformation, (b) strain localization at the upper end of the specimen, (c) and (d) propagation to the underlying layers, and (e) the final homogeneous deformation. The initial equidistance of the horizontal lines of the rectangular grid is 5 mm.

In particular, Wang and Cuitinho [2002] observed the formation of three or four highly deformed bands orthogonal to the loading direction. In their experiments, localization does not initiate at the upper end of the specimen as in our tests. The fact that in our tests the localization systematically starts at the upper end can be explained by the difference in the contact conditions. Indeed, in collateral tests made with uniform contact conditions we observed that localization starts simultaneously at the two bases.

3. Theoretical model

3.1. Basic ingredients. Let Ω_0 be the bounded open three-dimensional region occupied by the body in the reference configuration, and let f be the deformation that maps the points X of Ω_0 into the points $x = f(X)$. Assume that the body is made of an isotropic hyperelastic material, with a strain energy density of the form

$$w(F) = \tfrac{1}{2}\, \alpha\, F \cdot F + \Gamma(\det F)\,, \tag{1}$$

where F denotes the gradient of f, α is a positive material constant, and Γ is a nonnegative function such that

$$\lim_{\det F \to 0} \Gamma(\det F) = \lim_{\det F \to +\infty} \Gamma(\det F) = +\infty. \tag{2}$$

The gradient of w,

$$S = w_F(F) = \alpha F + \det F \ \Gamma'(\det F)\, F^{-T}, \tag{3}$$

is the Piola–Kirchhoff stress tensor. If we take $w(I) = 0$ and if we assume that the reference configuration $F = I$ is stress-free, from the conditions $w(I) = w_F(I) = 0$ we get

$$\alpha = -\Gamma'(1)\,, \qquad \tfrac{3}{2}\,\alpha + \Gamma(1) = 0. \tag{4}$$

For the function Γ we assume the expression

$$\Gamma(\det F) = c\,(\det F)^n \left(\frac{1}{n+2}\,(\det F)^2 - \frac{1}{n}\right) - \mu \ln(\det F) + \frac{\beta\sqrt{\pi}}{2\sqrt{k}}\,\operatorname{erf}\left(\sqrt{k}\,(\det F - a)\right) + \gamma\,, \tag{5}$$

where $\alpha, c, n, \mu, \beta, k$ are positive constants, with $a \leqslant 1$, $\operatorname{erf}(\cdot)$ is the error function

$$\operatorname{erf}(x) = \frac{2}{\sqrt{\pi}} \int_0^x e^{-t^2} dt\,, \tag{6}$$

and γ is a constant determined by the conditions (4). The expression chosen for Γ is the sum of two parts. The first part, similar to the one proposed in [Ogden 1997], takes into account the long-range effects, while the second part, the error function, provides a local effect at values of $\det F$ close to a. In (5), the growth conditions of (2) are satisfied for any positive c, μ, and n. In the particular case of confined compression in the direction e, one has
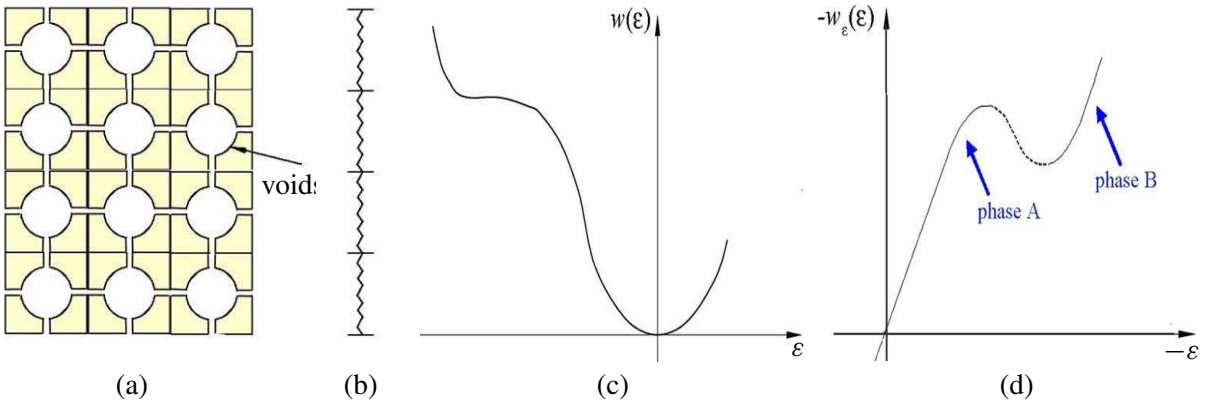
$$F = I + (\lambda - 1)e \otimes e\,, \qquad \det F = \lambda\,, \qquad 0 < \lambda < 1\,, \tag{7}$$

so that

$$S = \left(\lambda\Gamma'(\lambda) - \Gamma'(1)\right) I + (1 - \lambda)\left(\Gamma'(\lambda) + \Gamma'(1)\right) e \otimes e. \tag{8}$$

We see that S depends only on λ and on the function Γ. The component of S in the loading direction is

$$\sigma = S e \cdot e = \Gamma'(\lambda) - \lambda\,\Gamma'(1). \tag{9}$$

Figure 5. Subdivision of the body into cell layers (a), representation of each layer as a nonlinear elastic spring (b) with nonconvex energy (c), and nonmonotonic force-elongation curve (d).

For Γ as in (5), Equation (9) yields

$$\sigma = \left[\mu - \beta \exp\left(-k(1-a)^2\right)\right]\lambda + c\lambda^{n-1}\left(\lambda^2 - 1\right) - \mu\lambda^{-1} + \beta\exp\left(-k(\lambda - a)^2\right). \tag{10}$$

This is the equation that, with appropriate identifications of the constants μ, β, k, a, c, n, will be used to reproduce the experimental curves.

To begin, consider (10) as the force-elongation relation (σ, λ) of a nonlinear elastic spring. This relation is represented by a curve in which two ascending branches are separated by a descending branch as shown in Figure 5d. It does not match with the curves in Figure 3 and, what is more, it does not provide any description of strain localization. But, as it will be shown in the coming subsection, both goals can be reached by assembling in series a sufficiently large number of such springs.

3.2. *The discrete model.* Consider a chain of n springs connected in series (Figure 5a) in which each spring represents a horizontal layer of cells as shown in Figure 5b. We assume that all springs have the nonconvex strain energy of the type shown in Figure 5c, to which corresponds the force-elongation law shown in Figure 5d and expressed by (10).

The total energy of the system is the sum of the strain energies of the springs,

$$E\left(\varepsilon_1, \varepsilon_2, \ldots, \varepsilon_n\right) = \sum_{i=1}^{n} w(\varepsilon_i), \tag{11}$$

where ε_i is the elongation of the ith spring. The chain is subjected to the *hard device* condition:

$$\sum_{i=1}^{n} \varepsilon_i = n\varepsilon_0, \tag{12}$$

where ε_0 is the prescribed average elongation of the springs. If one of the ends of the chain is fixed, the total elongation $n\varepsilon_0$ of the chain coincides with the displacement imposed on the other end. Using condition (12), one can eliminate one variable, say ε_n, and rewrite the energy in the form

$$E\left(\varepsilon_1, \varepsilon_2, \ldots, \varepsilon_{n-1}\right) = \sum_{i=1}^{n-1} w(\varepsilon_i) + w\left(n\varepsilon_0 - \sum_{i=1}^{n-1} \varepsilon_i\right). \tag{13}$$

In an elastic structure, the equilibrium configurations are identified with the stationarity points of the energy, and the stable equilibrium configurations are identified with the (local or global) energy minimizers. For the present structure, which has a finite number of degrees of freedom, the equilibrium configurations are found by annihilating the partial derivatives of the energy

$$\frac{\partial E}{\partial \varepsilon_i}\left(\varepsilon_1, \varepsilon_2, \ldots, \varepsilon_{n-1}\right) = w'(\varepsilon_i) - w'\left(n\varepsilon_0 - \sum_{j=1}^{n-1} \varepsilon_j\right) = 0, \quad i = 1, 2, \ldots, n-1. \tag{14}$$

Recalling that $\varepsilon_n = n\varepsilon_0 - \sum_{j=1}^{n-1} \varepsilon_j$, the above equality can be given the form

$$w'(\varepsilon_i) = w'(\varepsilon_n), \qquad i = 1, 2, \ldots, n-1, \tag{15}$$

which tells us that the force is the same in all springs. The common value of the force in the springs will be denoted by σ. As to the conditions for a global or local minimum, a sufficient condition is that the Hessian matrix of the second partial derivatives of the energy,

$$\frac{\partial^2 E}{\partial \varepsilon_i \, \partial \varepsilon_j} = \begin{cases} w''(\varepsilon_j) + w''(\varepsilon_n) & \text{if } i = j, \\ w''(\varepsilon_n) & \text{if } i \neq j. \end{cases} \tag{16}$$

be positive definite. After setting $A_i = w''(\varepsilon_i)$, this matrix takes the form

$$H = \begin{bmatrix} A_1 + A_n & A_n & . & A_n \\ A_n & A_2 + A_n & . & A_n \\ . & . & . & . \\ A_n & A_n & . & A_{n-1} + A_n \end{bmatrix}. \tag{17}$$

It is known (see, for example, [Puglisi and Truskinovsky 2000]) that H is positive definite if and only if (a) all A_i, except at most one, are positive, and (b) if there is a negative $A_j < 0$, it must be the case that

$$\sum_{i=1}^{n} A_i^{-1} < 0. \tag{18}$$

Condition (b) has no practical interest if n is sufficiently large; see [Puglisi and Truskinovsky 2000]. In what follows, we neglect it altogether. Because $A_i = w''(\varepsilon_i)$, a positive A_i means that the elongation ε_i lies on one of the two ascending branches of the force-elongation curve. Therefore, we confine ourselves to equilibrium configurations in which all elongations ε_i lie on one of the ascending branches. We say that the ith spring is in phase A if ε_i belongs to the first ascending branch, and that it is in phase B if ε_i belongs to the second ascending branch.

3.3. *Strain localization.* Consider an equilibrium configuration with m springs in phase A, for which the force $\bar{\sigma}$ belongs to the interval $(\sigma_{\min}, \sigma_{\max})$, where $\sigma_{\min}$ and $\sigma_{\max}$ are the local minimum and the local maximum of the force-elongation curve; see Figure 6a. Let us call $\bar{\varepsilon}_1$ and $\bar{\varepsilon}_2$ the elongations
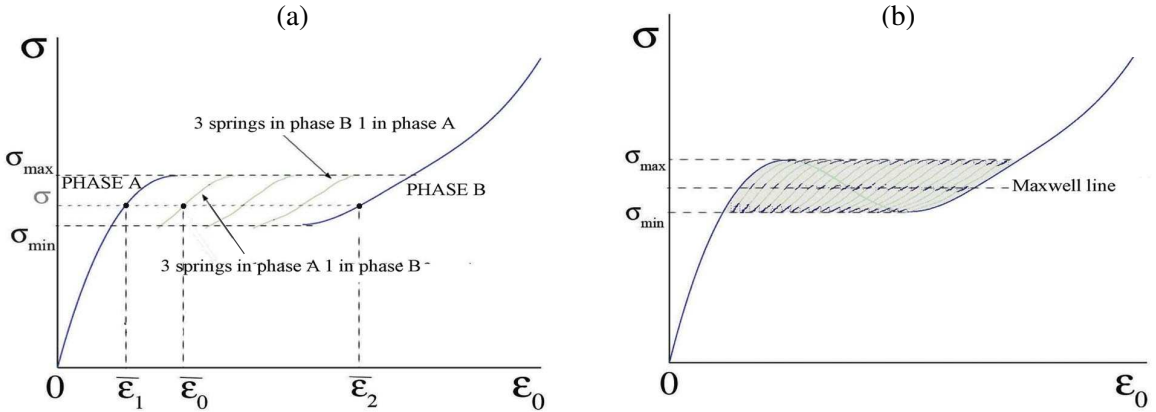
Figure 6. Response curves for (a) a system of 4 springs and (b) a system of 20 springs.

corresponding to $\bar{\sigma}$ in the first and second ascending branch, respectively. Then,

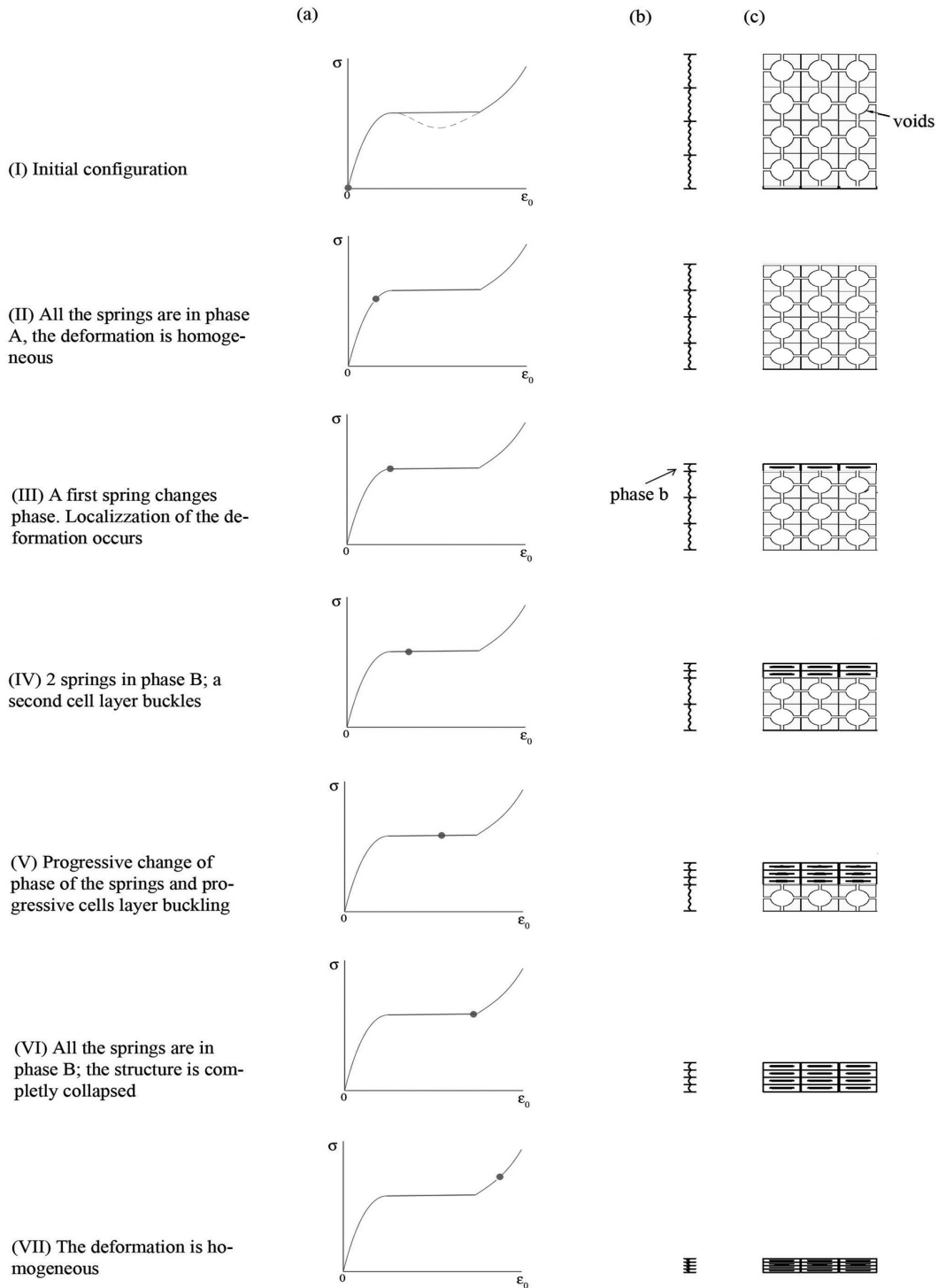$$\bar{\varepsilon}_0 = \frac{m}{n}\,\bar{\varepsilon}_1 + \frac{n-m}{n}\,\bar{\varepsilon}_2 \tag{19}$$

is the corresponding average elongation. By varying $\bar{\sigma}$, for each fixed m one can construct the stable equilibrium path $(\bar{\sigma}, \bar{\varepsilon}_0)$, and by varying m one gets all equilibrium paths made of the equilibrium configurations selected above. In Figure 6a, the equilibrium paths for a system of four springs are shown.

The cases $m = 0$ and $m = n$ correspond to homogeneous configurations. Indeed, for $m = n$, from (19), we get $\bar{\varepsilon}_0 = \bar{\varepsilon}_1$, so that the path $(\bar{\sigma}, \bar{\varepsilon}_0)$ coincides with the first ascending branch. For $m = 0$ we get $\bar{\varepsilon}_0 = \bar{\varepsilon}_2$, so that the path $(\bar{\sigma}, \bar{\varepsilon}_0)$ coincides with the second ascending branch. If one assumes that the evolution occurs along equilibrium curves made of local energy minimizers (see [Del Piero and Truskinovsky $\geq$ 2008]) then the system, when loaded starting from the initial configuration, initially follows the first ascending branch, until the branch ends when the force reaches the value $\sigma_{\max}$.

At this point, to further increase ε_0, there are no more single-phase equilibrium configurations. It is reasonable to assume that the system jumps to the closest branch, which corresponds to the configurations with one spring in phase B and three springs in phase A. This phase transition requires a nonequilibrium process in which the force decreases at constant ε_0. This process will not be analyzed here. Once the new equilibrium branch has been reached, the force again increases, until σ reattains the value $\sigma_{\max}$. Then the system jumps to the branch with two springs in phase B and so on. When all springs have undergone the phase transition, the system evolves following the second ascending branch, which corresponds to single-phase configurations with all springs in phase B. Thus, after reaching the value $\sigma_{\max}$ for the first time, the system first follows a wavy, approximately horizontal line, successively assuming configurations with the number m of springs in phase A gradually decreasing from n to zero, and then follows the second ascending branch. By comparing the two halves of Figure 6, one sees that the number of intermediate branches, and therefore nonequilibrium processes, increases with n. At the same time, each phase transition involves a smaller jump of σ. Therefore the whole regime of progressive phase change occurs more smoothly.

Let us compare the model's predictions with the deformation mechanism observed in experiments. In Figure 7, the first row represents the undeformed configuration, and the second row shows the system

(a) (b) (c)

(I) Initial configuration

voids

(II) All the springs are in phase A, the deformation is homogeneous

(III) A first spring changes phase. Localizzation of the deformation occurs

phase b

(IV) 2 springs in phase B; a second cell layer buckles

(V) Progressive change of phase of the springs and progressive cells layer buckling

(VI) All the springs are in phase B; the structure is completly collapsed

(VII) The deformation is homogeneous

Figure 7. Description of the deformation mechanism following the response curve (a), and the corresponding configurations of the springs (b) and of the cell-layers (c).

(a)   (b)
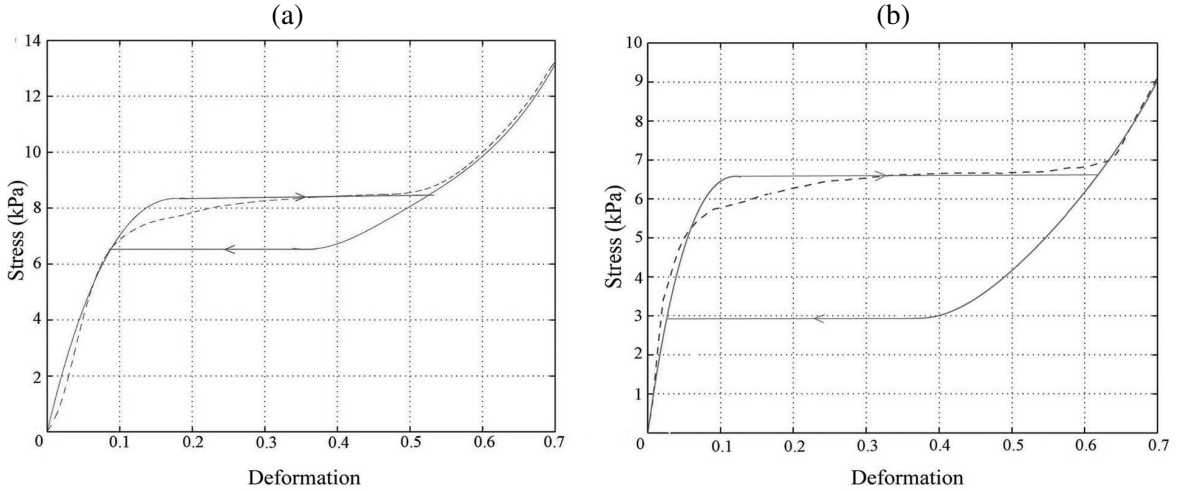
Figure 8. Theoretical response curves and hysteresis loop (solid lines), compared with average experimental response at loading (dotted line) for the 10 mm (a) specimens and the 50 mm (b) specimens.

following the first ascending branch of the response curve. Both correspond to a homogeneous configuration with all springs in phase A. A two-phase configuration with one spring more deformed than the others is shown in the third row, and the phase transitions of all springs, one after the other, are shown in the following rows. When all layers are strongly deformed as shown in the last row, the specimen is back to homogeneous deformation.

3.4. *Response at unloading.* At unloading, the model predicts a similar behavior: after reaching the force $\sigma_{\min}$, the system approximately follows the horizontal line $\sigma = \sigma_{\min}$, successively assuming configurations with m gradually increasing from zero to n. The hysteresis loop determined in this way has indeed been observed in experiments on polymer foams [Gong et al. 2005], on aluminium foams [Bart-Smith et al. 1998; Bastawros et al. 2000], and on shape memory alloys [Miyazaki and Otsuka 1989; Ortin 1992; Tanaka et al. 1996].

If the system is unloaded when $m > 0$, that is, when there are still springs in phase A, the system follows, backwards, the two-phase equilibrium curve for the given m until the value $\sigma_{\min}$ is attained. For further decreasing deformations, the system approximately follows the horizontal line $\sigma = \sigma_{\min}$, until all springs go back to phase A. A comparison of this prediction with experiments made by the authors is given in the next section.

4. Comparison with experiment

In Figure 8, the model's response is compared with the experimental results for the 10 and the 50 mm specimens. As explained in Section 2.2, the two groups of specimens are characterized by different material constants. The dotted curves are the average experimental curves of Figure 3 and the solid lines are the response curves of the model, with the values of the constitutive constants reported in Table 1. In the latter, according to our model's prediction, the plateaus should indeed be wavy lines. But the waves have been neglected, supposing that the number of springs is conveniently large.
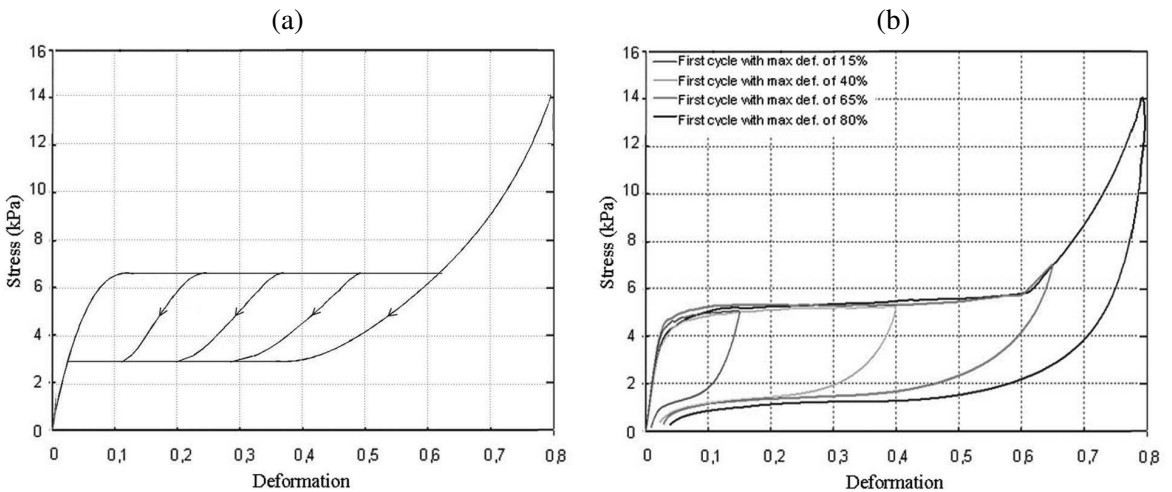
	10 mm specimens	*50 mm specimens*
α	4.2 kPa	2.92 kPa
μ	4.2 kPa	2.92 kPa
c	50.8 kPa	69.9 kPa
n	5	7
β	2.5 kPa	3.5 kPa
k	47	18
a	0.67	0.72

Table 1. Values of the constitutive constants.

The constants in Table 1 have been chosen for the best fitting of the experimental curves in the first loading branch, $\varepsilon_0 < 0.1$, and for elongations larger than $\varepsilon_0 > 0.3$. Indeed, our model does not predict the positive slope exhibited by the experimental curves in the range $0.1 < \varepsilon_0 < 0.3$. This part of the loading diagram has been studied in [Puglisi and Truskinovsky 2001; Marzano et al. 2003]. In [Puglisi and Truskinovsky 2001], curves with positive slope are obtained from chains made of springs with different energies.

Figure 9 compares the theoretical and experimental loading-unloading curves for 50 mm specimens, for different values of the maximum elongation $\varepsilon_{\max}$. The curves show a qualitative agreement in the shapes of the hysteresis loops. But there are also some discrepancies:

(i) In the model, all unloading curves begin at the upper plateau. In the experiments, the upper plateau ends at $\varepsilon_p \approx 60\%$, and yet the unloading curves for $\varepsilon_{\max} > 60\%$ do not follow backwards the unloading curve up to ε_p as predicted by the model.

(a)   (b)

Figure 9. Theoretical (a) and experimental (b) loading-unloading curves for the 50 mm specimens, showing the shapes of the hysteresis loops for different maximum elongations [Pampolini and Del Piero 2008].

(ii) In the model the lower plateau is horizontal, and it is the same for all $\varepsilon_{\max}$. In the experiments there are different lower plateaus for different $\varepsilon_{\max}$, and all have a variable positive slope. The transition from the descending curve to the plateau is not evident.

(iii) In the model, after a complete loading-unloading cycle, all curves end at the origin. In the experiments, there is a residual deformation whose amount increases with $\varepsilon_{\max}$.

It is possible to eliminate the discrepancies in point (ii) by introducing a damage variable (see [Pampolini and Del Piero 2008]), and to attribute those in point (iii) to residual plastic deformation. But both seem rather to be due to retarded elasticity, with a decay time much larger than the duration of the experiment. Indeed, our observations confirm those of [Gong et al. 2005], according to which the residual deformations are completely recovered when the specimen is left at rest for 48 hours.

References

[Bardenhagen et al. 2005] S. G. Bardenhagen, A. D. Brydon, and J. E. Guilkey, "Insight into the physics of foam densification via numerical simulation", *J. Mech. Phys. Solids* **53** (2005), 597–617.

[Bart-Smith et al. 1998] H. Bart-Smith, A.-F. Bastawros, D. R. Mumm, A. G. Evans, D. J. Sypeck, and H. N. G. Wadley, "Compressive deformation and yielding mechanisms in cellular Al alloys determined using X-ray tomography and surface strain mapping", *Acta Materialia* **46** (1998), 3583–3592.

[Bastawros et al. 2000] A.-F. Bastawros, H. Bart-Smith, and A. G. Evans, "Experimental analysis of deformation mechanism in a closed-cell aluminium alloy", *J. Mech. Phys. Solids* **48** (2000), 301–322.

[Del Piero and Truskinovsky ≥ 2008] G. Del Piero and L. Truskinovsky, "Elastic bars with decohesions". In preparation.

[Ericksen 1975] J. L. Ericksen, "Equilibrium of bars", *J. Elast.* **5** (1975), 191–201.

[Fedelich and Zanzotto 1992] B. Fedelich and G. Zanzotto, "Hysteresis in discrete systems of possibly interacting elements with a double-well energy", *J. Nonlinear Sci.* **2** (1992), 319–342.

[Froli and Royer-Carfagni 1997] M. Froli and G. F. Royer-Carfagni, "An experimental study of the Portevin -Le Chatelier effect in steel bars", in *Proc. 13th AIMETA National Congress of Theoretical and Applied Mechanics*, 1997.

[Froli and Royer-Carfagni 1999] M. Froli and G. F. Royer-Carfagni, "Discontinuous deformation of tensile steel bars: experimental results", *ASCE J. Engng Mech.* **12** (1999), 1243–1250.

[Gent and Thomas 1963] A. N. Gent and A. G. Thomas, "Mechanics of foamed elastic materials", *Rubber Chem. Technol* **36** (1963), 597–610.

[Gibson and Ashby 1997] L. J. Gibson and M. F. Ashby, *Cellular solids: structure and properties*, second ed., Cambridge University Press, 1997.

[Gioia et al. 2001] G. Gioia, Y. Wang, and A. M. Cuitinho, "The energetics of heterogeneous deformation in open-cell solid foams", *Proc. R. Soc. London A* **457** (2001), 1079–1096.

[Gong and Kyriakides 2007] L. Gong and S. Kyriakides, "On the crushing stress of open cell foams", *ASME J. Appl. Mechanics* **73** (2007), 807–814.

[Gong et al. 2005] L. Gong, S. Kyriakides, and W. Y. Jang, "Compressive response of open-cell foams. Part I: Morphology and elastic properties", *Int. J. Solids Struct.* **42** (2005), 1355–1379.

[Lakes et al. 1993] R. Lakes, P. Rosakis, and A. Ruina, "Microbuckling instability in elastomeric cellular solids", *J. Mater. Sci.* **28** (1993), 4667–4672.

[Marzano et al. 2003] S. Marzano, M. D. Piccioni, and G. Puglisi, "Un modello di isteresi per fili di leghe a memoria di forma", in *Proc. 16th AIMETA National Congress of Theoretical and Applied Mechanics*, 2003.

[Miyazaki and Otsuka 1989] S. Miyazaki and K. Otsuka, "Development of shape memory alloys", *ISIJ Int.* **29** (1989), 353–377.

[Müller and Villaggio 1977] I. Müller and P. Villaggio, "A model for an elastic-plastic body", *Arch. Ration. Mech. Anal.* **65** (1977), 25–46.

[Ogden 1997] R. W. Ogden, *Non-linear elastic deformations*, Dover Publications, New York, 1997.

[Ortin 1992] J. Ortin, "Preisach modeling of hysteresis for a pseudoelastic Cu-Zn-Al single crystal", *J. Appl. Phys.* **71** (1992), 1454–1461.

[Pampolini and Del Piero 2008] G. Pampolini and G. Del Piero, "Strain localization and cyclic damage of polyurethane foam cylinders: experimental tests and theoretical model", *Proc. AGS08, The Second Euro-Mediterranean Symposium on the Advances in Geomaterials and Structures, Hammamet* **1** (2008), 111–121.

[Puglisi and Truskinovsky 2000] G. Puglisi and L. Truskinovsky, "Mechanics of a discrete chain with bi-stable elements", *J. Mech. Phys. Solids* **48** (2000), 1–27.

[Puglisi and Truskinovsky 2001] G. Puglisi and L. Truskinovsky, "Hardening and hysteresis in transformational plasticity", in *Proc. 15th AIMETA National Congress of Theoretical and Applied Mechanics*, 2001.

[Tanaka et al. 1996] K. Tanaka, F. Nishimura, M. Matsui, H. Tobushi, and P.-H. Lin, "Phenomenological analysis of plateaus on stress-strain hysteresis in TiNi shape memory alloy wires", *Mechanics of Materials* **24** (1996), 19–30.

[Wang and Cuitinho 2002] Y. Wang and A. M. Cuitinho, "Full-field measurements of heterogeneous deformation patterns on polymeric foams using digital image correlation", *Int. J. Solids Struct.* **39** (2002), 3777–3796.

[Warren and Kraynik 1997] W. E. Warren and A. M. Kraynik, "Linear elastic behavior of a low-density Kelvin foam with open cells", *ASME J. Appl. Mech.* **64** (1997), 787–793.

GIAMPIERO PAMPOLINI: pampolini@lma.cnrs-mrs.fr
Laboratoire de Mécanique et d'Acoustique, 31 chemin Joseph-Aiguier, 13402 Marseille, France

GIANPIETRO DEL PIERO: dlpgpt@unife.it
Università di Ferrara, Via Saragat 1, 44100 Ferrara, Italy

SPATIAL BEHAVIOUR FOR CONSTRAINED MOTION OF A CYLINDER MADE OF A STRONGLY ELLIPTIC ANISOTROPIC MATERIAL

VINCENZO TIBULLO AND MASSIMO VACCARO

This paper studies the spatial behaviour for the motion of a semi-infinite cylinder composed of an anisotropic linear elastic material and subject to zero body force and zero lateral boundary conditions. The elasticity tensor is strongly elliptic, with motion induced by a time-dependent displacement specified pointwise over the base.

1. Introduction

We consider a semi-infinite prismatic cylinder occupied by an anisotropic linear elastic material and subject to zero body force, zero lateral boundary conditions, and zero initial conditions. The motion is induced by a time-dependent displacement specified pointwise over the base. The elasticity tensor is strongly elliptic.

The primary purpose of this paper is to examine how the solutions evolve with respect to the axial variable. To this end, we make an association with the solution of the initial boundary value problem of an appropriate time-weighted cross-section power function, and prove that the strong ellipticity conditions assure this to be an acceptable measure. We then establish a set of differential inequalities that describe the spatial behavior of the measure in concern. This proves that there is a positive constant γ such that the whole activity is zero in that part of the cylinder where the axial distance to the loaded end is greater than γt (that is, a domain influence result holds true), while in the remaining part an exponential decay estimate of Saint Venant type holds true. The results are illustrated for transversely isotropic materials as well as for the rhombic systems.

2. Formulation of problem

Consider a semi-infinite prismatic cylinder $B \subset \mathbb{R}^3$ whose bounded uniform cross section $D \subset \mathbb{R}^2$ has a piecewise continuously differentiable boundary ∂D. The origin of a rectangular Cartesian coordinate system is located in the cylinder's base, and the positive x_3−axis is directed along that of the cylinder. It is convenient to introduce the further abbreviation

$$B_z = \{x \in B : z > x_3\}. \tag{2.1}$$

Moreover, we employ $D(x_3, t)$ to indicate that relevant quantities are to be evaluated at time t over the cross section whose distance from the origin is x_3.

The cylinder is occupied by an anisotropic elastic material and is subject to a deformation in which the displacement field $u(x, t)$ is a smooth vector function satisfying the requirements of the classical

---

dynamical theory [Gurtin 1972]. The corresponding stress tensor $\mathbf{S}(x, t)$ has Cartesian components given by

$$S_{ij} = C_{ijkl}u_{k,l}, \tag{2.2}$$

where the constant elasticities C_{ijkl} possess the symmetries

$$C_{ijkl} = C_{klij} = C_{jikl} \tag{2.3}$$

and satisfy the strong ellipticity condition

$$C_{ijkl}m_i m_k n_j n_l > 0 \quad \text{for all nonzero vectors } (m_1, m_2, m_3), (n_1, n_2, n_3). \tag{2.4}$$

The cylinder is set in motion with a pointwise prescribed base displacement, zero body force, zero initial conditions, and zero displacement on the lateral surface. Furthermore, the prescribed displacements are such that a classical solution exists on the interval $[0, \infty)$. Consequently, the problem to be considered is specified by

$$(C_{jkl}u_{k,l})_{,j} = \rho \ddot{u}_i, \qquad (x, t) \in B \times [0, \infty), \tag{2.5}$$

$$u_i(x, 0) = 0, \qquad \dot{u}_i(x, 0) = 0, \quad x \in B, \tag{2.6}$$

$$u_i(x, t) = 0, \qquad (x, t) \in \partial D \times [0, \infty) \times [0, \infty), \tag{2.7}$$

$$u_i(x, t) = f_i(x_1, x_2, t), \qquad (x, t) \in D(0) \times [0, \infty), \tag{2.8}$$

where the dots denote differentiation with respect to time, a subscript comma indicates partial differentiation, ρ is the constant positive mass density, and $f_i(x_1, x_2, t)$ is a prescribed differentiable function compatible with the initial and lateral boundary conditions.

3. Transversely isotropic materials

Many natural and man made materials are classified as *transversely isotropic* (or *hexagonal*). Such materials are characterized by the fact that one can find a line that allows a rotation of the material about it without changing its properties. The plane, which is perpendicular to this line (the axis of rotational symmetry) is called a *plane of elastic symmetry* or *plane of isotropy*. A modern example of such a material is a laminate made of randomly oriented, chopped fibers that are in general placed in a particular plane. The effective material properties for a bundled structure have no preferred direction in that plane, which makes it a plane of elastic symmetry. Each plane that contains an axis of rotation is a plane of symmetry. Therefore, transversely isotropic materials admit an infinite number of elastic symmetries.

Necessary and sufficient conditions for strong ellipticity to hold for a transversely isotropic linearly elastic solid are established by Merodio and Ogden [2003] and Chiriţă [2006]. In this connection we recall the standard notation

$$c_{ij} = C_{iijj}, \quad i, j \in \{1, 2, 3\} \quad \text{(not summed)},$$

$$c_{22} = c_{11}, \quad c_{23} = c_{13}, \quad c_{44} = c_{55} = C_{2323} = C_{1313}, \quad c_{66} = C_{1212} = \tfrac{1}{2}(c_{11} - c_{12}), \tag{3.1}$$

corresponding to the direction of transverse isotropy coinciding with the x_3 coordinate axis. Apart from terms obtained by use of the symmetries (2.3), these are the only nonzero components C_{ijkl}. Then the

necessary and sufficient conditions for strong ellipticity to hold are [Merodio and Ogden 2003; Chiriţă 2006; Chiriţă and Ciarletta 1999]

$$c_{11} > 0, \quad c_{33} > 0, \quad c_{55} > 0, \quad c_{11} > c_{12}, \tag{3.2}$$

$$|c_{13} + c_{55}| < c_{55} + \sqrt{c_{11}c_{33}}. \tag{3.3}$$

Moreover, equations (2.5) become

$$\rho \ddot{u}_1 = c_{11}u_{1,11} + (c_{12} + c_{66})\, u_{2,21} + c_{66}u_{1,22} + (c_{13} + c_{55})\, u_{3,31} + c_{55}u_{1,33},$$

$$\rho \ddot{u}_2 = (c_{12} + c_{66})\, u_{1,12} + c_{66}u_{2,11} + c_{11}u_{2,22} + (c_{13} + c_{55})\, u_{3,32} + c_{55}u_{2,33}, \tag{3.4}$$

$$\rho \ddot{u}_3 = c_{55}\left(u_{3,11} + u_{3,22}\right) + (c_{13} + c_{55})\left(u_{1,1} + u_{2,2}\right)_{,3} + c_{33}u_{3,33}.$$

By a straightforward calculation from the basic equations (3.4) we obtain

$$
\begin{aligned}
\frac{\partial}{\partial t}&\Big\{\tfrac{1}{2}e^{-\sigma t}[\rho \dot{u}_i \dot{u}_i + c_{11}(u_{1,1} + u_{2,2})^2 + c_{66}(u_{1,2} - u_{2,1})^2 + c_{33}u_{3,3}^2 + c_{55}(u_{3,1}^2 + u_{3,2}^2 + u_{1,3}^2 + u_{2,3}^2) \\
&\qquad\qquad + 2(c_{13} + c_{55})(u_{1,3}u_{3,1} + u_{2,3}u_{3,2}) + 2(c_{66}u_{1,2}u_2)_{,1} - 2(c_{66}u_{1,1}u_2)_{,2}]\Big\} \\
&+ \tfrac{1}{2}\sigma e^{-\sigma t}[\rho \dot{u}_i \dot{u}_i + c_{11}(u_{1,1} + u_{2,2})^2 + c_{66}(u_{1,2} - u_{2,1})^2 + c_{33}u_{3,3}^2 + c_{55}(u_{3,1}^2 + u_{3,2}^2 + u_{1,3}^2 + u_{2,3}^2) \\
&\qquad\qquad + 2(c_{13} + c_{55})(u_{1,3}u_{3,1} + u_{2,3}u_{3,2}) + 2(c_{66}u_{1,2}u_2)_{,1} - 2(c_{66}u_{1,1}u_2)_{,2}] \\
&= e^{-\sigma t}\big\{\dot{u}_1[(c_{13} + c_{55})u_{3,1} + c_{55}u_{1,3}] + \dot{u}_2[(c_{13} + c_{55})u_{3,2} + c_{55}u_{2,3}] + c_{33}\dot{u}_3 u_{3,3}\big\}_{,3} \\
&+ e^{-\sigma t}\big\{\dot{u}_1[c_{11}u_{1,1} + (c_{12} + c_{66})u_{2,2}] + c_{66}u_{2,1}\dot{u}_2 + \dot{u}_3[c_{55}u_{3,1} + (c_{13} + c_{55})u_{1,3}]\big\}_{,1} \\
&+ e^{-\sigma t}\big\{c_{66}u_{1,2}\dot{u}_1 + \dot{u}_2[(c_{12} + c_{66})u_{1,1} + c_{11}u_{2,2}] + \dot{u}_3[c_{55}u_{3,2} + (c_{13} + c_{55})u_{2,3}]\big\}_{,2}, \tag{3.5}
\end{aligned}
$$

where σ is a strictly positive parameter at our disposal.

In view of our null initial and lateral boundary conditions (2.6) and (2.7), and by direct integration of (3.5) over $D(x_3, t) \times [0, t]$, we get

$$
\begin{aligned}
\frac{1}{2}&\int_{D(x_3,t)} e^{-\sigma t}[\rho \dot{u}_i \dot{u}_i + c_{11}(u_{1,1} + u_{2,2})^2 + c_{66}(u_{1,2} - u_{2,1})^2 + c_{33}u_{3,3}^2 \\
&\qquad\qquad + c_{55}(u_{3,1}^2 + u_{3,2}^2 + u_{1,3}^2 + u_{2,3}^2) + 2(c_{13} + c_{55})(u_{1,3}u_{3,1} + u_{2,3}u_{3,2})]\, \mathrm{d}a \\
&+ \frac{\sigma}{2}\int_0^t\int_{D(x_3,s)} e^{-\sigma s}[\rho \dot{u}_i \dot{u}_i + c_{11}(u_{1,1} + u_{2,2})^2 + c_{66}(u_{1,2} - u_{2,1})^2 + c_{33}u_{3,3}^2 \\
&\qquad\qquad + c_{55}(u_{3,1}^2 + u_{3,2}^2 + u_{1,3}^2 + u_{2,3}^2) + 2(c_{13} + c_{55})(u_{1,3}u_{3,1} + u_{2,3}u_{3,2})]\, \mathrm{d}a\, \mathrm{d}s \\
&= \left(\int_0^t\int_{D(x_3,s)} e^{-\sigma s}\{\dot{u}_\alpha[(c_{13} + c_{55})u_{3,\alpha} + c_{55}u_{\alpha,3}] + c_{33}\dot{u}_3 u_{3,3}\}\, \mathrm{d}a\, \mathrm{d}s\right)_{,3}. \tag{3.6}
\end{aligned}
$$

Moreover, on the basis of the lateral boundary condition (2.7), we have

$$\int_{D(x_3,t)} e^{-\sigma t}u_{\alpha,\alpha}u_{3,3}\, \mathrm{d}a = \left(\int_{D(x_3,t)} e^{-\sigma t}u_{\alpha,\alpha}u_3\, \mathrm{d}a\right)_{,3} + \int_{D(x_3,t)} e^{-\sigma t}u_{\alpha,3}u_{3,\alpha}\, \mathrm{d}a. \tag{3.7}$$

Employing the initial condition (2.6) gives

$$\int_{D(x_3,t)} e^{-\sigma t} u_{\alpha,\alpha} u_3 \, \mathrm{d}a = \int_0^t \int_{D(x_3,s)} e^{-\sigma s} \left(\dot{u}_{\alpha,\alpha} u_3 + u_{\alpha,\alpha} \dot{u}_3 - \sigma u_3 u_{\alpha,\alpha} \right) \mathrm{d}a \, \mathrm{d}s$$

$$= \int_0^t \int_{D(x_3,s)} e^{-\sigma s} \left(-\dot{u}_\alpha u_{3,\alpha} + u_{\alpha,\alpha} \dot{u}_3 - \sigma u_3 u_{\alpha,\alpha} \right) \mathrm{d}a \, \mathrm{d}s. \qquad (3.8)$$

Therefore, relations (3.7) and (3.8) imply

$$\int_{D(x_3,t)} e^{-\sigma t} u_{\alpha,\alpha} u_{3,3} \, \mathrm{d}a$$

$$= \left(\int_0^t \int_{D(x_3,s)} e^{-\sigma s} \left(-\dot{u}_\alpha u_{3,\alpha} + u_{\alpha,\alpha} \dot{u}_3 - \sigma u_3 u_{\alpha,\alpha} \right) \mathrm{d}a \, \mathrm{d}s \right)_{,3} + \int_{D(x_3,t)} e^{-\sigma t} u_{\alpha,3} u_{3,\alpha} \, \mathrm{d}a. \quad (3.9)$$

By combining relations (3.6) and (3.9) we obtain the identity

$$\frac{1}{2} \int_{D(x_3,t)} e^{-\sigma t} \rho \dot{u}_i \dot{u}_i \, \mathrm{d}a$$

$$+ \frac{1}{2} \int_{D(x_3,t)} e^{-\sigma t} [c_{11}(u_{1,1}+u_{2,2})^2 + c_{66}(u_{1,2}-u_{2,1})^2 + c_{33} u_{3,3}^2 + 2(c_{13}+\varkappa)(u_{1,1}+u_{2,2})u_{3,3}] \, \mathrm{d}a$$

$$+ \frac{1}{2} \int_{D(x_3,t)} e^{-\sigma t} [c_{55}(u_{3,1}^2 + u_{3,2}^2 + u_{1,3}^2 + u_{2,3}^2) + 2(c_{55}-\varkappa)(u_{1,3}u_{3,1} + u_{2,3}u_{3,2})] \, \mathrm{d}a$$

$$+ \frac{\sigma}{2} \int_0^t \int_{D(x_3,s)} e^{-\sigma s} \rho \dot{u}_i \dot{u}_i \, \mathrm{d}a \, \mathrm{d}s$$

$$+ \frac{\sigma}{2} \int_0^t \int_{D(x_3,s)} e^{-\sigma s} [c_{11}(u_{1,1}+u_{2,2})^2 + c_{66}(u_{1,2}-u_{2,1})^2 + c_{33}u_{3,3}^2 + 2(c_{13}+\varkappa)(u_{1,1}+u_{2,2})u_{3,3}] \, \mathrm{d}a \, \mathrm{d}s$$

$$+ \frac{\sigma}{2} \int_0^t \int_{D(x_3,s)} e^{-\sigma s} [c_{55}(u_{3,1}^2 + u_{3,2}^2 + u_{1,3}^2 + u_{2,3}^2) + 2(c_{55}-\varkappa)(u_{1,3}u_{3,1} + u_{2,3}u_{3,2})] \, \mathrm{d}a \, \mathrm{d}s$$

$$= \left(\int_0^t \int_{D(x_3,s)} e^{-\sigma s} \{ \dot{u}_\alpha [(c_{55}-\varkappa)u_{3,\alpha} + c_{55}u_{\alpha,3}] + \dot{u}_3 [c_{33}u_{3,3} + (c_{13}+\varkappa)u_{\alpha,\alpha}] \} \, \mathrm{d}a \, \mathrm{d}s \right)_{,3}, \quad (3.10)$$

where $\varkappa \in (0, 2c_{55})$ is a positive parameter at our disposal.

This identity suggests that we treat the spatial behaviour of solutions by introducing the following function

$$J_\varkappa(x_3, t) = - \int_0^t \int_{D(x_3,s)} e^{-\sigma s} \left\{ \dot{u}_\alpha \left[(c_{55} - \varkappa) u_{3,\alpha} + c_{55} u_{\alpha,3} \right] + \dot{u}_3 \left[c_{33} u_{3,3} + (c_{13} + \varkappa) u_{\alpha,\alpha} \right] \right\} \mathrm{d}a \, \mathrm{d}s,$$
$$(3.11)$$

with domain $x_3 \in [0, \infty)$, $t \in [0, \infty)$.

Theorem 1. *Let $u_i(x, t)$ be a solution of the initial boundary value problem defined by (3.4), (2.6), (2.7) and (2.8). Then $J_\varkappa(x_3, t)$ as defined by (3.11) represents a measure of the solution, and, for each $t > 0$, evolves as follows. There is a positive constant γ, depending on the elastic constants, such that*

(a) *for $x_3 \geq \gamma t$ we have $J_\varkappa (x_3, t) = 0$ so that*

$$u_i (x_1, x_2, x_3, t) = 0 \quad \text{for all } x_3 \geq \gamma t; \tag{3.12}$$

(b) *for $x_3 \leq \gamma t$, the spatial behavior is described by*

$$0 \leq J_\varkappa (x_3, t) \leq J_\varkappa (0, t) \exp\left(-\frac{\sigma}{\gamma} x_3\right). \tag{3.13}$$

Proof. From (3.10) and (3.11), we can deduce

$$-\frac{\partial J_\varkappa}{\partial x_3} (x_3, t)$$
$$= \frac{1}{2} \int_{D(x_3,t)} e^{-\sigma t} \rho \dot{u}_i \dot{u}_i \, da$$
$$+ \frac{1}{2} \int_{D(x_3,t)} e^{-\sigma t} [c_{11}(u_{1,1}+u_{2,2})^2 + c_{66}(u_{1,2}-u_{2,1})^2 + c_{33}u_{3,3}^2 + 2(c_{13}+\varkappa)(u_{1,1}+u_{2,2})u_{3,3}] \, da$$
$$+ \frac{1}{2} \int_{D(x_3,t)} e^{-\sigma t} [c_{55}(u_{3,1}^2 + u_{3,2}^2 + u_{1,3}^2 + u_{2,3}^2) + 2(c_{55}-\varkappa)(u_{1,3}u_{3,1} + u_{2,3}u_{3,2})] \, da$$
$$+ \frac{\sigma}{2} \int_0^t \int_{D(x_3,t)} e^{-\sigma s} \rho \dot{u}_i \dot{u}_i \, da \, ds$$
$$+ \frac{\sigma}{2} \int_0^t \int_{D(x_3,s)} e^{-\sigma s} [c_{11}(u_{1,1}+u_{2,2})^2 + c_{66}(u_{1,2}-u_{2,1})^2 + c_{33}u_{3,3}^2 + 2(c_{13}+\varkappa)(u_{1,1}+u_{2,2})u_{3,3}] \, da \, ds$$
$$+ \frac{\sigma}{2} \int_0^t \int_{D(x_3,s)} e^{-\sigma s} [c_{55}(u_{3,1}^2 + u_{3,2}^2 + u_{1,3}^2 + u_{2,3}^2) + 2(c_{55}-\varkappa)(u_{1,3}u_{3,1} + u_{2,3}u_{3,2})] \, da \, ds. \tag{3.14}$$

Now, in view of (3.3), we can choose $\varkappa \in (0, 2c_{55})$ so that

$$\max(-c_{13} - \sqrt{c_{11}c_{33}}, 0) < \varkappa < \min(2c_{55}, -c_{13} + \sqrt{c_{11}c_{33}}) \tag{3.15}$$

and hence to have

$$|c_{55} - \varkappa| < c_{55}. \tag{3.16}$$

Consequently, we obtain

$$c_{55}(u_{3,1}^2 + u_{3,2}^2 + u_{1,3}^2 + u_{2,3}^2) + 2(c_{55}-\varkappa)(u_{1,3}u_{3,1} + u_{2,3}u_{3,2}) \geq v_1(u_{3,1}^2 + u_{3,2}^2 + u_{1,3}^2 + u_{2,3}^2) \tag{3.17}$$

and

$$c_{11}(u_{1,1}+u_{2,2})^2 + c_{66}(u_{1,2}-u_{2,1})^2 + c_{33}u_{3,3}^2 + 2(c_{13}+\varkappa)(u_{1,1}+u_{2,2})u_{3,3}$$
$$\geq v_2[(u_{1,1}+u_{2,2})^2 + u_{3,3}^2], \tag{3.18}$$

where

$$v_1 = \min(2c_{55} - \varkappa, \varkappa), \quad v_2 = \frac{1}{2}\left(c_{11} + c_{33} - \sqrt{(c_{11} - c_{33})^2 + 4(c_{13} + \varkappa)^2}\right). \tag{3.19}$$

With these in mind, we can see that

$$
\begin{aligned}
-\frac{\partial J_\varkappa}{\partial x_3}(x_3, t) \geq{} & \frac{1}{2}\int_{D(x_3,t)} e^{-\sigma t}\rho\dot{u}_i\dot{u}_i\,\mathrm{d}a + \frac{1}{2}\int_{D(x_3,t)} e^{-\sigma t}v_2[(u_{1,1}+u_{2,2})^2 + u_{3,3}^2]\,\mathrm{d}a \\
& + \frac{1}{2}\int_{D(x_3,t)} e^{-\sigma t}v_1(u_{3,1}^2+u_{3,2}^2+u_{1,3}^2+u_{2,3}^2)\,\mathrm{d}a + \frac{\sigma}{2}\int_0^t\int_{D(x_3,s)} e^{-\sigma s}\rho\dot{u}_i\dot{u}_i\,\mathrm{d}a\,\mathrm{d}s \\
& + \frac{\sigma}{2}\int_0^t\int_{D(x_3,s)} e^{-\sigma s}v2[(u_{1,1}+u_{2,2})^2 + u_{3,3}^2]\,\mathrm{d}a\,\mathrm{d}s \\
& + \frac{\sigma}{2}\int_0^t\int_{D(x_3,s)} e^{-\sigma s}v_1(u_{3,1}^2+u_{3,2}^2+u_{1,3}^2+u_{2,3}^2)\,\mathrm{d}a\,\mathrm{d}s
\end{aligned}
$$

$$
\geq 0. \tag{3.20}
$$

On the other hand, by direct differentiation in (3.11) we obtain

$$
\frac{\partial J_\varkappa}{\partial t}(x_3, t) = -\int_{D(x_3,t)} e^{-\sigma t}\left\{\dot{u}_\alpha[(c_{55}-\varkappa)u_{3,\alpha} + c_{55}u_{\alpha,3}] + \dot{u}_3[c_{55}u_{3,3} + (c_{13}+\varkappa)u_{\alpha,\alpha}]\right\}\mathrm{d}a. \tag{3.21}
$$

Furthermore, by means of the arithmetic–geometric and Schwarz inequalities, we obtain

$$
\begin{aligned}
\left|\frac{\partial J_\varkappa}{\partial t}(x_3, t)\right| \leq{} & \int_{D(x_3,t)} e^{-\sigma t}\left\{\max(|c_{55}-\varkappa|, c_{55})[\varepsilon_1\dot{u}_\alpha\dot{u}_\alpha + \frac{1}{2\varepsilon_1}(u_{3,\alpha}u_{3,\alpha} + u_{\alpha,3}u_{\alpha,3})]\right. \\
& \left. + \max(|c_{13}+\varkappa|, c_{55})[\varepsilon_2\dot{u}_3\dot{u}_3 + \frac{1}{2\varepsilon_2}(u_{\alpha,\alpha}u_{\rho,\rho} + u_{3,3}^2)]\right\}\mathrm{d}a, \tag{3.22}
\end{aligned}
$$

so that, by setting $\varepsilon_1 = \sqrt{\dfrac{\rho}{2v_1}}$ and $\varepsilon_2 = \sqrt{\dfrac{\rho}{2v_2}}$, we get

$$
\begin{aligned}
\left|\frac{\partial J_\varkappa}{\partial t}(x_3, t)\right| \leq{} & \frac{c_{55}}{\sqrt{2\rho v_1}}\frac{1}{2}\int_{D(x_3,t)} e^{-\sigma t}\left[\rho\dot{u}_\alpha\dot{u}_\alpha + v_1\left(u_{3,\alpha}u_{3,\alpha} + u_{\alpha,3}u_{\alpha,3}\right)\right]\mathrm{d}a \\
& + \frac{\max\left(\sqrt{c_{11}c_{33}}, c_{55}\right)}{\sqrt{2\rho v_2}}\frac{1}{2}\int_{D(x_3,t)} e^{-\sigma t}\left[\rho\dot{u}_3\dot{u}_3 + v_2\left(u_{\alpha,\alpha}u_{\rho,\rho} + u_{3,3}^2\right)\right]\mathrm{d}a. \tag{3.23}
\end{aligned}
$$

Thus, if we set

$$
\gamma = \max\left(\frac{c_{55}}{\sqrt{2\rho v_1}}, \frac{\max\left(\sqrt{c_{11}c_{33}}, c_{55}\right)}{\sqrt{2\rho v_2}}\right), \tag{3.24}
$$

by means of the relations (3.20) and (3.23) we obtain the first-order partial differential inequality

$$
\left|\frac{\partial J_\varkappa}{\partial t}(x_3, t)\right| \leq -\gamma\frac{\partial J_\varkappa}{\partial x_3}(x_3, t), \qquad (x_3, t) \in [0, \infty) \times [0, \infty). \tag{3.25}
$$

Using an estimating procedure like the one above we obtain the first-order differential inequality

$$
\frac{\sigma}{\gamma}|J_\varkappa(x_3, t)| \leq -\frac{\partial J_\varkappa}{\partial x_3}(x_3, t), \qquad (x_3, t) \in [0, \infty) \times [0, \infty). \tag{3.26}
$$

We now proceed to find the spatial behavior of solutions as described by the differential inequalities above. We start with the study of differential inequality (3.25) and note that it is equivalent to

$$\frac{1}{\gamma} \frac{\partial J_{\varkappa}}{\partial t}(x_3, t) + \frac{\partial J_{\varkappa}}{\partial x_3}(x_3, t) \leq 0, \qquad (x_3, t) \in [0, \infty) \times [0, \infty) \tag{3.27}$$

and

$$-\frac{1}{\gamma} \frac{\partial J_{\varkappa}}{\partial t}(x_3, t) + \frac{\partial J_{\varkappa}}{\partial x_3}(x_3, t) \leq 0, \qquad (x_3, t) \in [0, \infty) \times [0, \infty). \tag{3.28}$$

Let us fix $t_0 > 0$ and assume that $x_3^0 > \gamma t_0$. If we set $x_3 = x_3^0 + \gamma (t - t_0)$ in relation (3.27), we deduce

$$\frac{d}{dx_3}\left[J_{\varkappa}\left(x_3, t_0 + \frac{x_3 - x_3^0}{\gamma}\right)\right] \leq 0, \tag{3.29}$$

so that, recalling that $0 \leq x_3 = x_3^0 - ct_0 \leq x_3^0$, we have

$$J_{\varkappa}\left(x_3^0, t_0\right) \leq J_{\varkappa}\left(x_3^0 - ct_0, 0\right) = 0. \tag{3.30}$$

Moreover, by setting $x_3 = x_3^0 - \gamma (t - t_0)$ in (3.28), we obtain

$$\frac{d}{dx_3}\left[J_{\varkappa}\left(x_3, t_0 - \frac{x_3 - x_3^0}{\gamma}\right)\right] \leq 0, \tag{3.31}$$

and hence we have

$$0 = J_{\varkappa}\left(x_3^0 + \gamma t_0, 0\right) \leq J_{\varkappa}\left(x_3^0, t_0\right). \tag{3.32}$$

Thus, by making $x_3^0 \to \infty$ in relations (3.30) and (3.32), we get

$$J_{\varkappa}\left(\infty, t_0\right) \equiv \lim_{x_3 \to \infty} J_{\varkappa}\left(x_3, t_0\right) = 0. \tag{3.33}$$

Consequently, by using the relations (3.14) and (3.32), we obtain

$$
\begin{aligned}
J_{\varkappa}(x_3, t) \\
= \frac{1}{2} \int_{B(x_3,t)} & e^{-\sigma t} \rho \dot{u}_i \dot{u}_i \, dv \\
+ \frac{1}{2} \int_{B(x_3,t)} & e^{-\sigma t}[c_{11}(u_{1,1}+u_{2,2})^2+c_{66}(u_{1,2}-u_{2,1})^2+c_{33}u_{3,3}^2+2(c_{13}+\varkappa)(u_{1,1}+u_{2,2})u_{3,3}]\, dv \\
+ \frac{1}{2} \int_{B(x_3,t)} & e^{-\sigma t}[c_{55}(u_{3,1}^2 + u_{3,2}^2 + u_{1,3}^2 + u_{2,3}^2) + 2(c_{55} - \varkappa)(u_{1,3}u_{3,1} + u_{2,3}u_{3,2})]\, dv \\
+ \frac{\sigma}{2} \int_0^t \int_{B(x_3,t)} & e^{-\sigma s} \rho \dot{u}_i \dot{u}_i \, dv\, ds \\
+ \frac{\sigma}{2} \int_0^t \int_{B(x_3,s)} & e^{-\sigma s}[c_{11}(u_{1,1}+u_{2,2})^2+c_{66}(u_{1,2}-u_{2,1})^2+c_{33}u_{3,3}^2+2(c_{13}+\varkappa)(u_{1,1}+u_{2,2})u_{3,3}]\, dv\, ds \\
+ \frac{\sigma}{2} \int_0^t \int_{D(x_3,s)} & e^{-\sigma s}[c_{55}(u_{3,1}^2 + u_{3,2}^2 + u_{1,3}^2 + u_{2,3}^2) + 2(c_{55} - \varkappa)(u_{1,3}u_{3,1} + u_{2,3}u_{3,2})]\, dv\, ds \\
\geq 0.
\end{aligned}
\tag{3.34}
$$

This proves that $J_\varkappa(x_3, t)$ represents an acceptable measure for the solution in concern.

Further, we choose $t > 0$ and $x_3 \geq \gamma t$. By setting $x_3 = \gamma t$ in (3.27) we obtain

$$\frac{d}{dt}[J_\varkappa(\gamma t, t)] \leq 0 \tag{3.35}$$

and hence we have

$$J_\varkappa(\gamma t, t) \leq J_\varkappa(0, 0) = 0. \tag{3.36}$$

On the other hand, in view of relation (3.20) and recalling that $x_3 \geq \gamma t$ we have

$$J_\varkappa(x_3, t) \leq J_\varkappa(\gamma t, t) \leq 0. \tag{3.37}$$

Consequently, the relations (3.34) and (3.37) imply relation (3.12). Moreover, the integration of the differential inequality (3.26) leads to the spatial estimate (3.13) and the proof of theorem is complete. □

4. Rhombic systems

Suppose the cylinder is filled by a rhombic elastic material with the group $\mathscr{C}_3$ generated by $\mathbf{R}^\pi_{e_3}$, $\mathbf{R}^\pi_{e_2}$ (here $\mathbf{R}^\theta_e$ is the orthogonal tensor corresponding to a right-handed rotation through the angle $\theta \in (0, 2\pi)$, about an axis in the direction of the unit vector $\mathbf{e}$). According to Gurtin [1972], such class of materials is characterized by

$$C_{1123} = C_{1131} = C_{1112} = C_{2223} = C_{2231} = C_{2212} = 0,$$
$$C_{3323} = C_{3331} = C_{3312} = C_{2331} = C_{2312} = C_{3112} = 0,$$
$$c_{11} = C_{1111}, \qquad c_{22} = C_{2222}, \qquad c_{33} = C_{3333},$$
$$c_{12} = C_{1122}, \qquad c_{23} = C_{2233}, \qquad c_{31} = C_{3311},$$
$$c_{44} = C_{2323}, \qquad c_{55} = C_{1313}, \qquad c_{66} = C_{1212}.$$

The strong ellipticity condition (2.4) becomes

$$c_{11}n_1^2 m_1^2 + c_{22}n_2^2 m_2^2 + c_{33}n_3^2 m_3^2 + c_{66}(n_1 m_2 + n_2 m_1)^2 + c_{44}(n_3 m_2 + n_2 m_3)^2$$
$$+ c_{55}(n_1 m_3 + n_3 m_1)^2 + 2c_{12}n_1 m_1 n_2 m_2 + 2c_{23}n_2 m_2 n_3 m_3 + 2c_{31}n_3 m_3 n_1 m_1 > 0, \tag{4.1}$$

for all nonzero vectors (m_1, m_2, m_3) and (n_1, n_2, n_3). It is equivalent to the conditions (see [Chiriţă and Ciarletta 1999])

$$c_{11} > 0, \quad c_{22} > 0, \quad c_{33} > 0, \quad c_{44} > 0, \quad c_{55} > 0, \quad c_{66} > 0,$$
$$-2c_{66} + \varkappa_3^i\sqrt{c_{11}c_{22}} < c_{12} < \varkappa_3^s\sqrt{c_{11}c_{22}},$$
$$-2c_{44} + \varkappa_1^i\sqrt{c_{22}c_{33}} < c_{23} < \varkappa_1^s\sqrt{c_{22}c_{33}}, \tag{4.2}$$
$$-2c_{55} + \varkappa_2^i\sqrt{c_{11}c_{33}} < c_{13} < \varkappa_2^s\sqrt{c_{11}c_{33}},$$

where $(\varkappa_1^i, \varkappa_1^s)$, $(\varkappa_2^i, \varkappa_2^s)$ and $(\varkappa_3^i, \varkappa_3^s)$ are solutions with respect to x, y and z of the equation

$$x^2 + y^2 + z^2 - 2xyz - 1 = 0, \tag{4.3}$$

with

$$|x| < 1, \qquad |y| < 1, \qquad |z| < 1,$$

$$x \in \left\{ \frac{c_{23}}{\sqrt{c_{22}c_{33}}}, \frac{c_{23}+2c_{44}}{\sqrt{c_{22}c_{33}}} \right\}, \quad y \in \left\{ \frac{c_{13}}{\sqrt{c_{11}c_{33}}}, \frac{c_{13}+2c_{55}}{\sqrt{c_{11}c_{33}}} \right\}, \quad z \in \left\{ \frac{c_{12}}{\sqrt{c_{11}c_{22}}}, \frac{c_{12}+2c_{66}}{\sqrt{c_{11}c_{22}}} \right\}. \quad (4.4)$$

The statement above is equivalent with relation (4.2), and all points $P(x, y, z)$ bounded by (4.4) and (4.4) lie inside the surface $S(x, y, z)$, defined by relation (4.3) above.

The basic equations (2.5) become

$$c_{11}u_{1,11} + c_{66}u_{1,22} + c_{55}u_{1,33} + (c_{12}+c_{66})\,u_{2,21} + (c_{13}+c_{55})\,u_{3,31} = \rho\ddot{u}_1,$$
$$(c_{12}+c_{66})\,u_{1,12} + c_{66}u_{2,11} + c_{22}u_{2,22} + c_{44}u_{2,33} + (c_{23}+c_{44})\,u_{3,32} = \rho\ddot{u}_2, \qquad (4.5)$$
$$(c_{13}+c_{55})\,u_{1,13} + (c_{23}+c_{44})\,u_{2,23} + c_{55}u_{3,11} + c_{44}u_{3,22} + c_{33}u_{3,33} = \rho\ddot{u}_3,$$

and consequently we have the identity

$$\frac{\partial}{\partial t}\left\{ \tfrac{1}{2}\big[\rho\dot{u}_i\dot{u}_i + c_{11}u_{1,1}^2 + c_{22}u_{2,2}^2 + c_{33}u_{3,3}^2 + c_{66}(u_{1,2}^2 + u_{2,1}^2) + c_{55}(u_{3,1}^2 + u_{1,3}^2) + c_{44}(u_{3,2}^2 + u_{2,3}^2) \right.$$
$$+ 2(c_{12}+\varkappa_3)u_{1,1}u_{2,2} + 2(c_{66}-\varkappa_3)u_{1,2}u_{2,1} + 2(c_{13}+\varkappa_2)u_{1,1}u_{3,3}$$
$$\left. + 2(c_{55}-\varkappa_2)u_{1,3}u_{3,1} + 2(c_{23}+\varkappa_1)u_{2,2}u_{3,3} + 2(c_{44}-\varkappa_1)u_{2,3}u_{3,2}\big]\right\}$$
$$= \{\dot{u}_1[c_{55}u_{1,3}+(c_{55}-\varkappa_2)u_{3,1}]+\dot{u}_2[c_{44}u_{2,3}+(c_{44}-\varkappa_1)u_{3,2}]+\dot{u}_3[(c_{13}+\varkappa_2)u_{1,1}+(c_{23}+\varkappa_1)u_{2,2}+c_{33}u_{3,3}]\}_{,3}$$
$$+\{\dot{u}_1[c_{11}u_{1,1}+(c_{12}+\varkappa_3)u_{2,2}+(c_{13}+\varkappa_2)u_{3,3}]+\dot{u}_2[c_{66}u_{2,1}+(c_{66}-\varkappa_3)u_{1,2}]+\dot{u}_3[c_{55}u_{3,1}+(c_{55}-\varkappa_2)u_{1,3}]\}_{,1}$$
$$+\{\dot{u}_1[c_{66}u_{1,2}+(c_{66}-\varkappa_3)u_{2,1}]+\dot{u}_2[(c_{12}+\varkappa_3)u_{1,1}+c_{22}u_{2,2}+(c_{23}+\varkappa_1)u_{3,3}]+\dot{u}_3[c_{44}u_{3,2}+(c_{44}-\varkappa_1)u_{2,3}]\}_{,2},$$
$$(4.6)$$

where $\varkappa_1$, $\varkappa_2$ and $\varkappa_3$ are positive parameters at our disposal.

So we have to introduce the function

$$K_\varkappa(x_3, t) = -\int_0^t \int_{D(x_3,s)} e^{-\sigma s}\{\dot{u}_1[(c_{55}-\varkappa_2)u_{3,1}+c_{55}u_{1,3}]+\dot{u}_2[(c_{44}-\varkappa_1)u_{3,2}+c_{44}u_{2,3}]$$
$$+\dot{u}_3[(c_{13}+\varkappa_2)u_{1,1}+(c_{23}+\varkappa_1)u_{2,2}+c_{33}u_{3,3}]\}\,\mathrm{d}a\,\mathrm{d}s \quad (4.7)$$

and note that identity (4.6) implies that

$$-\frac{\partial K_\varkappa}{\partial x_3}(x_3, t) = \frac{1}{2}\int_{D(x_3,t)} e^{-\sigma t}\rho\dot{u}_i\dot{u}_i\,\mathrm{d}a$$

$$+\frac{1}{2}\int_{D(x_3,t)} e^{-\sigma t}[c_{11}u_{1,1}^2 + c_{22}u_{2,2}^2 + c_{33}u_{3,3}^2$$
$$+2(c_{12}+\varkappa_3)u_{1,1}u_{2,2} + 2(c_{13}+\varkappa_2)u_{1,1}u_{3,3} + 2(c_{23}+\varkappa_1)u_{2,2}u_{3,3}]\,\mathrm{d}a$$

$$+\frac{1}{2}\int_{D(x_3,t)} e^{-\sigma t}[c_{66}(u_{1,2}^2 + u_{2,1}^2) + 2(c_{66}-\varkappa_3)u_{1,2}u_{2,1}]\,\mathrm{d}a$$

$$+\frac{1}{2}\int_{D(x_3,t)} e^{-\sigma t}[c_{44}(u_{2,3}^2 + u_{3,2}^2) + 2(c_{44}-\varkappa_1)u_{2,3}u_{3,2}]\,\mathrm{d}a$$

$$+\frac{1}{2}\int_{D(x_3,t)} e^{-\sigma t}[c_{55}(u_{3,1}^2 + u_{1,3}^2) + 2(c_{55}-\varkappa_2)u_{1,3}u_{3,1}]\,\mathrm{d}a$$

$$+\frac{\sigma}{2}\int_0^t\int_{D(x_3,s)}e^{-\sigma s}\rho\dot{u}_i\dot{u}_i\,\mathrm{d}a\,\mathrm{d}s$$

$$+\frac{\sigma}{2}\int_0^t\int_{D(x_3,s)}e^{-\sigma s}[c_{11}u_{1,1}^2+c_{22}u_{2,2}^2+c_{33}u_{3,3}^2$$

$$+2(c_{12}+\varkappa_3)u_{1,1}u_{2,2}+2(c_{13}+\varkappa_2)u_{1,1}u_{3,3}+2(c_{23}+\varkappa_1)u_{2,2}u_{3,3}]\,\mathrm{d}a\,\mathrm{d}s$$

$$+\frac{\sigma}{2}\int_0^t\int_{D(x_3,s)}e^{-\sigma s}[c_{66}(u_{1,2}^2+u_{2,1}^2)+2(c_{66}-\varkappa_3)u_{1,2}u_{2,1}]\,\mathrm{d}a\,\mathrm{d}s$$

$$+\frac{\sigma}{2}\int_0^t\int_{D(x_3,s)}e^{-\sigma s}[c_{44}(u_{2,3}^2+u_{3,2}^2)+2(c_{44}-\varkappa_1)u_{2,3}u_{3,2}]\,\mathrm{d}a\,\mathrm{d}s$$

$$+\frac{\sigma}{2}\int_0^t\int_{D(x_3,s)}e^{-\sigma s}[c_{55}(u_{3,1}^2+u_{1,3}^2)+2(c_{55}-\varkappa_2)u_{1,3}u_{3,1}]\,\mathrm{d}a\,\mathrm{d}s. \tag{4.8}$$

In view of the assumptions (4.2) we can choose $\varkappa_1\in[0,2c_{44}]$, $\varkappa_2\in[0,2c_{55}]$, $\varkappa_3\in[0,2c_{66}]$ so that $P(x,y,z)$, with coordinates

$$x=\frac{c_{23}+\varkappa_1}{\sqrt{c_{22}c_{33}}},\quad y=\frac{c_{13}+\varkappa_2}{\sqrt{c_{11}c_{33}}},\quad z=\frac{c_{12}+\varkappa_3}{\sqrt{c_{11}c_{22}}},$$

lies inside the region limited by the surface $S(x,y,z)$. Then the Sylvester criterion provides a straight-forward way toward conditions of positivity of the quadratic form

$$\mathscr{F}\left(u_{i,j}\right)=\left[c_{11}u_{1,1}^2+c_{22}u_{2,2}^2+c_{33}u_{3,3}^2+2\left(c_{12}+\varkappa_3\right)u_{1,1}u_{2,2}+2\left(c_{13}+\varkappa_2\right)u_{1,1}u_{3,3}+2\left(c_{23}+\varkappa_1\right)u_{2,2}u_{3,3}\right]$$
$$+\left[c_{66}\left(u_{1,2}^2+u_{2,1}^2\right)+2\left(c_{66}-\varkappa_3\right)u_{1,2}u_{2,1}\right]+\left[c_{44}\left(u_{2,3}^2+u_{3,2}^2\right)+2\left(c_{44}-\varkappa_1\right)u_{2,3}u_{3,2}\right]$$
$$+\left[c_{55}\left(u_{3,1}^2+u_{1,3}^2\right)+2\left(c_{55}-\varkappa_2\right)u_{1,3}u_{3,1}\right] \tag{4.9}$$

in terms of $u_{i,j}$. Therefore, we have

$$\mu_m u_{i,j}u_{i,j}\le\mathscr{F}\left(u_{r,s}\right)\le\mu_M u_{i,j}u_{i,j}, \tag{4.10}$$

where μ_m and μ_M are the positive minimum and maximum eigenvalues of the positive quadratic form $\mathscr{F}\left(u_{i,j}\right)$. Thus, the relations (4.8) to (4.10) qualify $K_\varkappa\left(x_3,t\right)$ as a valuable measure of the solution. Further the analysis for evolution of the measure $K_\varkappa\left(x_3,t\right)$ follows the procedure developed in the above section, thus leading to a spatial behavior like that described by the Theorem 1. Consequently, we can state the following result.

Theorem 2. *Let $u_i(x,t)$ be a solution of the initial boundary value problem defined by* (4.5), (2.6), (2.7) *and* (2.8). *Then $K_\varkappa\left(x_3,t\right)$ as defined by* (4.7) *represents a measure of the solution and, for each $t>0$, it evolves as follows. There is a positive constant v, depending on the elastic constants, such that*

(a) *for $x_3\ge vt$ we have $K_\varkappa\left(x_3,t\right)=0$ and hence*

$$u_i\left(x_3,t\right)=0\quad\text{for all }x_3\ge vt; \tag{4.11}$$

(b) *for $x_3\le vt$, the spatial behavior is described by*

$$0\le K_\varkappa\left(x_3,t\right)\le K_\varkappa\left(0,t\right)\exp\left(-\frac{\sigma}{v}x_3\right). \tag{4.12}$$

5. Conclusions

The spatial behavior of solutions to the initial boundary value problems in linear elastodynamics has been established based on the assumption of strong ellipticity of the elasticity tensor. A domain of influence theorem has been obtained proving that the whole activity is zero in that part of the cylinder whose axial distance from the loaded end is greater than a critical value. Moreover, inside of the influence domain, a spatial estimate of Saint Venant type has been established, which describes the exponential decay of solutions with respect to the distance from the loaded end. However, these results have been obtained for transversely isotropic and rhombic elastic materials only, since the necessary and sufficient conditions characterizing the strong ellipticity have been discovered recently. Extension to the whole class of anisotropic materials seems to be impossible as long as the characterization of their strong ellipticity remains an open problem.

We have to point out that the influence domain result (relations (3.12) and (4.11)) is independent of the parameter σ entering in the definition of the functions $J_{\varkappa}$ and $K_{\varkappa}$, while it appears in the exponential estimates (3.13) and (4.12) as a scaling parameter. Our analysis works when $\sigma = 0$ to prove the influence domain result, but the exponential estimates (3.13) and (4.11) fail to give information on the spatial evolution of solutions. In such case we have to apply the method developed by Chiriţă [1997] for the model of linear viscoelasticity. It is worthwhile to point out that we cannot make $\sigma \to \infty$, because in this case the functions $J_{\varkappa}$ and $K_{\varkappa}$ cannot be considered as measures of solutions.

References

[Chiriţă 1997] S. Chiriţă, "On Saint-Venant's principle in dynamic linear viscoelasticity", *Quart. Appl. Math.* **55**:1 (1997), 139–149. MR 98d:73037

[Chiriţă 2006] S. Chiriţă, "On the strong ellipticity condition for transversely isotropic linearly elastic solids", *An. Ştiinţ. Univ. Al. I. Cuza Iaşi. Mat. (N.S.)* **52**:2 (2006), 245–250. MR 2008f:74010

[Chiriţă and Ciarletta 1999] S. Chiriţă and M. Ciarletta, "Time-weighted surface power function method for the study of spatial behaviour in dynamics of continua", *Eur. J. Mech. A Solids* **18**:5 (1999), 915–933. MR 2000i:74044

[Gurtin 1972] M. E. Gurtin, *The linear theory of elasticity*, vol. VIa/2, edited by C. Truesdell, Springer, Berlin, 1972.

[Merodio and Ogden 2003] J. Merodio and R. W. Ogden, "A note on strong ellipticity for transversely isotropic linearly elastic solids", *Quart. J. Mech. Appl. Math.* **56**:4 (2003), 589–591. MR 2026873

VINCENZO TIBULLO: vtibullo@unisa.it
Università degli Studi di Salerno, via Ponte Don Melillo, 84084 Fisciano (SA), Italy

MASSIMO VACCARO: massimo_vaccaro@libero.it
Università degli Studi di Salerno, via Ponte Don Melillo, 84084 Fisciano (SA), Italy

POSTBUCKLING OF TRUSS-LATTICE SHEAR PANELS USING EXACT THEORY

PHILIP A. WILLIAMS, RICHARD BUTLER, HYUNSUN A. KIM AND GILES W. HUNT

A new solution is developed to model the stable postbuckling behaviour of a truss-lattice shear panel. The mode shapes are derived through load equilibrium conditions and are based on the load in the structural members. The load in each member of a single-cell panel can be calculated exactly, without the need for an iterative postbuckling path, and the method produces excellent results in initial and advanced postbuckling. Comparisons are drawn with an alternative analytical method and the commonplace finite element approach. A Rayleigh–Ritz method based on a Fourier approximation to the mode shape provides the useful progression from an unbuckled to a buckled structure giving excellent results in initial postbuckling, although is limited for advanced postbuckling. The standard finite element method for this problem produces accurate results but with limited detail around the buckling load owing to the presence of an imperfection in the shape of the initial mode, which is required to initiate the postbuckling analysis.

1. Introduction

Truss structures are widely recognised as being an efficient way to carry load, as they are lightweight and have high stiffness. A recent investigation has shown that a truss-lattice configuration exhibits a stable postbuckling behaviour under shear [Williams et al. 2007], similar to that of a continuous panel via development of a diagonal tension field [Wagner 1931; Kuhn et al. 1952]. It has been demonstrated that by arranging the members of a truss-lattice to align with the compression and tension diagonals of a shear panel, as shown in Figure 1, a similar diagonal tension field can be established [Kim et al. 2004]. With the tension members dominating, the postbuckling behaviour of the truss-lattice panel is stable.

A benefit of such a configuration is the potential weight savings. A preliminary study investigated a truss-lattice configuration with a set of diagonal members such as Figure 2 and compared it with a continuous shear panels for a range of loads [Williams et al. 2007]. It was shown that for a panel under relatively low shear load (with a shear flow less than 100 N/mm), a simple unbuckled truss-lattice can offer weight-saving of at least 59% over postbuckled continuous panels, increasing to 66% if postbuckling is permitted.

Analysis of geometrically nonlinear postbuckling of frame structures has been actively researched in the past few decades. A common subject of interest has been incremental-iterative techniques including stiffness-based finite element (FE) methods which can be used to model the postbuckling behaviour of the truss-lattice structures above. However, it is possible and useful, particularly for physical insight, to also describe the deformations and postbuckling behaviour analytically.
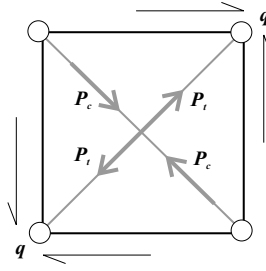
Figure 1. Shear flow q produces resultant axial forces P_c and P_t in a truss-lattice panel.

Developments in analyses of geometrically nonlinear frame structures, both in analytical understanding and in aspects of numerical techniques, have been summarised in an extensive review by Yang et al. [2003]. It is not therefore the intention to present a comprehensive survey of these developments here, but to introduce those methods that are relevant to this study.

The theory of beam columns is discussed in Timoshenko and Gere [1936] in which the elastic buckling behaviour and deflection of a beam under compressive loads can be described by sine and cosine functions of the applied load. This was extended by Williams [1964] to describe the nonlinear snap-through behaviour of a two-beam arch (or toggle). The beam theory stated in Timoshenko and Gere [1936] and used by Williams [1964] will be referred to as the exact solution, although there are some assumptions and approximations used in the formulation. Williams [1964], for example, follows the nonlinear behaviour of rigid jointed frameworks, which provides a good starting point for the struts to be considered here. The exact solution assumes a general mode shape described by trigonometric functions, which is defined in terms of the applied loads and boundary conditions of the members. No imperfection is required for the analysis, but the critical load of the structure must be found before analysing the postbuckling behaviour, and the assumption is made that deflections do not occur until the buckling load is reached. Only in-plane deflections are considered, and the examples given are such that the end-shortening and in-plane deflection of each member can be described exactly for a given applied load.

An alternative analytical procedure is the Rayleigh–Ritz analysis, which has been applied to many different postbuckling problems, including plates and struts [Thompson and Hunt 1973], although rarely with the introduction of a tension member. This analysis uses a Fourier expansion to approximate the mode shape, where the number of terms that are included determines the accuracy of the solution as the
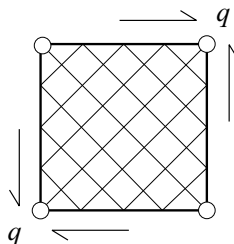
Figure 2. Multiple cell truss-lattice shear panel.

mode shape develops in postbuckling. By considering the total energy of the structure, it is possible to trace the in-plane prebuckling equilibrium solution, and hence measure the ratio of initial postbuckling to prebuckling stiffness.

The conventional approach to modelling this type of problem is via nonlinear FE analysis. The FE methodology is flexible and applicable to a wide range of problems, and a model can be set up in a relatively straight-forward manner with commercially available software. The analysis also gives an accurate result, although often at the expense of high computation time. To follow the postbuckling behaviour of a structure, one must first perform a buckling analysis to find the buckling load and mode shape. This mode shape can then be used as an imperfection, which is required for nonlinear postbuckling FE analysis. The requirement of an imperfection is one disadvantage with the FE approach as it causes out-of-plane bending deformation to occur before the critical load is reached. The FE method is mesh sensitive as it requires an appropriate number of correctly positioned elements; it can be costly, owing to the often high computation time; and the boundary conditions can often be difficult to model correctly, although it is not always apparent when mistakes are made.

This paper investigates the postbuckling behaviour of a truss-lattice shear panel by developing an analytical procedure using exact member theory. The mode shape of each member is dependent on the load in the member, and hence the postbuckling stiffness and deflection of each member can be calculated exactly for any given load. Comparisons are then drawn between the alternative analytical Rayleigh–Ritz method and FE analysis. Both analytical procedures are purpose driven and appropriate for modelling the truss-lattice in postbuckling and aimed at addressing some of the limiting features of the FE approach. Of particular interest is the use of fewer elements in the model definition, hence fewer equations to solve; the physical insight that each method introduces; and the principle of developing a method to be used specifically for the truss-lattice shear panel problem.

2. Truss-lattice shear panel

The truss-lattice considered in this paper comprises a series of diagonal struts arranged at $\pm 45°$ to the shear load, as shown in Figure 1, such that the resulting diagonal tension and compression are carried axially in the lattice members. We also consider a frame around the lattice consisting of rigid members with pinned corner joints. The shear flow q in Figure 1 is modelled as compression and tension loads P, which are applied at the corners and transferred to the internal members via the stiff frame as a displacement controlled mechanical system as shown in Figure 3. The lattice members are welded at their intersections but have a simply-supported connection to the frame. One crossover of diagonal members is referred to as one cell, highlighted in Figure 3(a), and the number of cells along one side of a square panel is given by the cell dimension n. The length of each member is ℓ, and hence the frame members are length $\sqrt{2}n\ell$. Rotating the model by $45°$, as shown in Figure 3(b), aligns the members with the global X and Y axis, and a shear deformation (given by effective shear strain γ) produces displacements in these global directions (Δ_X and Δ_Y respectively). These displacements are considered positive in compression and hence Δ_X is negative, as demonstrated in Figure 3(b).
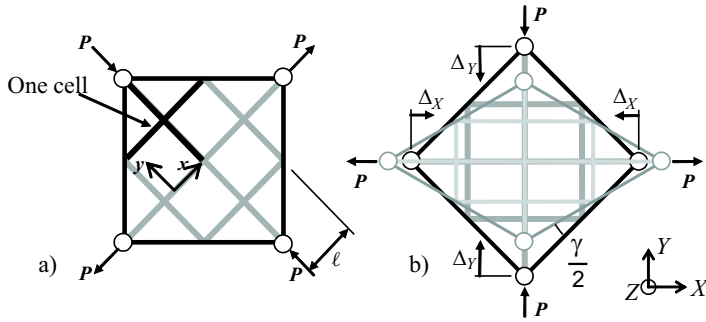
Figure 3. (a) Truss-lattice panel ($n = 2$) with rigid frame members under external diagonal loads P; (b) Deformed lattice, showing effective shear strain γ, and in-plane end displacements Δ_X and Δ_Y.

3. Analytical methods

Analytical methods do not require imperfections and so have the ability to pin-point the initial buckling load and to trace the initial postbuckling path more accurately than FE methods. In addition, no frame is required for the analytical methods as the displacements are described by the geometric relationships associated with a rigid frame. The frame has a very high stiffness in the FE approach, but it is still finite, and so the properties of the frame do have some effect on the results. Removing the frame in the analytical methods removes this variable and allows some additional physical insight into the behaviour of the lattice itself, although one must consider the properties of the frame when a realistic panel is to be modelled.

3.1. *Exact initial mode method.* This approach initially solves the eigenvalue problem to produce an exact buckling load and critical mode shape based on a single element for each member. A development is then made to the existing method to extend the analysis into postbuckling through consideration of equilibrium, boundary conditions, and compatibility conditions. The same mode shape is assumed throughout, based on the initial buckling mode, although the amplitudes are dependent on the loads applied to the members, and the assumption is later verified by comparison with FE results. The analysis extends successfully into the nonlinear postbuckling regime, although we note that the large deflection nonlinearities associated with solutions of the elastica problem have been omitted [Thompson and Hunt 1973]. The analysis is thus suitable for moderately large postbuckling deflections.

3.1.1. *Equilibrium.* We consider a moment equilibrium about a cut C along a general lattice member (shown in Figure 4) such that

$$M = -EI\frac{d^2w}{dx^2} = Pw + m - P_z x, \tag{1}$$

where E is the elastic modulus and I is the second moment of area relating to out-of-plane deflections. The load in the member P is positive in compression P_c and negative in tension P_t. The out-of-plane force P_z (which is always positive in the z-direction) and the moment m act at the end of each member.
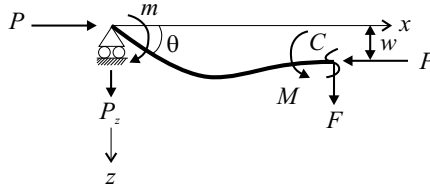
Figure 4. Forces and displacements for a general lattice member. The moment m at the pin joint is included for the general definition in Equation (1).

The whole structure must be in load equilibrium, hence the out-of-plane contributions P_z from each of the members must sum to zero. We shall return to this requirement later.

The following equations are applicable to both compression and tension members although the subscripts c and t respectively are used where appropriate. Equation (1) has a general solution

$$w = C_1 \cos \beta x + C_2 \sin \beta x - \frac{m}{P} + \frac{P_z x}{P} \tag{2}$$

in which

$$\beta^2 = P/EI, \tag{3}$$

and C_1 and C_2 are unknown coefficients to be found through application of the boundary conditions.

3.1.2. *Boundary conditions.* If we consider a single cell $n = 1$ model (with local coordinate x as shown in Figure 3(a)) with pinned corners and symmetry around the central members, the boundary conditions for this case are as follows. The deflection w at $x = 0$ is zero and solving for C_1 gives

$$C_1 = m/P. \tag{4}$$

At $x = \ell$ the gradient $\dot{w}$ is zero owing to symmetry (where a dot represents differentiation with respect to x

$$\dot{w} = -\frac{m\beta \sin \beta \ell}{P} + C_2 \beta \cos \beta \ell + \frac{P_z}{P} = 0,$$

and hence

$$C_2 = \frac{m\beta \sin \beta \ell - P_z}{P\beta \cos \beta \ell}. \tag{5}$$

Therefore, substituting Equations (4) and (5) into Equation (2) gives the following general equation for the out-of-plane deflection of a compression member

$$w_c = \frac{m_c}{P_c}\left(\cos \beta_c x + \frac{\sin \beta_c \ell \sin \beta_c x}{\cos \beta_c \ell} - 1\right) + \frac{P_{zc}}{P_c}\left(x - \frac{\sin \beta_c x}{\beta_c \cos \beta_c \ell}\right). \tag{6}$$

As tension load P_t is considered negative in this analysis, the deflection of a tension member w_t is

$$w_t = \frac{m_t}{P_t}\left(\cos \beta_t x + \frac{\sin \beta_t \ell \sin \beta_t x}{\cos \beta_t \ell} - 1\right) + \frac{P_{zt}}{P_t}\left(x - \frac{\sin \beta_t x}{\beta_t \cos \beta_t \ell}\right), \tag{7}$$

and β_t must be imaginary in accordance with Equation (3).

For a pin joint, the moment m is zero, which further simplifies Equations (6) and (7) to give

$$w_c = \frac{P_{zc}}{P_c}\left(x - \frac{\sin \beta_c x}{\beta_c \cos \beta_c \ell}\right), \quad w_t = \frac{P_{zt}}{P_t}\left(x - \frac{\sin \beta_t x}{\beta_t \cos \beta_t \ell}\right). \tag{8}$$

3.1.3. *Compatibility.* A compatibility condition is applied at the intersection of the lattice members where the central out-of-plane deflection w^* must be the same for both members and is defined by Equations (6) and (7) at $x = \ell$. Differentiating Equations (6) and (7) at $x = 0$ gives the angle of rotation θ, and applying the compatibility condition and rearranging gives

$$m = \frac{(\sin \beta\ell - \beta\ell \cos \beta\ell)}{P\beta Z}\theta - \frac{(1 - \cos \beta\ell)}{PZ}w^* \tag{9}$$

and

$$P_z = \frac{(1 - \cos \beta\ell)}{PZ}\theta - \frac{\beta \sin \beta\ell}{PZ}w^*, \tag{10}$$

where Z is the determinant of the basic member matrix with the solution

$$Z = \frac{(2 - 2\cos \beta\ell - \beta\ell \sin \beta\ell)}{P^2}. \tag{11}$$

3.1.4. *Initial buckling.* From the Wittrick–Williams algorithm for calculating the critical buckling load of elastic structures [Wittrick and Williams 1973], the critical load of the truss-lattice can be determined by first constructing a stiffness matrix for the whole structure and then finding the values for load that give zero values for the determinant of this matrix. This procedure finds the critical loads and produces corresponding mode shapes for the structure. It does not determine the amplitudes of the modes nor any postbuckling behaviour.

3.1.5. *Postbuckling.* Applying the boundary condition for a pin joint, $m = 0$, to Equation (9) gives

$$\theta = \frac{\beta(1 - \cos \beta\ell)}{(\sin \beta\ell - \beta\ell \cos \beta\ell)}w^*. \tag{12}$$

Substituting Equation (12) into Equation (10) gives P_z in terms of w^* and the applied load P such that

$$P_z = \left(\frac{(1 - \cos \beta\ell)^2}{(\sin \beta\ell - \beta\ell \cos \beta\ell)} - \sin \beta\ell\right)\frac{\beta w^*}{PZ}. \tag{13}$$

We now consider the out-of-plane equilibrium. Owing to symmetry, the out-of-plane reactions P_{zc} produced when the compression members buckle must be equal for the two compression ends in the single cell model, as must the reactions for the tension members P_{zt}. Hence for equilibrium,

$$P_{zc} = -P_{zt}. \tag{14}$$

Therefore the values of load in the members must produce P_z in Equation (13) such that Equation (14) is satisfied, and hence there is a transcendental relationship between P_t and P_c.

In Figure 3(b), the displacements in the X and Y directions are geometrically linked due to the rigid frame member. Describing these in terms of the effective shear strain γ gives

$$\Delta_Y = \ell\left[1 - \sqrt{2}\sin\left(\frac{\pi}{4} - \frac{\gamma}{2}\right)\right] \approx \ell\left(\frac{\gamma}{2} + \frac{\gamma^2}{8}\right), \quad \Delta_X = \ell\left[1 - \sqrt{2}\cos\left(\frac{\pi}{4} - \frac{\gamma}{2}\right)\right] \approx -\ell\left(\frac{\gamma}{2} - \frac{\gamma^2}{8}\right), \tag{15}$$

where the first three terms of the power series expansion are used for the trigonometric factors. We note that a positive (compression) load produces a positive displacement in Y, and conversely a negative (tensile) load produces a negative displacement in X.

The displacements of the ends of the members can also be described as the sum of the end-shortening required to form the deflected mode shape and the axial strain due to the load in the member

$$\Delta_Y = \frac{1}{2} \int_0^\ell \dot{w}_c^2 \, dx + \frac{P_c \ell}{EA}, \qquad \Delta_X = \frac{1}{2} \int_0^\ell \dot{w}_t^2 \, dx + \frac{P_t \ell}{EA}, \qquad (16)$$

where A is the cross-sectional area of the truss members.

The transcendental nature of Equations (1)–(16) makes a direct solution impossible. Instead, an iterative procedure is adopted such as that detailed in Figure 5. The mode shapes must first be defined in terms of the loads P_c and P_t and the central deflection w^* (substituting Equations (11) and (13) into Equations (8)). Problem-specific values must then be assigned to the variables EI, EA, ℓ, and the critical load calculated. An initial value for P_t must first be assumed (just above the critical load P^{crit}), and P_{zt} is calculated using Equation (13). The corresponding P_c is computed iteratively to determine P_{zc} such that
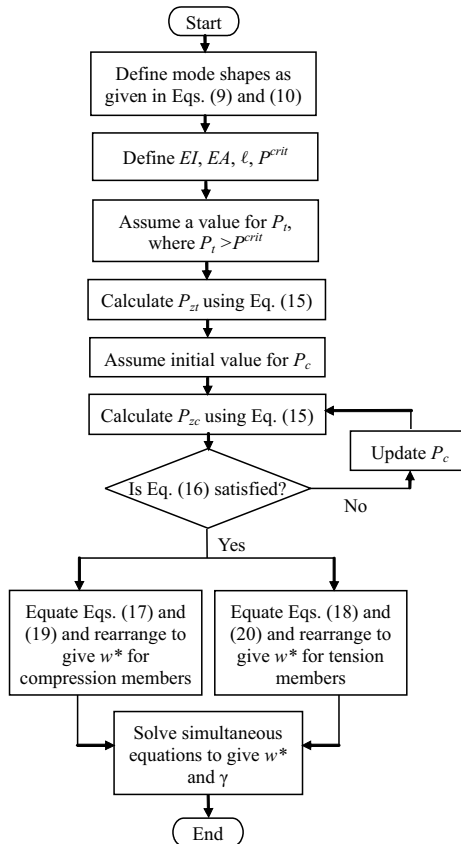
Figure 5. Flow diagram for the iterative procedure required to solve the postbuckling exact initial mode method.

the equilibrium condition in Equation (14) is satisfied. The analysis can be extended by incrementally increasing values for P_t as the load in tension is expected to increase, but the analysis is not dependent on the size of the step.

Once the values of the loads are known, the deflections and displacements are found by first equating the corresponding Δ_X and Δ_Y displacements in Equations (15)–(16) and rearranging to give w^* in terms of γ, then solving the two subsequent simultaneous equations. With incremental values for P_t, the postbuckling performance is traced until a limiting criterion is reached. The applied load P is taken as the mean of the tension and compression loads and is used as an indication to the extent of progress into the postbuckling region with five times the critical load defined as the end condition for the iterative procedure of Figure 5. The process requires significant algebraic manipulation and a numerical solution which has been implemented within the algebraic manipulation package Maple [Maple 2005].

3.2. *Rayleigh–Ritz method.* This approach uses a Fourier expansion approximation to the mode shape and considers a minimum energy solution to the development of the mode in postbuckling. With the modal development described by its shape alone rather than including the load in the members as in the previous analyses, the Rayleigh–Ritz method provides a useful visual tool and provides information which is overlooked by the other methods.

The mode shape of the tension and compression members in Equations (8) can be expressed in a more simplified form by the N degree-of-freedom Fourier approximation,

$$w_c = Q_1 \ell \sin\left(\frac{\pi x}{2\ell}\right) + Q_3 \ell \sin\left(\frac{3\pi x}{2\ell}\right) + Q_5 \ell \sin\left(\frac{5\pi x}{2\ell}\right) + \cdots + \left(\sum_{i=1}^{N} Q_i\right)\ell \sin\left(\frac{(N+1)\pi x}{2\ell}\right) \quad (17)$$

$$w_t = Q_2 \ell \sin\left(\frac{\pi x}{2\ell}\right) + Q_4 \ell \sin\left(\frac{3\pi x}{2\ell}\right) + Q_6 \ell \sin\left(\frac{5\pi x}{2\ell}\right) + \cdots \quad (18)$$

with ($i = 1 \ldots N$, N even) where the Q_i are the amplitudes of the modal contributions [Thompson and Hunt 1973], written in terms of the total strut length (2ℓ). Equal central deflection in the two components is enforced by the final term in the x-series, where negative values for the even-numbered Q_i would be expected in the final solution.

If we consider the potential energy V of the deformed shape for the whole model, there is bending energy U_B and axial (or membrane) energy U_M with work done by the applied load $P\varepsilon = P\Delta_X + P\Delta_Y$, such that $V = 2U_B + 2U_M - 2P\varepsilon$, where

$$U_B = \frac{EI}{2}\int_0^\ell \ddot{w}_c^2\,dx + \frac{EI}{2}\int_0^\ell \ddot{w}_t^2\,dx, \quad U_M = \frac{EA}{2\ell}\left(\Delta_X - \frac{1}{2}\int_0^\ell \dot{w}_c^2\,dx\right)^2 + \frac{EA}{2\ell}\left(\Delta_Y - \frac{1}{2}\int_0^\ell \dot{w}_t^2\,dx\right)^2.$$

It should be noted that in-plane stretching is automatically included dependent on the axial stiffness EA and monitored by a single extra degree of freedom that averages the corner shearing displacements, $\Delta = (\Delta_Y - \Delta_X)/2$.

By introducing a set of sliding incremental coordinates a linear approximation to the nontrivial fundamental (prebuckling) solution is then readily accommodated [Thompson and Hunt 1973]. Unlike the previous analysis which assumed zero deflection before buckling, this allows important comparisons between pre- and postbuckling stiffness.

The unbuckled (fundamental) equilibrium path is found by minimising the energy with respect to Δ with the out-of-plane displacements set to zero. Postbuckling equilibrium states are then represented by the set of N nonlinear equations that come from setting the derivatives of V with respect to Q_i equal to zero. Rather than attempting to find an exact or numerical solution, an ordered Taylor series approximation to the postbuckling equilibrium path is obtained from these by applying the so-called perturbation technique, based on expansion of the energy function about the critical equilibrium state [Thompson and Hunt 1973]. All analysis is carried out within the algebraic manipulation package Maple [Maple 2005].

4. Finite element method

The truss-lattice has been modelled with the FE software ABAQUS using simple Euler–Bernoulli beams [ABAQUS 2003] with eight elements for each length ℓ giving sufficiently accurate results for the buckling analysis. The frame members are pinned at the corners to allow displacements in the XY plane. These members are modelled with high axial and bending stiffness to simulate a rigid loading frame. Constraints are applied to the model at the four corners to prevent displacements in X and Z at the top and bottom and in Y and Z at the sides, and symmetry is enforced about the central members. Only buckling out of the XY plane is considered (although buckling in-plane is also possible, as demonstrated in Williams et al. [2007]) by specifying the second moment of area of the lattice members I to be much greater in-plane than out-of-plane. A linear eigen-buckling method is used to find the critical buckling loads and corresponding mode shapes, and the initial mode shape is imported as an imperfection for the nonlinear Riks method for postbuckling analysis [Riks 1979].

5. Results and discussion

The FE results from ABAQUS are compared with those from the Maple solutions of the exact method and the energy method for one cell.

5.1. *Mode shapes.* The mode shapes in Figure 6(a) demonstrate that when the compression members buckle out-of-plane, the mode is initially global (long wavelength) then moving into a more localised short-wave mode in postbuckling, Figure 6(b). This development from global to local mode is particularly prominent with increasing numbers of cells such as the $n = 3$ and $n = 4$ models in Figure 6, where some elements change from positive deflection to negative as the localised mode develops.

5.2. *Analytical method results.* In a single cell the initial buckling mode from both methods is a global buckle in which the compression member is dominated by a half sine mode with a slight dip in the centre due to the presence of higher modal contributions (as given in Equation (17)). As the postbuckling develops the central node is constrained by the tension member so that the shape becomes more lo-calised with large deflections developing in the mid-regions of the compression member but a reducing deflection at the central node. This is modelled in the Rayleigh–Ritz method through the development of the higher modal contributions and is driven by the additional load carried in the tension member. All three formulations performed satisfactorily in describing the mode shapes and their development in postbuckling from global to local.
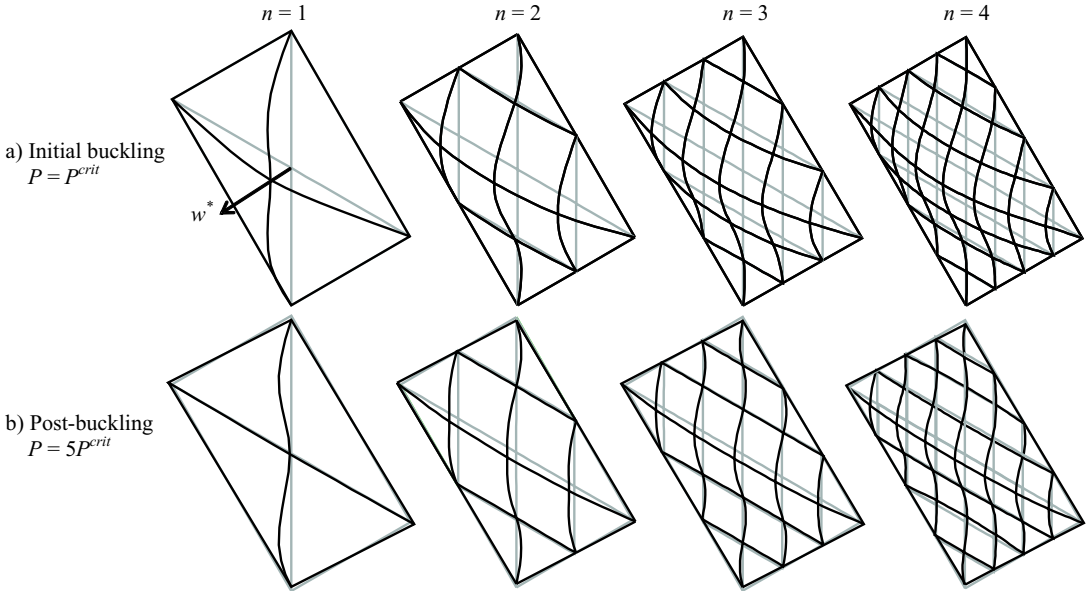
Figure 6. Initial buckling and postbuckling mode shapes with increasing numbers of cells. The central out-of-plane deflection w^* is shown for the initial mode of the $n = 1$ lattice. The initial buckling and postbuckling modes are not shown to the same scale.

In calculating the critical load using the exact initial mode and FE methods, it has been assumed that there are no geometric displacements prior to buckling. However, in practice the in-plane stiffness of the members will determine the displacements that occur. This prebuckling deformation is considered here using the Rayleigh–Ritz analysis. Table 1 gives both the critical load and the pre- to postbuckling ratio from the Rayleigh–Ritz analysis as the in-plane (EA) stiffness is altered in comparison to the bending stiffness (EI) of the lattice members. The critical load is nondimensionalised with respect to the Euler load for the total length 2ℓ.

With a lower in-plane stiffness, larger axial deformations are permitted prior to buckling. The members are linearly elastic, and with the geometric conditions defined in Equations (15) a greater proportion of the applied load is stored in the compression rather than tension members. With additional load in compression, buckling occurs at a lower value of applied load when the in-plane stiffness is lower, hence the reduced critical loads in Table 1.

Ratio $A\ell^2/I$	Critical load/Euler load	Post/prebuckling stiffness ratio
10^5	6.246	0.834
10^4	6.207	0.833
10^3	5.846	0.827

Table 1. Critical load and ratio of pre- to postbuckling stiffness for the Rayleigh–Ritz method.

Number of elements	Percentage error in buckling load
2	1.474
3	0.356
4	0.120
5	0.050
6	0.024
7	0.014
8	0.008
9	0.005
10	0.003

Table 2. Error in buckling load with increased number of elements.

The Rayleigh–Ritz method has the advantage of providing a natural comparison of postbuckling to prebuckling stiffness. For the one cell model, this is approximately 0.83, as shown in Table 1. As we move further into postbuckling and the tension member carries most of the additional load, the ratio would be expected to approach a value of 0.5.

5.3. *Finite element results.* Two factors influence the performance of the FE analysis of the problem: The number of elements used to construct the model, and the imperfection required for postbuckling analysis.

Beam elements with a cubic polynomial shape function are used to model the lattice members in FE. Sufficient elements must be used to achieve the correct mode shape, and the more localised the buckling becomes, the more elements are required. Eight elements per length ℓ are sufficient to be within 0.01% of the buckling load calculated using the exact initial mode solution, as shown in Table 2.

Williams et al. [2007] identified that the first symmetric mode of the eigen-analysis is sufficient to initiate the out-of-plane postbuckling analysis which is the subject of interest in this study and is thus used here. The effect of different levels of imperfection in postbuckling is presented in Figure 7 with amplitude ranging from 0.01% to 0.3% of the length ℓ. Higher values of imperfection cause greater rounding of the curve at the bifurcation point and a slight overshoot of the maximum deflection, so there is a definite loss of accuracy associated with the use of an imperfection as shown in Figure 7. It is not obvious what level of imperfection is required when constructing a particular model: With too small an imperfection the Riks method in ABAQUS fails to converge, and with too great an imperfection there is a loss of accuracy around the critical load. For the single cell analysis an imperfection with amplitude of approximately 0.01% of the length ℓ was found to be the minimum that could be used for the analysis.

5.4. *Discussion.* Under shear load, the truss-lattice panel exhibits a global initial buckling mode as seen in the $n = 1$ model in Figure 6(a). All three methods demonstrate a half sine dominated mode shape in the compression member with a partial constraint imposed by the tension member. The global mode is further demonstrated for models with more cells using the FE method in Figure 6(a).

Increasing the load beyond the critical load takes the lattice into the postbuckling regime and a more localised short-wave mode shape is adopted. The $n = 3$ and 4 models in Figure 6, for example, progress
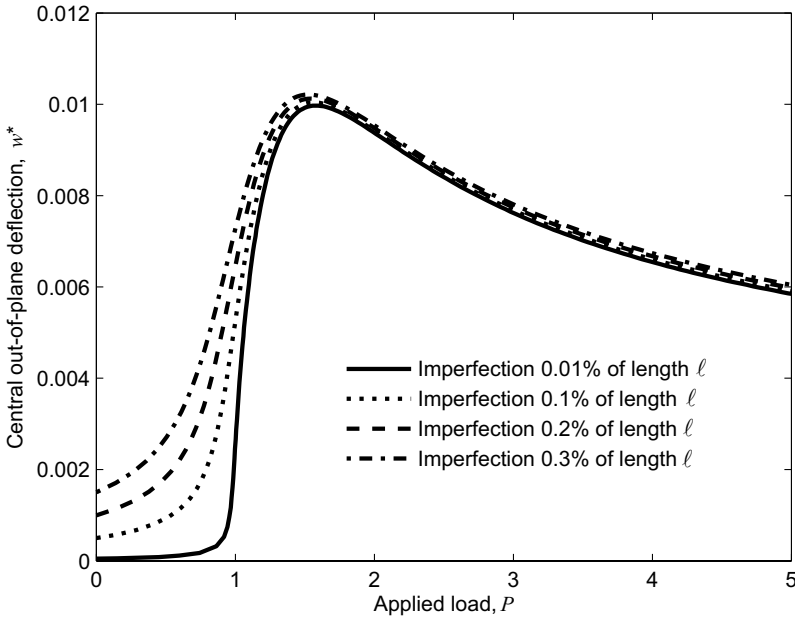
Figure 7. The effect of imperfection on the postbuckling behaviour in an FE analysis. Applied load is nondimensionalised with respect to the critical load, and deflection with respect to the total member length 2ℓ.

from just one antinode along the central compression member at initial buckling to five antinodes in postbuckling. For the single cell models in Figure 6 the localisation is due to the restriction imposed by the dominating tensile member which acts to reduce the central deflection.

When the compression member buckles, little additional load can be carried in the member. This is demonstrated in Figure 8 which shows the load carried in the compression and tension members against the average applied load. These are all nondimensionalised with respect to the critical load. For both the FE and exact method results the load in the buckled compression member is shown to remain approximately constant which results in transfer of load from the compression member to the tension member. The tension member thus gives the whole structure both stiffness and stability in postbuckling similar to the diagonal tension field developed in a continuous shear panel [Kuhn et al. 1952].

The central out-of-plane displacement of the single cell model for each of the three methods is plotted against the average applied load (nondimensionalised against the critical load) in Figure 9, for values of $A\ell^2/I$ of the order of 10^4 (see Table 1). Whilst the critical load eigenvalue solutions from the FE and exact methods are apparently not affected by the axial stiffness of the members, Table 1 demonstrates that in reality they would be, with reduced buckling load with lower in-plane stiffness. For each of the three methods the increasing tensile load acts first to constrain and then to suppress the out-of-plane deflection of the central node w^* as a localised buckle develops.

The exact initial mode method requires no imperfection and so adopts the correct postbuckling path from outset. The governing equations (Equations (1)–(16)) require a deflection of the central node in order to calculate the loads and mode shapes but this is assumed to be zero until the buckling load is
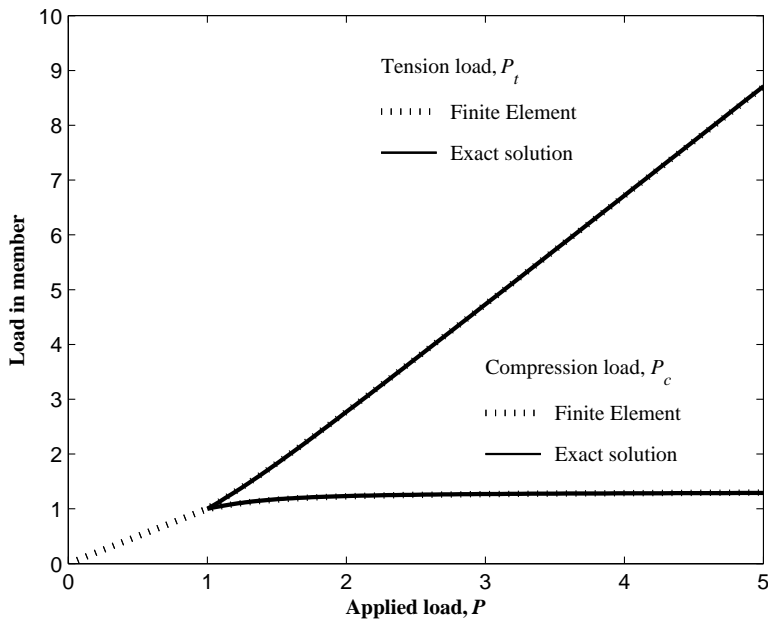
Figure 8. Load in compression and tension members after buckling. All loads nondimensionalised with respect to critical load.

reached. These equations are therefore limited to the postbuckling region and linear elastic theory must be used instead to find the load distribution and displacements before buckling. An initial buckling analysis must first be performed to determine the critical load, and hence two stages are required in the calculation of the postbuckling path.

The Rayleigh–Ritz method also requires no imperfection, and can follow both the prebuckling and initial postbuckling performance. The results presented in Figure 9 are first-order perturbation approximations, which are sufficient for the initial postbuckling results [Thompson and Hunt 1973]. The initial postbuckling stiffness is correct [Thompson and Hunt 1973], with a buckling mode developing at the critical load. However, whereas the two other methods compare well over the complete postbuckling range, this first-order Rayleigh–Ritz method is only approximate as the buckling develops and the subsequent deflection is always higher than the other results. Whilst the energy approach can be used to model large curvatures [Thompson and Hunt 1973], the development of the mode shape from global to local and the associated reduction in w^* are difficult to model with a Fourier approximation over the whole postbuckling range.

The FE method does require an imperfection as discussed earlier, and the level of imperfection has a dramatic effect on the prebuckling and initial postbuckling performance. Ultimately the presence of an imperfection, even if small, affects the accuracy of the results. (The imperfection used in Figure 9 was the minimum, at 0.01% of the length ℓ.) However, with small imperfection the FE results converge quickly upon the other results soon after buckling, and the accuracy appears to be maintained well into postbuckling.
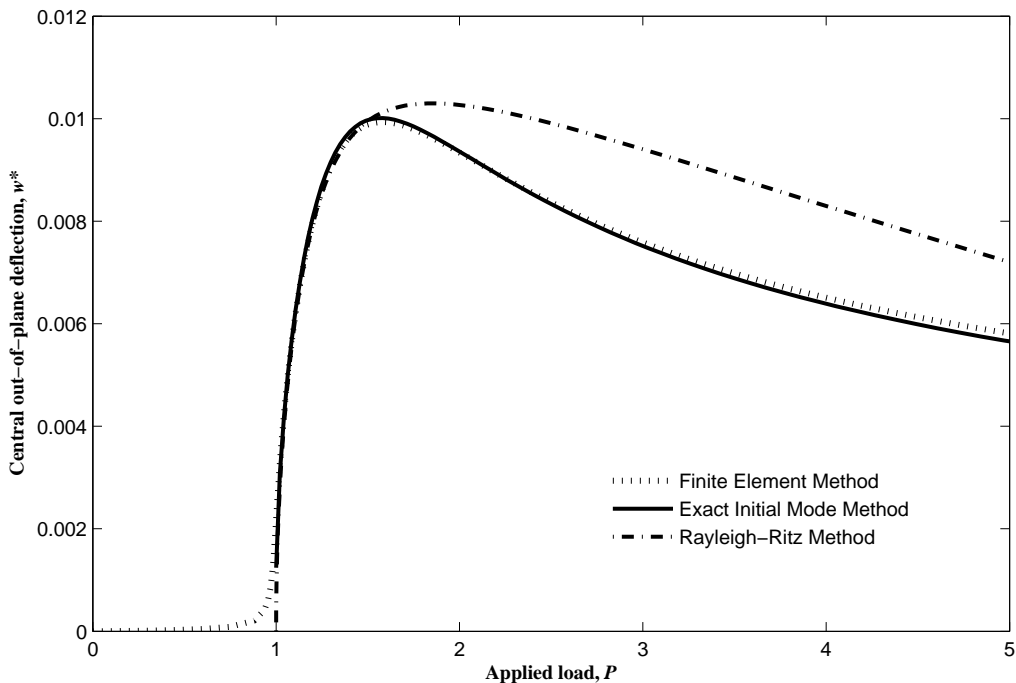
Figure 9. Out-of-plane deflection against applied load at the critical value. Loads nondi-
mensionalised with respect to critical load and deflection with respect to total member
length 2ℓ.

6. Conclusions

The stable postbuckling behaviour of truss-lattice shear panels has been studied using three complemen-
tary analysis techniques each contributing something different to the understanding of the behaviour of
the lattice in postbuckling.

The truss-lattice shear panel has been developed and tested within an FE context and has similar
buckling and postbuckling characteristics to a continuous shear panel. The FE postbuckling analysis
must be considered in two parts owing to an initial imperfection being required for the nonlinear analysis.
The presence of the imperfection then serves to reduce accuracy in the vicinity of the critical buckling
load.

The initial buckling load and mode shape for a single cell model can be extracted exactly using
the Wittrick–Williams algorithm, and the newly developed theory gives excellent correlation with the
FE results in the postbuckling range. Again, two stages are required in the analysis, but the absence of
imperfection allows the postbuckling response to be followed accurately. The tension member dominates
in postbuckling, and the subsequent reduction in amplitude of the centre of the lattice permits the use of
the equations without the need to consider large curvature.

The Rayleigh–Ritz energy method also accurately predicts the critical buckling load and initial post-
buckling path and enables an evaluation of the ratio of pre- to postbuckled stiffness. The Fourier ap-
proximation enables a useful analysis based on the shape into which the mode develops. However, the

advanced postbuckled mode shape is not suited to the Fourier approximation used, and the increase in the number of terms required would make this method much less efficient than the others in determining the behaviour of the truss-lattice far into the postbuckling range.

The results demonstrate the usefulness of considering complementary methods when conducting non-linear analyses. The standard FE approach is relatively straightforward to establish and with sufficient elements produces accurate postbuckling results. The accuracy of the FE method is limited only by the required imperfection which does not form part of the exact solution or Rayleigh–Ritz analyses. The exact solution method shows excellent correlation in postbuckling, and the Rayleigh–Ritz method provides the link between pre- and postbuckling with accurate predictions for the initial postbuckling behaviour.

References

[ABAQUS 2003] ABAQUS, *Version 6.4 Documentation*, ABAQUS Inc., 2003.

[Kim et al. 2004] H. A. Kim, R. Butler, and P. A. Williams, "Buckling and post-buckling analysis of shear panels for optimisation", in *Computational mechanics, WCCM VI in conjunction with APCOM'04*, Beijing, China, 2004.

[Kuhn et al. 1952] P. Kuhn, J. P. Peterson, and L. R. Levin, "A summary of diagonal tension: Part 1 - methods of analysis", Technical report NACA TN-2661, 1952.

[Maple 2005] Maple, *Maplesoft Version 10 Documentation*, Maple, 2005. Division of Waterloo Maple Inc.

[Riks 1979] E. Riks, "An incremental approach to the solution of snapping and buckling problems", *Int. J. Solids Struct.* **15**:7 (1979), 529–551.

[Thompson and Hunt 1973] J. M. T. Thompson and G. W. Hunt, *A general theory of elastic stability*, Wiley, London, 1973.

[Timoshenko and Gere 1936] S. P. Timoshenko and J. M. Gere, *Theory of elastic stability*, McGraw-Hill Book Company, Inc., NY, 1936.

[Wagner 1931] H. Wagner, "Flat sheet metal girders with very thin web: Part III - sheet metal girders with spars resistant to bending. The stress in uprights - diagonal tension fields", Technical report NACA TM-606, 1931.

[Williams 1964] F. W. Williams, "An approach to the non-linear behaviour of the members of a rigid jointed plane framework with finite deflections", *Q. J. Mech. Appl. Math.* **17**:4 (1964), 451–469.

[Williams et al. 2007] P. A. Williams, H. A. Kim, and R. Butler, "Bimodal buckling of optimised truss-lattice shear panels", in *48th AIAA/ASME/ASCE/AHS/ASC structures, structural dynamics, and materials conference*, Honolulu, HI, 23–26 April 2007. paper no. AIAA-2007-2122.

[Wittrick and Williams 1973] W. H. Wittrick and F. W. Williams, "Algorithm for computing critical buckling loads of elastic structures", *J. Struct. Mech.* **1**:4 (1973), 497–518.

[Yang et al. 2003] Y. B. Yang, J. D. Yau, and L. J. Leu, "Recent developments in geometrically nonlinear and postbuckling analysis of framed structures", *Appl. Mech. Rev.* **56**:4 (2003), 431–449.

PHILIP A. WILLIAMS: P.Williams@bath.ac.uk
Department of Mechanical Engineering, University of Bath, Bath, BA2 7AY, United Kingdom

RICHARD BUTLER: R.Butler@bath.ac.uk
Department of Mechanical Engineering, University of Bath, Bath, BA2 7AY, United Kingdom

HYUNSUN A. KIM: H.A.Kim@bath.ac.uk
Department of Mechanical Engineering, University of Bath, Bath, BA2 7AY, United Kingdom

GILES W. HUNT: G.W.Hunt@bath.ac.uk
Department of Mechanical Engineering, University of Bath, Bath, BA2 7AY, United Kingdom

APPLICATION OF A LUMPED DISSIPATION MODEL TO REINFORCED CONCRETE STRUCTURES WITH THE CONSIDERATION OF RESIDUAL STRAINS AND CYCLES OF HYSTERESIS

FRANCISCO ADRIANO DE ARAÚJO AND SERGIO PERSIVAL BARONCINI PROENÇA

The nonlinear analysis model for reinforced concrete plane frame structures is based on the simplified concept of the localization of irreversible physical processes at previously definite zones, denominated here as generalized hinges. However, when both damage due to the microcracking of concrete and sliding mechanisms (aggregate interlocking) at crack surfaces are taken into consideration, hysteresis loops can be reproduced if the loading history includes unloading cycles. The thermodynamic approach of the model is herein developed with reference to generalized variables due to its application in the framework of the classical theory of bars under bending load. According to this model, there are three scalar variables: a damage variable, the plastic rotation of the section and the sliding-associated rotation of the section. By comparison with available experimental responses, the numerical examples illustrate the good performance of the model.

1. Introduction

As a natural progress of the constitutive modeling of materials coupling different phenomena such as elasticity, plasticity and microcracking, the Continuous Damage Mechanics has been efficiently applied since the early eighties. Some of the resulting models encompassing complex responses are nowadays greatly diffused. Among the coupled phenomena considered, one can mention creep damage [Murakami 1981; Kachanov 1984], fatigue damage [Marigo 1985], creep-damage-fatigue interaction [Lemaitre and Chaboche 1974], ductile damage [Simo and Ju 1987; Tai 1990], reinforced concrete damage [Mazars 1984], reinforced and fiber concrete under seismic response [La Borderie et al. 1991].

Concerning reinforced concrete modeling, most of the subsequent publications have, as a common ground, the high level of complexity in terms of formulation and required discretization especially on what concerns numerical analysis. However, when their application to framed structures is considered, such complexities increase the computational costs and imply loss in efficiency. Hence, despite consideration of coupled phenomena, the so-called simplified models were explored as a more adequate alternative. Pioneering works in this direction include [Riva and Cohn 1990a; 1990b; Mulas and Filippou 1990; Alves and Lubliner 1992; Flórez-López 1993].

A common feature of the simplified models is to assume that the material nonlinear response related phenomena are lumped in zones of energy dissipation. Actually, this concept was originally proposed in lumped plasticity models [Maier et al. 1973; Cohn and Franchi 1979; Riva and Cohn 1990a; 1990b].

Keywords: damage mechanics, plastic hinge, hysteresis.

With the major focus on reinforced concrete framed structures, the Flórez-López simplified model presumes that the damage and plasticity evolutive processes are localized at regions of length zero denominated as generalized hinges. The formulation adopted is based on the thermodynamics of solids and accounts for the appearance of permanent strains and stiffness reduction in elements submitted to monotonic loading or reversible loading without sign inversion.

On the other hand, still within the framework of the complex constitutive modeling, the subject of the damping of structural dynamic response resulting from microcracking evolutive processes in the material was originally treated in [Mazars et al. 2000] by employing Continuous Damage Mechanics. The reproduction of hysteretic loops observed experimentally in uniaxial stress-strain diagrams of concrete under unloading and reloading cycles was the most basic issue considered. Based on the aforementioned, two dissipative phenomena present in concrete are considered: diffuse microcrack growth (damage) and the sliding tendency combined with aggregate interlocking between microcracks faces.

The formulation of the Marzar model is also based on the framework of the thermodynamics of solids. Accordingly, the phenomena to be modeled can be represented by two internal state variables: a scalar damage variable and a sliding strain variable. Hence, in order to derive the constitutive model, a thermodynamic potential representing the free energy at a certain state and a dissipative potential are defined. From the free energy potential one can derive the well-known associated variables while from the dissipative potential, one derives the evolution laws for the internal state variables.

With the major aim being the analysis of plane reinforced concrete framed structures, the present work proposes the insertion of Mazars' formulation in the scope of the simplified model formulated originally by Flórez-López [1993] and in such way that the same phenomena described in the complex model remain considered. However, since generalized stress (bending moment) and strain variables (rotation) are now involved, the internal variable related to the sliding effect is defined as a sliding rotation. A major hypothesis considered is an ideal bonding between concrete and steel bars, since debonding could affect hysteresis loops.

Essentially, three new elements are then introduced: the possibility of occurrence of residual strains due to concrete as well as steel behavior (in the original model only the plastic flow of steel is considered), the employment of an alternative damage criterion function and the introduction of a sliding-associated rotation variable ϕ_s (invoked from the hysteresis loops).

2. Thermodynamic framework of the model

Since this is a model for framed plane structures, in which the dissipative processes are located in zones of null dimensions, the structures are admitted to be formed by bar elements with the possibility of forming hinges at their ends. Away from the hinged zones, the elements remain in elastic regime as shown in Figure 1.

The total hinge rotations result from the effect of different phenomena: elastic strain, damage and plasticity of concrete, steel plasticity and sliding between microcrack faces. In the present idealized model, it is considered that the latter effect is manifested in parallel with the other phenomena and can be represented separately as illustrated in Figure 2. The figure compares the initial (a) and deformed (b) configurations of the ends of an element according to bending theory (plane sections, shear strain disregarded).
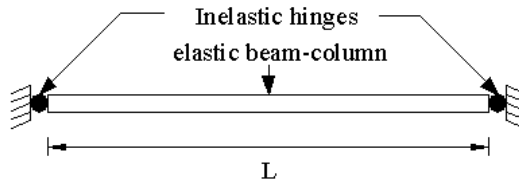
Figure 1. Bar element of the lumped dissipation models.

The nomenclature indicated in Figure 2 has the following meaning:

- k_e is the beam-column elastic stiffness;
- $k_d(d)$ is the portion of hinge stiffness associated to damage;
- $k_s(d)$ is the hinge stiffness associated to slip;
- ϕ is the total hinge rotation;
- ϕ_e is the portion of rotation resulting from elastic deformation of the beam;
- ϕ_d is the portion of hinge rotation due to damage;
- ϕ_p is the portion of rotation due to plastification (concrete and steel) at hinge;
- ϕ_s is the rotation due to slip (it represents the sliding between the concrete fracture surfaces).

In correspondence to the various terms of rotation: rotation due to damage, rotation due to plastification and rotation due to sliding, the moment at the element edge is divided into terms of denominated moment: moment due to damage, moment due to plastification and, in another term, moment due to slip, which is also dependent on the level of damage of the structure. The bending due to slip is related to the sliding-associated rotation which can develop during both the loading process and the reloading and
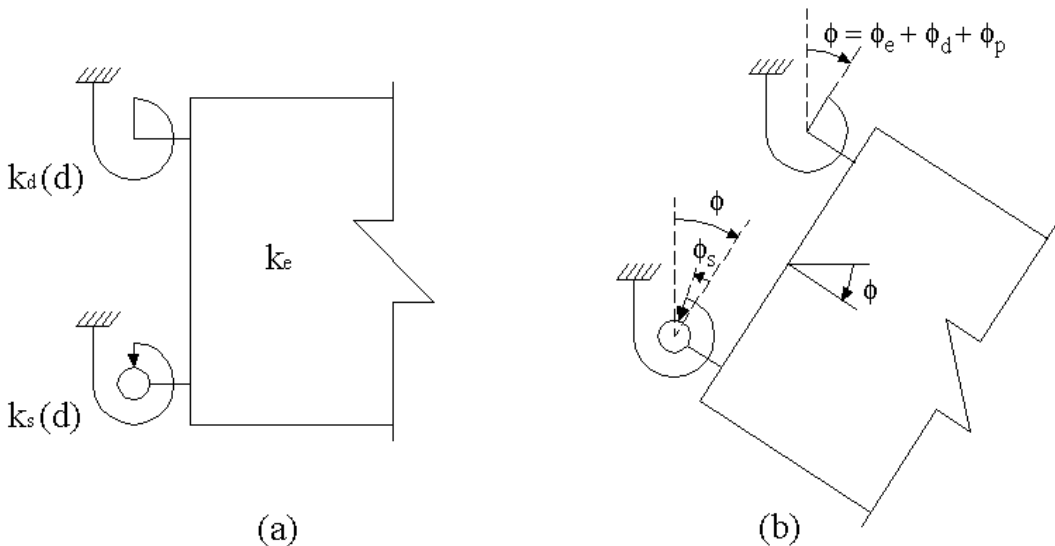
Figure 2. Physical representation of hinge stiffness and rotations: (a) initial configuration; (b) deformed configuration.

unloading cycles. Plastification, which develops from only loading processes, does not however show this characteristic.

Three criteria are hence introduced to control the evolution of the model variables: the damage criterion which identifies the possibility of evolution of the damage variable, the plastification criterion which indicates the possibility of evolution of plastic rotation, and the slip criterion which accuses the possibility of evolution of any slip rotation. It is worth observing that since slip is associated to movement between microcrack surfaces and the latter in turn translate in damage, slip rotation will only occur with the occurrence of damage.

The formulation of the model follows a thermodynamics-based approach applied to solids [Lemaitre and Chaboche 1985], such that the model variables and the corresponding evolution laws maintain coherence with the principles of thermodynamics.

Consider therefore a typical bar element with end hinges as shown in Figure 3. The same figure presents the positive conventions for degrees of freedom of interest (axial strains are not considered).

The scalar damage variable and the representative variables (vectorial) of the portion of rotation and the strain hardening can together be denominated as internal state variables. The existence of a certain amount of energy claimed to be free, or that can be made available for accomplishing work from a current element state is assumed.

As usual, the damage is supposed to directly affect the initial rigidity of the material. On the other hand, in order to account for aggregate interlocking, a plasticity-based approach is used to model the sliding effect. However, since a certain level of coupling is supposed to exist between the internal state variables, the damage variable appears also multiplying the sliding term in the free energy. As a consequence, in the model, sliding occurs only after the appearance of damage, which is physically consistent.

Therefore, adopting the Helmholtz specific free energy as the free energy potential and admitting that the bar element, in its current state, presents a certain level of damage, plastic rotation and slip rotation (with a certain associated strain hardening level), we propose the potential

$$\chi = \chi_{dp} + \chi_s \,,$$

where $\chi_{dp} = \frac{1}{2}(\phi - \phi_p)^T \underline{K_{ed}(d)} \,(\phi - \phi_p)$, $\chi_s = \frac{1}{2}(\phi - \phi_s)^T \underline{K_s(d)} \,(\phi - \phi_s) + \frac{1}{2}\, b\, \alpha^T \alpha$, and

- χ is the total free energy potential;

- χ_{dp} is the portion of free energy after deducing the effects of damage and the plastification;

- χ_s is the portion of free energy associated to the slip process and strain hardening between microcrack faces;
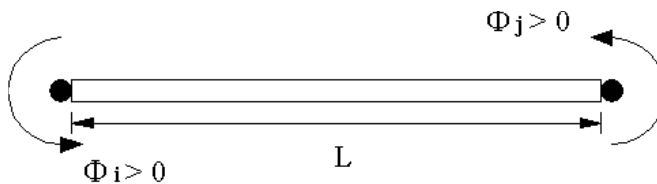
Figure 3. Bar element under study and positive convention for end rotations.

- $\phi = \left(\begin{smallmatrix} \phi_i \\ \phi_j \end{smallmatrix} \right)$ is the vector of total rotations at the i-th and j-th ends of the element;

- $\phi_p = \left(\begin{smallmatrix} \phi_{pi} \\ \phi_{pj} \end{smallmatrix} \right)$ is the vector of plastic rotations at the element extremities;

- $\phi_s = \left(\begin{smallmatrix} \phi_{si} \\ \phi_{sj} \end{smallmatrix} \right)$ is the vector of slip rotations at the element extremities;

- $\alpha = \left(\begin{smallmatrix} \alpha_i \\ \alpha_j \end{smallmatrix} \right)$ is the vector of the strain hardening variable associated to components of slip rotation;

- b is a material parameter;

- $\underline{K_{ed}(d)}$ is the element elastic-damage stiffness matrix;

- $\underline{K_s(d)}$ is the element slip stiffness matrix.

For the elasto-damaged stiffness matrix we adopt an expression similar to that presented by Flórez-López [1993]. Such a matrix is made up of contributions of the beam-column elastic stiffness and the hinge damage stiffness:

$$\underline{K_{ed}(d)} = \begin{pmatrix} \dfrac{(1-d_i)(4-d_j)}{4-d_i d_j} \dfrac{4EI}{L} & \dfrac{4(1-d_i)(1-d_j)}{4-d_i d_j} \dfrac{2EI}{L} \\[3mm] \dfrac{4(1-d_i)(1-d_j)}{4-d_i d_j} \dfrac{2EI}{L} & \dfrac{(1-d_j)(4-d_i)}{4-d_i d_j} \dfrac{4EI}{L} \end{pmatrix},$$

where

- d_i, d_j are variables that quantify the damage suffered by the hinge at extremities i and j respectively;

- $E = \dfrac{E_c(A_c - A_s) + E_s A_s}{A_c}$ is the homogenized modulus of elasticity; with E_c, E_s the Young's moduli of concrete and steel respectively, and A_c, A_s the concrete cross section and the total steel reinforcement areas respectively;

- I is the moment of inertia of complete bar transversal section;

- L is the element length.

Invoking the components of the main diagonal of the stiffness matrix of the element in a pure elastic state, we postulate the part of stiffness due to slip effect between microcrack faces in the present work to take the form

$$\underline{K_s(d)} = \frac{4EI}{L} \begin{pmatrix} d_i & 0 \\ 0 & d_j \end{pmatrix}. \tag{2-1}$$

The introduction of the damage level in each hinge in the slip stiffness matrix is intentional with the aim of reproducing the coupling between damage and slip, more specifically, the dependence of the latter in relation to the former. Actually, experimental observations justify the fact that every inelastic phenomenon of concrete is manifested from the appearance and evolution of microcracks [Ragueneau et al. 2000]. In addition, the diagonal structure of the slip matrix implies that no coupling is assumed between hinges.

The thermodynamic admissibility of the model is guaranteed by imposing the Clausius–Duhem inequality which implies that dissipation of the deformation process cannot be negative. Considering that in the case of the classical bending theory, strain results from the effects of bending moments and ignoring

any other nonmechanical effect such as thermal effects, we can write the relation expressing the evolution of dissipation as

$$M \cdot \dot{\phi} - \dot{\chi} \geq 0. \tag{2-2}$$

In the previous relation, the first term is the *rate* (the time variation, to better represent an evolutive process) of internal energy involved in the bending process. The dot on the variable represents the derivative of the variable with respect to time.

Assume the thermodynamic potential can be linearized in the neighbourhood of current values of the state variables. Then it follows that

$$\dot{\chi} = \frac{\partial \chi}{\partial \phi} \cdot \dot{\phi} + \frac{\partial \chi}{\partial \phi_p} \cdot \dot{\phi}_p + \frac{\partial \chi}{\partial \phi_s} \cdot \dot{\phi}_s + \frac{\partial \chi}{\partial d} \cdot \dot{d} + \frac{\partial \chi}{\partial \alpha} \cdot \dot{\alpha}.$$

The linearized potential can now be substituted in (2-2) thus resulting in

$$\left(M - \frac{\partial \chi}{\partial \phi} \right) \cdot \dot{\phi} - \frac{\partial \chi}{\partial \phi_p} \cdot \dot{\phi}_p - \frac{\partial \chi}{\partial \phi_s} \cdot \dot{\phi}_s - \frac{\partial \chi}{\partial d} \cdot \dot{d} - \frac{\partial \chi}{\partial \alpha} \cdot \dot{\alpha} \geq 0. \tag{2-3}$$

The last inequality must be valid for any process including a purely reversible process where

$$\dot{\phi}_p = \dot{\phi}_s = \dot{d} = \dot{\alpha} = 0.$$

One way to ensure that this process is included in inequality (2-3) consists of imposing the following condition now expressed in matrix notation:

$$M = \frac{\partial \chi}{\partial \phi} = \underline{K_{ed}(d)}(\phi - \phi_P) + \underline{K_s(d)}(\phi - \phi_s), \tag{2-4}$$

which defines M as the thermodynamic variable associated with ϕ. By analogy, thermodynamic variables associated to the other state variables can be defined

$$M_{dp} = \frac{\partial \chi}{\partial \phi_p} = -\underline{K_{ed}(d)}(\phi - \phi_p), \tag{2-5}$$

$$M_s = \frac{\partial \chi}{\partial \phi_s} = -\underline{K_s(d)}(\phi - \phi_s), \tag{2-6}$$

$$Y = \frac{\partial \chi}{\partial d} = \frac{1}{2} \frac{\partial}{\partial d} \left((\phi - \phi_p)^T \underline{K_{ed}(d)}(\phi - \phi_p) \right) + \frac{1}{2} \frac{\partial}{\partial d} \left((\phi - \phi_s)^T \underline{K_s(d)}(\phi - \phi_s) \right), \tag{2-7}$$

$$X = \frac{\partial \chi}{\partial \alpha} = b\alpha. \tag{2-8}$$

Thus M_{dp}, M_s, Y and X are the thermodynamic variables associated to respectively, the state variables ϕ_p, ϕ_s, d and α. In particular, still, due to the fact that the modelling of strain hardening will be based on its analogy with plasticity, the variable X will here be denominated as the kinematic strain hardening moment.

What can easily be observed from (2-4), (2-5) and (2-6) is that the resulting total moment at the extremities of the element consists of two parts: one involving the elastic rigidity penalized by the damage (M_{dp}) and the other involving an additional rigidity related to the aggregate interlocking effect (M_s). In particular, this term is also dependent on the damage level in such way that the expected stiffening effect is reproduced. Moreover, it is also important to note that (2-6) defining the associated
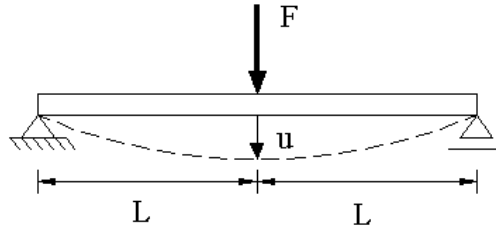
Figure 4. Bending test scheme.

sliding moment includes a rotation term. This term reduces when the sliding rotation increases thus reducing the moment even if the damage attains unit value. What happens finally is that the hysteresis loops and resulting irreversible strains given by the model are enlarged as the damage increases, which is consistent with the experimental responses as the one illustrated in Figure 5.

Moreover, considering (2-3) and equations (2-4)–(2-8), we conclude that the dissipated energy is nonnegative provided the following condition is satisfied:

$$M_{dp} \cdot \dot{\phi}_p + M_s \cdot \dot{\phi}_s - Y \cdot \dot{d} - X \cdot \dot{\alpha} \geq 0.$$

Relative to those portions that are dependent on the effects of slip, it can be shown that positive dissipation is automatically verified so long as the evolution laws of the internal variable associated to this phenomenon (ϕ_s and α) are derived from a convex dissipation potential [Ragueneau et al. 2000] (this aspect will be reviewed in the next section). In order to ensure that $-Y \cdot \dot{d} \geq 0$ for the modeling in the present work, the damage criterion proposed by Alva [2004] is invoked from experimental results.

3. Damage, plasticity and flow criteria

Consider the structural system illustrated in Figure 4 in terms of generalized variables. The system response can be evaluated by the midsection bending moment versus midsection rotation diagram as illustrated in Figure 5.
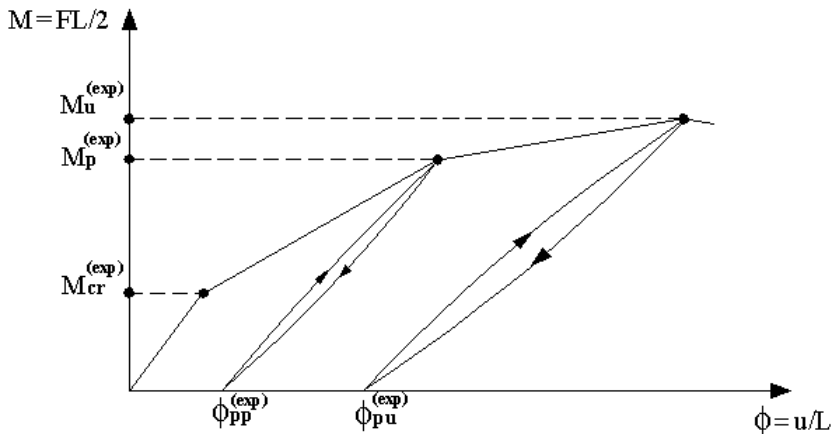
Figure 5. The mid-span moment-rotation experimental diagram.

In Figure 5 the following characteristic parameters are highlighted:

- $M_{cr}^{(\text{exp})}$ is the critical moment at the beginning of damage of concrete;

- $M_p^{(\text{exp})}$ is the moment corresponding to the beginning of plastification of steel;

- $M_u^{(\text{exp})}$ is the peak moment corresponding to the maximum strength of the section;

- $\phi_{pp}^{(\text{exp})}$ is the residual rotation due to damage of concrete at the start of steel plastification;

- $\phi_{pu}^{(\text{exp})}$ is the plastic (peak) rotation corresponding to the peak moment.

These parameters can be determined experimentally by carrying out the experimental test schematized in Figure 4.

As already mentioned, the total moment at the extremities of the element is composed of two distinct parts ($M = M_{dp} + M_s$). Figure 11, placed much further in the text for convenience, illustrates these parts. It is worth remembering that only bending moments at the element extremity i are considered. The part M_{dp} is associated to damage and plasticity of concrete and steel. This portion is used directly in the criteria that define the start and evolution of damage and plasticity in hinges.

For those functions, the proposal in [Alva 2004] and an adaptation of the expression presented by Flórez-López [1998] are respectively adopted. These criteria are given by

$$g = G - G_{cr} - \theta \frac{q \ln(1-d)}{1-d} \le 0 , \tag{3-1a}$$

$$f = \left| \frac{M_{dp}}{1-d} - c\phi_p \right| - M_{cr} \le 0, \tag{3-1b}$$

where

$$G = \frac{1}{2S_0}\left(\frac{M_{dp}}{1-d}\right)^2, \qquad G_{cr} = \frac{M_{cr}^{\,2}}{2S_0}, \qquad \theta = \exp(-\gamma(1-d)),$$

with $S_0 = \frac{4EI}{L}$, d is the damage at the extremity of the element, M_{dp} is the operating moment, ϕ_p is the plastic rotation, γ is a parameter to be determined from the experimental response of the element, c and q are additional parameters to be determined indirectly.

It is worth remembering again that in hinges the previous functions are associated exclusively to the damage and plastification processes. Therefore, the parameter M_{cr} introduced in (3-1b) is not exactly equal to $M_{cr}^{(\text{exp})}$ shown in Figure 5. With the aim of employing the experimental values $M_{cr}^{(\text{exp})}$, $M_p^{(\text{exp})}$, $M_u^{(\text{exp})}$ in the parametric identification, it is considered that M_{cr} is related to $M_{cr}^{(\text{exp})}$ through the penalty factor η whose value depends on the average width of the hysteresis loops. The same proposal is extended to other model parameters of interest. Therefore, the penalization in question takes the following set of relations:

$$\begin{cases} M_{cr} = \eta \cdot M_{cr}^{(\text{exp})}, \\ M_p = \eta \cdot M_p^{(\text{exp})}, \\ M_u = \eta \cdot M_u^{(\text{exp})}. \end{cases} \tag{3-2}$$

It is worth saying before hand that the value $\eta = 0.9$ was the most representative value for the examples considered in this work. In Figure 6, an interpretation for the relations in (3-2) is given.
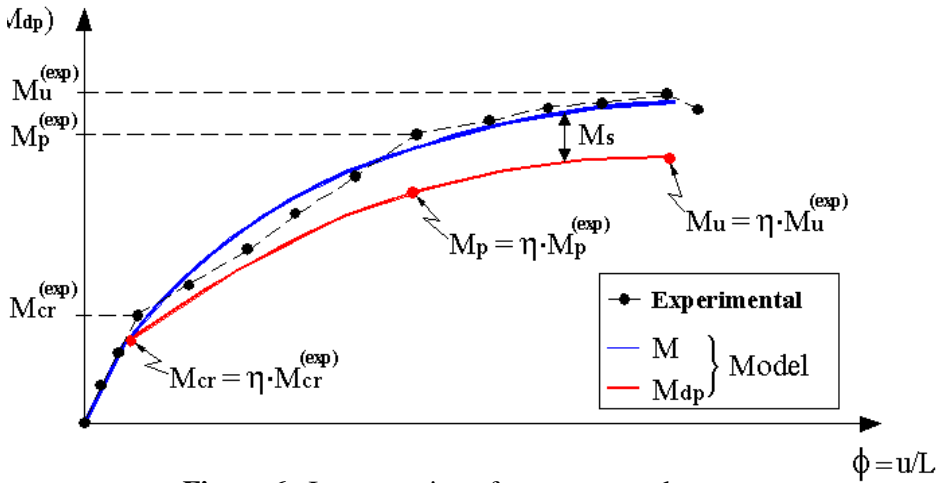
Figure 6. Interpretation of moment penalty.

Expression (3-1a), originally presented by Alva [2004], introduces a new parameter γ, in the definition for θ, that needs to be identified from experimental tests on the damage of the hinge. Along this direction, as a first step, the evolution law that governs the damage d appearing in the relation θ must be identified from successive values of stiffness corresponding to the slopes of the unloading curves as illustrated in Figure 7. These stiffness values also serve for constructing the experimental response curve which relates the damage to the thermodynamic moment G (assuming $M_{dp} = M$). In the following step, the value of γ is obtained from best fit between the experimental and the numerically obtained curves which represent the damage versus thermodynamic moment G relation; see Figure 8.

In order to consider the processes of plastification of concrete and the steel-concrete, the behavior described in Figure 9 is proposed to the parameter c, which appears in (3-1b). Basically, there are two groups of values, c_p and c_u, corresponding to the already cited plastification. A transition between the two groups of values is also assumed in order to prevent numerical problems.
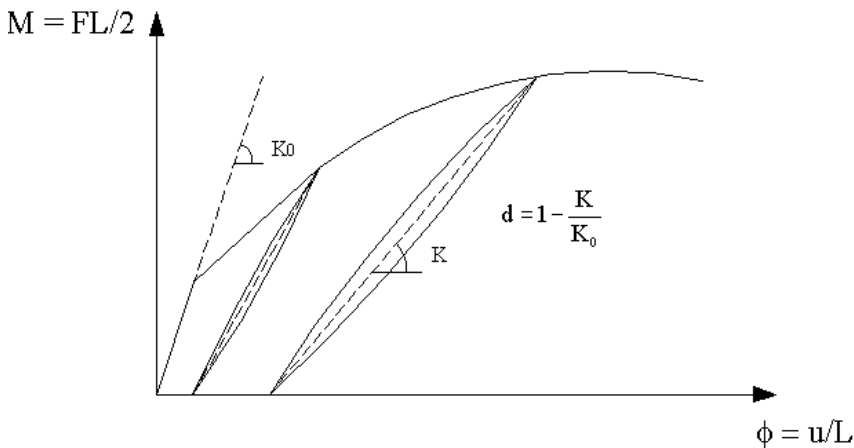
Figure 7. Determination of the experimental values of the damage.
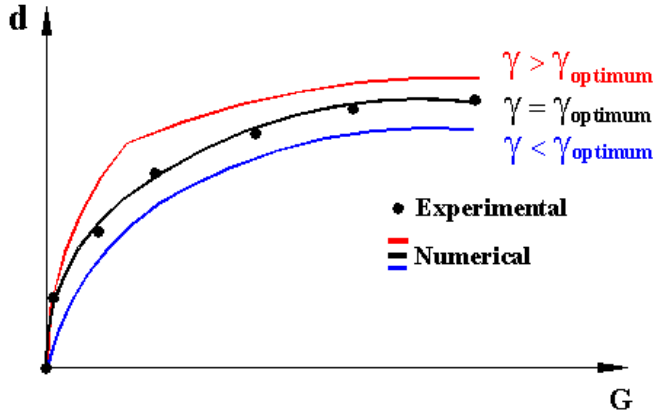
Figure 8. Calibration of the variable γ.

Note that the bending moment M_y is used as reference for the transition part between the values of c. In the present work, the relation

$$M_y = \frac{3M_p + M_u}{4},$$

which corresponds to dividing the interval (M_p, M_u) into four equally spaced subintervals, with M_y being one of the extremities of first subinterval, is adopted.

For the remaining parameters c_p, c_u and q, no well defined mechanical interpretation is given; simply speaking, the values of these parameters can be determined indirectly by imposing certain complementary conditions. On determining these values, two other reference parameters d_u and d_p are observed to appear. For example, the following conditions determine the constants q and d_u:

$$\begin{cases} g = 0, M_{dp} = M_u, d = d_u \Rightarrow (1 - d_u)^2 G_{cr} + \theta_u q (1 - d_u) \ln(1 - d_u) - \dfrac{M_u^2}{2S_0} = 0, \\[4mm] g = 0, \dfrac{\partial (M_{dp}^2)}{\partial d} = 0, d = d_u \Rightarrow -2(1 - d_u) G_{cr} - \theta_u q (h_u \ln(1 - d_u) + 1) = 0, \end{cases} \tag{3-3}$$
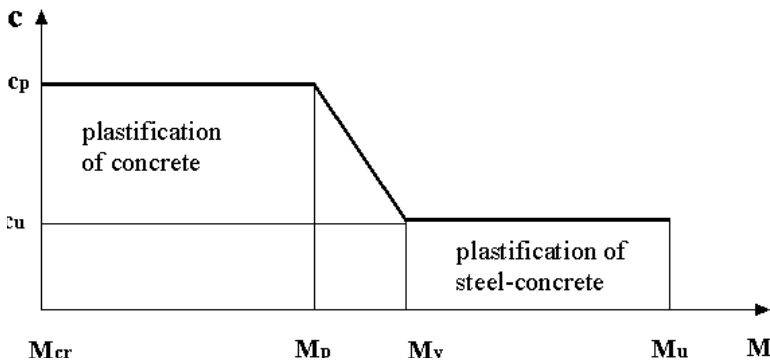
Figure 9. Behavior of parameter c.

where $\theta_u = \exp(-\gamma(1 - d_u))$ and $h_u = 1 + \gamma d_u - \gamma$. Respectively, the conditions in (3-3) impose that for the ultimate moment that verifies the criterion with the equality, a corresponding damage d_u exists and for this damage level there is a corresponding maximum for M_{dp}.

On the other hand the solution of the following equation provides the value for d_p:

$$g = 0, M_{dp} = M_p, d = d_p \Rightarrow \frac{M_p{}^2}{2(1 - d_p)^2 S_0} - G_{cr} - \theta_p \frac{q \ln(1 - d_p)}{1 - d_p} = 0,$$

where $\theta_p = \exp(-\gamma(1 - d_p))$ and d_p is the damage corresponding to the moment of plastification of steel reinforcement.

The constants c_p and c_u are obtained from the following equations

$$\begin{cases} f = 0, M_{dp} = M_p \Rightarrow c_p = \dfrac{1}{\phi_{pp}}\left(\dfrac{M_p}{1 - d_p} - M_{cr}\right), \\[2mm] f = 0, M_{dp} = M_u \Rightarrow c_u = \dfrac{1}{\phi_{pu}}\left(\dfrac{M_u}{1 - d_u} - M_{cr}\right), \end{cases}$$

thus completing the process of obtaining all necessary damage and plastification parameters. Considering the criterion that defines the start and evolution of the rotation in hinges, which thus reflects the slip between the microcrack surfaces, we propose the following form:

$$f_s = |M_s - X| - M_k \le 0, \tag{3-4}$$

where the constant M_k is large enough to prevent numerical problems, but still very small such that the evolution of slip occurs nearly simultaneously with the evolution of damage. Figure 10 includes a representation of relation (3-4).

The inequality (3-4) applies to the loading, unloading and reloading stages. As it will be seen later in the solution strategy, violation of the condition $f_s \le 0$ will serve to characterize, for the loading step under consideration, whether or not the slip process evolves, the degree of resistance to its evolution being represented at a minor or major scale by the value of X.

With relation to the evolution laws of the slip associated internal variables expressed by $\dot{\phi}_s$ and $\dot{\alpha}$, a procedure analogous to that used in the nonassociative plasticity theory is adopted. Therefore the dissipative energy is employed with essentially similar expressions to those of the slip criterion. However, in order
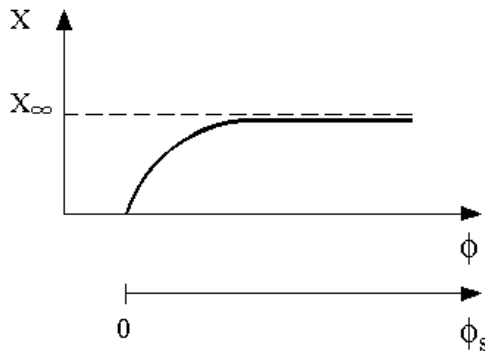
Figure 10. The kinematic nonlinear strain hardening moment.

to introduce the possibility of describing nonlinear strain hardening, the following form is considered for the dissipative potential:

$$\psi_s = |M_s - X| + \tfrac{3}{4}aX^2 - M_k, \tag{3-5}$$

where a is a material parameter. The term $\tfrac{3}{4}aX^2$ is responsible for strain hardening nonlinearity and for the tendency to reach an asymptotic value as it will be shown afterwards.

Hence, imposing the normality rule on the surface of the dissipative potential, we can give the evolution laws for the internal variables as

$$\dot{\phi}_s = \dot{\lambda}\frac{\partial \psi_s}{\partial M_s}, \tag{3-6a}$$

$$\dot{\alpha} = -\dot{\lambda}\frac{\partial \psi_s}{\partial X}, \tag{3-6b}$$

where $\dot{\lambda}$ maintains the similarity with the plastic multiplier of plasticity and the negative sign of the expression of $\dot{\alpha}$ guarantees positive dissipation.

A condition introduced in the model is that the kinematic strain hardening moment, now nonlinear, tends to an asymptotic value X_∞ as the values of rotation become higher since under such a situation the slip between microcrack faces ceases to increase.

To obtain this limit value, (2-8) is considered thus leading to

$$\dot{X} = b\dot{\alpha}. \tag{3-7}$$

From a combination of expression (3-7), (3-6b) and (3-5), we have

$$\dot{X} = b\dot{\lambda}(\text{sign}(M_s - X) - \tfrac{3}{2}aX). \tag{3-8}$$

Admit $\text{sign}(M_s - X) = 1$. Therefore, $\lim_{\frac{3}{2}aX \to 1} \dot{X} = 0$. Therefore, the limit value for X can be obtained when the equality

$$X_\infty = \frac{2}{3a}$$

is true. The curve presented in Figure 10 is obtained from the numerical integration of expression (3-8).

Finally, the meaning of each terms of the moments considered in this model are shown in Figure 11.

The hysteresis loop is here characterized by the noncoincidence of the curves defined in the unloading and reloading stages in the moment-rotation diagram. The model under analysis is aimed at generating hysteresis loops of unloading and reloading cycles as shown in Figure 12.

Figure 12 (a) is a representation of the contribution of various rotation terms ϕ_e, ϕ_p, ϕ_d that make up the total rotation $\phi = \phi_e + \phi_p + \phi_d$ for the load level corresponding to point B.

4. Implementation of the model

The model was implemented using a special proposed nonlinear analysis plane frame software. The main strategy employed was the Newton–Raphson incremental-iterative method with a step-by-step load application followed by successive corrections of equilibrium [Ortiz and Simo 1986]. The integration of the constitutive model including a determination of the damage variable, plastic rotation, slip rotation and the variable associated to the kinematic nonlinear strain hardening of the hinges at each iteration follows an iterative approach.

The damage evolution in each hinge is obtained by imposing nullity condition on the damage criterion (3-1a) since this criterion must have already been violated in the i-th ($g^{(i)} > 0$) iteration step. Therefore, for the $(i + 1)$-th iteration we have

$$\Delta d^{(i+1)} = \frac{-g^{(i)}}{\frac{\partial g}{\partial d}\big|^{(i)}} = \frac{g^{(i)}}{\left(\theta_q\left(\frac{\ln(1-d)-1}{(1-d)^2}\right) + \gamma\theta_q\left(\frac{\ln(1-d)}{1-d}\right) + \frac{2G}{1-d}\right)\big|^{(i)}}.$$

Having updated the damage $d^{(i+1)} = d^{(i)} + \Delta d^{(i+1)}$, we verify the damage criterion again, with the successive update of damage until the criterion $g \leq 0$ is verified.

The evolution of plastic rotation of each hinge is also obtained by imposing the nullity condition on the plasticity criterion (3-1b) since this criterion must have been violated in i-th iteration ($f^{(i)} > 0$). Therefore, for the $(i + 1)$-th iteration we have

$$\Delta\phi_p{}^{(i+1)} = \frac{-f^{(i)}}{\frac{\partial f}{\partial\phi_p}\big|^{(i)}} = \frac{f^{(i)}}{(\text{sign}(\lambda)c)|^{(i)}},$$

where

$$\lambda = \frac{M}{1-d} - c\phi_p, \qquad \text{sign}(\lambda) = \begin{cases} +1 & \text{if } \lambda > 0, \\ -1 & \text{if } \lambda < 0. \end{cases}$$

After updating the plastic rotation $\phi_p{}^{(i+1)} = \phi_p{}^{(i)} + \Delta\phi_p{}^{(i+1)}$, the plasticity criterion is again verified. The successive updating of rotation is continued until the criterion $f \leq 0$ is verified.

Relative to the plastic multiplier, considering a hinge j of the finite element, as illustrated in Figure 3, we linearize the representative surface of the sliding criterion $f_s = 0$ using current values of the state variables in the i-th iteration of the same i-th step:

$$f_s{}^{(i+1)} = f_s{}^{(i)} + \frac{\partial f_s}{\partial M_s}\bigg|^{(i)} \left(M_s{}^{(i+1)} - M_s{}^{(i)}\right) + \frac{\partial f_s}{\partial X}\bigg|^{(i)} \left(X^{(i+1)} - X^{(i)}\right) = 0. \tag{4-1}$$
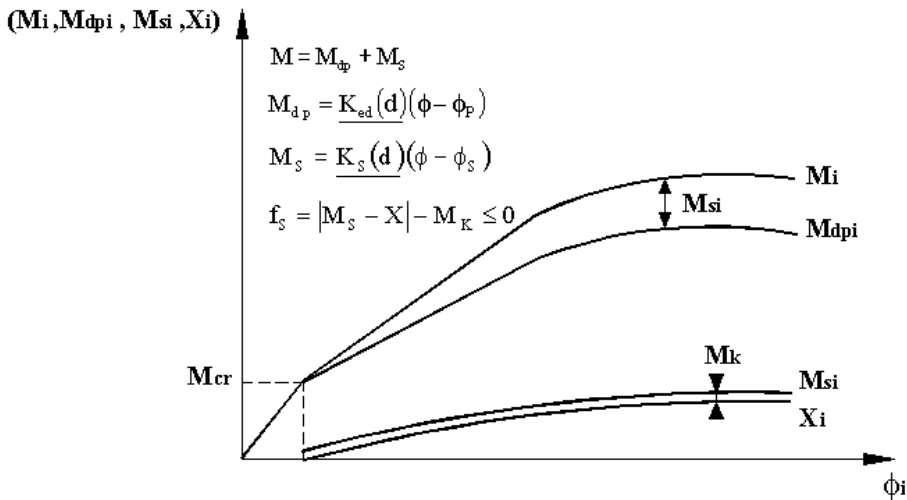
Figure 11. Various terms of the moments used in the model.
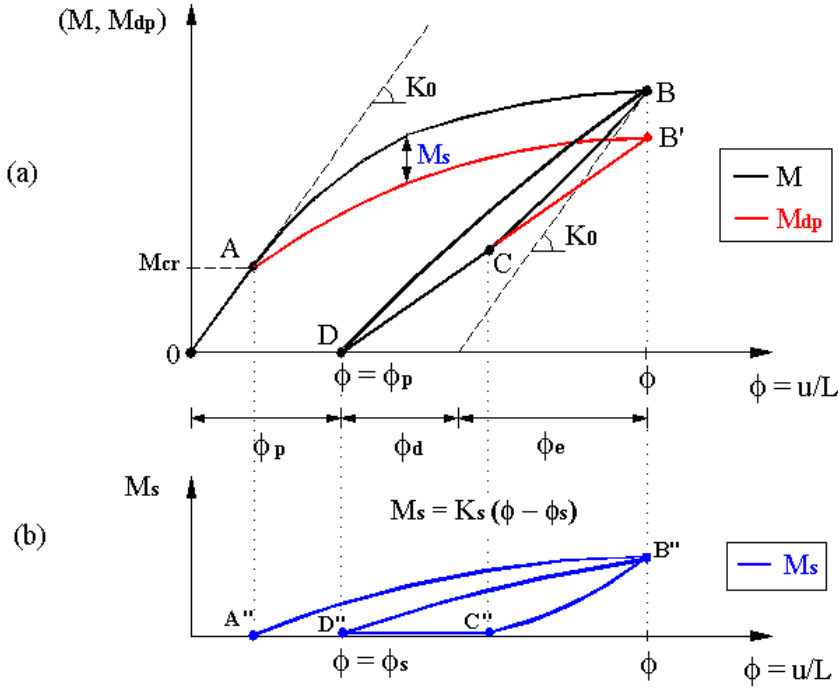
Figure 12. Hysteresis loop of (a) M, M_{dp} versus ϕ (b) M_s versus ϕ.

Knowing that for hinge j, in the i-th iteration we have

$$\dot{M}_s{}^{(i)} = -K_{s22}\dot{\phi}_s{}^{(i)} = -K_{s22}\left(\dot{\lambda}\frac{\partial\psi_s}{\partial M_s}\right)^{(i)}, \qquad \dot{X}^{(i)} = b\dot{\alpha}^{(i)} = -b\left(\dot{\lambda}\frac{\partial\psi_s}{\partial X}\right)^{(i)}. \tag{4-2}$$

By adopting an explicit relation such that

$$\dot{M}_s{}^{(i)}\Delta t = M_s{}^{(i+1)} - M_s{}^{(i)}, \qquad \dot{X}^{(i)}\Delta t = X^{(i+1)} - X^{(i)},$$

and substituting (4-2) in (4-1), we have

$$\Delta\lambda^{(i)} = \dot{\lambda}^{(i)}\Delta t = \frac{-f_s{}^{(i)}}{\frac{\partial f_s}{\partial M_s}\Big|^{(i)} K_{s22} \frac{\partial\psi_s}{\partial M_s}\Big|^{(i)} + \frac{\partial f_s}{\partial X}\Big|^{(i)} b \frac{\partial\psi_s}{\partial X}\Big|^{(i)}},$$

where K_{s22} is a component of the matrix given in (2-1). We have also

$$\frac{\partial f_s}{\partial M_s}\Big|^{(i)} = \text{sign}\left(M_s{}^{(i)} - X^{(i)}\right), \qquad \frac{\partial\psi_s}{\partial M_s}\Big|^{(i)} = \text{sign}\left(M_s{}^{(i)} - X^{(i)}\right),$$

$$\frac{\partial f_s}{\partial X}\Big|^{(i)} = -\text{sign}\left(M_s{}^{(i)} - X^{(i)}\right), \qquad \frac{\partial\psi_s}{\partial X}\Big|^{(i)} = \text{sign}\left(M_s{}^{(i)} - X^{(i)}\right) + \tfrac{3}{2}aX^{(i)},$$

where

$$a = \frac{2}{3X_\infty}, \quad \text{sign}\left(M_s{}^{(i)} - X^{(i)}\right) = \begin{cases} +1 & \text{if } \left(M_s{}^{(i)} - X^{(i)}\right) > 0, \\ -1 & \text{if } \left(M_s{}^{(i)} - X^{(i)}\right) < 0. \end{cases}$$

Therefore once the slip criterion (3-4) is violated, the update of internal variables for the $(i+1)$-th iteration of the load step is carried out as shown in the following equations:

$$\phi_s{}^{(i+1)} = \phi_s{}^{(i)} + \Delta\lambda^{(i)}\frac{\partial\psi_s}{\partial M_s}\bigg|^{(i)}, \qquad X^{(i+1)} = X^{(i)} - \Delta\lambda^{(i)}b\frac{\partial\psi_s}{\partial X}\bigg|^{(i)}, \qquad M_s{}^{(i+1)} = K_{s22}\big(\phi - \phi_s{}^{(i+1)}\big).$$

Having obtained the new values, the slip criterion is again verified proceeding by successive updating until the criterion $f_s \leq 0$ is verified. A similar procedure is applied to hinge i.

5. Strategy for considering the inversion of sign of the loading

In order to extend the model to include response under dynamic loading, it is necessary to determine the possibility of sign of the load being inverted. Based on this, the strategy proposed in [Flórez-López 1995] by defining two sets of independent variables, one associated to positive load and the other associated to negative loads according to the convention presented in Figure 13, is adopted.

Two scalar damage variables d^+ for $M > 0$ and d^- for $M < 0$, both with independent behaviors, are considered. However, for the plastic rotation ϕ_p, as well as for the slip rotation ϕ_s, only a single variable continues to exist. In each case there are the evolution laws that start to depend on the sign of the load. The damage, plastification and kinematic strain hardening criteria then assume a particular form depending on the sign of the loads. Thus, for positive load we have

$$g^+ = G^+ - G_{cr}^+ - \theta^+\frac{q^+ \ln(1-d^+)}{1-d^+} \leq 0, \qquad f^+ = \left|\frac{M_{dp}^+}{1-d^+} - \alpha c^+\phi_p\right| - ((1-\alpha)c^+p + M_{cr}^+) \leq 0,$$

$$f_s^+ = |M_s^+ - X^+| M_k^+ \leq 0,$$

while for negative load we have

$$g^- = G^- - G_{cr}^- - \theta^-\frac{q^- \ln(1-d^-)}{1-d^-} \leq 0, \qquad f^- = \left|\frac{M_{dp}^-}{1-d^-} - \alpha c^-\phi_p\right| - ((1-\alpha)c^-p + M_{cr}^-) \leq 0,$$

$$f_s^- = |M_s^- - X^-| M_k^- \leq 0,$$

where $p = \max|\phi_p|$ and $0 \leq \alpha \leq 1$.

6. Examples of application

In order to evaluate the efficiency of the model under study, in the first example, results of experimental and numerical analyses for a beam presented in [Mazars et al. 2000] were compared. The cross section geometry and steel reinforcement is shown in Figure 14.
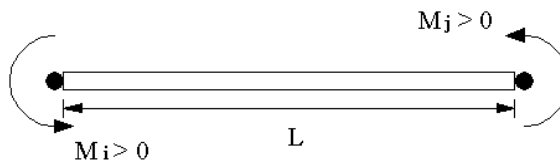
Figure 13. Positive convention for the nodal/end moments.
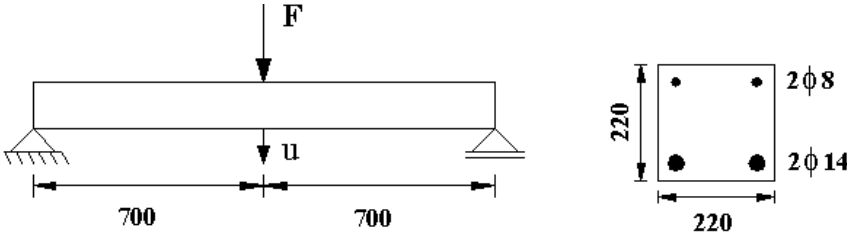
Figure 14. Geometry and beam reinforcement [Mazars et al. 2000].

In Figure 15, the numerical response is compared to the experimental response. Besides the numerical response obtained from the model under study, the response from another damage model [La Borderie et al. 1991] was also reproduced (in this model the damage is diffused in the element while the reinforcement bars are discretized into layers). The parameters of interest in the numerical modeling were calibrated based on the experimental result in [Ragueneau et al. 2000]. The values adopted are:

Properties of concrete:

$$E_C = 28000\,\text{MPa}, \quad \nu = 0.2, \quad \gamma_C = 2500\,\text{kg/m}^3.$$

Properties of steel:

$$E_S = 200000\,\text{MPa}, \quad f_y = 450\,\text{MPa},$$
$$E_{ST} = 4000\,\text{MPa}, \quad \gamma_S = 7850\,\text{kg/m}^3.$$

Parameters of the La Borderie [1991] model:

$$\beta_1 = 1\,\text{MPa}, \quad \beta_2 = -10\,\text{MPa}, \quad y_{01} = 3.05 \times 10^{-4}\,\text{MPa},$$
$$y_{02} = 5 \times 10^{-3}\,\text{MPa}, \quad A_1 = 4.0 \times 10^3\,\text{MPa}^{-1}, \quad A_2 = 6.8\,\text{MPa}^{-1},$$
$$B_1 = 0.95, \quad B_2 = 0.7705, \quad \sigma_f = 2.6\,\text{MPa}.$$
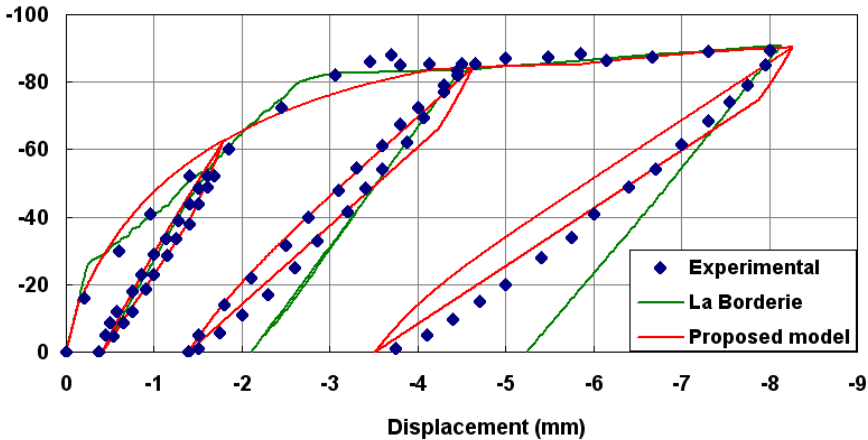
Figure 15. Load/displacement curve for beam in [Mazars et al. 2000].

Parameters of the simplified model under study:

$$M_{cr} = 5.04 \,\text{kN·m}, \qquad M_p = 26.1 \,\text{kN·m}, \qquad M_u = 28.35 \,\text{kN·m},$$
$$\gamma = 6, \qquad \phi_{pp} = 1.8 \times 10^{-3} \text{rad}, \qquad \phi_{pu} = 7.0 \times 10^{-3} \text{rad},$$
$$X_\infty = 3.15 \,\text{kN·m}, \qquad b = 5000 \,\text{kN·m}, \qquad M_k = 0.0315 \,\text{kN·m}.$$

The La Borderie [1991] model was used in the discretization process with 14 equal elements while for the simplified model, the structure was discretized in two equal elements.

A close observation of the curves in Figure 15 shows the La Borderie [1991] model satisfactorily reproduces the displacement curve. However this model is not capable of reproducing the two experimentally observed hysteresis curves. Moreover, the residual displacements are shown to be considerably distant from experimental results (in this model both plastifications of concrete and steel reinforcement are considered).

The displacement curve obtained from the simplified model under study is shown to be very realistic. Above all, it is worth emphasizing that this model is capable of reproducing hysteresis loops and also reproduces residual displacements with a remarkably high precision.

The second example explores the efficiency of the simplified model to reproduce the behavior of a structure submitted to loading with inversion of sign. The results of experimental and numerical analyses carried out for a frame presented by Alva [2004] are given. For this structure, the geometry and reinforcement distribution are shown in Figure 16.

In this test, the general loading procedure consisted of applying a constant point load of $F_N = 240 \,\text{kN}$ in the column direction to simulate gravitational load, and of a variable load at the beam end to simulate
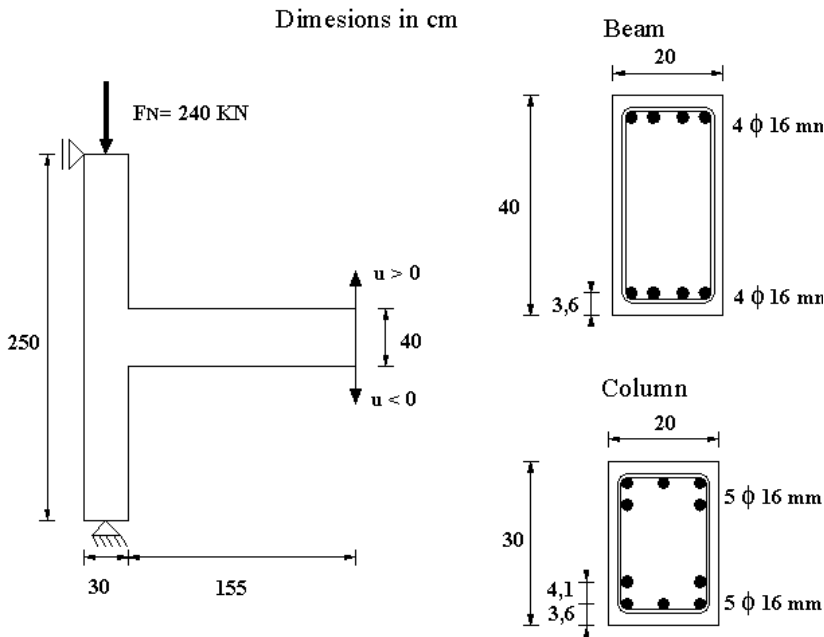
Figure 16. Frame subjected to load with sign inversion [Alva 2004].
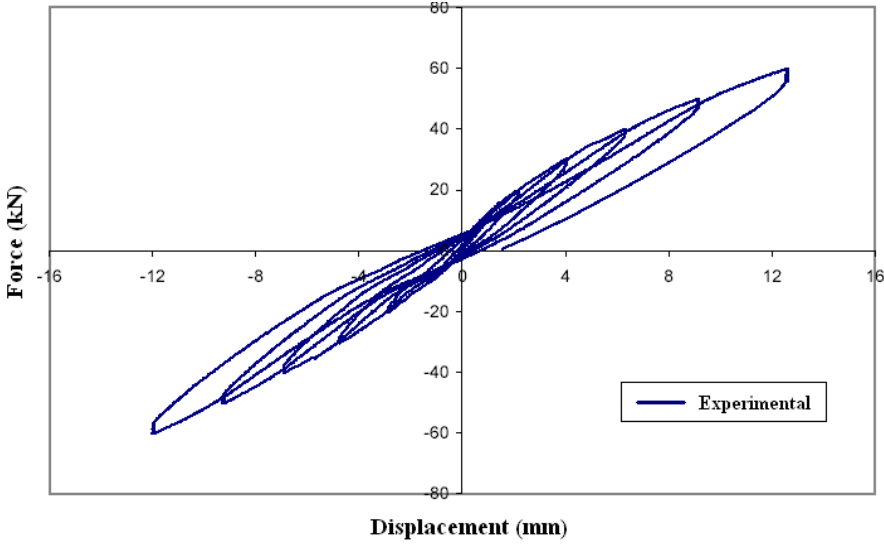
Figure 17. Beam end experimental load-displacement curve [Alva 2004].

cyclic load in multiple floor buildings [Alva 2004]. The sign convention for displacements measured at the beam end is indicated in Figure 16.

Figure 17 presents the experimental force-displacement response. The cyclic loading process at the beam end was initiated after the column normal load had been applied. The maximum and minimum applied loads were ± 10 kN, ± 20 kN, ± 30 kN, ± 40 kN, ± 50 kN and ± 60 kN, in totalizing six cycles.

The model in [La Borderie et al. 1991] and the simplified model under study are employed in simulating the numerical response. The material properties and the necessary parameters considered for application of these models are shown. For the model in [La Borderie et al. 1991], average concrete parameters are used while for the simplified model, the parameters employed were obtained from the results of [Alva 2004]:

Properties of the concrete:

$$E_C = 28315 \text{ MPa}, \qquad \nu = 0.2, \qquad \gamma_C = 2500 \text{ kg/m}^3.$$

Properties of steel:

$$E_S = 200000 \text{ MPa}, \qquad f_y = 600 \text{ MPa},$$
$$E_{ST} = 10500 \text{ MPa}, \qquad \gamma_S = 7850 \text{ kg/m}^3.$$

Parameters of the model in [La Borderie et al. 1991]:

$$\beta_1 = 0.8 \text{ MPa}, \qquad \beta_2 = -10 \text{ MPa}, \qquad y_{01} = 1.0 \times 10^{-4} \text{ MPa},$$
$$y_{02} = 1 \times 10^{-3} \text{ MPa}, \qquad A_1 = 8.0 \times 10^3 \text{ MPa}^{-1}, \qquad A_2 = 6.8 \text{ MPa}^{-1},$$
$$B_1 = 0.85, \qquad B_2 = 0.7705, \qquad \sigma_f = 2.6 \text{ MPa}.$$

The simplified model parameters for both $M > 0$ and $M < 0$ are:

Beam:

$$M_{cr} = 11.7\,\text{kN·m}, \qquad M_p = 139.5\,\text{kN·m}, \qquad M_u = 167.4\,\text{kN·m},$$
$$\gamma = 10, \qquad \phi_{pp} = 2.5 \times 10^{-3}\text{rad}, \qquad \phi_{pu} = 11.0 \times 10^{-3}\text{rad},$$
$$X_\infty = 18.6\,\text{kN·m}, \qquad b = 7000\,\text{kN·m}, \qquad M_k = 0.186\,\text{kN·m}.$$

Column:

$$M_{cr} = 17.1\,\text{kN·m}, \qquad M_p = 117.9\,\text{kN·m}, \qquad M_u = 130.5\,\text{kN·m},$$
$$\gamma = 5, \qquad \phi_{pp} = 1.0 \times 10^{-3}\text{rad}, \qquad \phi_{pu} = 4.0 \times 10^{-3}\text{rad},$$
$$X_\infty = 14.5\,\text{kN·m}, \qquad b = 7000\,\text{kN·m}, \qquad M_k = 0.145\,\text{kN·m}.$$

In the case of applying the model in [La Borderie et al. 1991], the structure was discretized in 9 elements: 4 column elements of equal length and 5 beam elements. In the case of the simplified model, only two column and one beam elements were considered.

Figure 18 presents the numerical response obtained from the model in [La Borderie et al. 1991]. The figure shows that although this model reproduces the plastic strain associated to the concrete, it underestimates the experimental residual displacement. It is worth observing also that the unloading path is described by practically straight line which is a little distant from the experimental curve.

Figure 19 presents the numerical response obtained from applying the model under study with hysteresis. As can be observed, the model satisfactorily reproduces the structural behavior and is capable of reproducing residual displacements associated to the plastic behavior of concrete, which are much closer to experimental results.
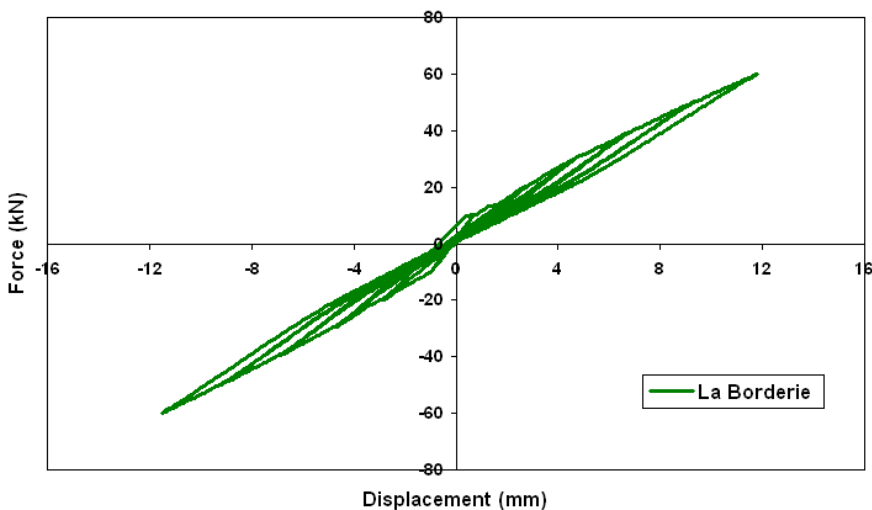
Figure 18. Beam end numerical load-displacement curve, the model in [La Borderie et al. 1991].
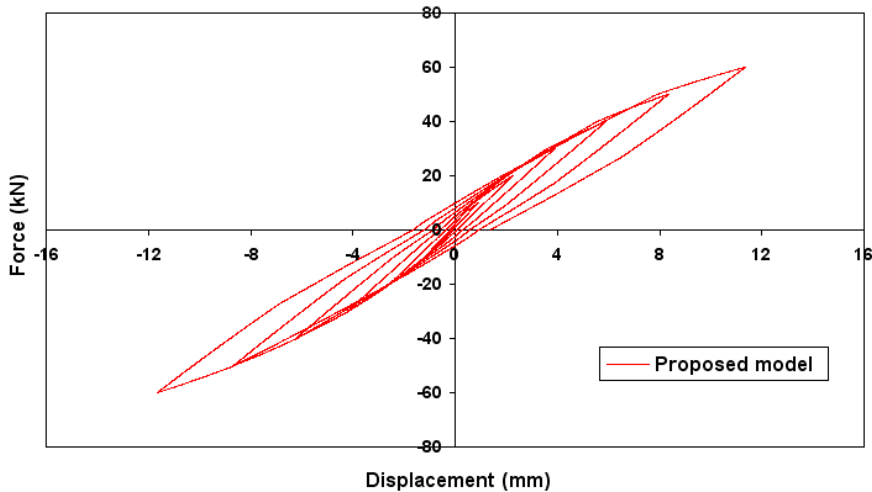
Figure 19. Beam end numerical load-displacement curve, proposed model.

7. Conclusions

The formulation of the simplified model is based on generalized variables that are consistent with the classical bending theory of bars. The parameters involved (cracking and plastification moments, and the corresponding kinematic parameters) can be obtained from conventional moment-rotation experimental procedures.

To evaluate the efficiency of the model, the results from the obtained model were compared with known experimental responses of reinforced concrete structures under load with the possibility of sign inversion. The numerically obtained force-displacement diagrams were shown to satisfactorily reproduce the experimental response. It was evidenced that the relative movement between the fracture surfaces in the concrete, particularly revealed during the unloading and reloading cycles, is important for any refined consideration of the effects of damage on structural behavior.

References

[Alva 2004] G. M. S. Alva, *Theoretical and experimental study of reinforced concrete frame joints behaviour under cyclic loads*, Doctoral Thesis, São Carlos School of Engineering. University of São Paulo. São Carlos, 2004. in portughese.

[Alves and Lubliner 1992] B. K. Alves and J. Lubliner, "A damage mechanics model for beams: Application to reinforced concrete beams", pp. 277–286 in *Numerical methods in engineering*, edited by H. Alder et al., Barcelona, 1992. Proc. CIMNE.

[Cohn and Franchi 1979] Z. M. Cohn and A. Franchi, "Strupl: A computer system for structural plasticity", *J. Struct. Div., ASCE* **105**:4 (1979), 789–804.

[Flórez-López 1993] J. Flórez-López, "Calcul simplifié de portiques endommageables", *Rev. Eur. Éléments Finis* **2**:1 (1993), 47–74.

[Flórez-López 1995] J. Flórez-López, "Simplified model of unilateral damage for RC frames", *J. Struct. Eng.* **121**:12 (1995), 1765–1772.

[Flórez-López 1998] J. Flórez-López, "Frame analysis and continuum damage mechanics", *Eur. J. Mech. A Solids* **17**:2 (1998), 269–283.

[Kachanov 1984] L. M. Kachanov, "On brittle fracture of a thin plastic interlayer in creep conditions", pp. 191–199 in *Mechanics of material behavior*, edited by G. Dvorak and R. Shield, Elsevier, Amsterdam, 1984.

[La Borderie 1991] C. La Borderie, *Phénomènes unilatéraux dans un matériau endommageable: modélisation et application à l'analyse de structure en béton*, Thèse doctorat, Université de Paris VI, Paris, 1991.

[La Borderie et al. 1991] C. La Borderie, G. Pijaudier-Cabot, and J. Mazars, "Response of plain and reinforced concrete structures under cyclic loadings", Rapport Interne 123, Laboratoire de Mécanique et Technologie, Cachan, France, 1991.

[Lemaitre and Chaboche 1974] J. Lemaitre and J. L. Chaboche, "A non-linear model of creep-fatigue damage cumulation and interation", in *Iutam symp. of mechanics of viscoelastic media and bodies*, Springer, Gothenburg, 1974.

[Lemaitre and Chaboche 1985] J. Lemaitre and J. C. Chaboche, *Mécanique de matériaux solides*, Dunod-Bordas, Paris, 1985.

[Maier et al. 1973] G. Maier, L. De Donato, and L. Corradi, "Inelastic analysis of reinforced concrete frames by quadratic programming", pp. 265–288 in *Symp. on inelasticity and nonlinearities in struct. concr.*, Univ. of Waterloo, Canada, 1973.

[Marigo 1985] J. J. Marigo, "Modeling of brittle and fatigue damage for elastic material by growth of microvoid", *Eng. Fract. Mech.* **21** (1985), 861.

[Mazars 1984] J. Mazars, *Application de la mécanique de l'endommagement au comportement non linéaire et à la rupture du béton de structure*, Thèse (Doctorat d'etat), Université Paris 6, Paris, 1984.

[Mazars et al. 2000] J. Mazars, F. Ragueneau, and G. Pijaudier-Cabot, "Continuum damage modelling for concrete structures in dynamic situations", pp. 259–294 in *Continuum damage mechanics of materials*, Damage mechanics of materials and structures, Cachan, France, 2000. Cachan, CNRS. 36p.(Lectures series), 2000.

[Mulas and Filippou 1990] M. G. Mulas and F. C. Filippou, "Analytical procedures in the study of seismic response of reinforced concrete frames", *Eng. Struct.* **12** (Jan. 1990), 37–48.

[Murakami 1981] S. Murakami, "Effects os cavity distribution in constitutive equations of creep and creep damage", in *Euromech colloque on damage mechanics*, Cachan, France, 1981.

[Ortiz and Simo 1986] M. Ortiz and J. C. Simo, "An analysis of a new class of integration algorithms for elastoplastic constitutive relations", *Int. J. Numer. Methods Eng.* **23** (1986), 353–366.

[Ragueneau et al. 2000] F. Ragueneau, C. La Borderie, and J. Mazars, "Damage model for concrete-like materials coupling cracking and friction, contribution towards structural damping: first uniaxial applications", *Mech. Cohes.-Frict. Mat.* **5** (2000), 607–625.

[Riva and Cohn 1990a] P. Riva and M. Z. Cohn, "Engineering approach to non-linear analysis of concrete structures", *J. Struct. Div., ASCE* **116**:8 (1990), 2162–2185.

[Riva and Cohn 1990b] P. Riva and M. Z. Cohn, "Engineering approach to non-linear analysis of concrete structures", *J. Struct. Div., ASCE* **116**:8 (1990), 2162–2185.

[Simo and Ju 1987] J. C. Simo and J. W. Ju, "Stress and strain based continuum damage models, I: Formulation", *Int. J. Solids Struct.* **23** (1987), 821.

[Tai 1990] W. H. Tai, "Plastic damage and ductile fracture in mild steels", *Eng. Fract. Mech.* **37** (1990), 853.

Francisco Adriano de Araújo: fco-adriano@bol.com.br
Escola de Engenharia de São Carlos, Departamento de Engenharia de Estruturas, Av. Trabalhador São-carlense, 400, 13566-590 São Carlos SP, Brazil

Sergio Persival Baroncini Proença: persival@sc.usp.br
Escola de Engenharia de São Carlos, Departamento de Engenharia de Estruturas, Av. Trabalhador São-carlense, 400, 13566-590 São Carlos SP, Brazil
http://www.set.eesc.usp.br/public/pessoas/professor.php?id=23

SUBMISSION GUIDELINES

ORIGINALITY

Authors may submit manuscripts in PDF format on-line. Submission of a manuscript acknowledges that the manuscript is *original and has neither previously, nor simultaneously, in whole or in part, been submitted elsewhere.* Information regarding the preparation of manuscripts is provided below. Correspondence by email is requested for convenience and speed. For further information, write to:

LANGUAGE

Manuscripts must be in English. A brief abstract of about 150 words or less must be included. The abstract should be self-contained and not make any reference to the bibliography. Also required are keywords and subject classification for the article, and, for each author, postal address, affiliation (if appropriate), and email address if available. A home-page URL is optional.

FORMAT

Authors are encouraged to use LaTeX and the standard article class, but submissions in other varieties of TeX, and, exceptionally in other formats, are acceptable. Electronic submissions are strongly encouraged in PDF format only; after the refereeing process we will ask you to submit all source material.

REFERENCES

Bibliographical references should be listed alphabetically at the end of the paper and include the title of the article. All references in the bibliography should be cited in the text. The use of BibTeX is preferred but not required. Tags will be converted to the house format (see a current issue for examples), however, in the manuscript, the citation should be by first author's last name and year of publication, e.g. "as shown by Kramer, et al. (1994)". Links will be provided to all literature with known web locations and authors are encouraged to provide their own links on top of the ones provided by the editorial process.

FIGURES

Figures prepared electronically should be submitted in Encapsulated PostScript (EPS) or in a form that can be converted to EPS, such as GnuPlot, Maple, or Mathematica. Many drawing tools such as Adobe Illustrator and Aldus FreeHand can produce EPS output. Figures containing bitmaps should be generated at the highest possible resolution. If there is doubt whether a particular figure is in an acceptable format, the authors should check with production by sending an email to:

production@mathscipub.org

Each figure should be captioned and numbered so that it can float. Small figures occupying no more than three lines of vertical space can be kept in the text ("the curve looks like this:"). It is acceptable to submit a manuscript with all figures at the end, if their placement is specified in the text by means of comments such as "Place Figure 1 here". The same considerations apply to tables.

WHITE SPACE

Forced line breaks or page breaks should not be inserted in the document. There is no point in your trying to optimize line and page breaks in the original manuscript. The manuscript will be reformatted to use the journal's preferred fonts and layout.

PROOFS

Page proofs will be made available to authors (or to the designated corresponding author) at a web site in PDF format. Failure to acknowledge the receipt of proofs or to return corrections within the requested deadline may cause publication to be postponed.